Technical Report Documentation Page

1. Report No.	2. Government Accession No.	3. Recipient's Catalog No.
FHWA/TX-99/1391-1		

4. Title and Subtitle	5. Report Date
LONG-TERM BEHAVIOR OF GROUND ANCHORS AND TIEBACK WALLS	November 1998
	6. Performing Organization Code

7. Author(s)	8. Performing Organization Report No.
Jean-Louis Briaud, Richard Griffin, Albert Yeung, Alfonso Soto, Abdul Suroor, and Heemun Park	Report 1391-1

9. Performing Organization Name and Address	10. Work Unit No. (TRAIS)
Texas Transportation Institute The Texas A&M University System College Station, Texas 77843-3135	11. Contract or Grant No. Project No. 0-1391

12. Sponsoring Agency Name and Address	13. Type of Report and Period Covered
Texas Department of Transportation Research and Technology Transfer Office P. O. Box 5080 Austin, Texas 78763-5080	Research: September 14, 1995 - August 31, 1998
	14. Sponsoring Agency Code

15. Supplementary Notes

Research performed in cooperation with the Texas Department of Transportationand the U.S. Department of Transportation, Federal Highway Administration.

Research Study Title: Long-Term Behavior of Ground Anchors and Tieback Walls

16. Abstract

The purpose of this project is to advance the state of knowledge on the long-term behavior of ground anchors and make practical recommendations. Two important issues were addressed: long-term movements and corrosion.

For the long-term movements, some of the main findings from the physical and numerical simulations are: 1. Given the same total anchor length, grouted anchors with a short tendon bond length have higher capacities and lower creep rates than grouted anchors with a long tendon bond length. 2. The capacity of grouted anchors in a stiff clay was found to increase over five years even when under load over the five years. 3. The power law model $s_1/s_2=(t_1/t_2)^n$ where s_1 and s_2 are the anchor movements at time t_1 and t_2 fit the data well and may be used to predict long-term movements. 4. A delayed failure occurred in triaxial tests on a clay when the stress level was larger than the yield stress of the soil. 5. Long-term horizontal movements can develop in anchored walls if the vertical capacity of the soldier piles is not sufficient to resist the downdrag from the retained soil. 6. The power law model can also be used for the long-term movement of walls. 7. The bending moment profile over the long term tends to shift towards smaller moments at the anchor points. 8. The anchor loads seem to vary very little as a function of time (±10% after five years). 9. An earth pressure coefficient chart is given to design anchored walls for a targeted deflection.

For the corrosion issues, some of the main findings from the laboratory tests and literature review are: 1. Anchor failures have been reported and attributed primarily to a lack of protection and bending stresses. 2. About half of the failures occurred at the anchor head, half within the unbonded length, and very few within the bonded length. 3. The time to failure varied from a few weeks to 31 years. 4. The usual indicators of corrosion were confirmed by laboratory tests: soil resistivity, soil pH. 5. The Electrochemical Impedance Spectroscopy test (EIS) is proposed for measuring the corrosion rate for a given soil. 6. The EIS tests performed in the laboratory showed that the corrosion rate of the steel varies drastically for various protection coatings from 0.34 mm/yr for no protection to 10^{-8} mm/yr for fusion bonded epoxy with 3×10^{-3} mm/yr for grout cover. 7. The time to failure of an anchor can be estimated once the corrosion rate is known.

17. Key Words	18. Distribution Statement
Long-term Behavior, Ground Anchors, Tieback Walls, Anchored Walls, Grouted Anchors, Clay, Sand, Load Tests, Full Scale Wall, Finite elements, Triaxial Tests, Corrosion, Protection Systems, pH, Resistivity, Electrochemical Impedance Spectroscopy Test, Corrosion Rates	No restrictions. This document is available to the public through NTIS: National Technical Information Service 5285 Port Royal Road Springfield, Virginia 22161

19. Security Classif.(of this report)	20. Security Classif.(of this page)	21. No. of Pages	22. Price
Unclassified	Unclassified	280	

LONG TERM BEHAVIOR OF GROUND ANCHORS AND TIEBACK WALLS

by

Jean-Louis Briaud
Research Engineer
Texas Transportation Institute

Richard Griffin
Associate Professor
Texas A&M University

Albert Yeung
Engineer
Binnie Black & Veatch, Hong-Kong Limited

Alfonso Soto
Graduate Assistant Research
Texas Transportation Institute

Abdul Suroor
Graduate Assistant Research
Texas Transportation Institute

and

Heemun Park
Graduate Assistant Research
Texas Transportation Institute

Report 1391-1
Project Number 1391
Research Project Title: Long-Term Behavior of Ground Anchors and Tieback Walls

Sponsored by the
Texas Department of Transportation
In cooperation with the
U.S. Department of Transportation
Federal Highway Administration

November 1998

TEXAS TRANSPORTATION INSTITUTE
The Texas A&M University System
College Station, Texas 77843-3135

IMPLEMENTATION RECOMMENDATIONS

1. In the case of grouted anchors, make use of short tendon bond lengths (see Sections 2.2.8, 2.2.9, 2.5.2 (13), and Figure 99).

2. Do not rely on a reload test to accept an anchor (see Section 2.2.10 and Figures 34a and 35).

3. Use the power law model ($s_1/s_2 = (t_1/t_2)^n$) to predict the long-term movement of anchors and tieback walls from the knowledge of short-term movements (see Section 2.2.11 and Figures 41 to 46). For anchors the n value in this study varied from 0.002 to 0.015; for the wall in this study the n value was about 0.1.

4. For tieback walls, ensure that the resistance of the soldier piles below the excavation level is sufficient to minimize the vertical settlement due to downdrag (see Section 2.5.2(3) and Figures 62, 63, and 76).

5. Use the earth pressure coefficient vs. normalized wall displacement charts to select anchor loads on the basis of allowable deflections (see Figures 96 and 97).

6. Make use of soil resistivity and soil pH values to estimate corrosion potential (see Tables 14 to 17).

7. Make use of the Electrochemical Impedance Spectroscopy test to estimate the corrosion rate and anchor life for a given soil and a given protection system.

8. Ensure that anchors are properly protected particularly near the anchor head and along the unbonded length.

9. Investigate the influence of reloading on the long-term creep behavior of ground anchors (load tests).

10. Investigate the possibility of delayed failure on anchors (load tests).

11. Develop a method to predict the power law model n value from soil tests.

12. Develop instruments to measure soil pH and soil resistivity in the field.

13. Make use of sacrificial anchors on projects for inspection as a function of time.

DISCLAIMER

The contents of this report reflect the views of the authors who are responsible for the facts and accuracy of the data presented herein. The contents do not necessarily reflect the official views or policies of the Texas Department of Transportation (TxDOT) or the U.S. Department of Transportation, Federal Highway Administration. This report does not constitute a standard, specification, or regulation. In addition, the above assumes no liability for its contents or use thereof.

ACKNOWLEDGMENT

This project was sponsored by the Texas Department of Transportation in cooperation with the U.S. Department of Transportation, Federal Highway Administration. Mr. Mark McClelland was the project director for TxDOT; his positive attitude and his technical input were very much appreciated. Mr. Giancarlo Santerelli of Bencor and Mr. Dave Weatherby of Schnabel Foundations were special consultants on this project; their experience with full scale anchors and their support with field work is very much appreciated. Dr. Radakrishna of Prairie View A&M University and his team reviewed the literature on permanent ground anchors; their contribution is very much appreciated. This project benefitted from a recently completed project sponsored by the Federal Highway Administration (FHWA) and Schnabel Foundation; Mr. Al DiMillio at FHWA and Mr. Dave Weatherby of Schnabel are thanked for their inspiring support. This report was proofread and edited by Mrs. Patsy Astle; her attention to details and her contagious good humor are very much appreciated.

TABLE OF CONTENTS

TABLE OF CONTENTS (continued)

TABLE OF CONTENTS (continued)

TABLE OF CONTENTS (continued)

TABLE OF CONTENTS (continued)

TABLE OF CONTENTS (continued)

LIST OF FIGURES

LIST OF FIGURES (continued)

LIST OF FIGURES (continued)

LIST OF FIGURES (continued)

LIST OF FIGURES (continued)

LIST OF TABLES

1. INTRODUCTION

Ground anchors are used for temporary and permanent structures. The purpose of this project is to advance the state of knowledge on the long-term behavior of permanent ground anchors and make practical recommendations on the basis of the findings.

Two important issues related to the long-term behavior of ground anchors are long-term movements and corrosion. These two issues are addressed in chapters 2 and 3 respectively. The long-term movement issue is studied through laboratory tests on clay, field tests on full scale anchors at the Texas A&M University National Geotechnical Experimentation Site (clay site), and measurements over a five-year period on an instrumented full scale tieback wall at the Texas A&M University National Geotechnical Experimentation Site (sand site).

The corrosion issue is studied through a survey of failures, examination of full scale anchors at two sites, and a series of laboratory tests on corrosion rates under different soil and protection conditions.

2. LONG-TERM MOVEMENTS

The issue of long-term movement of ground anchors was studied in the laboratory and in the field.

2.1 LABORATORY TESTING

Several issues were addressed in the laboratory tests. The first one is the difference between constant rate of displacement (CRD) triaxial tests and constant load increment (CLI) triaxial tests. The second one is the accumulation of displacements under constant load in the triaxial test. The third one is the existence of a delayed failure threshold and how to predict it. This part of the study is detailed in Suroor et al. (1998).

2.1.1 CRD vs. CLI Triaxial Tests

Conventional triaxial tests are performed under a constant rate of displacement (CRD). Ground anchor tests on the other hand are performed under constant load increments (CLI). In order to study the difference between the two modes of loading, CRD and CLI triaxial tests were performed (Tables 1 and 2) on a prepared porcelain clay (Table 3). The engineering properties of this porcelain clay are summarized in Table 3.

The porcelain clay was prepared at 28% water content and then air dried to about 17% water content; indeed, at this water content the porcelain clay exhibited the behavior of an over-consolidated clay with post-peak softening. All triaxial tests were unconsolidated-undrained tests (UU) with about 35 kPa of confining pressure. The samples were 38 mm in diameter and about 80 mm in height. The displacement rate for the CRD tests was 0.23 mm/min. The loading rate for the CLI tests was a load increment every two minutes on the average with a total of between 10 and 15 increments to reach the peak strength.

Examples of CRD test results are shown in Figure 1 while examples of CLI tests are shown in Figure 2. The first observation is that the peak strength is quite sensitive to the water content since a change in water content from 16.2% to 17.9% can almost double the strength. The second observation is the difference in shape of the curves; the CRD curves show a classical bump with post-peak strain softening towards a residual strength while the CLI curves stop at the peak strength with no indication on the residual strength since failure occurs under that constant load. The word constant load is used instead of constant stress because the load is constant while the stress decreases slightly since the cross section area increases as the sample deforms. The third observation is that the strain to failure seems to be of comparable magnitude in both types of tests.

The undrained shear strength s_u obtained from both types of tests is compared in Figure 3. The figure indicates that s_u from CLI tests is slightly higher than s_u from CRD tests (32% on the average). In order to compare the complete response, the stress-strain curves were normalized and replotted (Figures 4 and 5), then an average CRD curve and an average CLI curve were generated. These average curves are compared in Figure 6; the comparison indicates a slightly stiffer response in the CLI test while the strain at failure is a little bit larger for the CLI test. These differences

Table 1. Details of Constant Rate of Displacement (CRD) Tests

Test #	Test Cond.	Type of Soil	Final w, %	Confin./ Back Pressure, kPa	Peak Deviator Stress, kPa	Axial Strain at Failure, %	Rate of Displacement, mm/min	Behavior Obtained/ Remarks
UCRD-1	CD	Natural clay	31	40	132	2.9	0.064	OC
UCRD-2	CD	"	30	10/3	317	3.25	0.064	OC w/BP
UCRD-3	CD	"	22.9	28/23	61	5.4	0.064	OC w/BP
UCRD-4	CD	"	23	28/23	134	12.1	0.064	OC w/BP
UCRD-5	CD	"	23.6	28/24	270	2.5	0.064	OC w/BP
PRCD-7	CU	Porcelain	25	35	150	7.5	0.064	OC
PRCD-8	CU	"	21.4	53	184	14.2	0.064	NC
PRCD-9	UU	"			1719	2.6	0.23	
PRCD-10	UU	"	17.9	35	1039	9.9	0.23	Brittle
PRCD-11	UU	"	20.4	35	338	11.2	0.23	OC
PRCD-12	UU	"	19.5	35	425	18.2	0.23	NC
PRCD-13	UU	"	13	70	745	9.2	0.23	Brittle
PRCD-14	UU	"	16.7	35	390	8.3	0.23	OC
PRCD-15	UU	"	11.4	35	971	8.1	0.23	Brittle
PRCD-16	UU	"	17.1	70	250	14.8	0.23	NC
PRCD-17	UU	"	18	35	175	9.4	0.23	OC
PRCD-18	UU	"	20.4	35	158	16.4	0.23	NC
PRCD-19	UU	"	19	35	237	13.3	0.23	OC
PRCD-20	UU	"	17.9	35	450	7.4	0.23	OC
PRCD-21	UU	"	17.3	35	653	16.7	0.23	NC
PRCD-22	UU	"	17.2	35	580	7.6	0.23	OC
PRCD-23	UU	"	17.2	28	510	9.6	0.23	OC
PRCD-24	UU	"	16.7	35	545	7.2	0.23	OC
PRCD-25	UU	"	16.2	35	805	6.9	0.23	OC
PRCD-26	UU	"	18.2	35	535	6.8	0.23	OC
PRCD-27	UU	"	18.6	35	412	5.9	0.23	OC
PRCD-28	UU	"	18.8	35	342	6.6	0.23	OC
PRCD-29	UU	"	18.6	50	560	4.7	0.23	OC
PRCD-30	UU	"	18.8	35			0.23	NC
PRCD-31	UU	"	18.4	35			0.23	NC w/PPET
PRCD-32	UU	"	17	35	560	7.9	0.23	OC w/PPET
PRCD-33	UU	"	16.4	35				
PRCD-34	UU	"					0.23	NC

Table 2. Constant Load Increment (CLI) Tests on Porcelain

Test #	Test Cond.	Type of Soil	Final w, %	Confin./ Pore Pressure, kPa	Peak/Failure Deviator Stress, kPa	Axial Strain at Failure, %	Load Increment, kg/min
PCLI-1	UU	Porcelain	16.7	35	858/839	9.5	8/2
PCLI-2	UU	"	18.5	35	390/368	15	8/3
PCLI-3	UU	"	17	35	729	14.9	4/2
PCLI-4	UU	"	17.8	35	737/730	12.9	4/2
PCLI-5	UU	"	17.1	35	838	8.8	8/1
PCLI-6	UU			35	759	11.6	8/1
PCLI-7	UU	"	16.2	35	915/903	9.7	8/3
PCLI-8	UU	"	17.8	35	596/567	15.8	8/3
PCLI-9	PPET/UU	"	18.6	35/28.5	502/496	14.8	8/3
PCLI-10	PPET/UU	"	18	35/27.9	525/503	9.3	8/3
PCLI-11	PPET/UU	"	18.1	35/31.8	529/515	13.6	8/3
PCLI-12	PPET/UU	"	17.5	35/31.7	592/569	12.1	8/3
UCLE-1	UU	Natural Clay		35	352	4.4	8/3

Table 3. Properties of the Porcelain Clay

Liquid limit, %	34.40
Plastic limit, %	20.25
Plasticity index (PI), %	14.15
Specific gravity	2.72
Water content, %	28.51
Shear strength, kPa	12.51 (mini vane)
Bulk unit weight (kN/m^3)	18.0
USCS soil classification	CL
pH	6.0
Electrical conductivity (mmhos/cm)	1.2

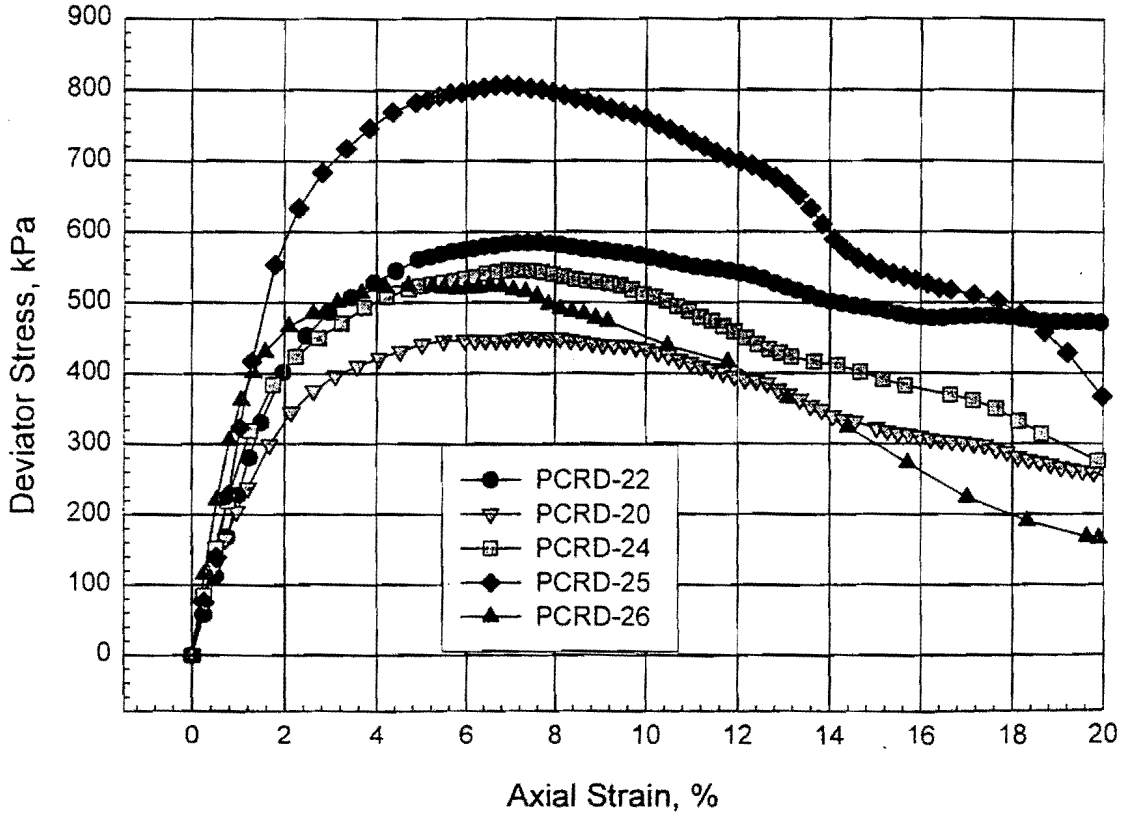

Figure 1. Examples of CRD Triaxial Tests

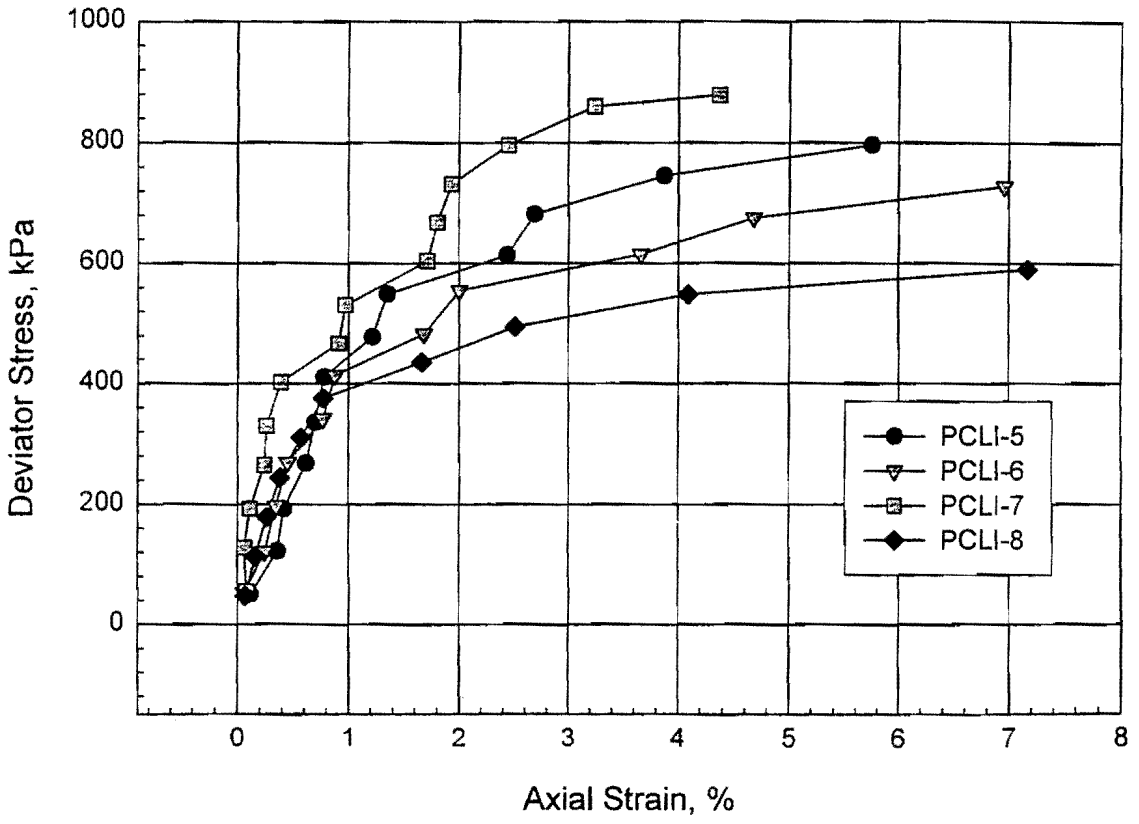

Figure 2. Examples of CLI Triaxial Tests7

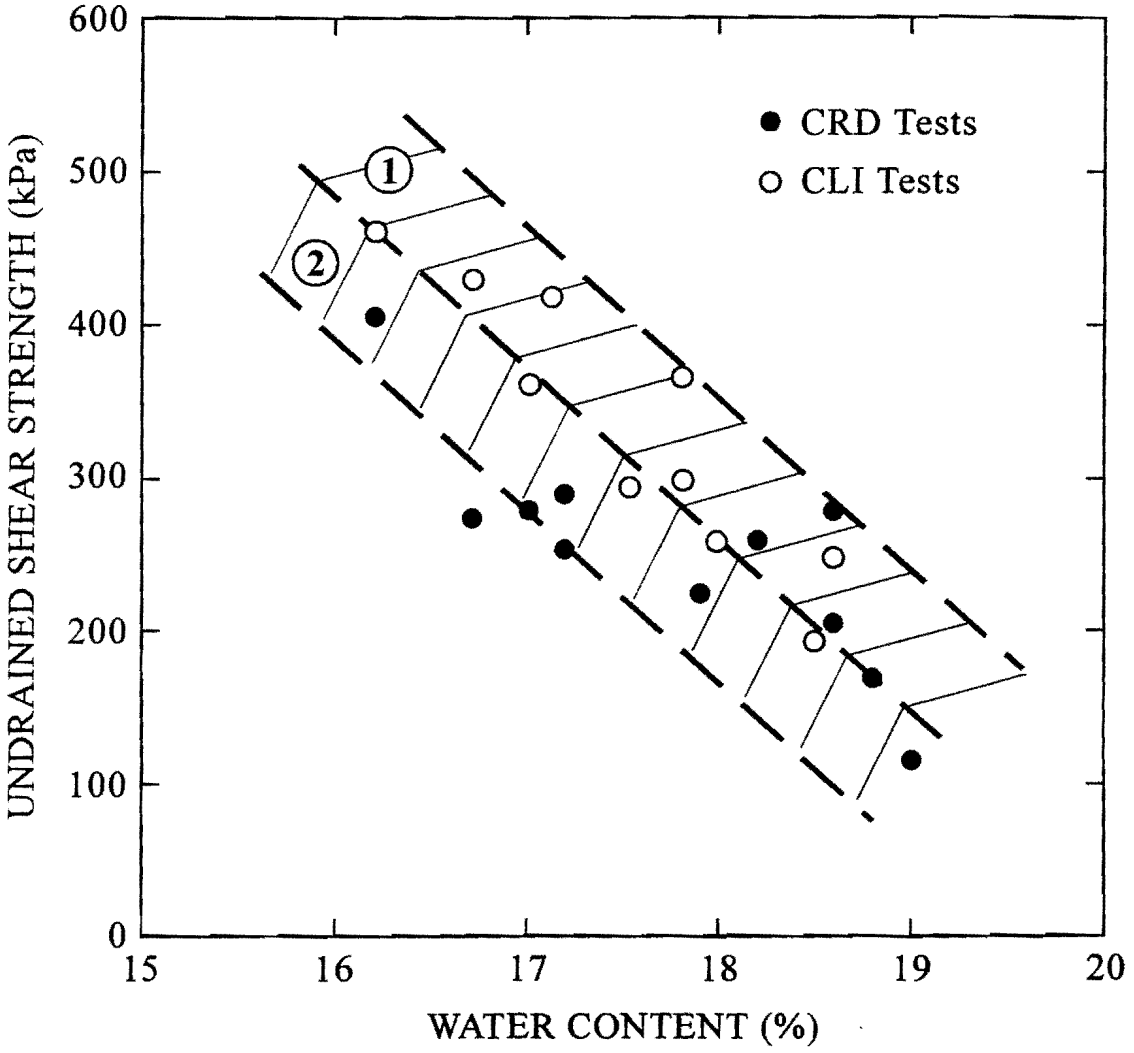

Figure 3. Examples of CLI and CRD Undrained Shear Strength

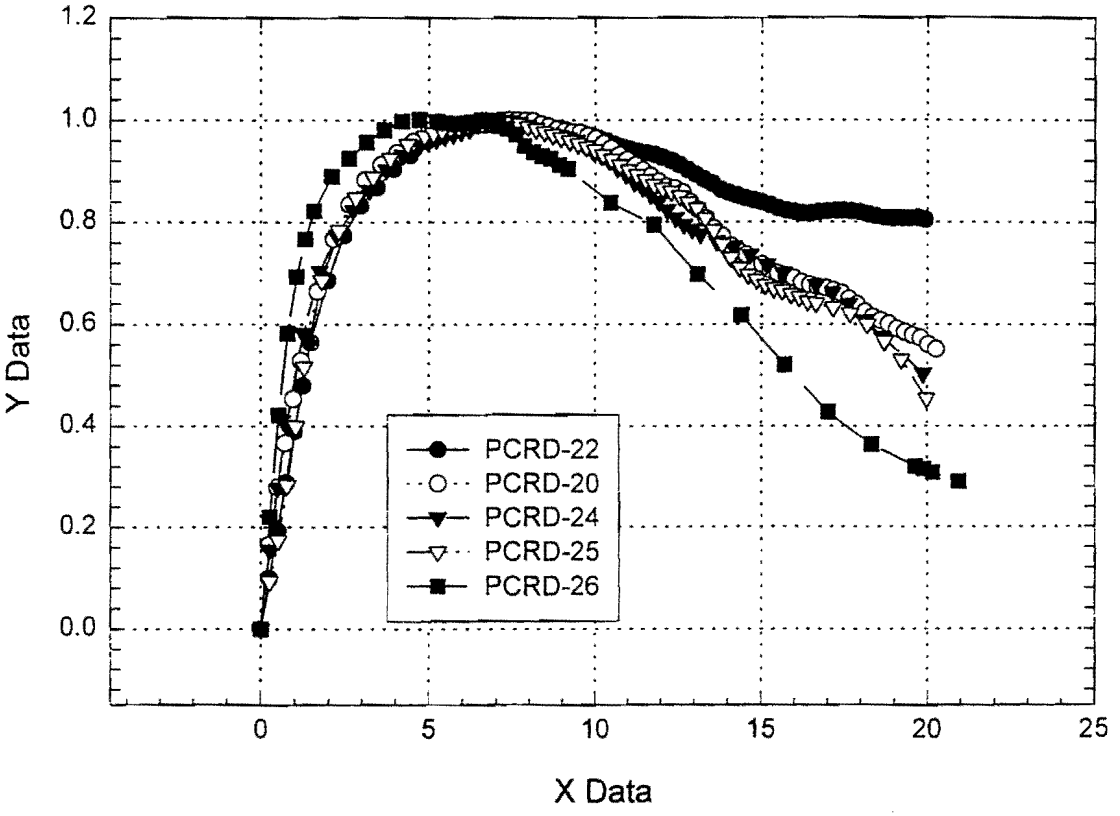

Figure 4. Normalized CRD Stress-Strain Curves

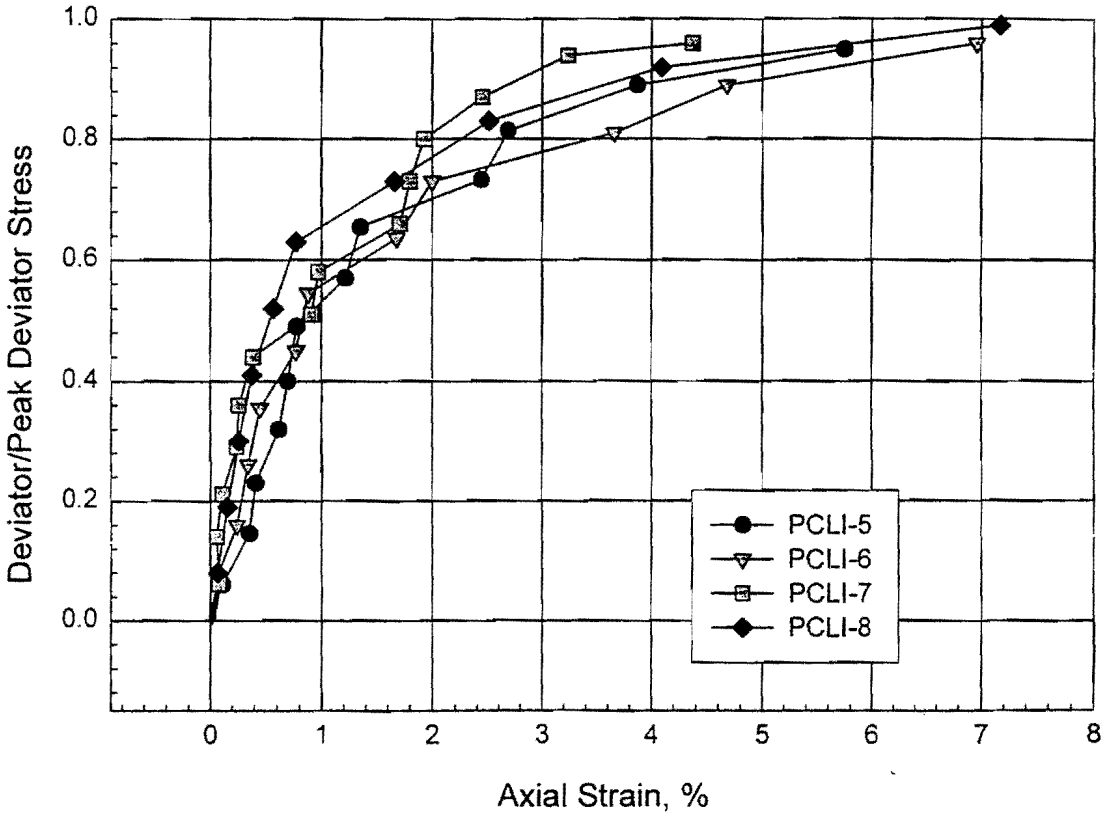

Figure 5. Normalized CLI Stress-Strain Curves

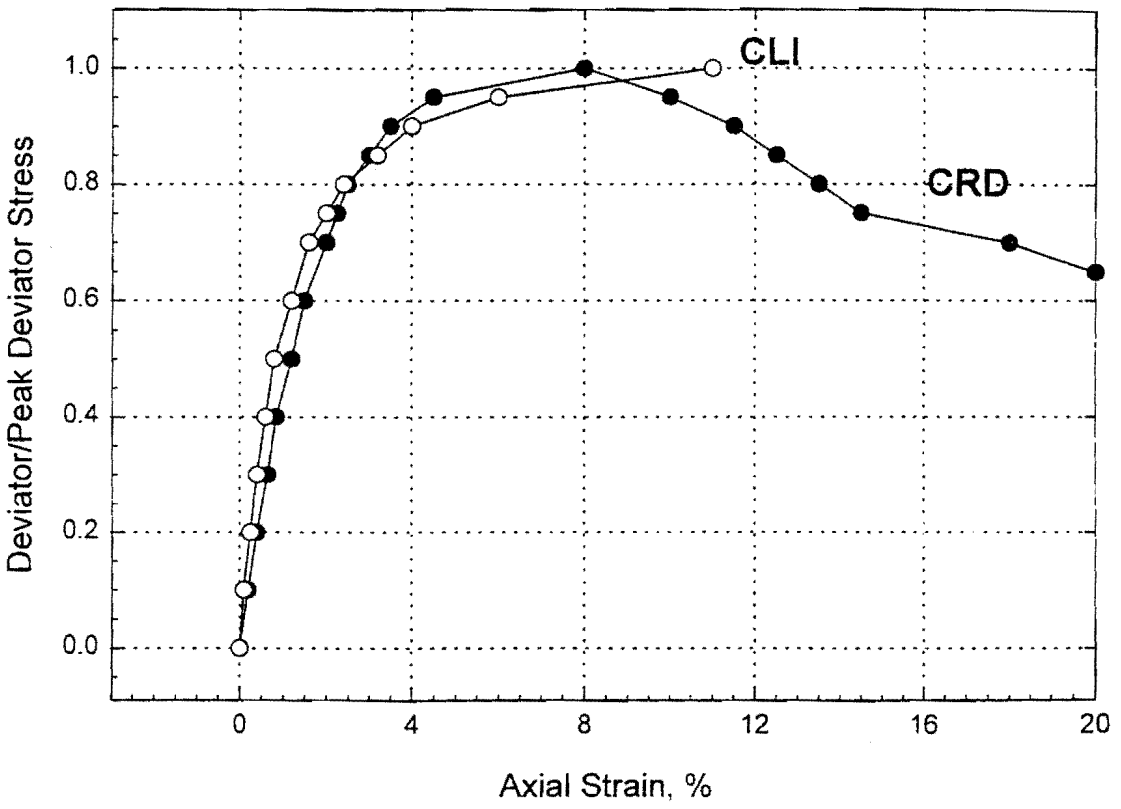

Figure 6. Comparison of Normalized CRD and CLI Curves

cannot be attributed to loading rate effects since the CRD test reached the peak strength in about 28 min (80 x 0.08/0.23 = length x strain: rate) while the CLI test reached the peak strength in 26 min (13 steps x 2 min/step).

In conclusion, these tests indicate that the CLI triaxial tests which are more representative of anchor loading conditions give higher strength and stiffness than the commonly used CRD triaxial tests.

2.1.2 Accumulation of Strain vs. Time, Delayed Failure

Besides the comparison with the CRD tests, the purpose of the CLI tests was to study the accumulation of strain vs. time and in particular the possibility of a delayed failure under a sustained load. Under a given load during the CLI test, the soil can exhibit one of three types of behavior: stable continuous deformation (Figure 7), gradual failure (Figure 8), or sudden delayed failure (Figure 9). The last two examples are shown as stress-strain curves on Figure 10. There is some indication that the stress-strain path taken by the sample under constant load (CLI tests) cuts across the hump identified in the CRD test.

The power law model has been proposed to describe the strain vs. time curves.

$$s = s_1 \left(\frac{t}{t_1}\right)^n \tag{1}$$

where s is the strain at time t and s_1 the strain at time t_1. The time t_1 is usually taken as one minute. A straight line on a log s/s_1 vs. log t/t_1 indicates that the model fits the data well and can be used to obtain the slope n. Figure 11 shows that the model fits the data well until high-stress levels. The value of n appears to increase linearly with the load level as shown on Figure 12.

2.1.3 Predicting the Delayed Failure

The possibility for a soil to fail suddenly after a continuous but apparently stable deformation process under a constant load is of concern. Indeed this is the type of loading that the soil is subjected to by a permanent ground anchor. Figure 9 shows a test where up until 1,000 minutes there was no indication of a possible failure; in fact the strain rate was consistently decreasing. However, at that point the strain rate started to increase and at 4,000 minutes the sample failed suddenly. This is an example of sudden delayed failure. Figure 8 shows another test where the strain rate essentially decreased until 3,000 minutes but then increased to a higher value. This is an example of gradual failure. At lower load levels, the tests lead to a strain rate which decreased until the end of the test. It appears that a threshold exists below which delayed failure under sustained load does not occur. Finding this threshold and predicting its value becomes important. Since Figure 10 indicates that the stress-strain path seems to cut across the hump of the CRD stress-strain curve, it was thought that the residual strength of the clay might well be the delayed failure threshold. The fact that the residual strength is not a clearly determined value made the use of the residual strength impossible. Indeed, the stress-strain curve continues to show a decrease in stress until 20% strain without a clear plateau.

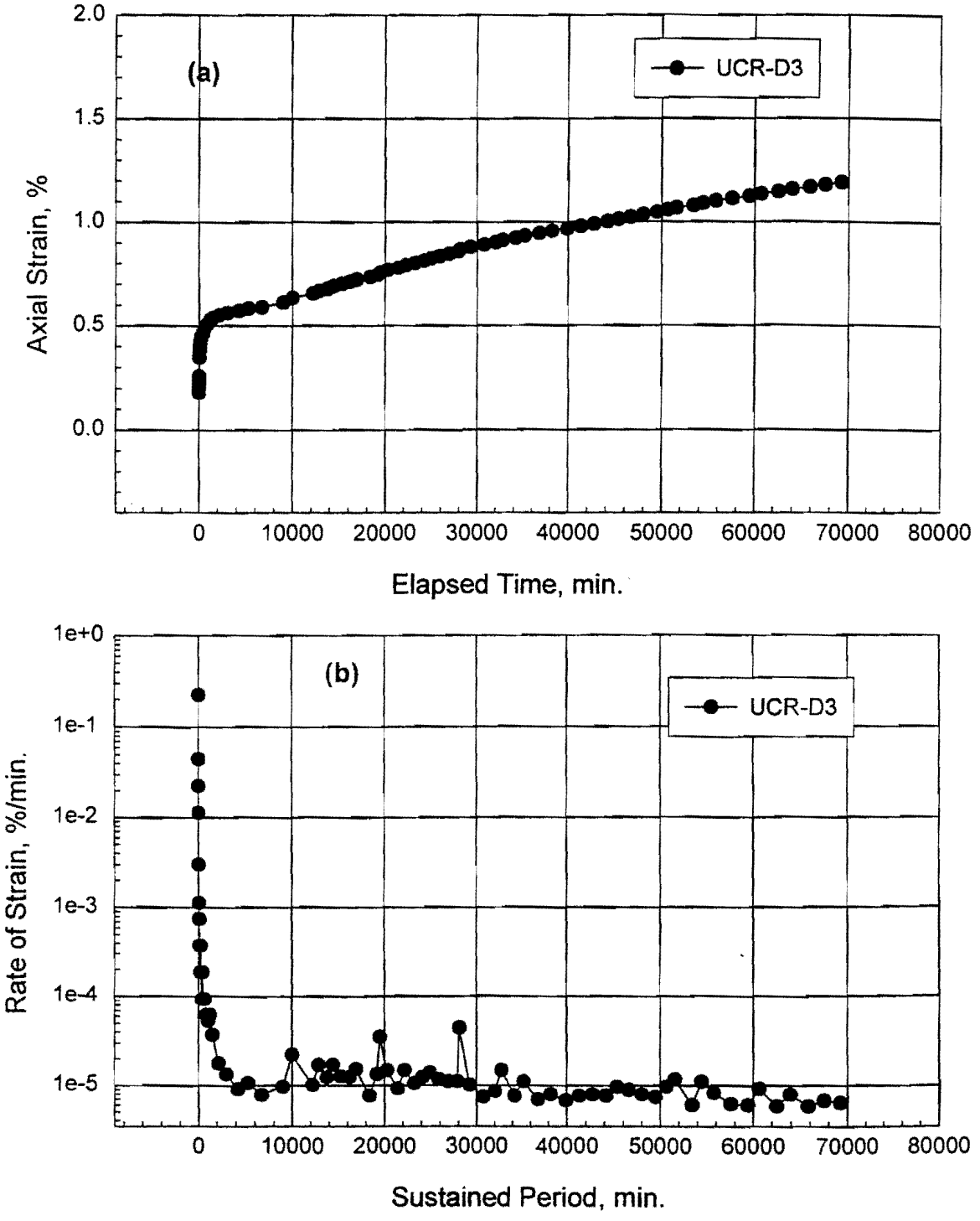

Figure 7. Stable Continuous Deformation

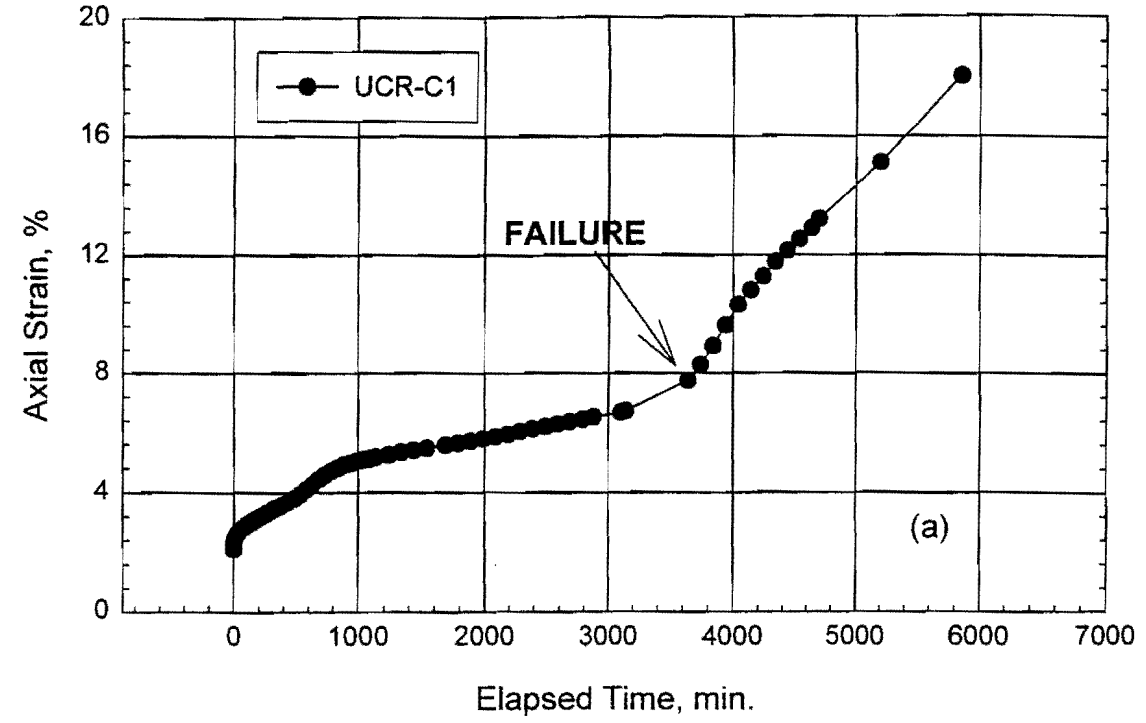

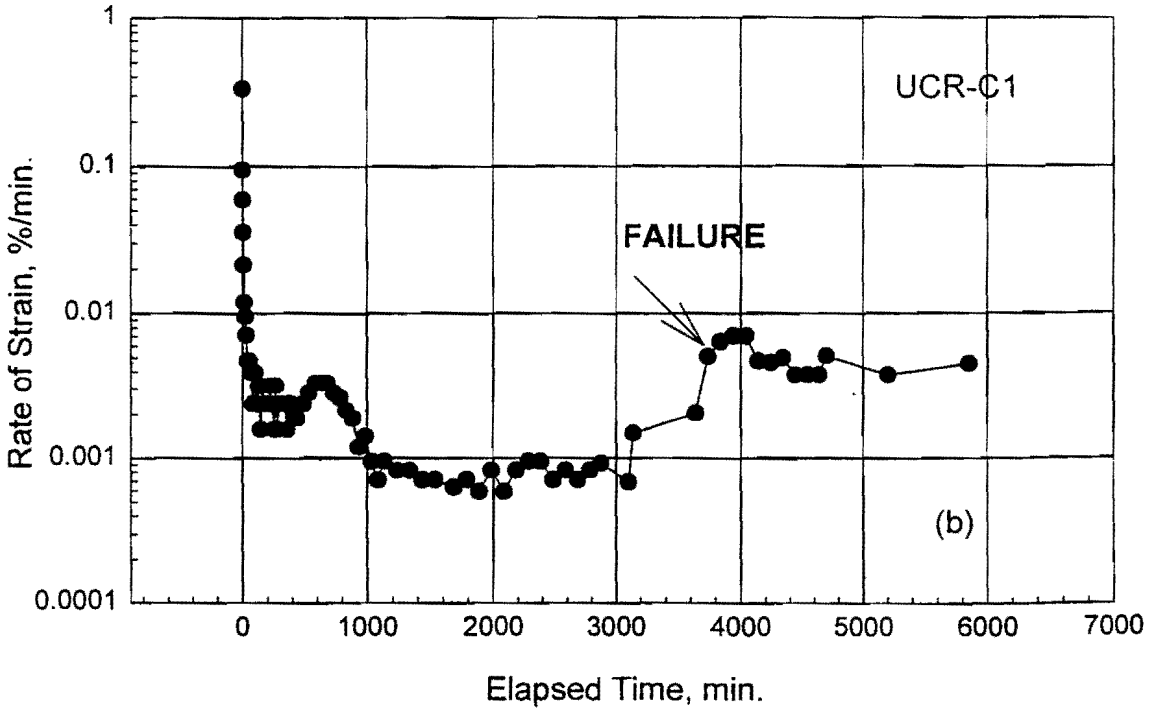

Figure 8. Gradual Failure

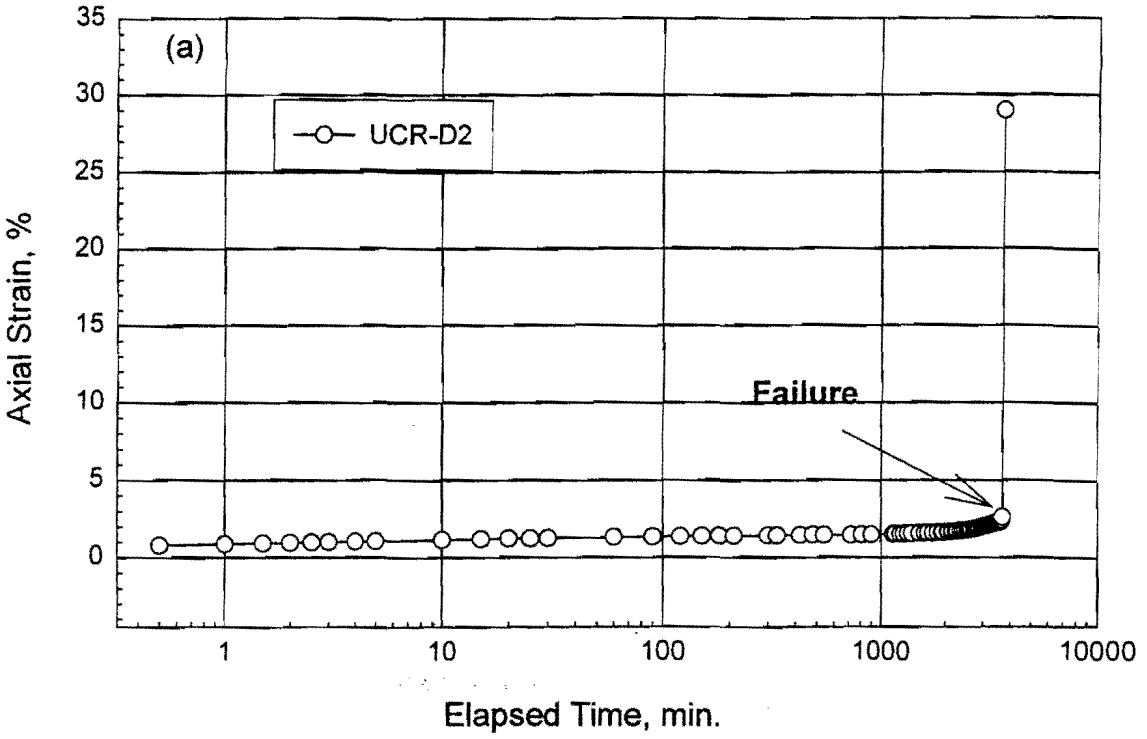

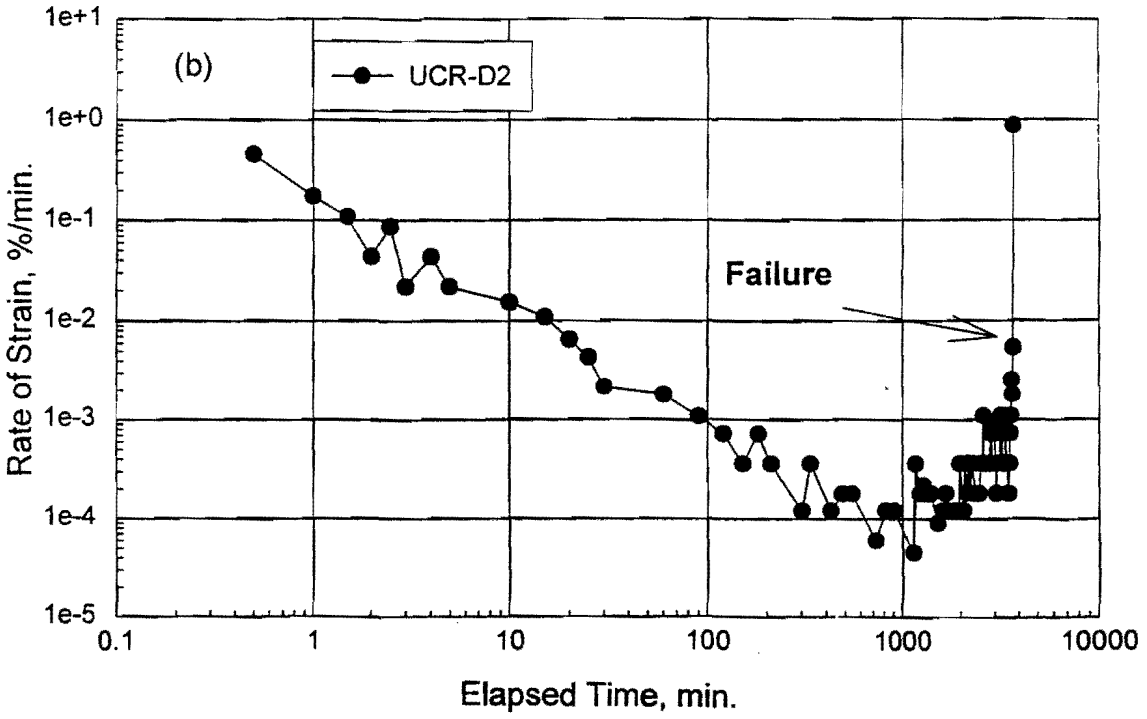

Figure 9. Sudden Delayed Failure

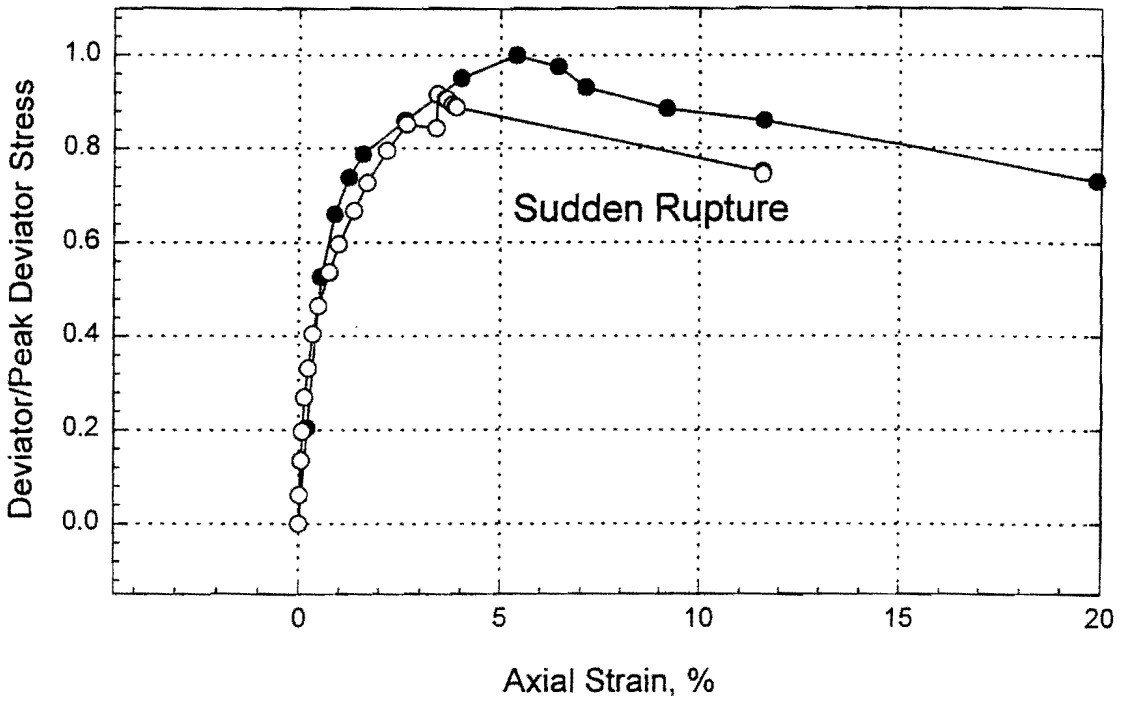

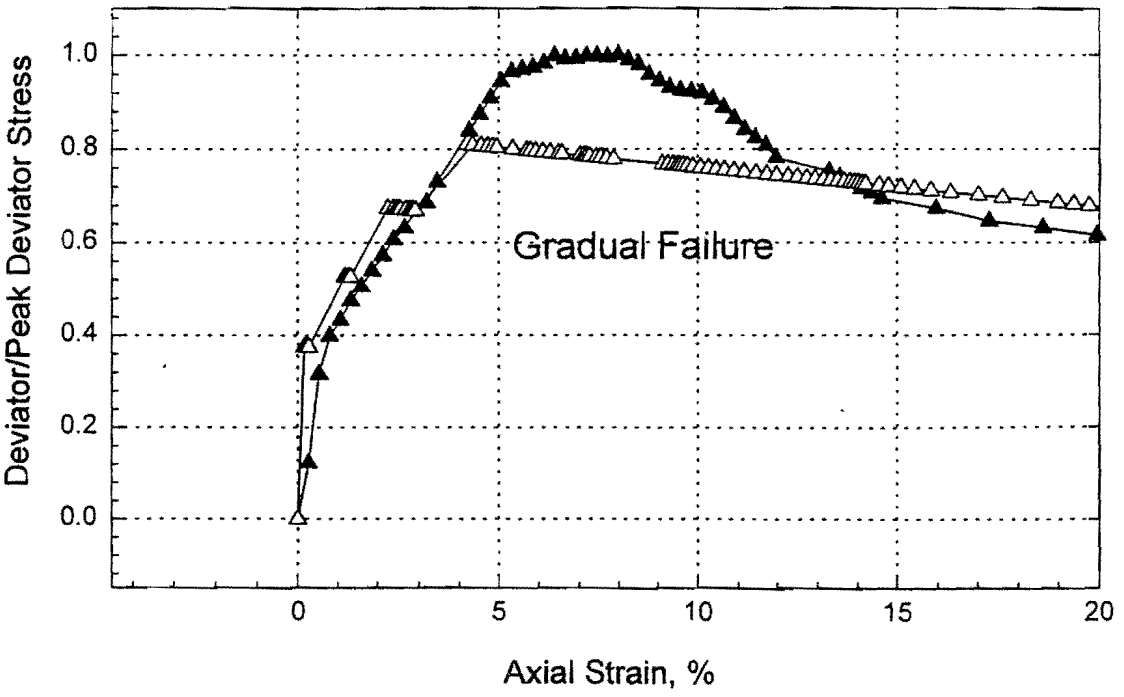

Figure 10. Failures Under Constant Load

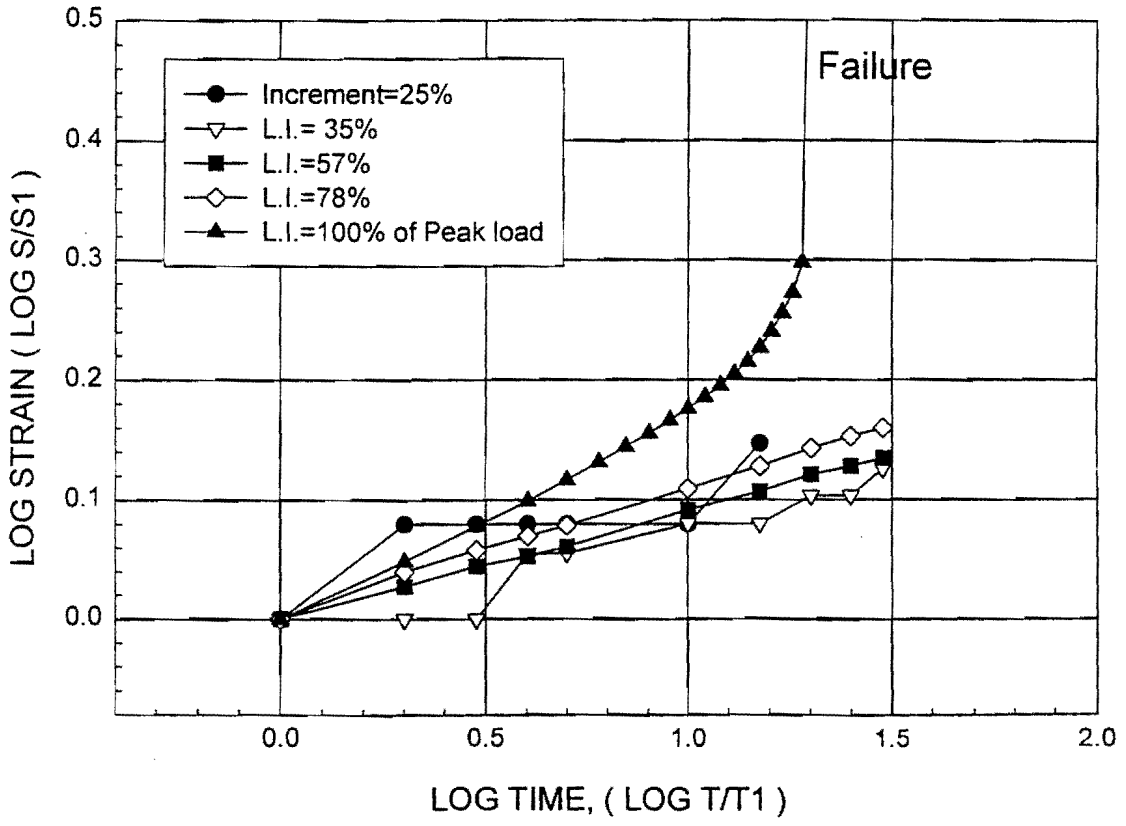

Figure 11. Log Strain vs. Log Time Plots

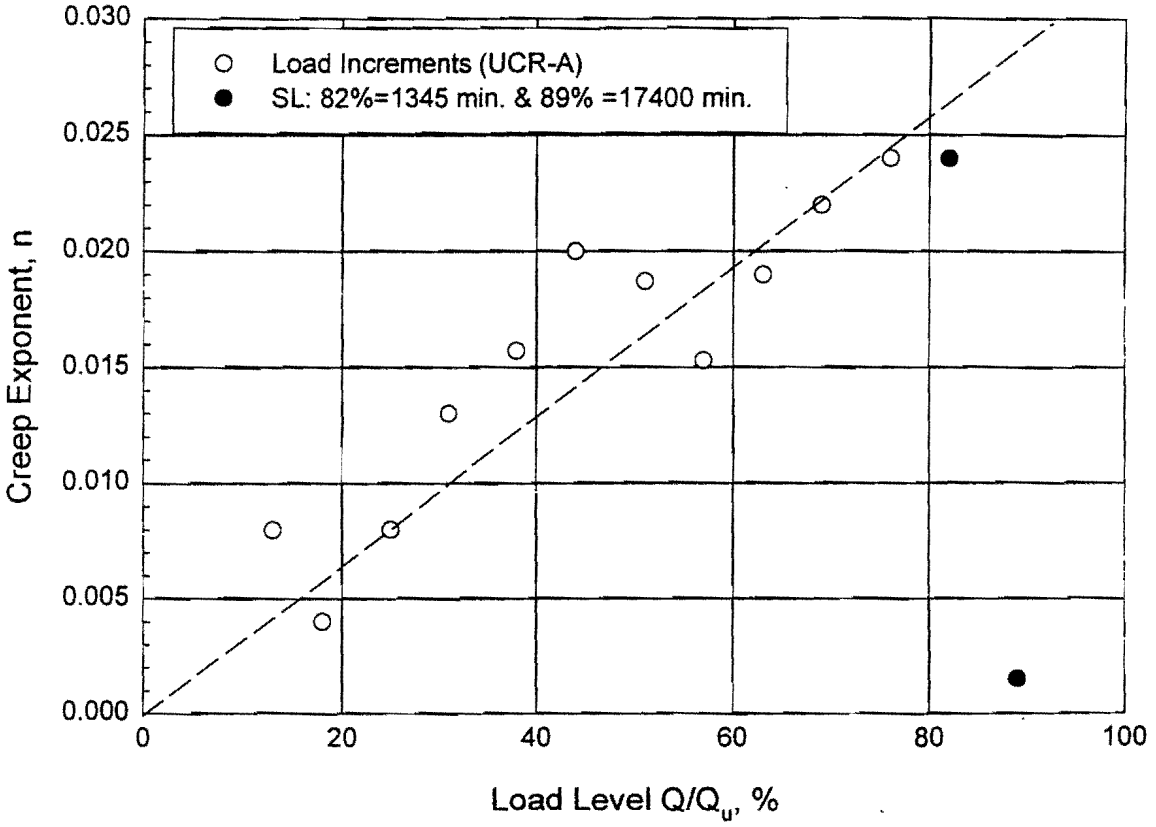

Figure 12. Time Exponent vs. Load Level

The yield strength of a clay is defined as the point before the peak of the log stress vs. log strain curve where the curvature is maximum (Figure 13). Figures 14, 15, and 16 show some examples of CLI test results where the stress level (SL) is compared to the yield strength (YL). The data tends to show that for a given soil when the stress level is above the yield strength, delayed failure occurs and when the stress level is at or below the yield strength, delayed failure does not occur. Furthermore, the time that it takes for the delayed failure to occur is related to the stress level. Figure 17 shows the ratio of sustained stress to yield strength as a function of the time to failure for different clays (Casagrande and Wilson, 1951). The time to the delayed failure decreases as the stress level increases.

Therefore, it appears that the yield strength of the clay represents a useful way of obtaining the stress threshold above which a delayed failure is likely to occur.

2.2 FIELD TESTING OF ANCHORS AT NGES - CLAY SITE

In order to investigate the long-term behavior of grouted anchors in clay, 10 full scale anchors were installed at the National Geotechnical Experimentation Site located at Texas A&M University. After a background, the soil at the NGES is described, then the anchors and load tests, then the influence of various factors on the behavior of the anchors including creep movements, then a comparison of the behavior in 1991 (Powers and Briaud, 1993) and 1997 (Soto, Briaud, and Yeung, 1997).

2.2.1 Background

The topic of permanent grouted anchors has been reviewed in a sequence of publications by the Federal Highway Administration (Nicholson et al., 1982; Otta et al., 1982; Pfister et al., 1982; and Weatherby, 1982) which culminated with the summary report by Cheney (1988).

The steps involved in the design of low pressure grouted straight shafted anchors in clay are as follows: first, the anchor direction and the design load Q_d are determined. For tieback walls, Q_d is determined from the earth pressure distribution exerted against the wall. Second, the required tendon cross section is established. Third, the anchor length L_a (Figure 18) necessary to resist safely the design load Q_d is calculated as:

$$L_a = \frac{Q_d \times F}{\pi D f_{max}} \qquad (2)$$

where F is the factor of safety, D the diameter of the anchor hole, and f_{max} the shear strength of the interface between the soil and the grout. Values of F reported in the literature vary from 1.6 to 3.0 (Bustamante and Doix, 1985, Canadian Foundation Engineering Manual, 1985, Otta et al., 1982, Cheney, 1988, Littlejohn, 1990). It is important to ensure that the anchor bond length, L_a, is adequate to support the design load and the proof test load without transferring axial force into the active failure zone. Fourth, the tendon bond length L_b (Figure 18) necessary to transfer the load from the steel tendon to the grout column is estimated. Fifth, the unbonded length L_u (Figure 18) is calculated so that the anchor length L_a is entirely outside the mass of soil which would be associated with a failure of the structure. Sixth, the compressive stress in the grout of the unbonded

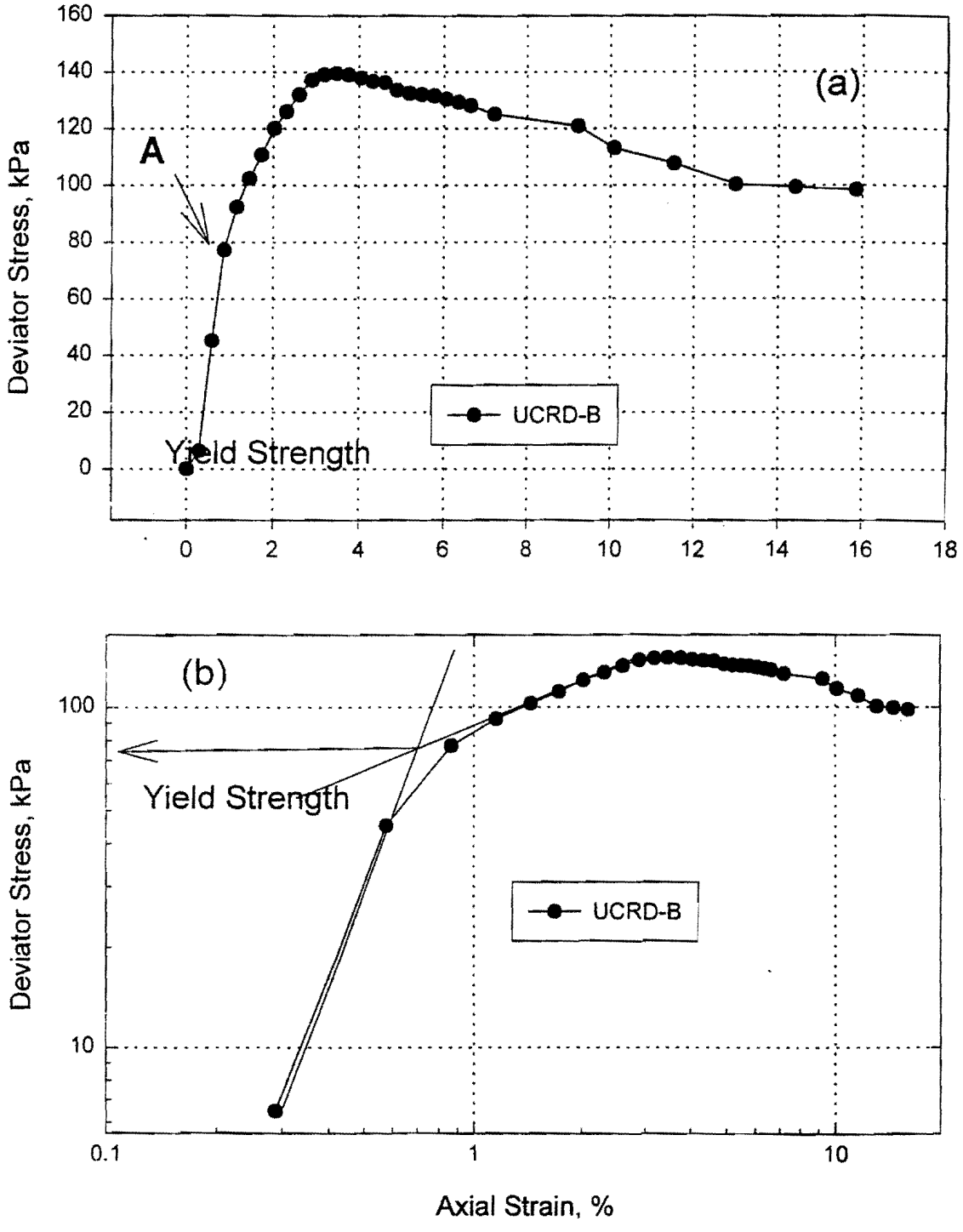

Figure 13. Definition of the Yield Strength

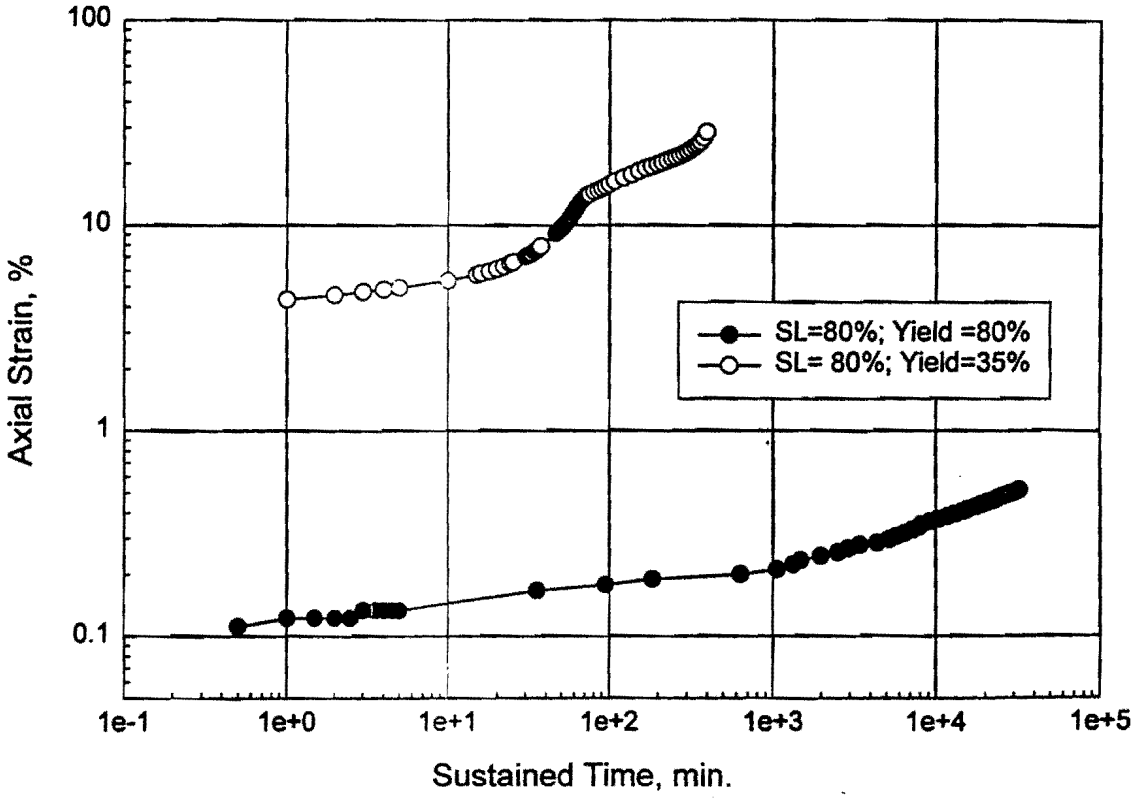

Figure 14. Strain vs. Time: Same Sustained Load, Different Yield Strengths

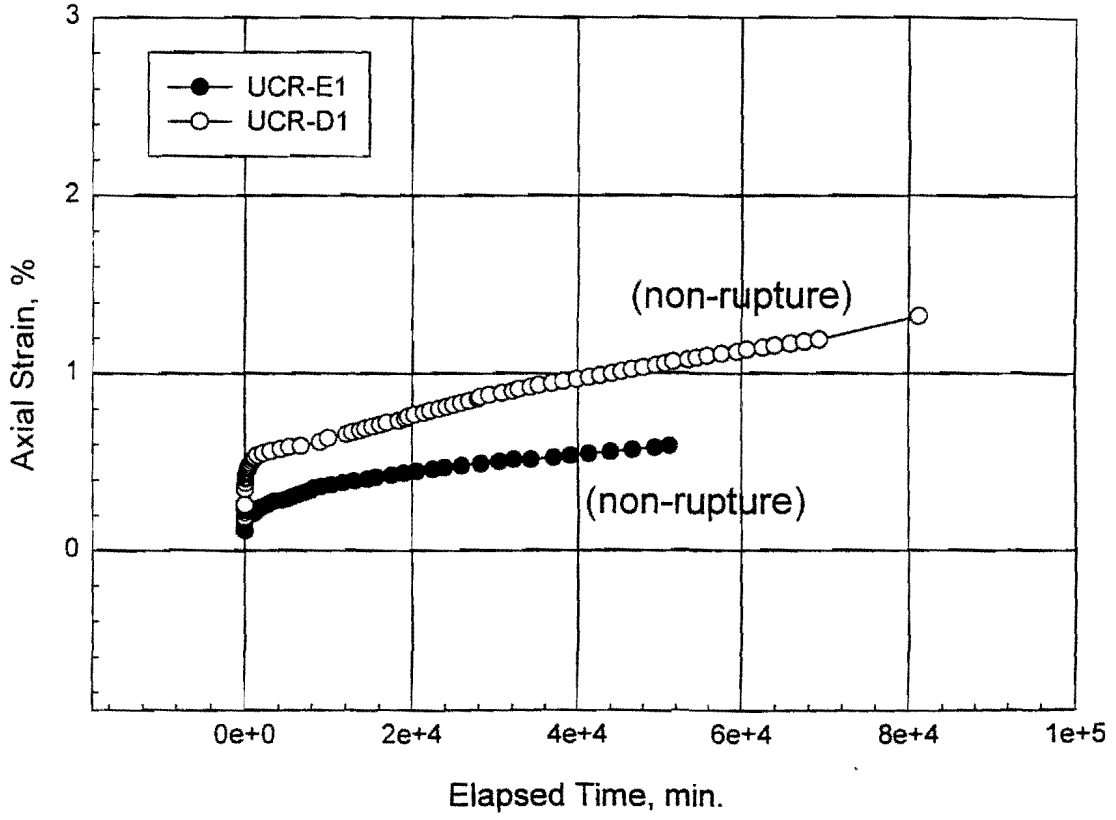

Figure 15. Strain vs. Time: Same Yield Strength, Different Sustained Load

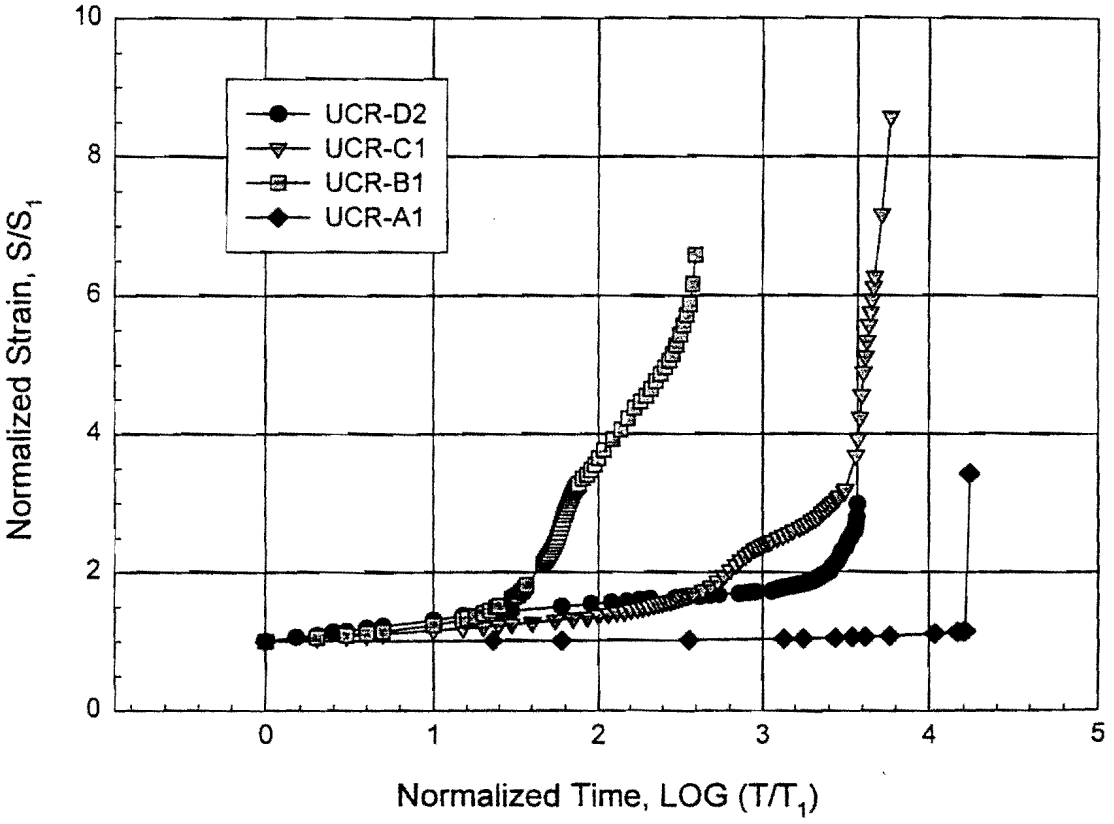

Figure 16. Strain vs. Time for Different Yield Strengths and Sustained Loads

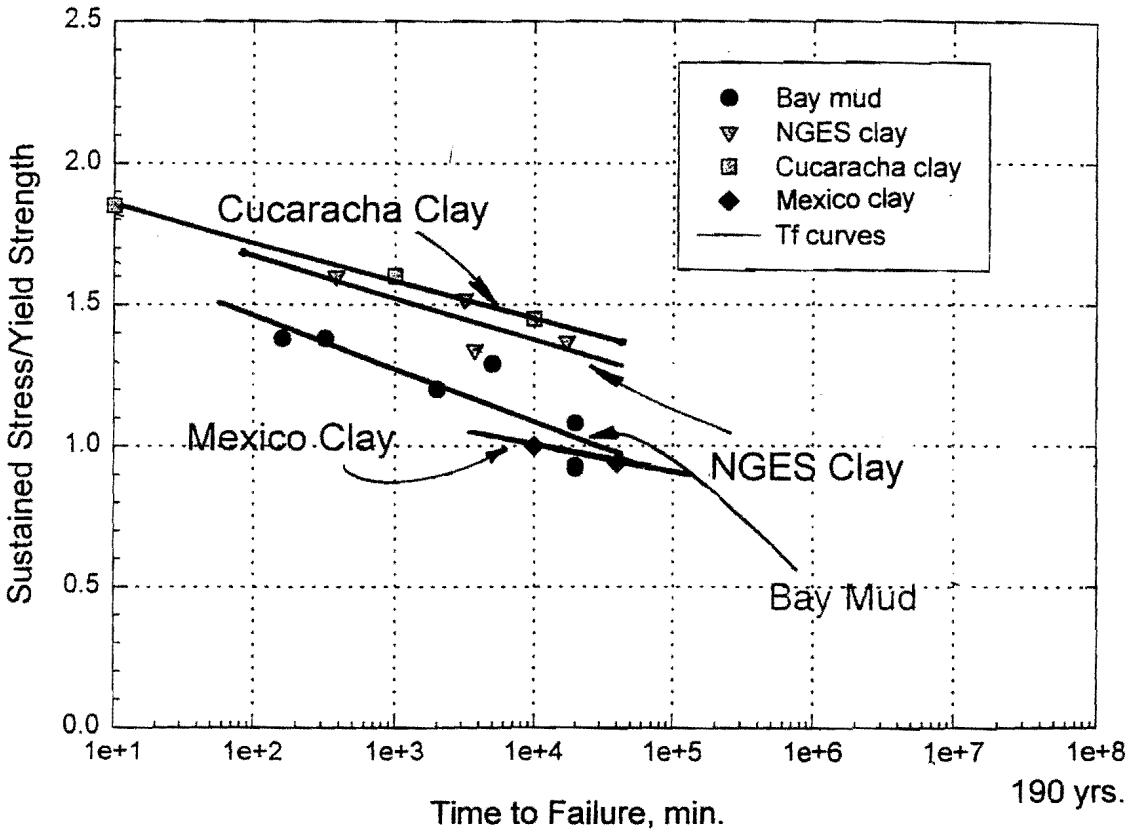

Figure 17. Stress Ratio vs. Time to Failure (after Casagrande and Wilson, 1951)

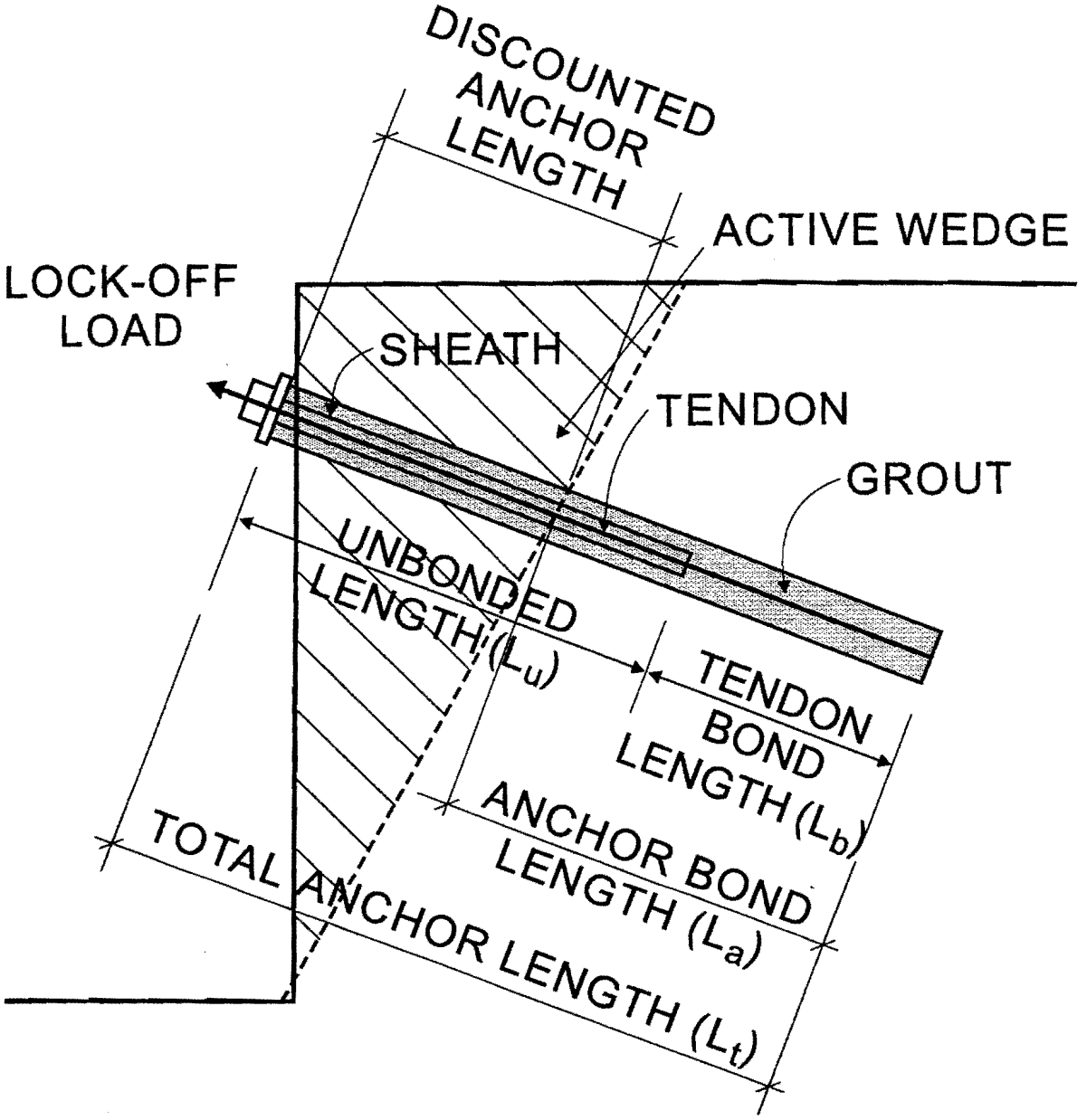

Figure 18. Schematic of Grouted Anchor

length must be within acceptable limits; this last condition is rarely a problem and often is not checked in design.

The construction of a grouted anchor consists of creating a hole, inserting a steel tendon (single bar or multi-strand), and injecting grout to fill the annulus between the tendon and the soil. The tendon is equipped with centralizers to keep the tendon in the center of the hole. The bottom part of the tendon length is bare and is directly bonded to the grout; this is the tendon bond length. The top part of the tendon length is in a grease-filled plastic sheath; this is the unbonded length.

The grouting is performed under pressure for pressure grouted anchors; further distinction is made here between high pressure, low pressure, and gravity tremie. Regroutable anchors are subjected to repeated injections after partial curing of the grout. The anchors in this study are low pressure grouted anchors in stiff clay. Once the anchor is constructed and the grout has cured, the anchor is proof tested in tension to demonstrate that under 1.33 Q_d the creep movement as a function of time is less than 2 mm per log cycle of time. Note that this limit corresponds to about 15 mm of movement in a 100-year period if the creep rate remains constant.

From the soil point of view then, two aspects are important: the ultimate resistance Q_u of the anchor, which involves the maximum unit skin friction, f_{max}, and the creep movement as a function of time under 1.33 Q_d.

2.2.2 Shear Strength of Soil Grout Interface, f_{max}

The following discussion is concerned with low pressure grouted and tremie grouted anchors in clays. The load which will fail the anchor at the soil-grout interface during a pull-out test mobilizes the shear strength, f_{max}, of that interface and is called here the ultimate load Q_u. An estimate of the anchor ultimate load Q_u is necessary before construction to ensure that the anchor design load Q_d can be carried safely by the soil. In design, the ultimate load Q_u is given by:

$$Q_u = \pi \, D \, L_a \, f_{max} = F_{max} \, L_a \qquad (3)$$

where F_{max} is the maximum friction load per unit length of anchor and L_a is the anchor bond length as shown in Figure 18. The actual diameter of the grouted anchor is unknown and typically the diameter of the drilling tool is used for D. Often in practice, the parameter F_{max} is used and quoted in references. This is misleading because F_{max} depends on D. The use of f_{max} is fundamentally correct and should be encouraged.

The shear strength f_{max} of the soil interface is correlated to the undrained shear strength s_u of the clay by quoting the factor α which is the ratio of f_{max} over s_u. Figure 19 gives examples of measured and recommended α values for low pressure straight shaft grouted anchors; it is compared with data for drilled shafts by Kulhawy and Jackson (1989) and by Reese and O'Neill (1988). The parameter f_{max} can also be correlated to other soil properties such as the pressuremeter limit pressure p_L (Bustamante and Doix 1985, interpreted into English by Briaud, 1992, Ch. 13).

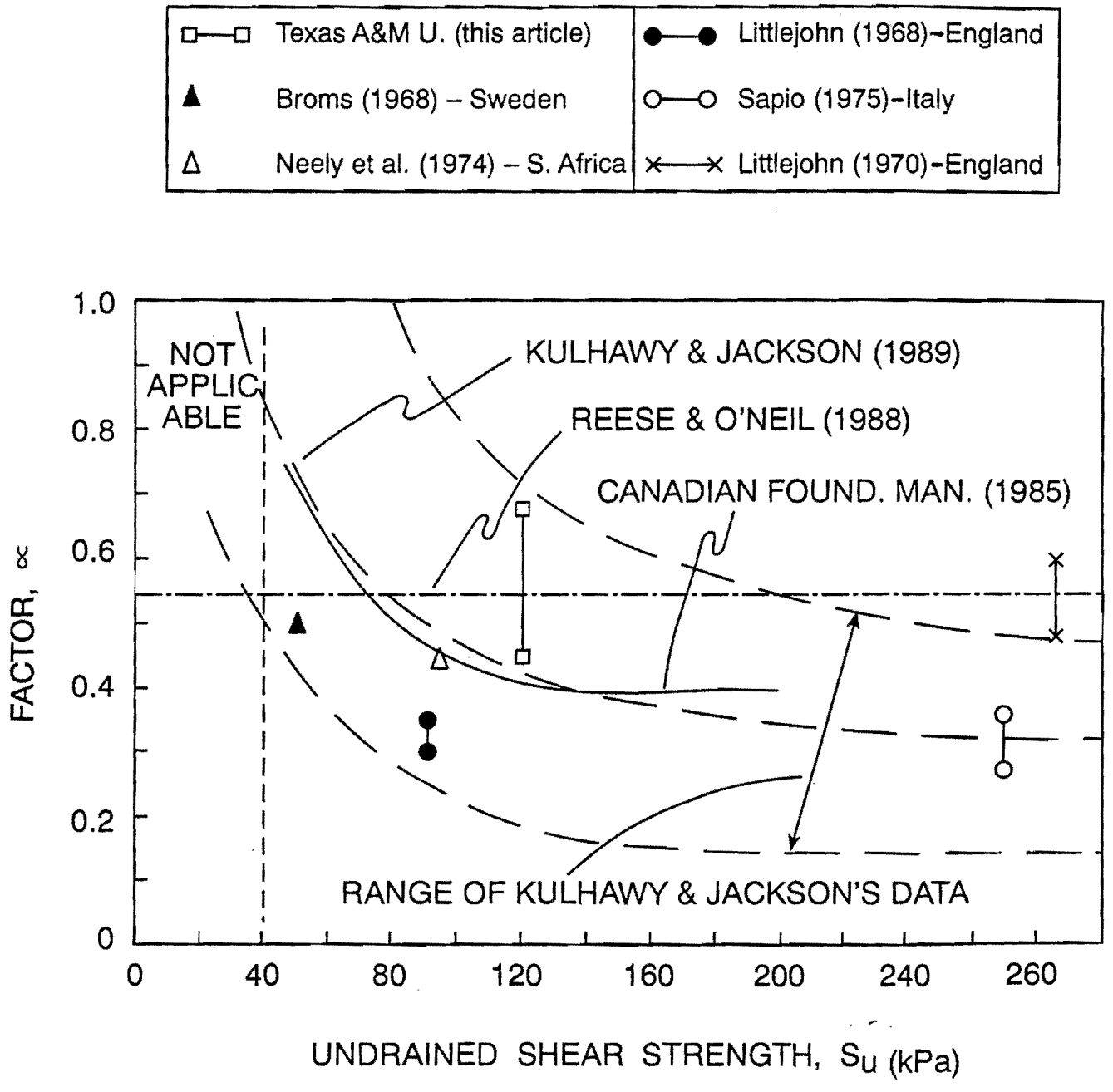

Figure 19. α Values for Low Pressure Grouted Anchors in Clay

2.2.3 Creep Movement

Anchors are subjected to sustained tensile loads during the life of the structure. Under these loads, anchors exhibit time-dependent or creep movements which must be acceptably low for the structure to perform properly. Creep movement as a function of time is measured during the anchor testing program. Typically, graphs of creep movement vs. log time are plotted for each load step (Figure 20). The creep movement and the time are the ones occurring after the beginning of the load step. The slope s in mm per log cycle of time is calculated for each load step. In the United States, anchors are accepted when the slope s is less than 2 mm per log-cycle of time for a load equal to 1.33 times the design load applied during 60 minutes (Weatherby, 1982; Cheney, 1988). This creep movement is due to the creep in the steel tendon, the progressive cracking of the grout in tension, and the creep of the soil in shear. The distribution of load among the three materials is discussed next.

2.2.4 Load Distribution

Figures 21 and 23 are an illustration using simplifying assumptions and describing the load distribution in the various components of the anchor. The anchor considered in Figures 21 through 23 is consistent with the actual anchors tested: it has a total length of 13.8 m, a tendon bond length of 4.6 m, and a tendon unbonded length of 9.2 m. The anchor diameter is 305 mm, the cross section area of the tendon A_T is 980 mm^2, and the grout cross sectional area A_G is 72045 mm^2. The modulus E_S used for the tendon is 2.07 x 10^8 kN/m^2 and the modulus E_G used for the grout is 2.07 x 10^7 kN/m^2. The undrained shear strength of the clay averages 125 kN/m^2 and the shear strength of the grout-soil interface f_{max} is considered to be constant and equal to 59 kN/m^2. Considering f_{max} to be constant along the shaft of the anchor is a simplifying assumption used for illustrative purposes only.

Two conditions are considered: the ultimate anchor load Q_u from the soil point of view and the anchor design load, Q_d. The ultimate load, Q_u, is the load which causes failure of the soil in shear at the grout-soil interface. At Q_u, the cumulative load resisted in shear by the soil may vary as shown schematically in Figure 21a. It is equal to zero at the bottom of the anchor and to the ultimate load Q_u at the ground surface (labeled Q_{S3} = 780 kN in the example). The linear variation shown assumes that the shear strength of the grout-soil interface f_{max} is constant along the shaft. This simplifying assumption is used for illustration purposes only and would not be true in non-uniform soil conditions. The cumulative load resisted in shear by the soil along the tendon bond length is 260 kN in the example (Q_{S2} in Figure 21a). At any point M along the anchor the load in the steel tendon plus the load in the grout is equal to the load resisted in shear at the soil-grout interface between the bottom of the anchor and point M. At Q_u the load in the grout varies as shown in Figure 21b. It is equal to zero at the bottom of the anchor and increases to the maximum tension load Q_{G1} that the grout can resist without cracking. This load can be estimated by

$$Q_{G1} = A_g E_g \varepsilon_{crack} \quad (4)$$

where A_g is the grout cross section area, E_g the modulus of the grout, and ε_{crack} the failure strain for the grout in tension which is about 10^{-4}. In the example, Q_{G1} is 149 kN. Above that point the axial

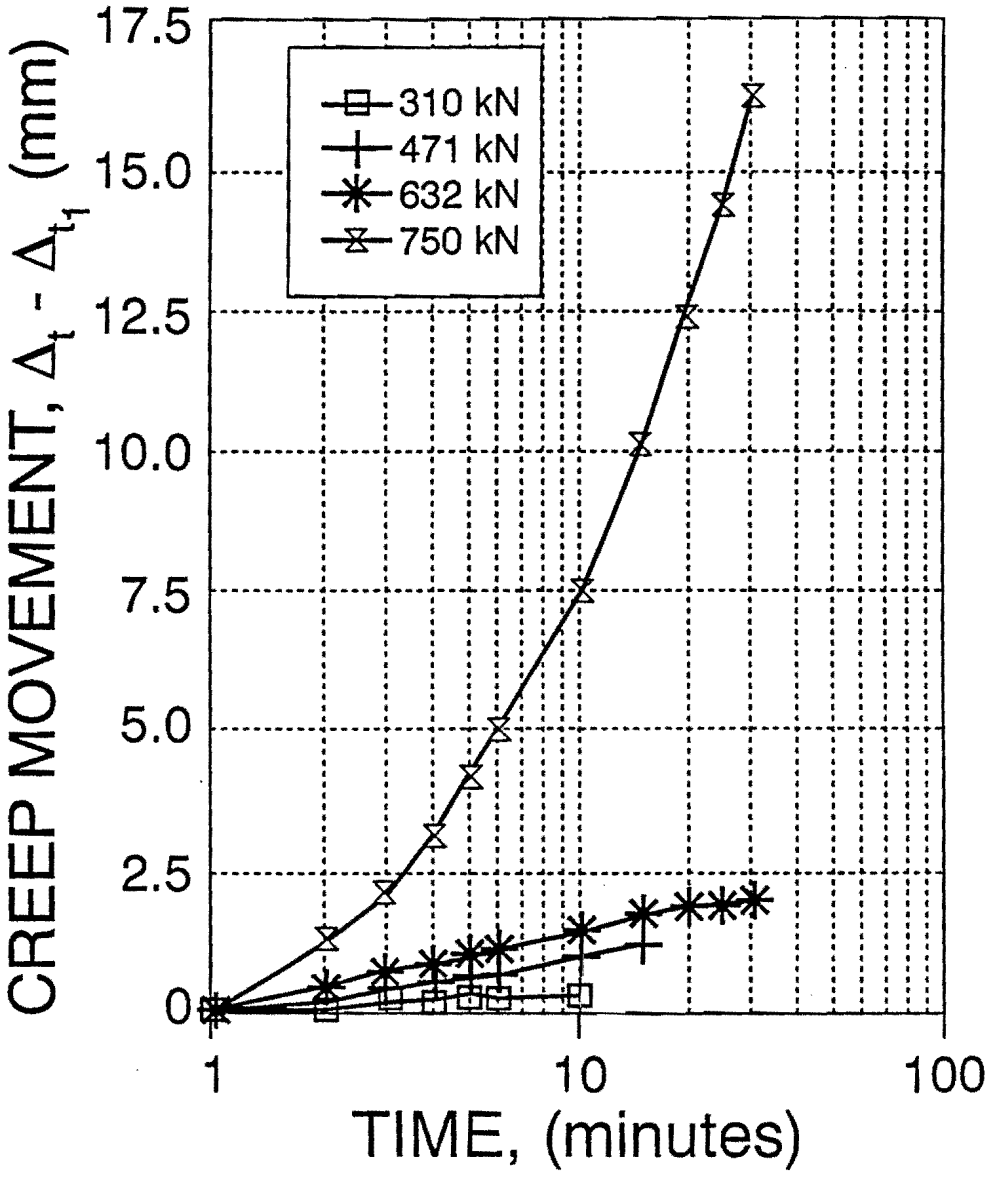

Figure 20. Creep Movement vs. Time Curves for Anchor 8 (First Load)

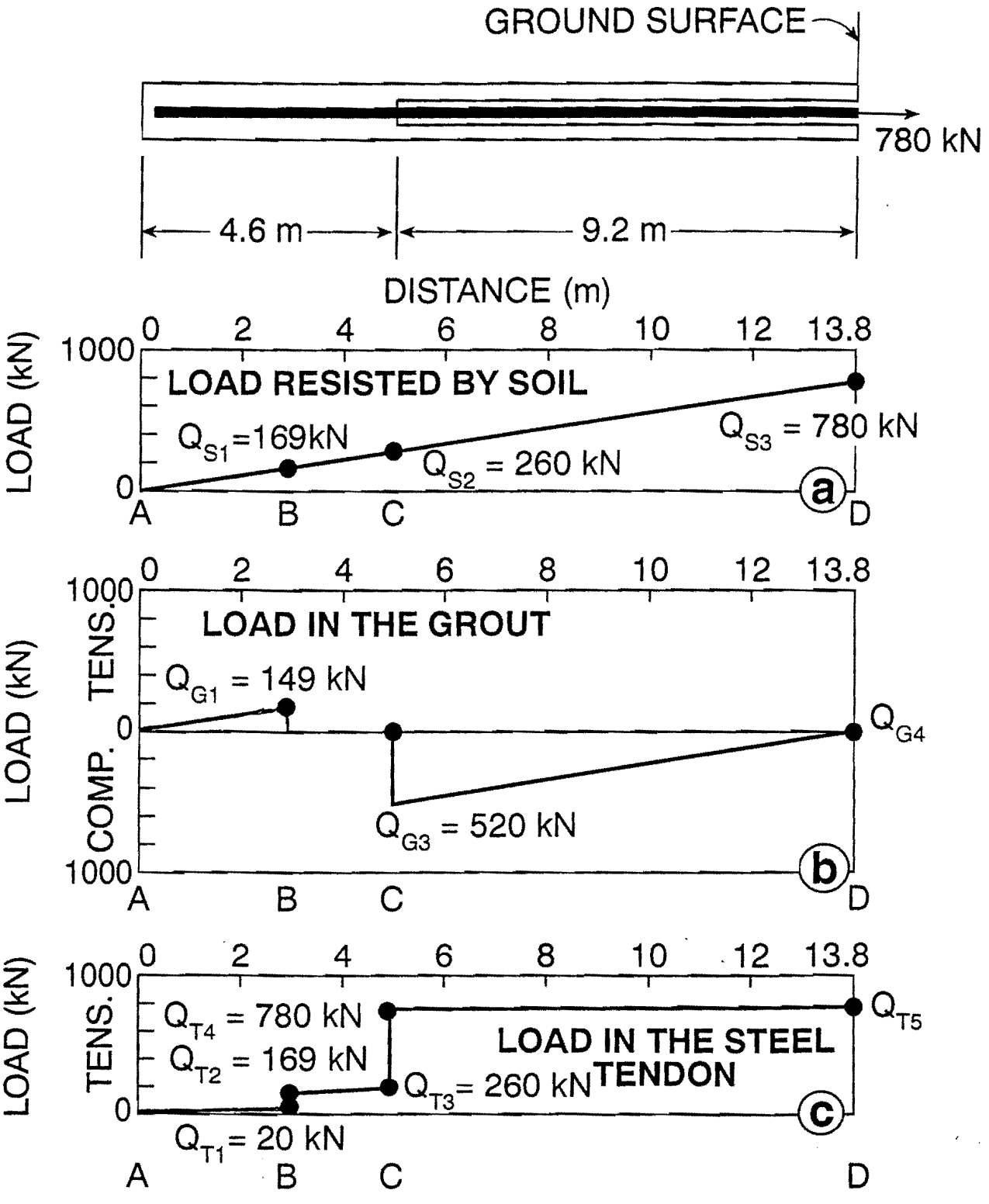

Figure 21. Schematic Load Distribution near Ultimate Load

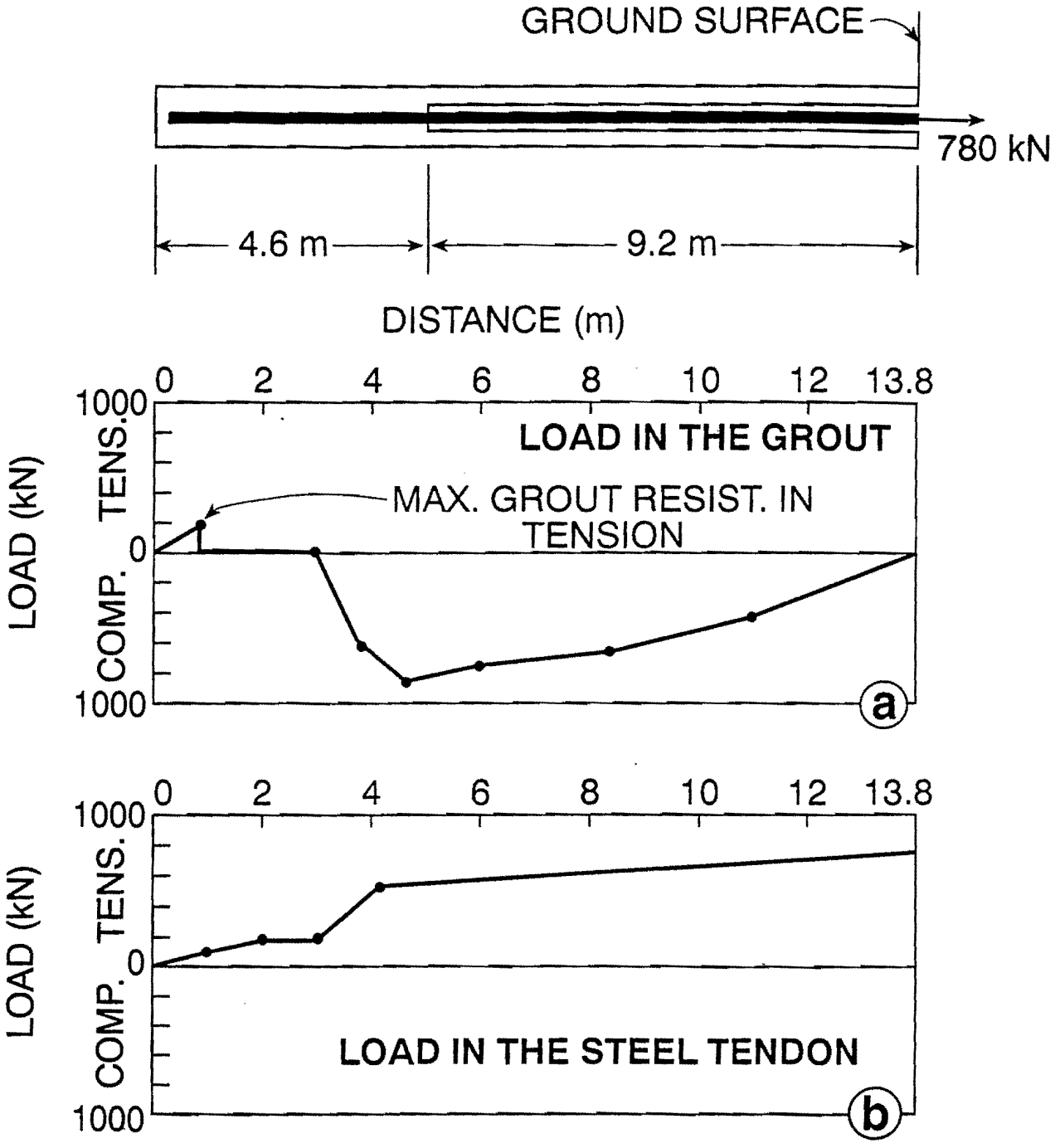

Figure 22. Measured Load Distribution for Anchor 1 near Ultimate Load

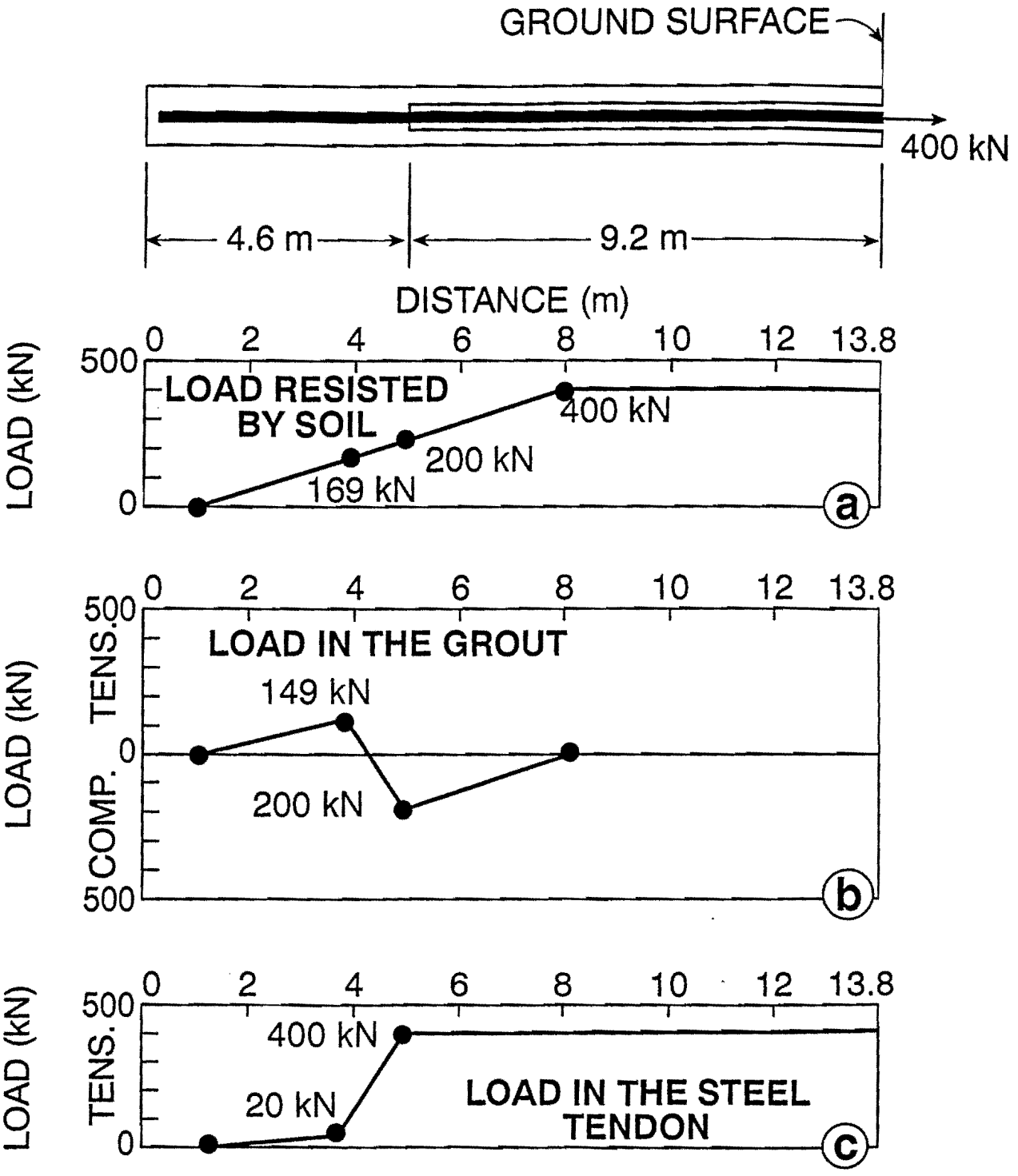

Figure 23. Schematic Load Distribution at Design Load

load in the grout drops to zero until the strain in the steel tendon becomes less than ε_{crack} again. Immediately above the boundary between the tendon bond length and the unbonded length, the grout is in compression. The load in the grout at that point is equal to the load that can be resisted in shear at the soil grout interface between the tendon bond length/unbonded length boundary and the top of the anchor. In the example this is 780-260=520 kN.

At Q_u, the load in the steel tendon varies as shown in Figure 21c. It is equal to zero at the bottom of the anchor and increases to a load Q_{T1} where the grout is at Q_{G1}. Compatibility of strain between the two materials leads to evaluating Q_{T1} as:

$$Q_{T1} = A_T E_T \varepsilon_{crack} \tag{5}$$

where A_T is the cross section area of the steel tendon and E_T the modulus of the steel tendon. In the example, Q_{T1} is 20 kN. The sum $Q_{T1} + Q_{G1}$ is equal to the load Q_{S1} resisted by the soil between the bottom of the anchor and point B where Q_{G1} occurs. Point B on Figure 21 is located at a distance l_1 from the bottom of the anchor such that:

$$l_1 = \frac{Q_{S1}}{\pi D f_{max}} \tag{6}$$

Above point B, the grout load is zero and the load in the steel tendon is equal to the load resisted by the soil. At the beginning of the unbonded length, the load in the steel tendon is equal to the load at the top of the anchor since there is no load transfer along the unbonded length.

Figure 22 shows the load distribution obtained from the measurements on an actual test anchor, anchor 1, at a load near the ultimate load. The trends are similar to Figure 21. At the design load Q_d, the load distribution is different and is as shown schematically in Figure 23. Note that the soil zone which is the most stressed is around the bonded to unbonded length transition.

2.2.5 National Geotechnical Experimentation Site

Ten anchors were constructed and load tested at one of the National Geotechnical Experimentation Sites located on the Texas A&M University Riverside Campus. The soil at that site is predominantly a very stiff overconsolidated clay (Figure 24) which has been tested numerous times starting in 1977 (Briaud, 1992; Marcontell and Briaud, 1994; Tao and Briaud, 1995; Simon and Briaud, 1996). The clay deposit at the location of the anchor project consists of a 6.5 m thick layer of very stiff clay with the following average characteristics (Figures 25 and 26): water content $w = 24.4\%$, plastic limit $w_p = 20.9\%$, liquid limit $w_L = 53.7\%$, natural unit weight $\gamma_t = 19.6$ kN/m^3, undrained shear strength $s_u = 110$ kN/m^2, cone penetrometer tip resistance $q_c = 2$ MPa, pressuremeter limit pressure $p_L = 0.8$ MPa, and SPT blow count N = 12 blows/0.3m. The overconsolidation of this layer is high as judged by the high ratio of modulus E_o over limit pressure p_L for the pressuremeter ($E_o/p_L = 25$). A ratio of about 12 would be expected for a normally consolidated clay (Briaud, 1992).

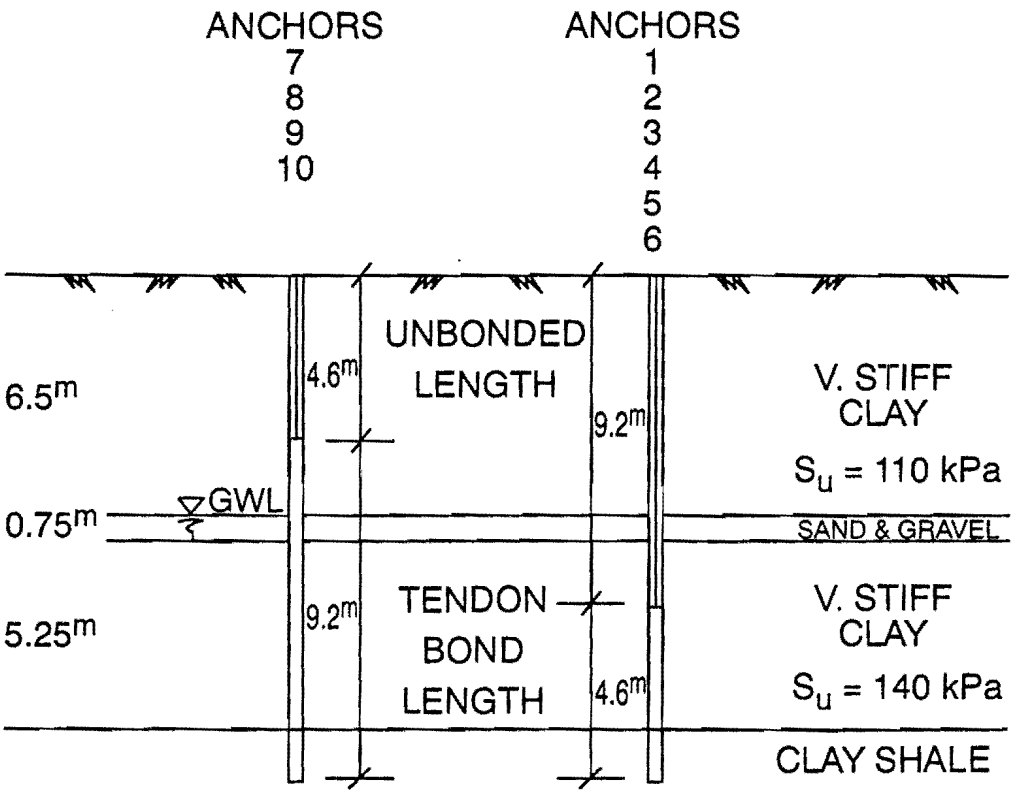

Figure 24. Stratigraphy and Anchor Location

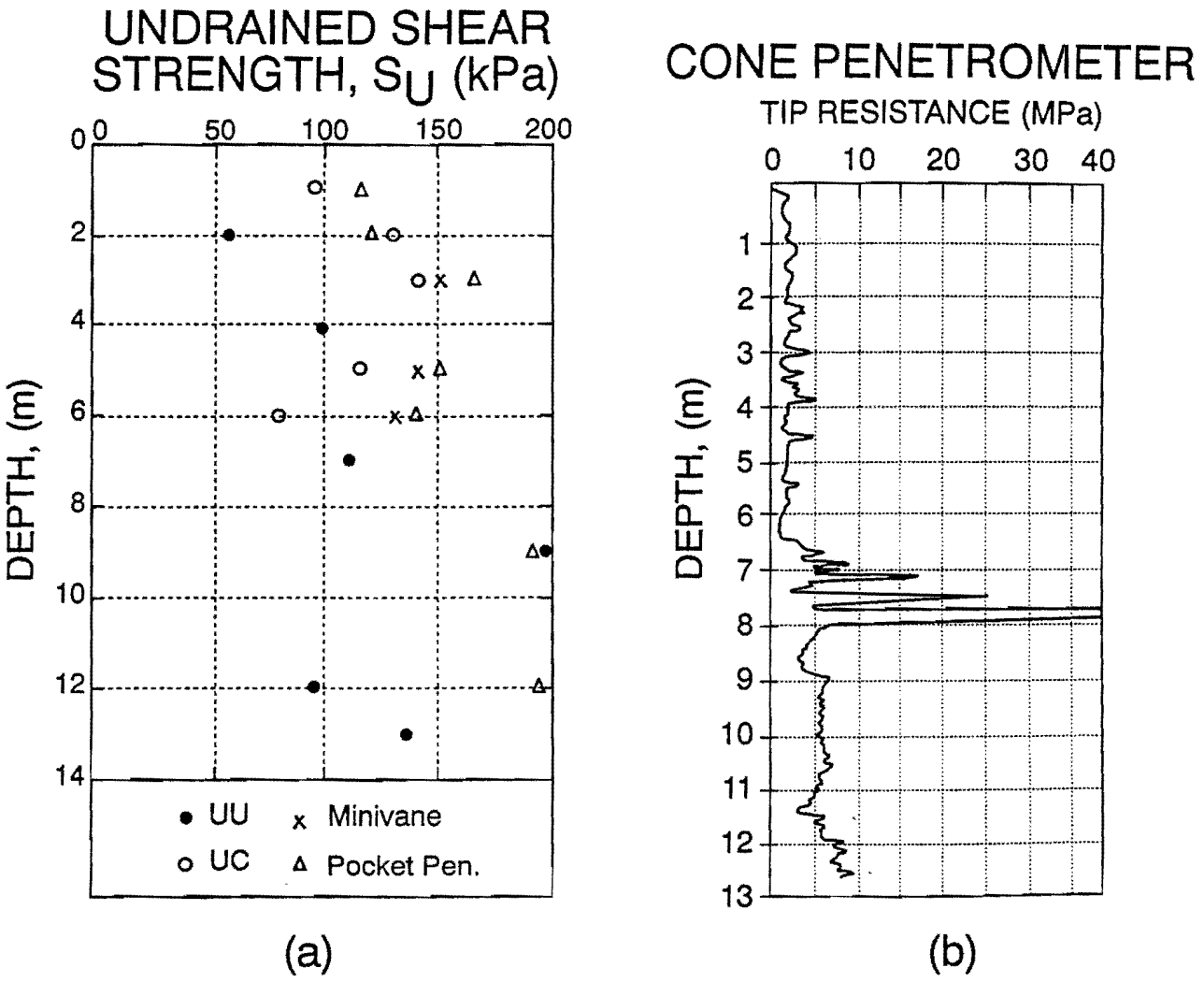

Figure 25. Soil Properties: (a) Undrained Shear Strength; (b) CPT Point Resistance

(a)

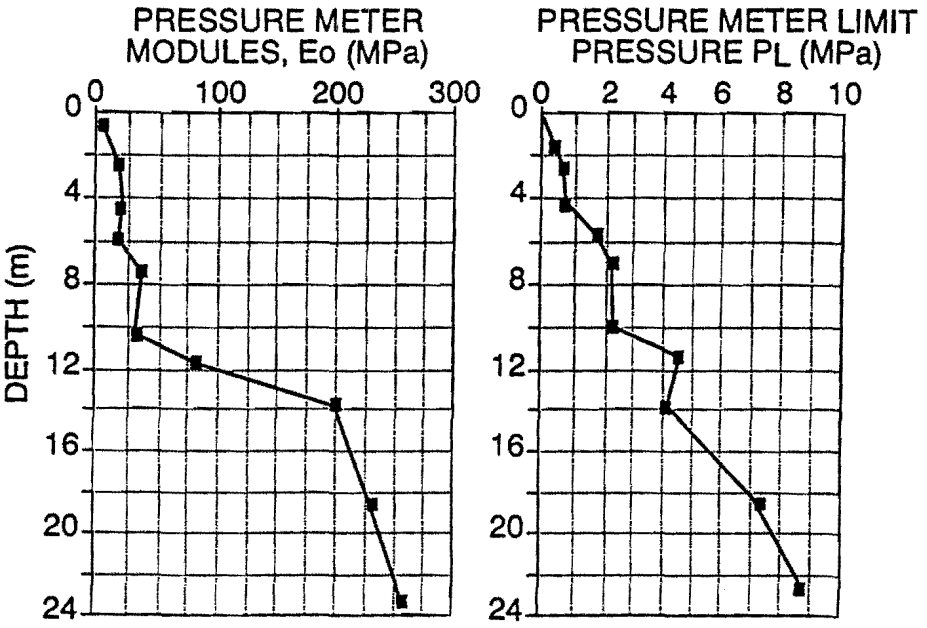

(b)

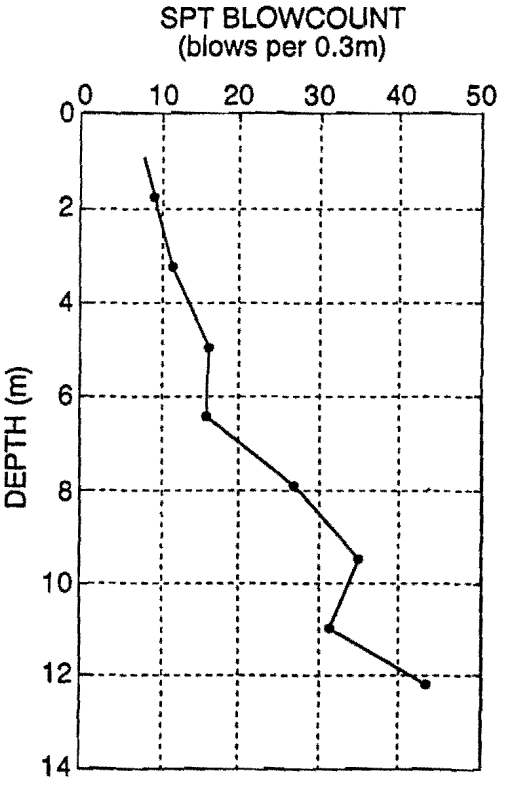

Figure 26. Soil Properties: (a) Pressuremeter Results; (b) SPT Blow Count

The water table is 6 m deep and a 0.5 m to 1 m thick layer of sand and gravel exists around 6.5 m depth. Below this sand and gravel layer extends a layer of very stiff clay down to 12.5 m with the following average characteristics (Figures 25 and 26): water content w = 24.5%, plastic limit w_p = 22%, liquid limit w_L = 65.5%, natural unit weight γ_t = 19.5 kN/m^3, undrained shear strength s_u = 140 kN/m^2, cone penetrometer tip resistance q_c = 6 MPa, pressuremeter limit pressure p_L = 2.2 MPa, SPT blow count N = 32 blows/0.3 m. The overconsolidation of this layer is moderate as judged by the moderate ratio of modulus E_o over limit pressure P_L for the pressuremeter (E_o/P_L = 16).

Below this layer is a layer of clay shale down to at least 30 m. This shale has average index properties similar to the hard clay, but a much higher stiffness and strength. The pressuremeter modulus E_o averages 230 MPa and the limit pressure p_L = 6.5 MPa. The overconsolidation of this layer is very high as judged by a very high E_o/p_L of 35.

The top layer of clay is a flood plain deposit of Pleistocene age (Jennings et al., 1996). The next sand layer is a channel deposit, also of Pleistocene age. Both layers were deposited by the ancient Brazos River about 200,000 years ago. The two deeper layers of clay were deposited in a series of marine transgressions and regressions; they are of Eocene age and approximately 40 million years old. Erosion of the Eocene marine clay took place before the Pleistocene river sediments were deposited.

2.2.6 Anchors and Load Tests

Ten anchors were installed by drilling dry with a continuous flight hollow stem auger (Figure 24). The outside diameter of the auger flight was 305 mm and the inside diameter of the hollow stem was 102 mm. Before drilling, the tendon equipped with a point was placed in the auger until the drill point was flush with the open drilling head on the auger. Drilling proceeded until a depth of 13.8 m. The auger was then slowly extracted without rotation while grout was pumped into the annulus between the soil and the tendons. A grout pressure of 0.7 MPa was maintained until the head of the auger was near the ground surface.

The grout slump varied from 165 mm to 254 mm, and the compressive strength at 26 days varied from 22 MPa to 46 MPa. The steel tendon for each anchor consisted of seven strands of seven wires each for a total cross section area of 980 mm^2 with a guaranteed ultimate tensile strength of 1860 MPa. The tendons of anchors 1 through 6 were sheathed so as to have an unbonded length of 9.2 m, while the tendons of anchors 7 through 10 were sheathed so as to have an unbonded length of 4.6 m. All anchors were embedded 13.8 m in the clay deposit, going through the four soil layers as shown on Figure 24.

Anchors 1, 2, 7, 8, 9, and 10 were instrumented with vibrating wire strain meters on the steel strands and vibrating wire embedment gauges in the grout mass. A total of 68 instruments were installed in the bonded lengths and at the beginning of the unbonded lengths of the six anchors.

The installation of the 10 anchors and the subsequent load testing took place from November 1990 to July 1991. The load tests were tension or uplift tests performed by pulling on the tendons with a hollow jack (Figure 27). The jack was placed above a steel frame against which it reacted.

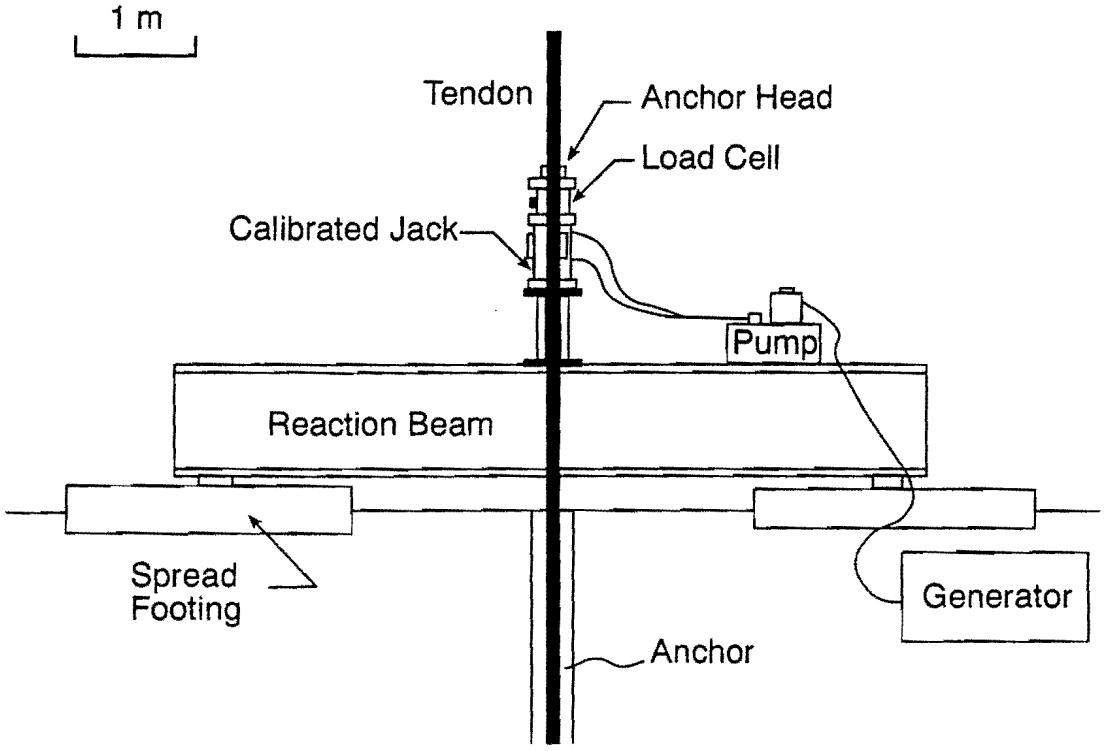

Figure 27. Load Test Setup

The steel frame rested on two spread footings approximately 2.5 m × 2.5 m in size, embedded 1 m below the ground surface and with an edge to edge clear spacing of 2.3 m or 7.5 m anchor diameters. The load was recorded through a load cell placed above the jack and the displacement was recorded with respect to a settlement beam for the short-term load tests and with respect to a deep bench mark anchored below the tip of the anchors and placed next to each anchor for the long-term load-hold tests.

Different types of load tests were performed: proof tests, performance tests, creep tests, and 70-day load-hold tests. The loading history for each of those types of tests is shown in Figure 28. In the United States, every working anchor installed on a particular project is subjected to a proof test just prior to locking the anchor at its working load. Usually, 5% of all working anchors are subjected to a performance test to demonstrate the short-term cyclic load-carrying capacity of the anchors. Creep tests are performed occasionally to investigate the long-term load-carrying capacity of an anchor. A 70-day load-hold test was specific to this study.

2.2.7 Load Test Results and Maximum Friction

As an example of the results, Figure 29a shows the load movement curve obtained for a proof test on anchor 5, Figure 29b for a performance test on anchor 6, and Figure 30a for a creep test on anchor 7.

The movement measured at the anchor head was the total movement including the elastic movement mostly due to the elasticity of the tendon in the unbonded length and the residual movement mostly due to non-recoverable movement and to the change in effective unbonded length. The residual movement is the movement read after unloading the anchor to a nominal alignment load of 20 kN from a given load step, and the elastic movement is the difference between the total movement and the residual movement (Figure 30b). Note that the elastic movement line is very close to the initial slope of the total movement curve. The slope of that line (Δ/P) is equal to $L_e/A_T E_T$ where L_e is the equivalent elastic length of the anchor.

The ultimate load for each anchor was defined as the load obtained for a residual displacement of one-tenth of the anchor diameter (B/10) or for a total displacement of B/10 plus the elastic elongation of the anchor unbonded length. This large displacement was not reached for all load tests. The ultimate load was, therefore, obtained only for the anchors which reached that displacement or nearly reached that displacement (maximum load applied divided by extrapolated ultimate load ≥ 0.8) so that the ultimate load could be evaluated with reasonable confidence. The ultimate loads are given in Table 4 together with the corresponding grout-soil interface shear strength f_{max} averaged over the length of the anchor.

Using the average properties of the clay deposit and the average f_{max} values, the following ratios are obtained:

- f_{max}/s_u varied between 0.43 and 0.66, and averaged 0.52,
- f_{max}/q_c varied between 0.014 and 0.021, and averaged 0.016,
- f_{max}/p_L varied between 0.036 and 0.055, and averaged 0.043, and

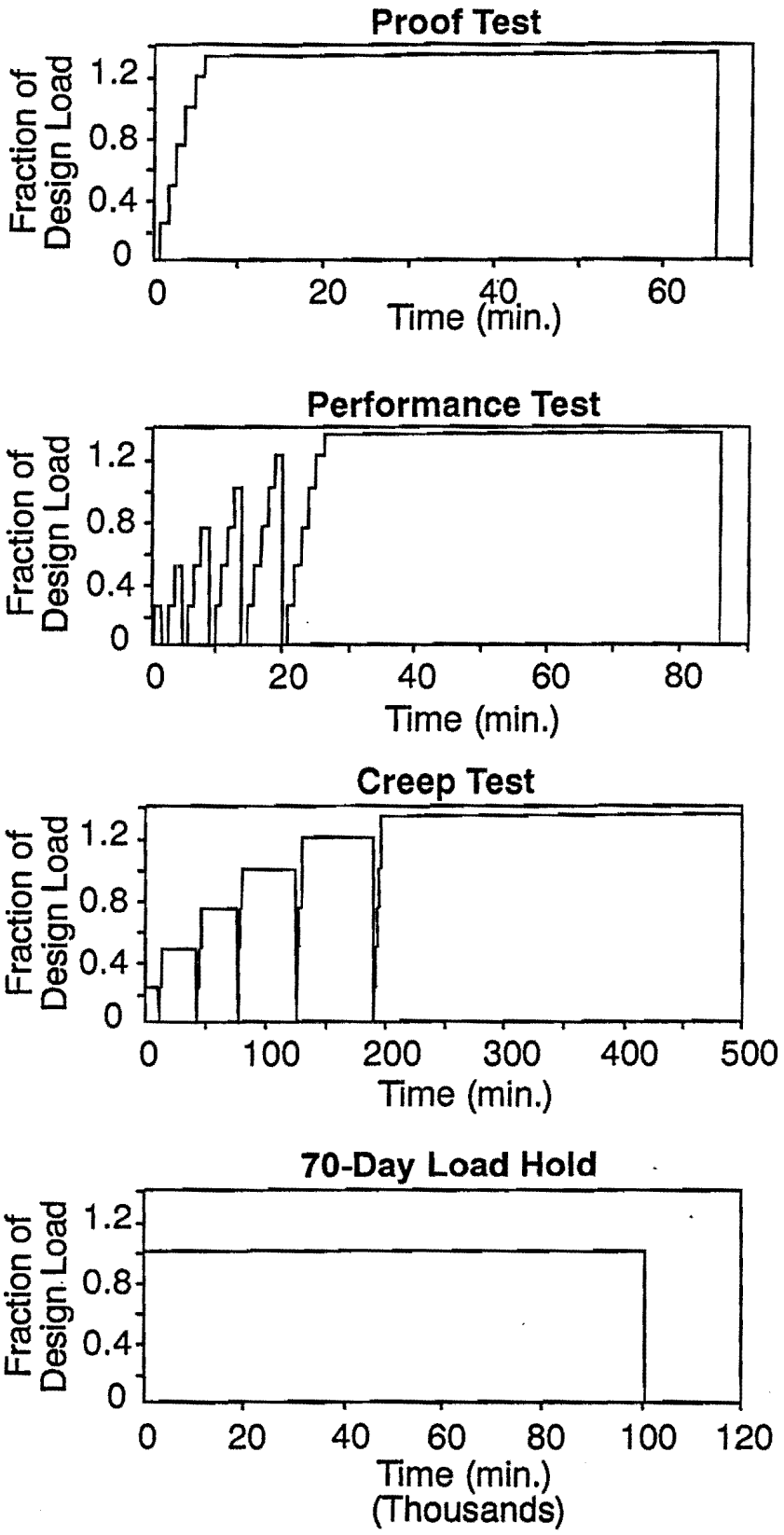

Figure 28. Load History for Four Load Test Types

(a)

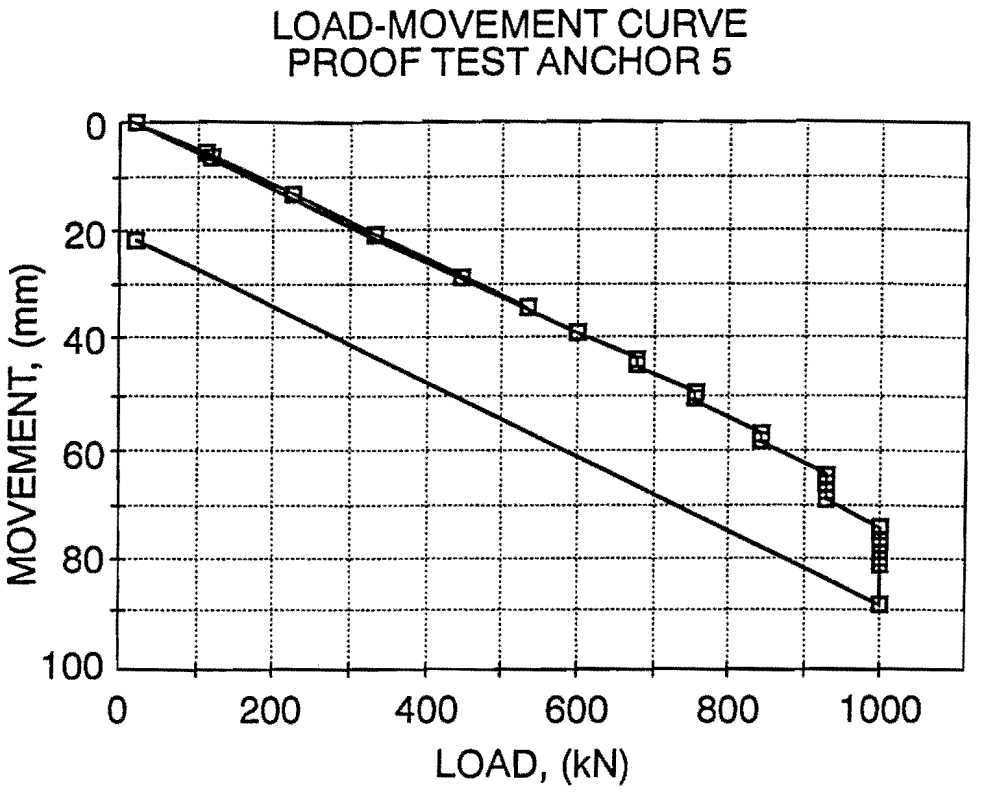

(b)

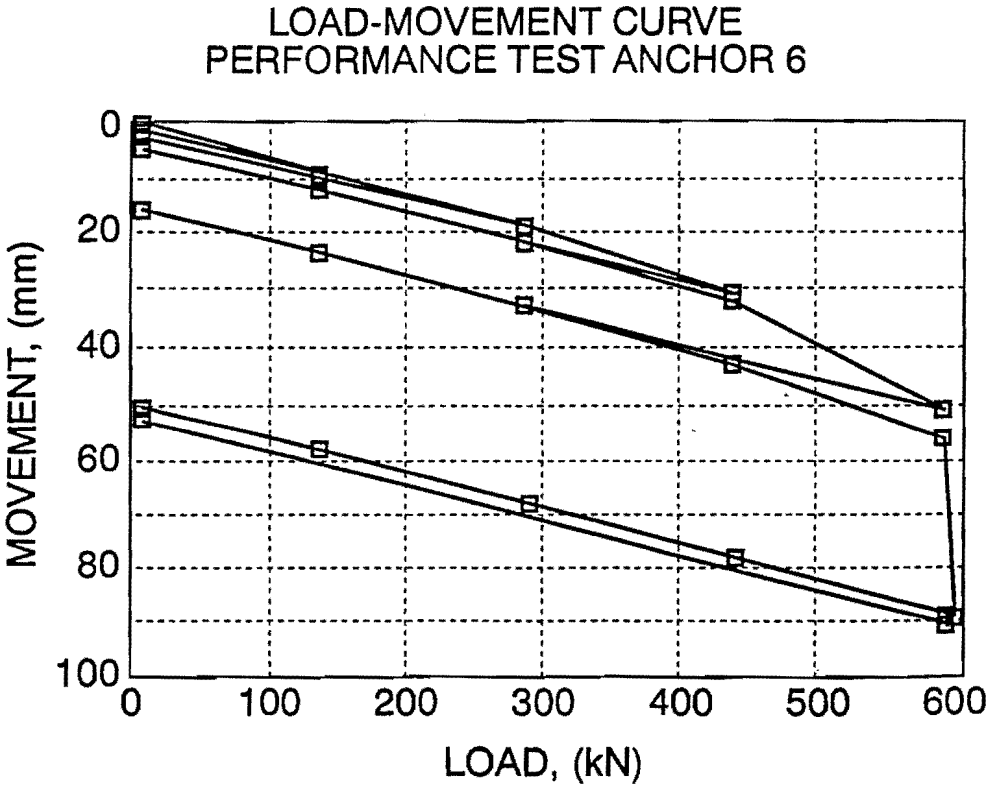

Figure 29. Load Movement Curves: (a) Anchor 5; (b) Anchor 6

(a)

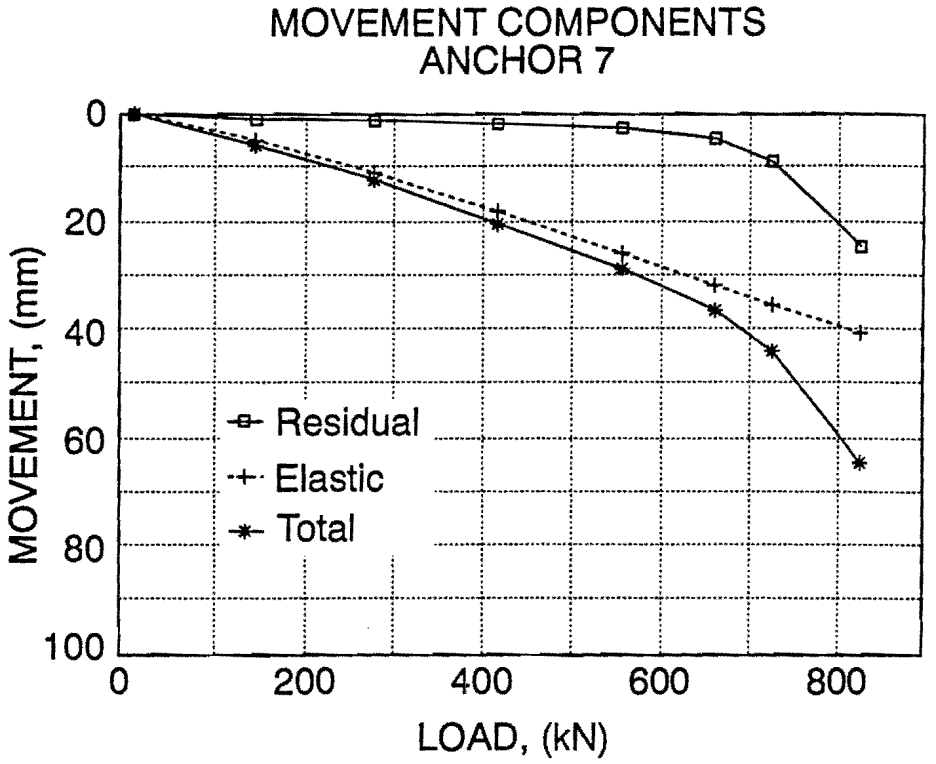

(b)

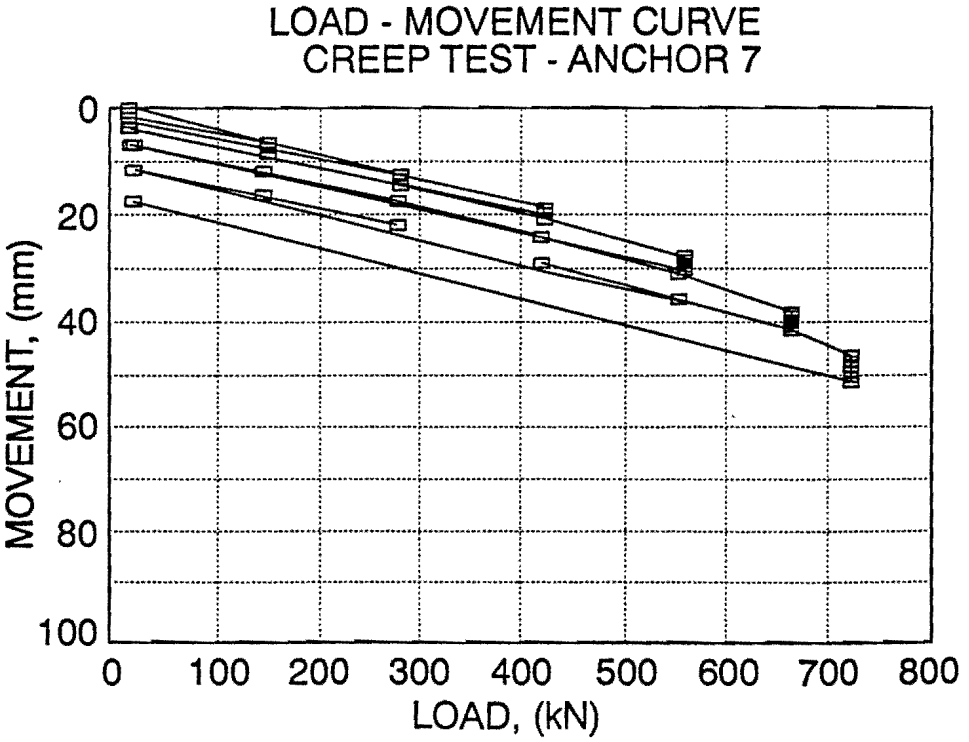

Figure 30. Load Movement Curves for Anchor 7

- f_{max}/N varied between 2.5 and 3.7, and averaged 2.9 with f_{max} in kPa and N in blows per 0.3m.

Table 4. Data for 10 Anchors

Anchor Number (1)	Ultimate Load (kN) (2)	Bonded Anchor Length (m) (3)	Friction Stress at Failure (kN/m^3) (4)	α values (5)
1	867	4.57	65.9	0.53
2	1080	4.57	82.1	0.66
3	ID[a]	4.57	—	—
4	934	4.57	71.0	0.57
5	ID[a]	4.57	—	—
6	712[b]	4.57	54.1	0.43
7	801	9.15	60.9	0.49
8	747	9.15	56.8	0.45
9	ID	9.15	60.9	0.49
10	801	9.15	60.9	0.49

[a]Insufficient displacement.
[b]Installation difficulties encountered; 60% of anchor not grouted under pressure but simply free-fall.

Some of these results are shown on Figure 19.

2.2.8 Influence of Bonded Length on Ultimate Load

In Table 4, the average ultimate load for the anchors with a short bonded length (4.6 m) is 961 kN while the average ultimate load for the anchors with a longer bonded length (9.2 m) is 783 kN. Note that the ultimate load of anchor 6 was not used in the average because of the installation difficulties with this anchor; indeed, after a first unsuccessful installation attempt, a second location was selected. However, the hose broke after pressure grouting 6.1 m and the remaining 7.7 m were grouted by free-fall.

The ultimate load for the anchors with a short bonded length is 23% larger on the average than the ultimate load for the anchors with a longer bonded length. This finding is consistent with the findings of Chaouch and Briaud (1991, 1992) who performed pull-out load tests on two drilled and grouted piles at the same site; one drilled and grouted pile was pulled from the top, the other one was pulled from the bottom. The bottom loaded pile carried 37.5% more load than the top loaded pile. The anchors in this project penetrate through three different strata. However, the vertical

variations of soil properties can not explain the results because at ultimate load, f_{max} is mobilized in all layers regardless of the tendon bond length.

The reason for the difference in capacity comes from the grout which is mostly loaded in tension if the load is applied close to the top (long tendon bond length) and mostly in compression if the load is applied close to the bottom (short tendon bond length). Grout cracks at about 100 microstrains of tension. Under typical anchor loads, a certain length of grout will crack and the steel tendon will resist the tensile load within that zone. The axial stiffness (AE) of such a cracked section is much smaller than the axial stiffness of the same section where the grout is in compression. The load transfer curves for stiff clays such as the one at this site exhibit post-peak strain softening properties (Figure 31). As a result, if the anchor is flexible (long bonded length) by the time the bottom of the anchor reaches its peak friction value, the top of the anchor is at the residual friction value and the friction along the anchor is somewhere between the peak value and the residual value. On the other hand, if the anchor is more rigid (short bonded length), the difference in movement between the top and bottom of the anchor is smaller than for the flexible case and all parts of the anchor can mobilize the peak friction at the same time, or close to it (Figure 31).

This is known as the length effect on pile capacity (Murff, 1980). This effect explains the 23% difference found in these anchor tests and leads to the conclusion that, all other dimensions being equal, the highest anchor capacity is reached for the shortest tendon bond length. This leads us to think that an anchor with a zero tendon bond length would be best. These anchors, known as compression anchors, give rise to different problems such as large grout compressive stresses and the possible need to reinforce the grout body. Therefore, it appears preferable at this time to aim for a short tendon bond length rather than a compression anchor such as the one shown in Figure 32. Another advantage is that if two anchors in a tieback wall have the same overall length, the anchor with the short tendon bond length concentrates the soil stresses in a zone which is further away from the wall face since it is near the bottom of the anchor. This, in turn, reduces wall movement since the stressed zone is further away from the wall.

2.2.9 Influence of Bonded Length on Creep Movement

As pointed out earlier, it is common practice to plot creep results in the form of creep movement (Δ_t - Δ_{t_1}) vs. the decimal logarithm of time (log t), where Δ_t is the upward movement of the anchor head (tendon) at a time t after applying the load Q, and Δ_{t_1} is the upward movement under the same load Q at the time t_1 equal to one minute after the beginning of the load step. Such plots are presented for the first loading sequence on anchor 8 (Figure 20) and for the reloading sequence on anchor 5 (Figure 33).

The average slope of each line on these creep movement plots can be calculated; these slopes represent the creep rate s in mm per log cycle of time. A value of s can be obtained for each load level Q and a plot of s vs. Q can be prepared. Figure 34a shows such a plot for all of the anchors with a long tendon bond length (9.2 m), while Figure 34b is for the anchors with a short tendon bond length (4.6 m). As can be expected, the creep rate increases as the load increases.

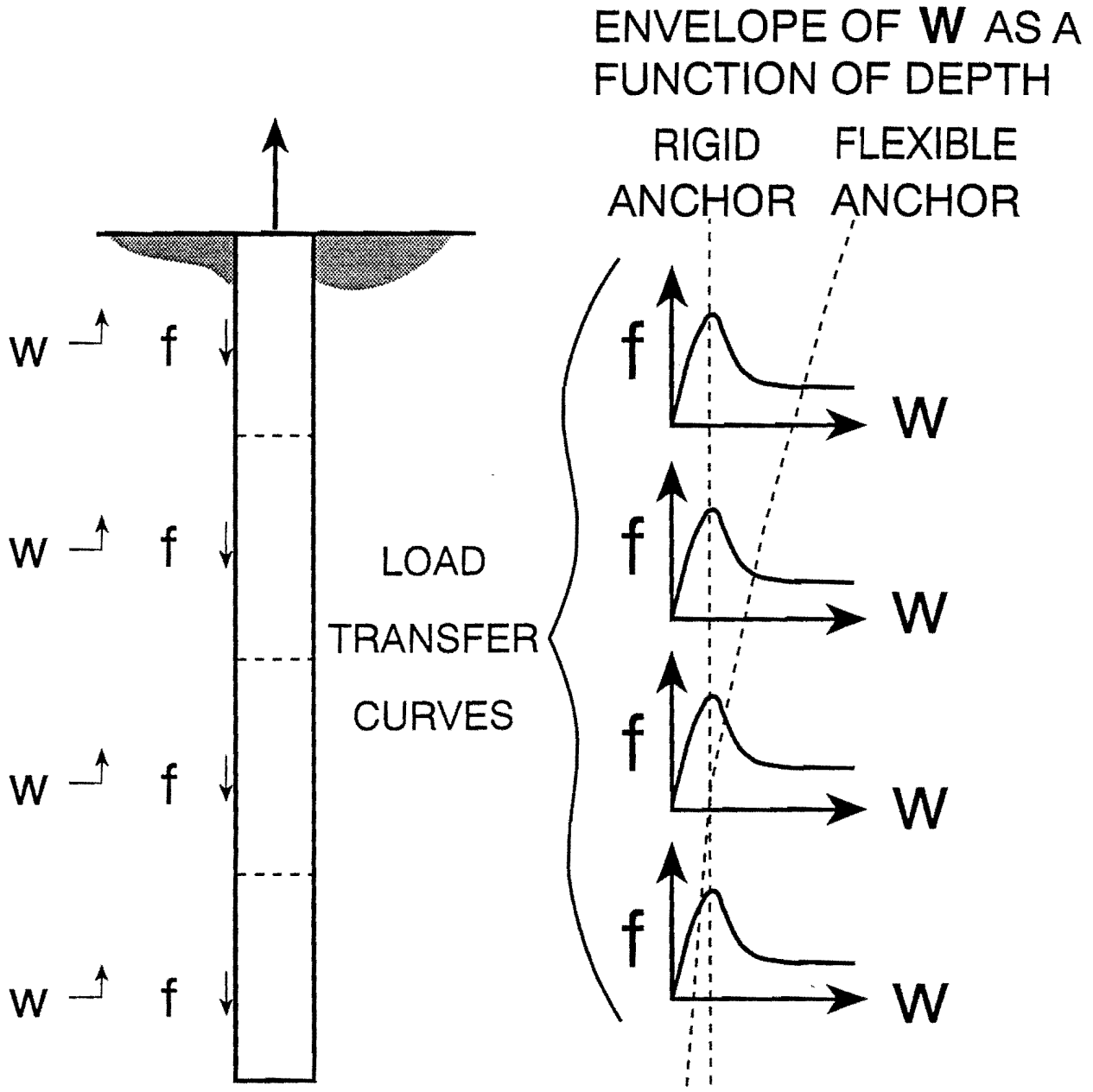

Figure 31. Axial Stiffness Effect on Anchor Capacity

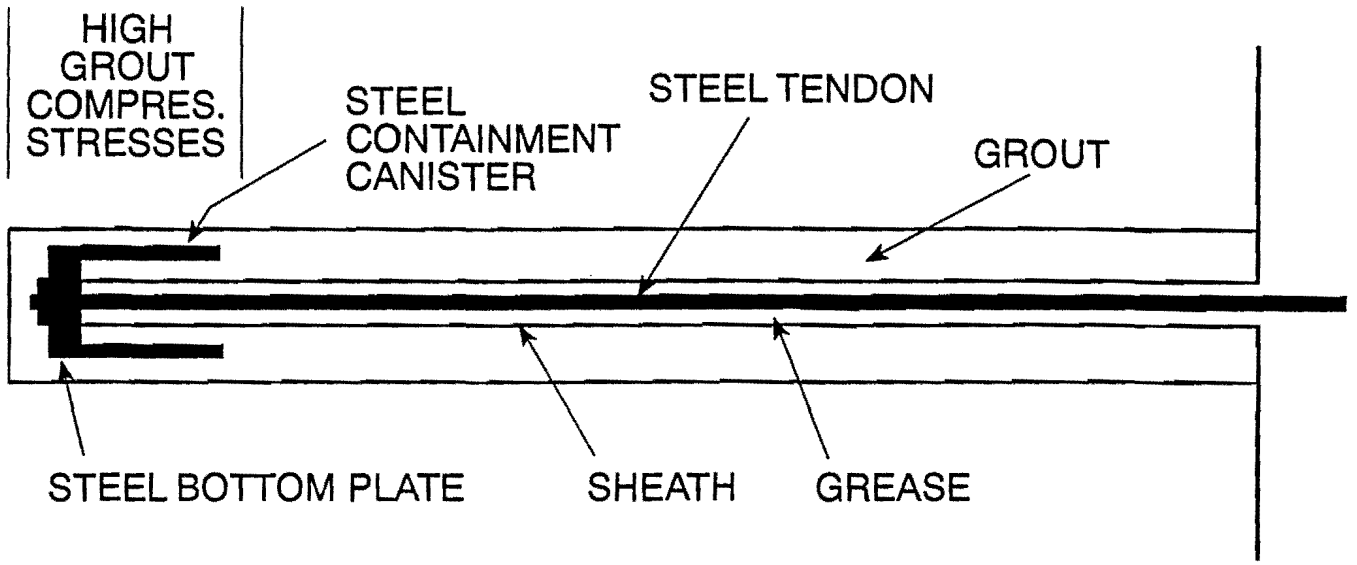

Figure 32. Anchor Scheme for Zero Bonded Length

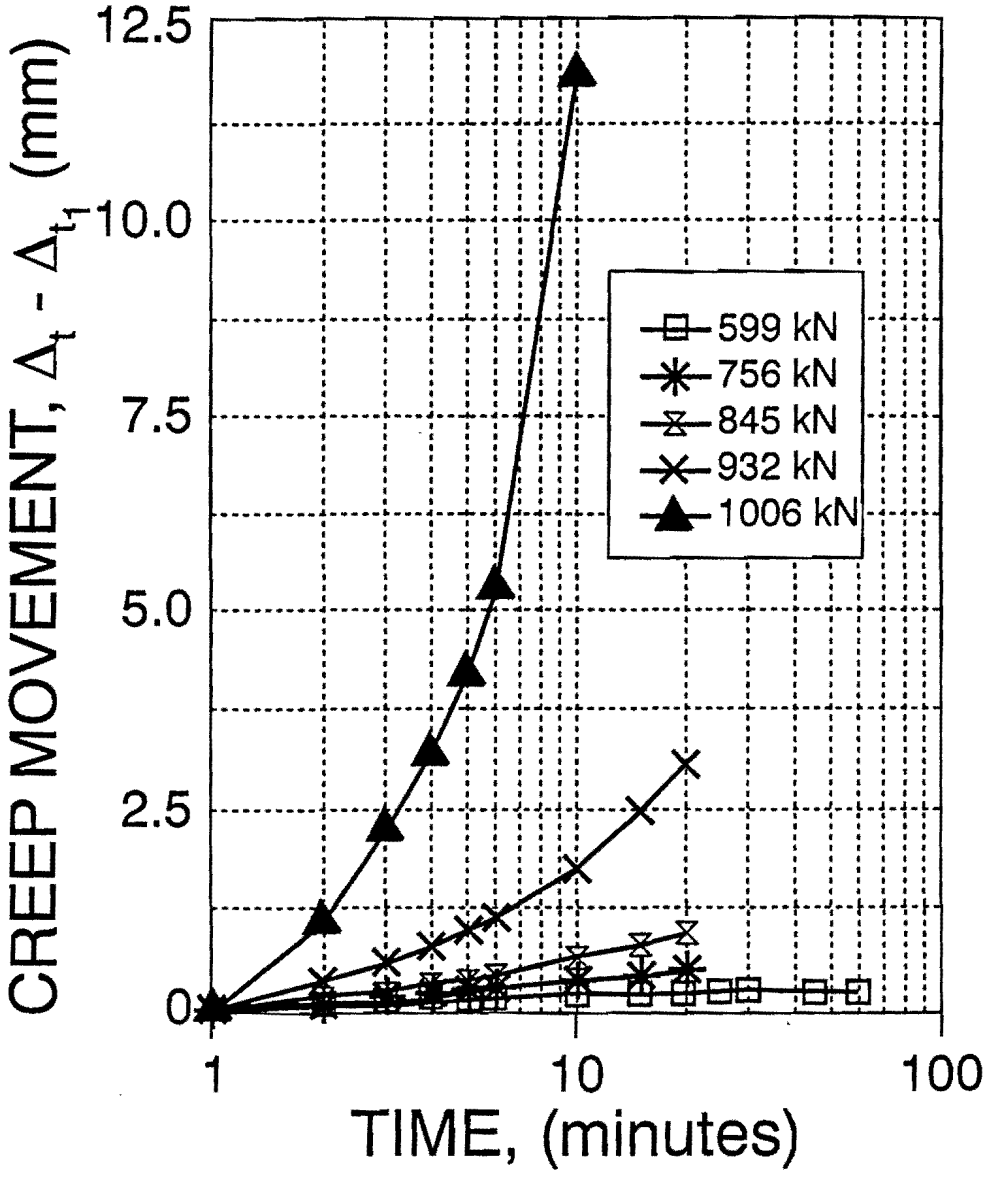

Figure 33. Creep Movement vs. Time Curves for Anchor 5

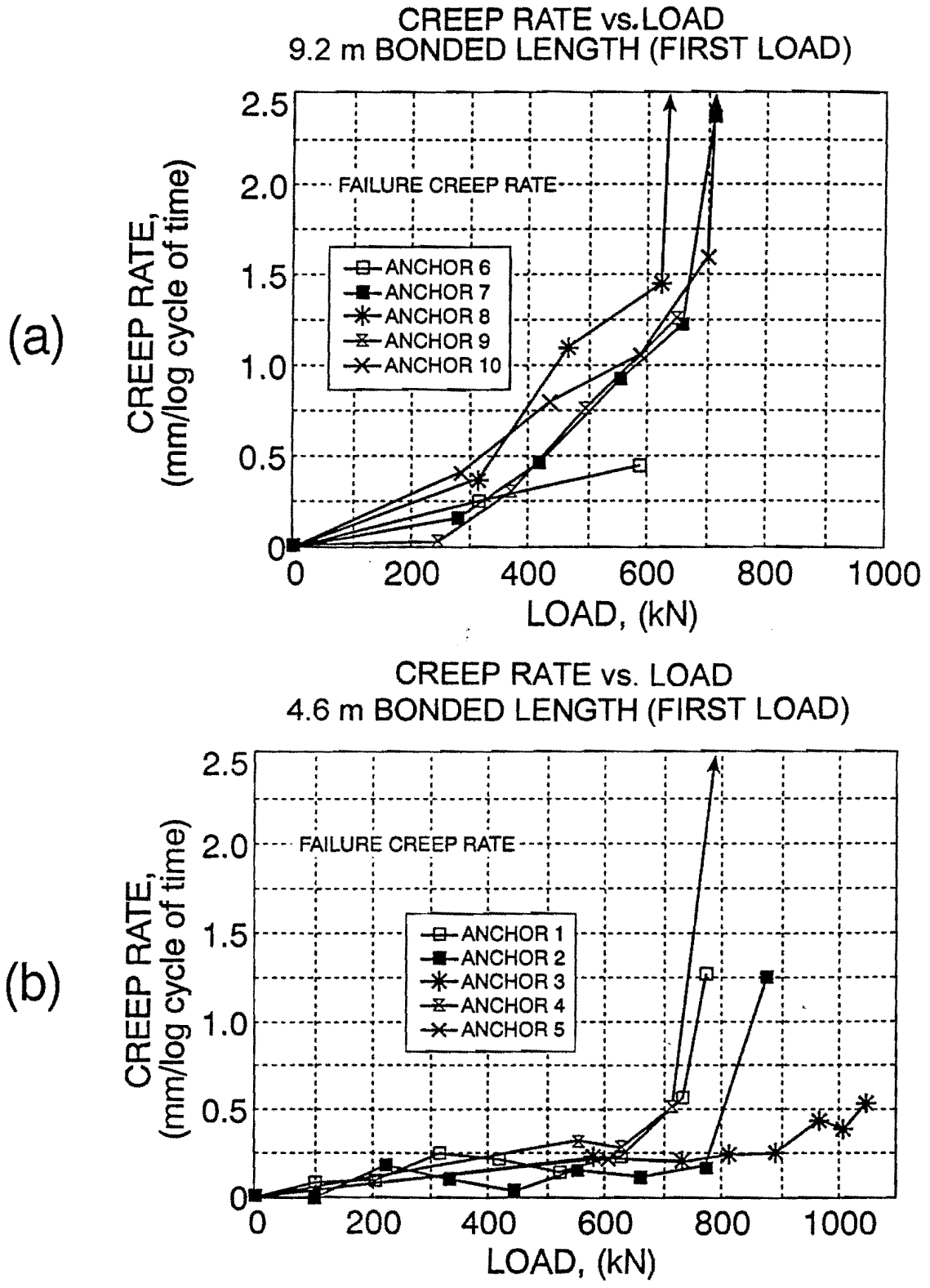

Figure 34. Creep Rate vs. Load Curves for First Loading on (A) 9.2 m Bonded Length and (b) 4.6 m Bonded Length

A comparison of Figures 34a and 34b shows clearly that the anchors with a short tendon bond length creep a lot less than the anchors with a long tendon bond length for similar levels of axial load. At 400 kN for example, the creep rate is about 0.56 mm/l.c. for the anchors with a long tendon bond length and only 0.2 mm/l.c. or 2.8 times less for those with a short tendon bond length. The reduction is significant and is possibly due to the grout being in compression over a longer portion of the anchor. The difference may also exist because the point of maximum soil stress (boundary between the unbonded and bonded tendon zone) is in the upper and somewhat softer clay for the anchors with a long tendon bond length while it is in the lower somewhat stronger clay for the anchors with a short tendon bond length.

2.2.10 Influence of Reloading on Creep Movement

The anchors were subjected to a first loading test in March and April of 1991. The maximum load applied in this first loading series of tests varied from 600 kN to 1,000 kN. Anchors 5 through 10 were subjected to a reloading test hours after the first loading test was finished. The maximum load applied in this reloading series of tests was approximately the same as in the first loading tests.

Figure 34a shows the creep rate vs. load curve for the first loading tests on the anchors with the long bonded length. Figure 35 shows the same graph for the reloading tests. Comparing Figures 34a and 35 shows that the creep rate is significantly less during the reloading test. For example, at 400 kN the creep rate is about 0.2 mm/l.c. for the first loading and only 0.1 mm/l.c. (or two times less) for the reloading tests. The reduction is significant and is attributed to the preloading effect of the first loading tests.

One very important question remains unanswered: is this preloading effect a permanent effect or a temporary one? If it is permanent, then reloading tests should be allowed to prove that anchors satisfy the acceptance criterion (less than 2 mm/log cycle of time under 1.33 × design load). If it is temporary, then reloading tests should not be allowed. Also, if it is temporary, how long does the preloading effect last? Research is needed in this area. Limited experience on anchor tests performed by Schnabel Foundation on one hand, and on spread footing tests performed at the Texas A&M University National Geotechnical Experimentation Site on the other hand, indicates that the effect is temporary.

2.2.11 Other Obervations on Creep Movement

Several models were considered to fit the trends of the curves on the $(\Delta_t - \Delta_{t_1})$ vs. log t graphs (Figures 20 and 33). It was observed that at low load level these curves exhibit a slight downward curvature, that at medium load level the curves are straight lines, while at high load level the curves exhibit an upward curvature. These observations lead to the following model recommendations.

$$\text{for } \frac{Q}{Q_f} \le 0.5, \qquad \frac{\Delta_t}{\Delta_{t_1}} = \left(1 + \log \frac{t}{t_1}\right)^n \tag{7}$$

$$\text{for } 0.5 \le \frac{Q}{Q_f} \le 0.8, \quad \frac{\Delta_t}{\Delta_{t_1}} = 1 + \log \left(\frac{t}{t_1}\right)^n \tag{8}$$

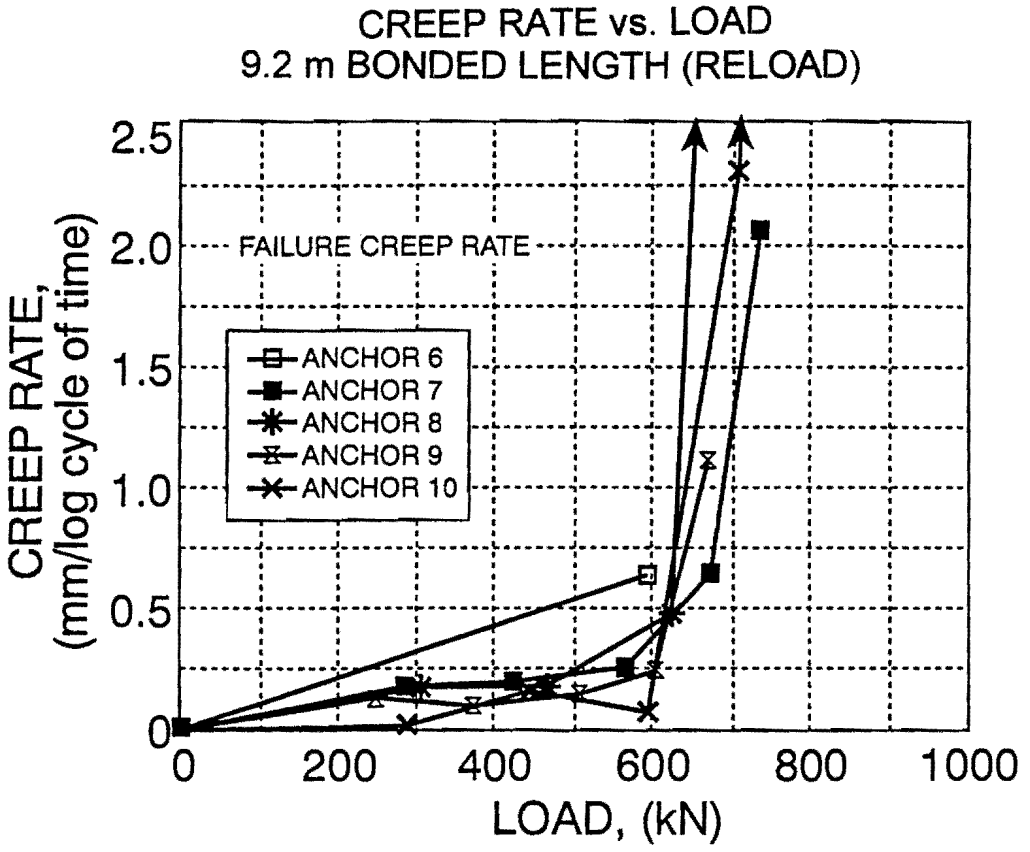

Figure 35. Creep Rate vs. Load Curves for Reload on 9.2 m Bonded Length

$$\text{for } \frac{Q}{Q_f} \geq 0.8, \qquad \frac{\Delta_t}{\Delta_{t_1}} = \left(\frac{t}{t_1}\right)^n \tag{9}$$

The viscous exponent n was found in these experiments to be approximately equal to 0.5 for Equations 7 and 8 and between 0.002 and 0.015 and 1 for Equation 9.

The ultimate load Q_u is defined as the load corresponding to a total displacement of one-tenth of the anchor diameter plus the elastic elongation of the anchors unbonded length (B/10 + PL/AE). The failure load is defined as the load Q_f for which the creep movement accumulates at a rate equal to 2 mm per log cycle of time during the first loading of the anchor. The load Q_f was determined for anchors 4, 7, 8, and 10. The ratio Q_f/Q_u varied very little (0.83 to 0.89) and averaged 0.86.

Observation of Figures 34 and 35 indicates that a creep load threshold Q_t exists; below Q_t the creep rate is small, and above Q_t the creep rate is much larger. This is particularly clear for Figures 34b and 35. The ratio of Q_t/Q_u for these experiments was approximately 0.70. Since the design load Q_d is at most equal to $Q_f/1.33$, then the factors of safety would be at least 1.55 against the soil ultimate load, at least 1.33 against the creep failure load, and at least 1.09 against the creep threshold load.

The creep rate under the design load for these anchors was calculated. It averaged 0.9 mm/l.c. for the anchors with the long tendon bond length (9.2 m) and 0.22 mm/l.c. for the anchors with the short tendon bond length (4.6 m). This corresponds to 6.9 mm in 100 years and 1.7 mm in 100 years, respectively.

2.2.12 Load Loss as a Function of Time

Once the anchor is locked-off at the design load Q_d, the load varies as a function of time during the life of the structure. One of the concerns with anchors in clays is the creep of the soil around the anchor and the resulting decrease in load as time goes by. To investigate this load loss problem, the situation was simulated by locking off anchors 1, 2, 3, and 4 for 70 days with the same setup as the one used for the load tests (Figure 27). During those 70 days, periodic measurements were made of the load in the load cell and of the displacement of the load cell with respect to a separate deep benchmark. The load cell moved down slightly during the 70 days, probably due to the creep settlement of the spread footings and the shrink-swell characteristics of the clay. The total movement of the load cell after 70 days varied from 0.75 mm to 2 mm and averaged 1.4 mm. The movement readings $\Delta(t)$ were used to correct the load read on the load cell (P_{UNC}) to the load that would have been read on the load cell had the load cell not moved (P_{COR}).

$$P_{COR} = P_{UNC} + \frac{\Delta(t)\, A_T\, E_T}{L_e} \tag{10}$$

where A_T is the cross section of the steel tendon, E_T its modulus of elasticity, and L_e the elastic length of the anchor back calculated from the load test data; L_e is slightly larger than the unbonded length.

Figure 36 shows a plot of the anchor load for anchor 2 (P_{UNC} or P_{COR}) normalized to the lock-off load read at time t = 1 minute after lock-off as a function of the time t normalized to t_1 = 1 minute. This figure is typical and shows that the load loss is quite small, 0.88% of the lock-off load per log cycle of time in this case. Overall the percent load loss per log cycle of time varied from 0.5%/l.c. to 1.4%/l.c. and averaged 0.9%/l.c. Such an average leads by extrapolation to a load loss of 7% of the lock-off load for a period of 100 years. This seems to be a very acceptable number. One of the reasons for this low load loss is that even if the displacement Δ of the anchor head or of the anchor bonded length is significant, the load loss will be small because the tendon is long and flexible. Indeed,

$$Load\ Loss = \frac{\Delta \times A_T E_T}{L_e} \tag{11}$$

in which $A_T E_T$ is small and L_e is large. In this respect, the anchors with the longest unbonded length will have the smallest load loss. This is another advantage of using anchors with shorter tendon bond length.

In Figure 36, a change in slope can be observed after about 50,000 minutes (35 days), with an increase in the load loss rate after that time. This change in slope coincides with the beginning of the drilling process for an oil well located about one mile away from the NGES site. This change may also reflect the end of the preloading effect due to the earlier tests on anchor 2.

Anchors 1, 2, 7, and 8 were retested in August 1997. The loading sequence was that of a creep test with approximately 30 minute load steps. The load test results are shown in Figures 37 through 40. The ultimate loads were determined as for the 1991 data. The results of the 1991 and 1997 ultimate loads are compared in Table 5. As can be seen, all anchors gained strength over the six-year period. The gain was at least 20% and there was no apparent difference between the two anchors which were kept under tension for the six-year duration (anchor 1 under 523 kN and anchor 2 under 606 kN) and the two which were not (anchors 7 and 8).

The movement vs. time curves for each load step are presented in Figures 41 through 44. On the figures s is the movement after the beginning of the load step, t is the time since the beginning of the load step, s_1 is the movement one minute after the beginning of the load step, and t_1 is one minute. A power law model has been used to describe the accumulation of movement under a sustained load:

$$s = s_1 \left(\frac{t}{t_1}\right)^n \tag{12}$$

where n is the creep exponent, and the slope of the log s/s_1 vs. log t/t_1 curve. These curves are presented in Figures 41 to 44. The slopes n were calculated and are presented as a function of the load level on Figures 45 and 46. These figures confirm that the anchors with short tendon bond length (anchors 1 and 2) creep less than anchors with long tendon bond length (anchors 7 and 8). Indeed, the n values are much lower on the average for anchors 1 and 2 than for anchors 7 and 8.

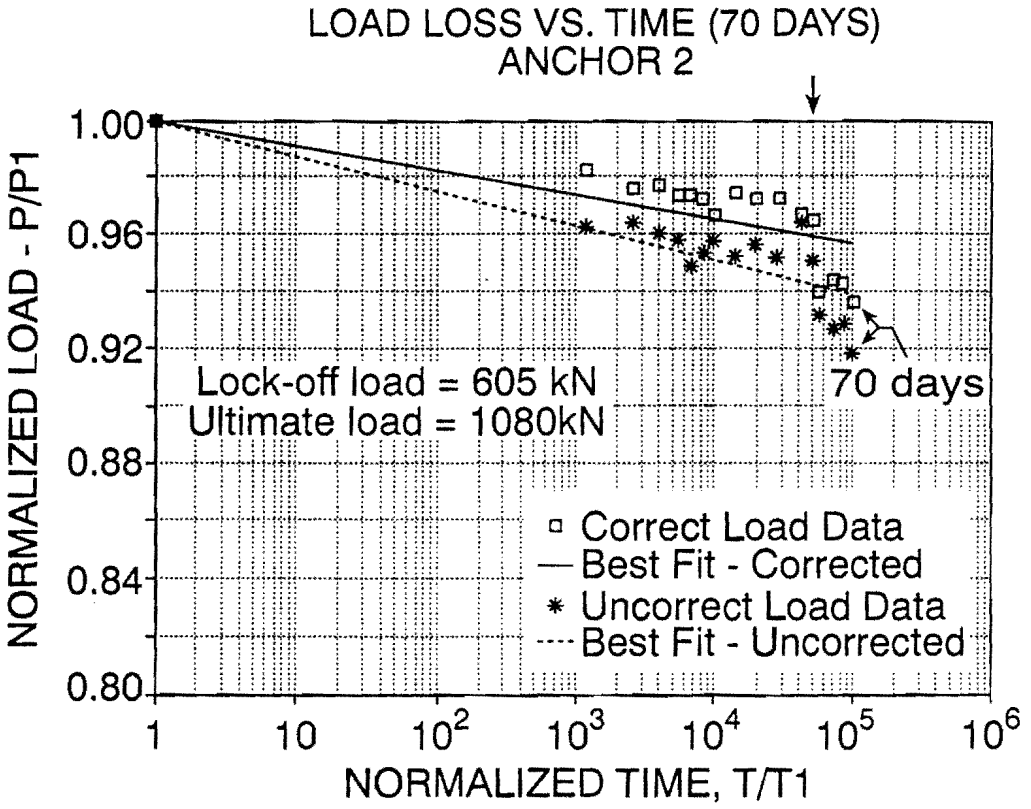

Figure 36. Load Loss vs. Time Curve for Anchor 2

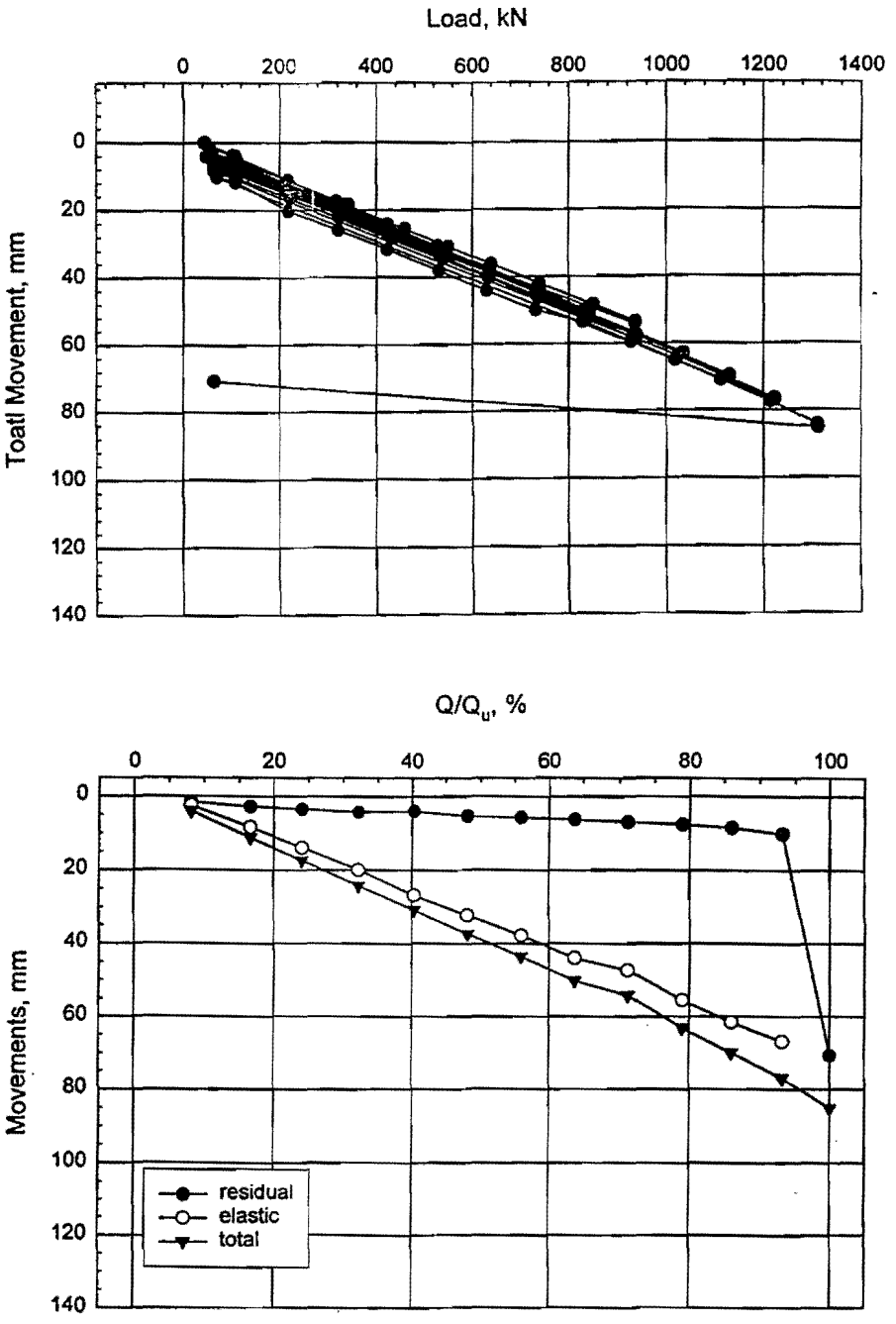

Figure 37. Load-Movement Curve for Anchor 1 (1997)

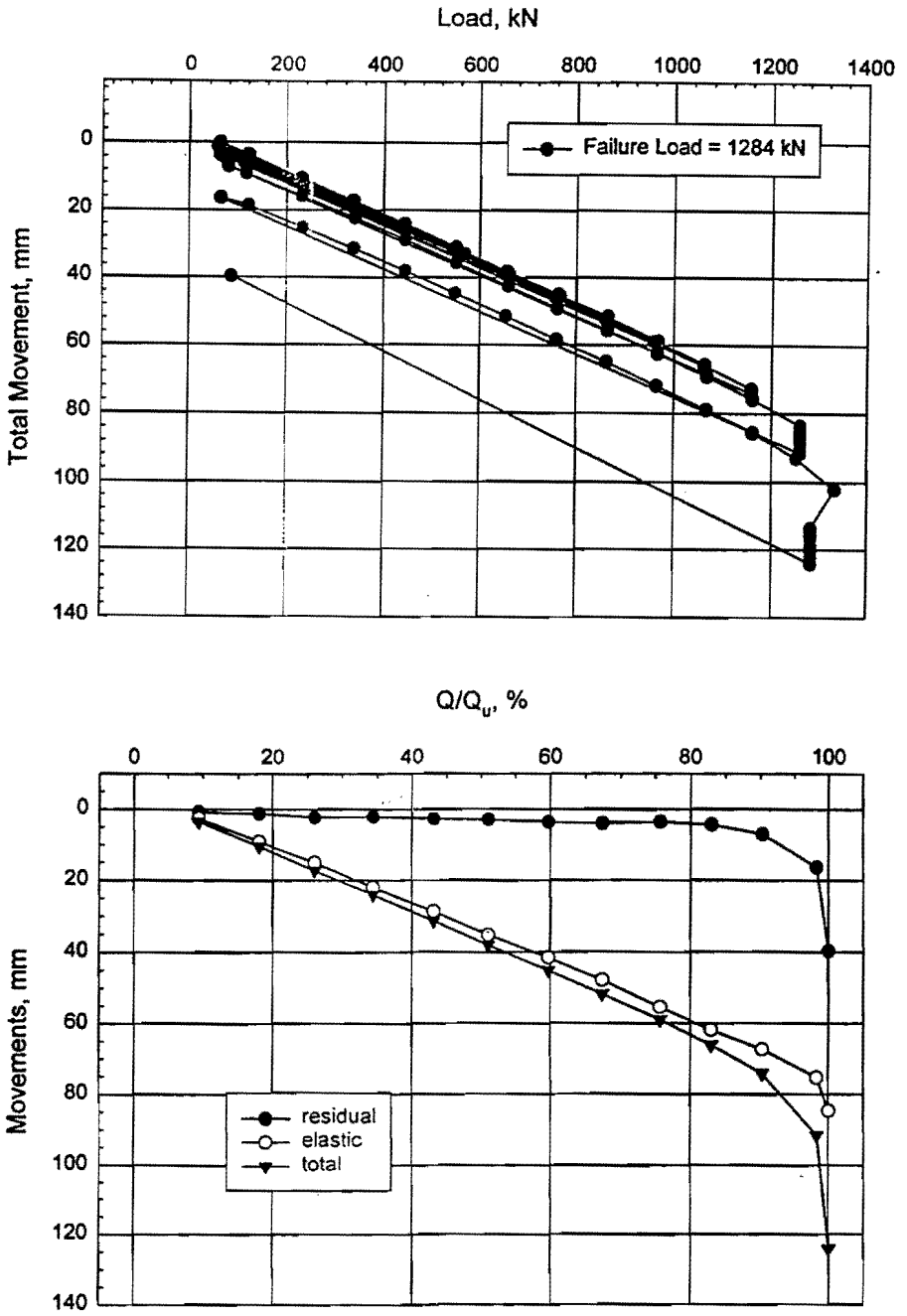

Figure 38. Load-Movement Curve for Anchor 2 (1997)

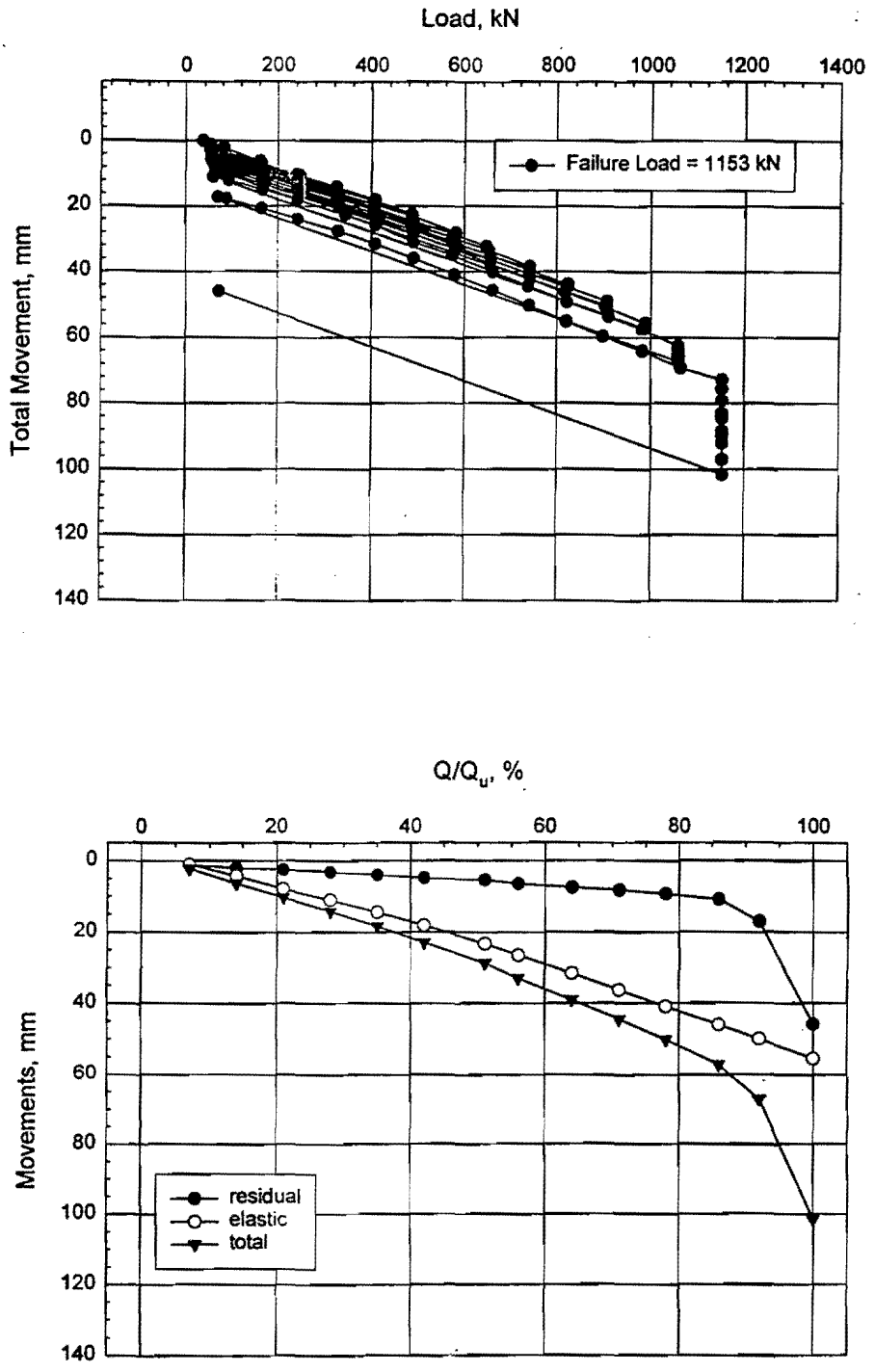

Figure 39. Load-Movement Curve for Anchor 7 (1997)

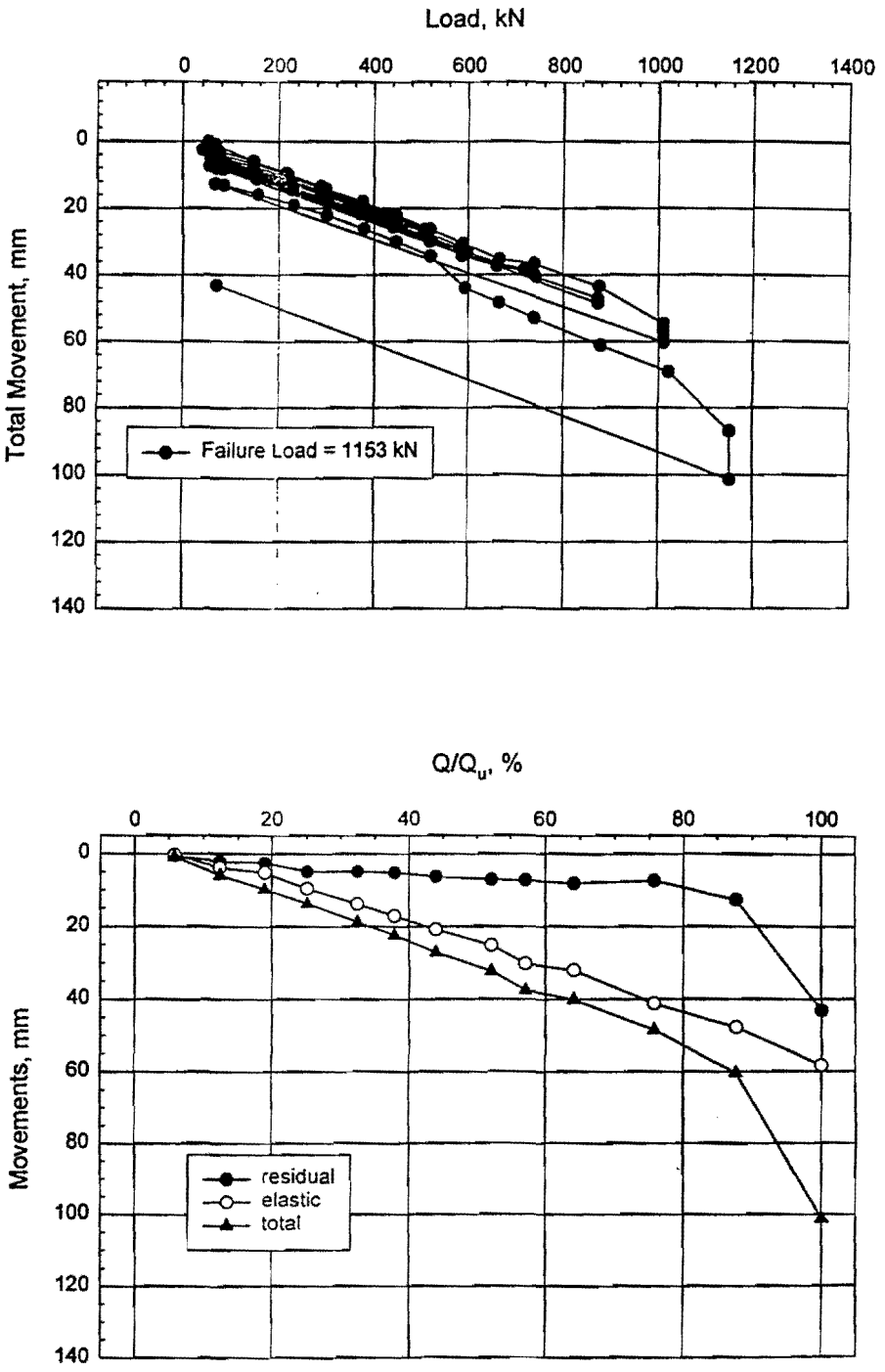

Figure 40. Load-Movement Curve for Anchor 8 (1997)

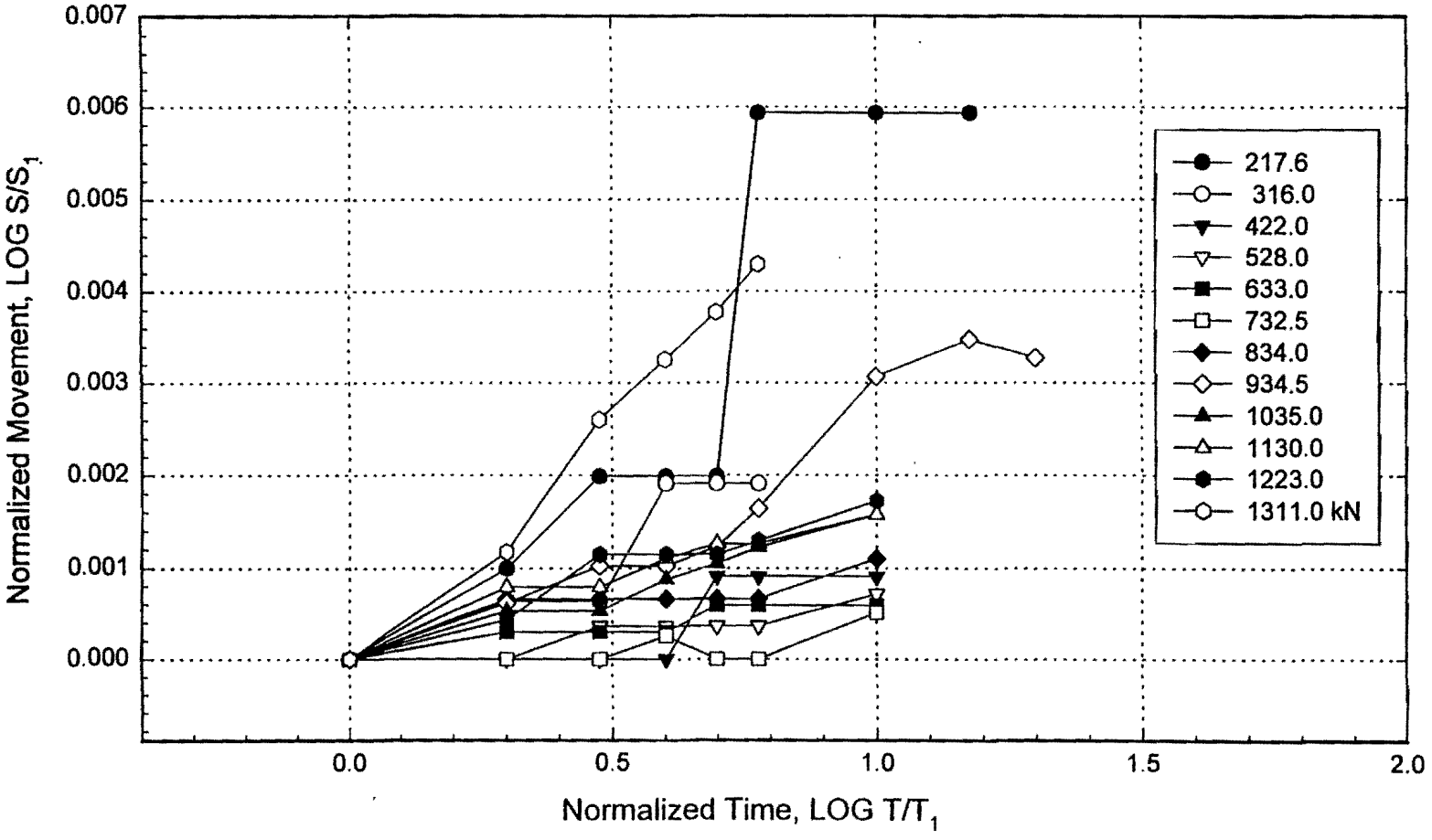

Figure 41. Movement-Time Curve for Anchor 1 (1997)

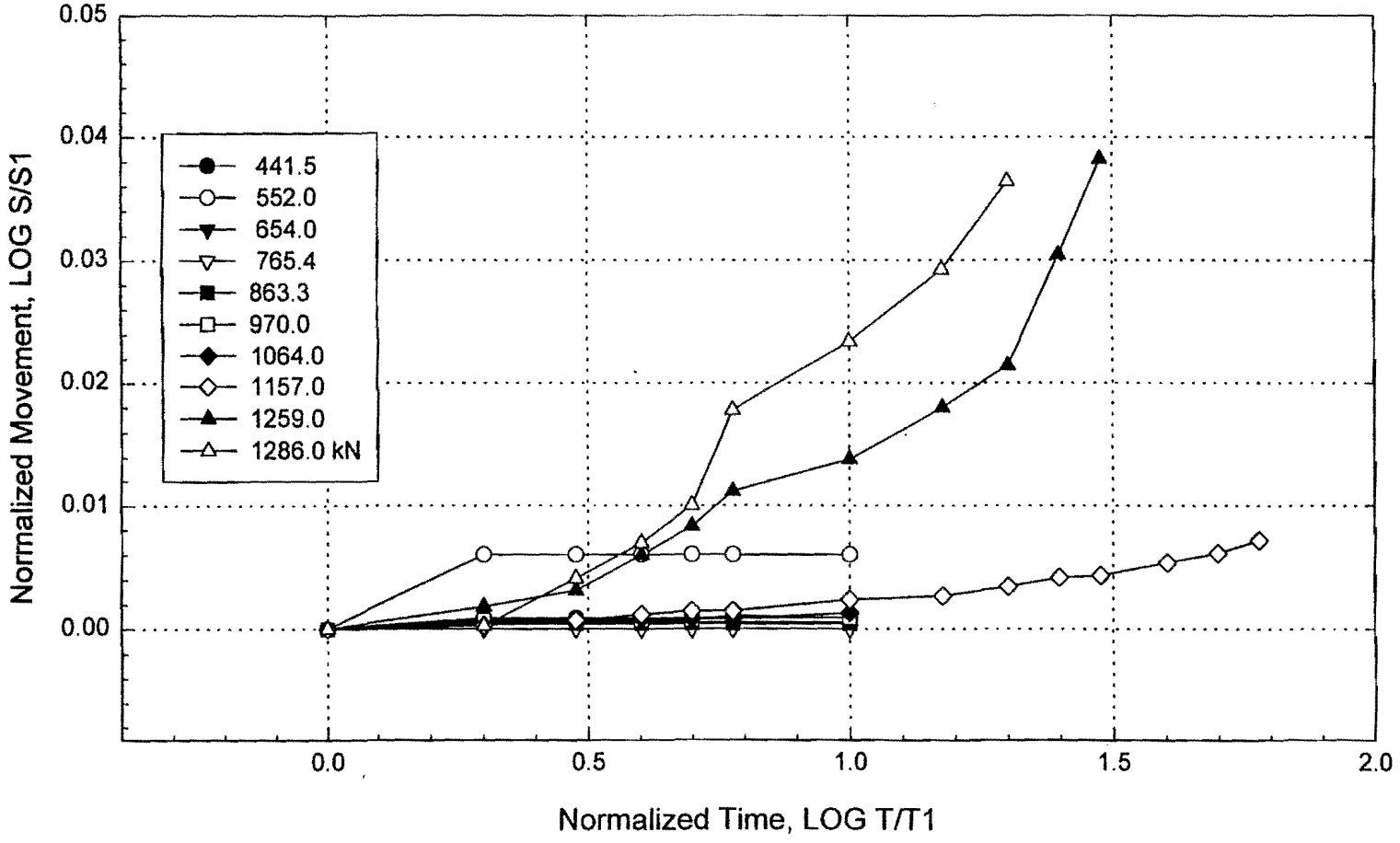

Figure 42. Movement-Time Curve for Anchor 2 (1997)

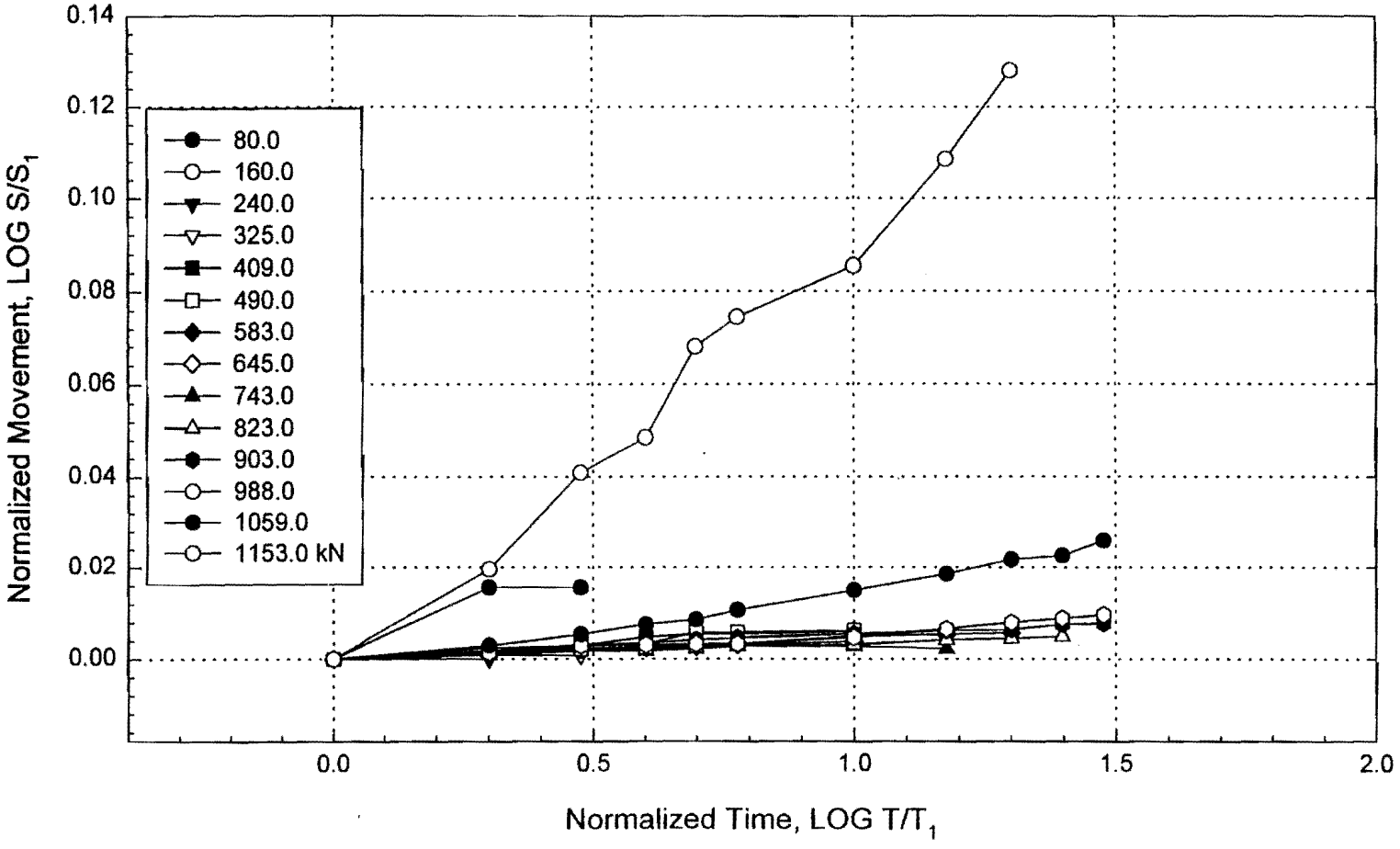

Figure 43. Movement-Time Curve for Anchor 7 (1997)

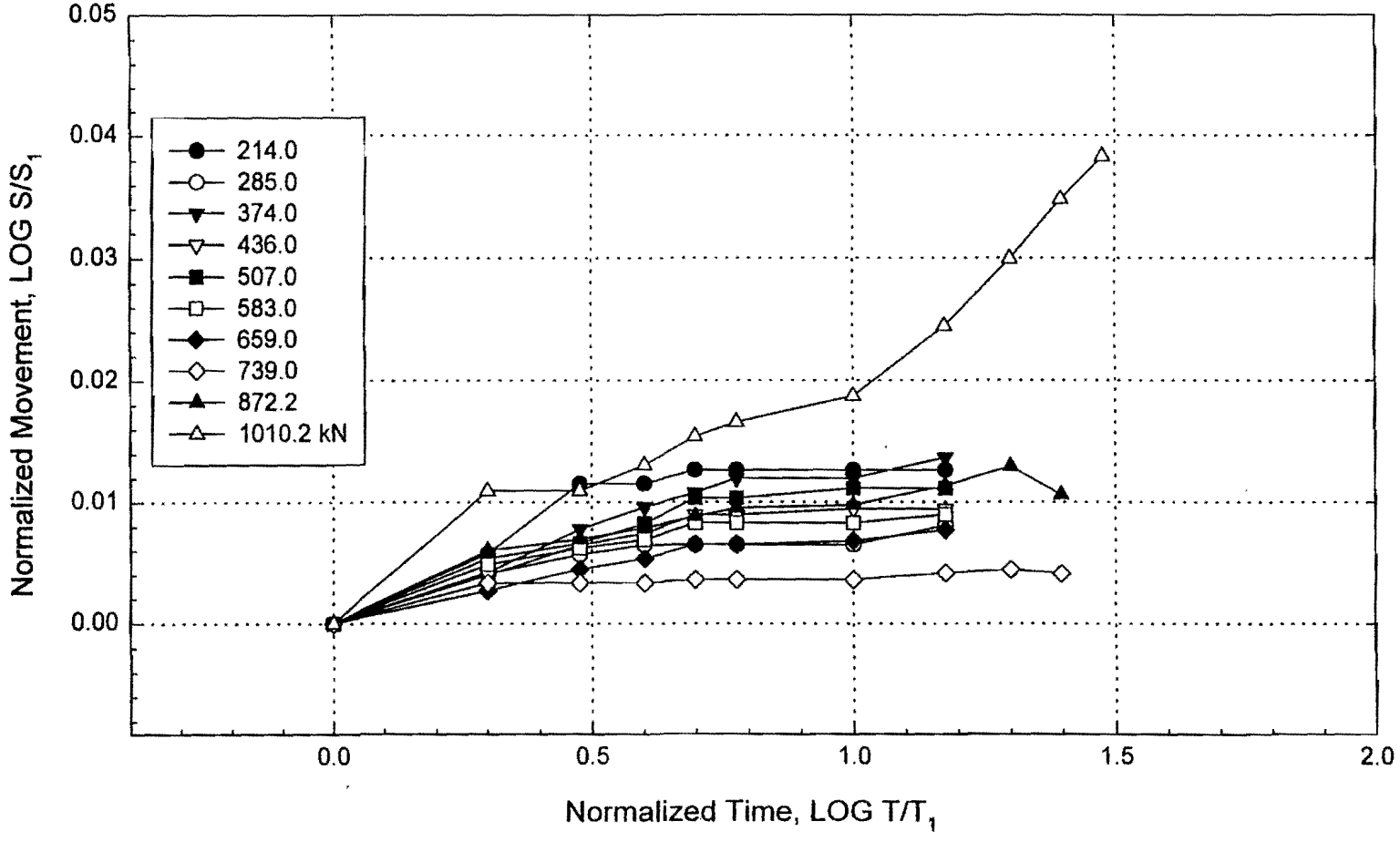

Figure 44. Movement-Time Curve for Anchor 8 (1997)

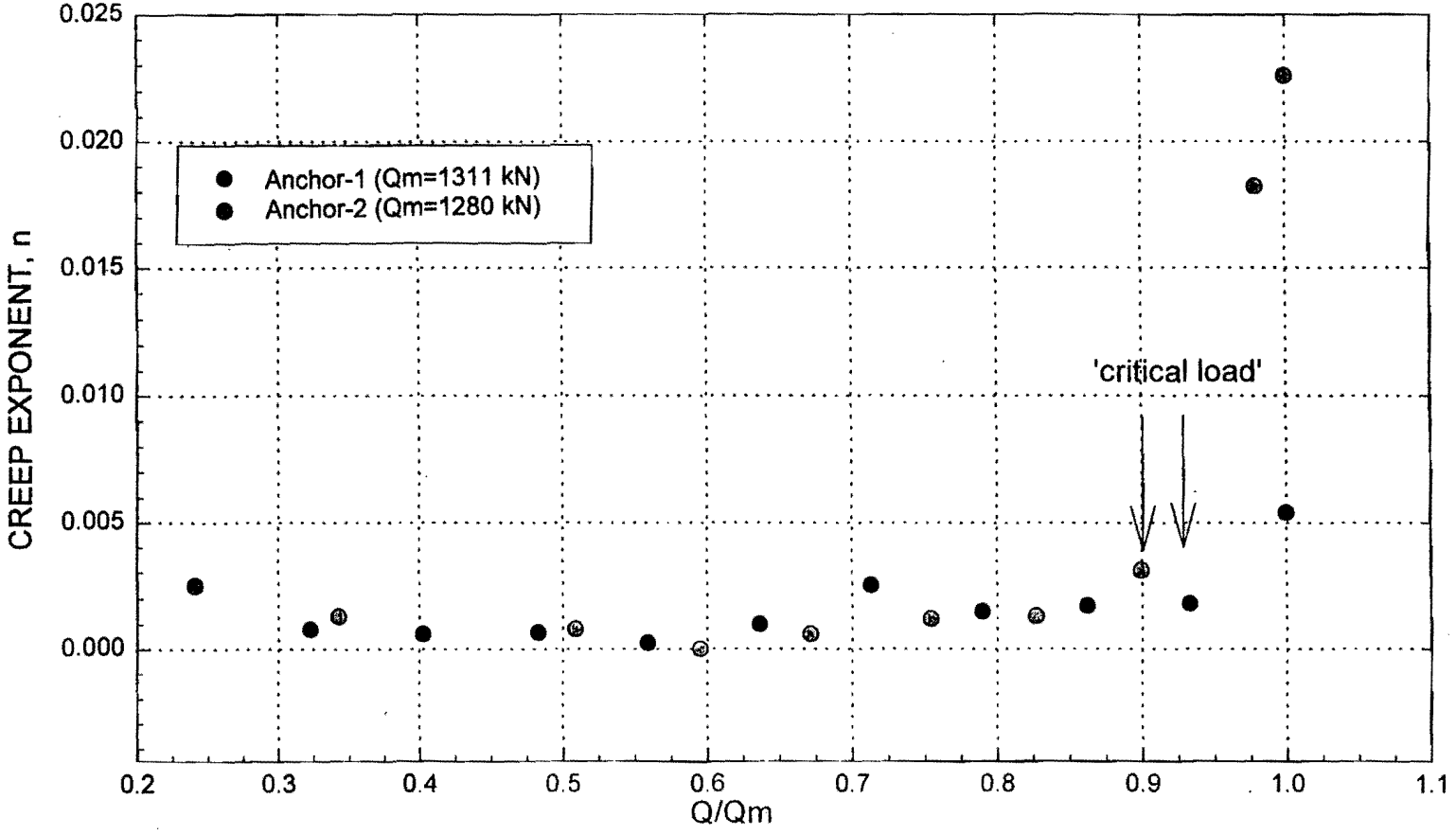

Figure 45. Creep Exponent – Load Level Curve (Anchors 1 & 2)

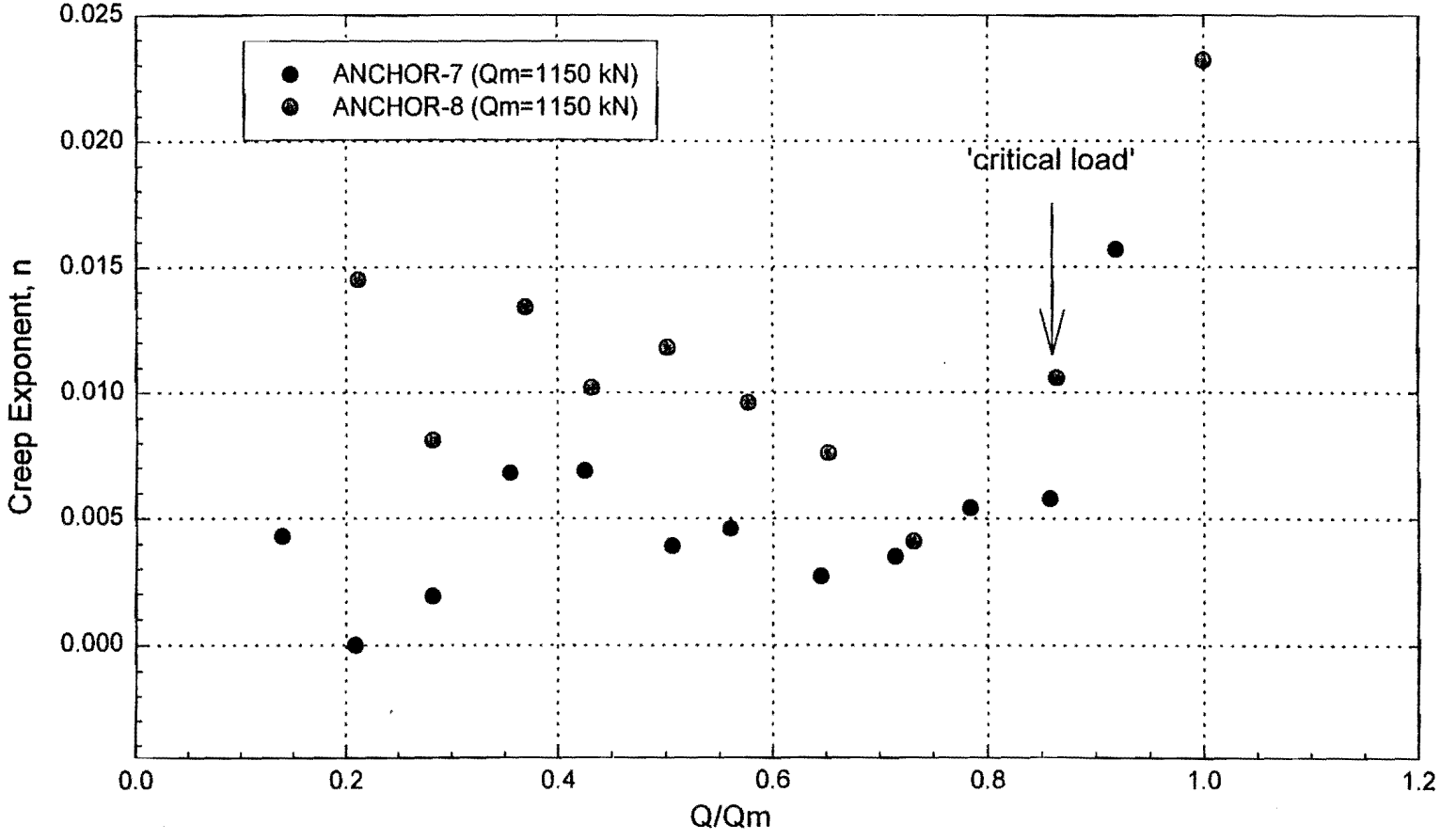

Figure 46. Creep Exponent - Load Level Curve (Anchors 7 & 8)

Table 5. Comparison of 1991 and 1997 Ultimate Loads

Anchor Number	Date Installed	Date Tested	Capacity (kN)	Date Tested	Capacity (kN)	Date Tested	Capacity (kN)
1	1-16-91	4-9-91	867	7-15-91*	978(?)	8-30-97	1245
2	1-16-91	4-11-91	1080(?)	7-13-91*	1156(?)	8-30-97	1255
7	12-19-90	3-7-91	801	3-18-91	738	8-30-97	1090
8	12-19-90	3-7-91	747	3-7-91	738	8-30-97	1060

Note: All capacities correspond to a residual movement of 25 mm.
*Denotes capacity after 70-day load-hold test.
(?) Capacity calculated by extrapolating load-movement curve.

2.3 LONG-TERM OBSERVATIONS ON TIEBACK WALL AT NGES-TAMU SAND SITE

In 1991 a full scale instrumented tieback wall was constructed, instrumented, and monitored at the National Geotechnical Experimentation Site (NGES) on the Riverside Campus of Texas A&M University. The wall was built under the scope of a project entitled "Permanent Ground Anchor Walls" sponsored by the Federal Highway Administration and Schnabel Foundation. This wall is a 60 m long and 7.5 m high soldier-beam and wood lagging wall with pressure injected tiebacks. In 1996, the instrumentation of the wall was read again. The 1996 results are compared to the 1991 results at the end of this section.

2.3.1 Soil Properties

The soil at the location of the wall is a medium dense clayey sand or silty sand from 0 m to 3.5 m, a medium dense clean poorly graded sand from 3.5 m to 7.5 m, and a medium dense clayey sand from 7.5 m to 13 m. The ground water level is 9.5 m below the top of the wall.

Several in situ tests were performed at the wall site during 1990 and 1991, including standard penetration tests, cone penetrometer tests, preboring pressuremeter tests, dilatometer tests, and borehole shear tests. The in situ test location at the wall site is shown in Figure 53. The sand has the following average properties: total unit weight of 18.5 kN/m^3, SPT blow count increasing from 10 blows/0.3 m at the surface to 27 blows/0.3 m at the bottom of the piles (9.15 m), borehole shear test friction angle of 32 ° with no cohesion, CPT point resistance of 7 Mpa, PMT modulus of 8 Mpa, and PMT limit pressure of 0.5 Mpa (Lim and Briaud, 1996).

2.3.2 Description of the Wall

The full-scale tieback wall was designed by the Schnabel Foundation Company. The wall is a soldier beam and wood lagging wall with pressure injected tiebacks. The wall is divided into two symmetric sections: one-half of the wall has only one row of anchors while the other half has two rows of anchors. Each section of the wall is sub-divided into a driven soldier beam subsection and a drilled soldier beam subsection (Figures 47 and 48). The wall is approximately 60 m long and 9.15 m high, which is comprised of 7.5 m of excavation height and 1.65 m of embedment depth below the excavation level. The 1.65 m embedment depth of the soldier beam is the minimum recommended penetration depth for normal conditions in the Schnabel design practice for tieback walls.

The soldier piles were installed every 2.44 m, wood lagging boards were installed between the piles as the excavation proceeded. The high pressure grouted anchors were inclined downward at 30° to the horizontal, located 1.8 m and 4.8 m below the top of the wall, and installed every 2.4 m horizontally in the case of the two row anchor section. In the one row anchored section, the tiebacks were installed at 2.7 m depth and every 4.9 m horizontally. The anchors consisted of 32 mm steel bars and were installed in 89 mm diameter holes filled with grout under a pressure ranging between 1.4 and 4.1 Mpa.

2.3.3 Wall Construction

The wall was built by driving, drilling, and grouting H beams vertically in the ground at a spacing of about 2.44 m center to center. Excavation started on one side of this row of soldier beams. As excavation proceeded, wood-lagging was placed horizontally between the H soldier beams to retain the soil. The first row of anchors was placed and grouted at a depth of 1.8 m from the ground level. The anchors were stressed to the design load. After curing of the anchor grout, excavation resumed with wood-lagging until the next row of anchors was placed and grouted. This process continued until the final excavation level was reached. The construction sequence for the one row and two row tieback sections of the wall is illustrated in Figures 49 and 50.

2.3.3.1 Fill

The area of the wall was raised up by 2.1 m with respect to the original ground level in order to avoid having to excavate below the water table. This was done before any construction began. About 0.3 m of topsoil was excavated in the area of the wall using scrapers. Then the area was filled with the soil obtained from a cut within 64 m in front of the wall site. The fill was built up in 0.3 m layers. Each layer was compacted until the desired height. The fill has an area of 60 m x 31.7 m on the top and it sloped away. It was completed in November 1990.

2.3.3.2 Soldier Beams and Wood-Lagging

The wall is divided into a one row anchored section and a two row anchored section corresponding to soldier beams labeled 13 to 18 and 5 to 12, respectively (Figures 47 and 48). All the soldier beams were installed with a 2.44 m center to center spacing. Beams No. 7 to 10 were

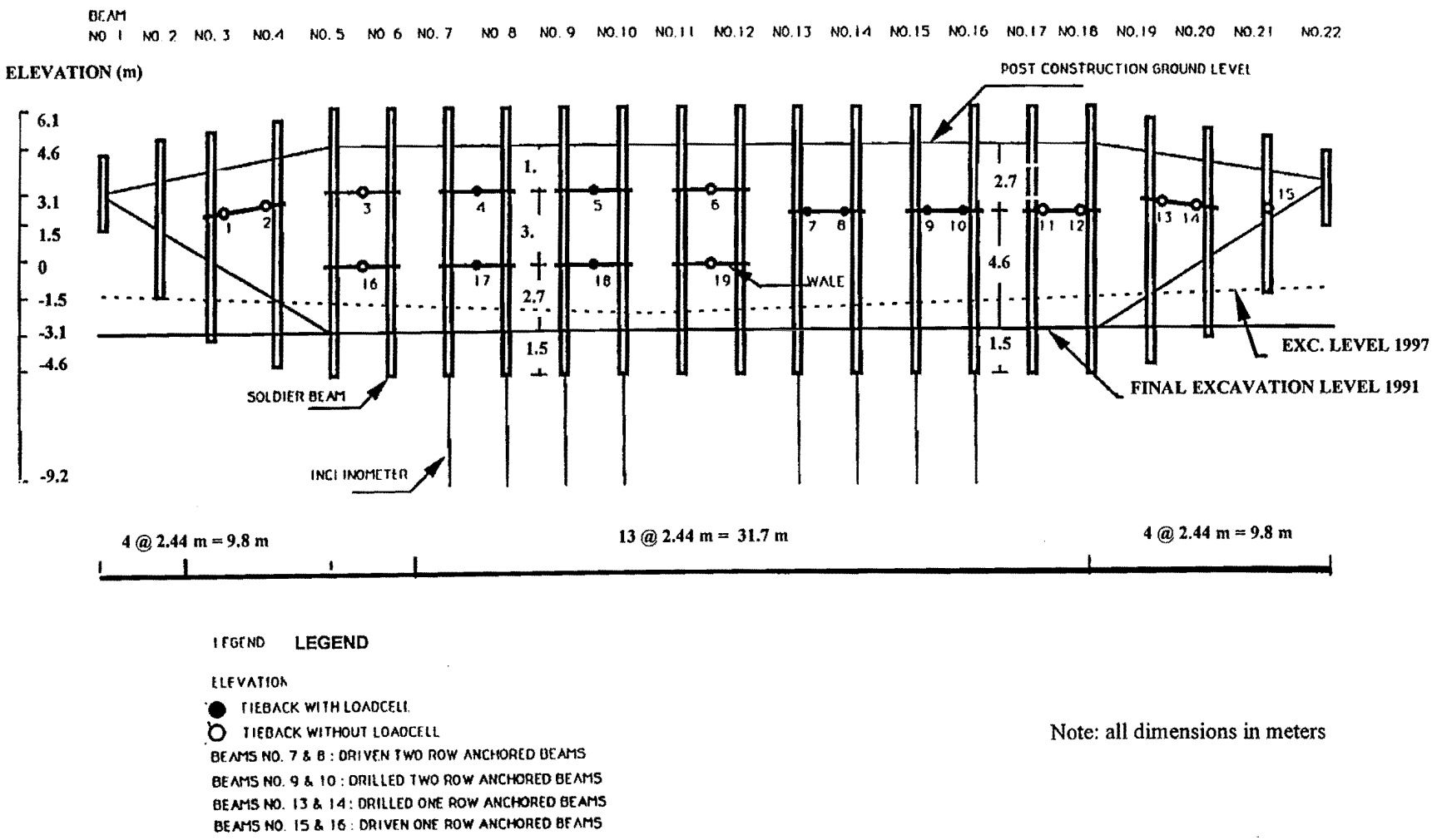

LEGEND LEGEND

ELEVATION

● TIEBACK WITH LOADCELL

○ TIEBACK WITHOUT LOADCELL

BEAMS NO. 7 & 8 : DRIVEN TWO ROW ANCHORED BEAMS

BEAMS NO. 9 & 10 : DRILLED TWO ROW ANCHORED BEAMS

BEAMS NO. 13 & 14 : DRILLED ONE ROW ANCHORED BEAMS

BEAMS NO. 15 & 16 : DRIVEN ONE ROW ANCHORED BEAMS

Note: all dimensions in meters

Figure 47. Full Scale Tieback Wall: Front View

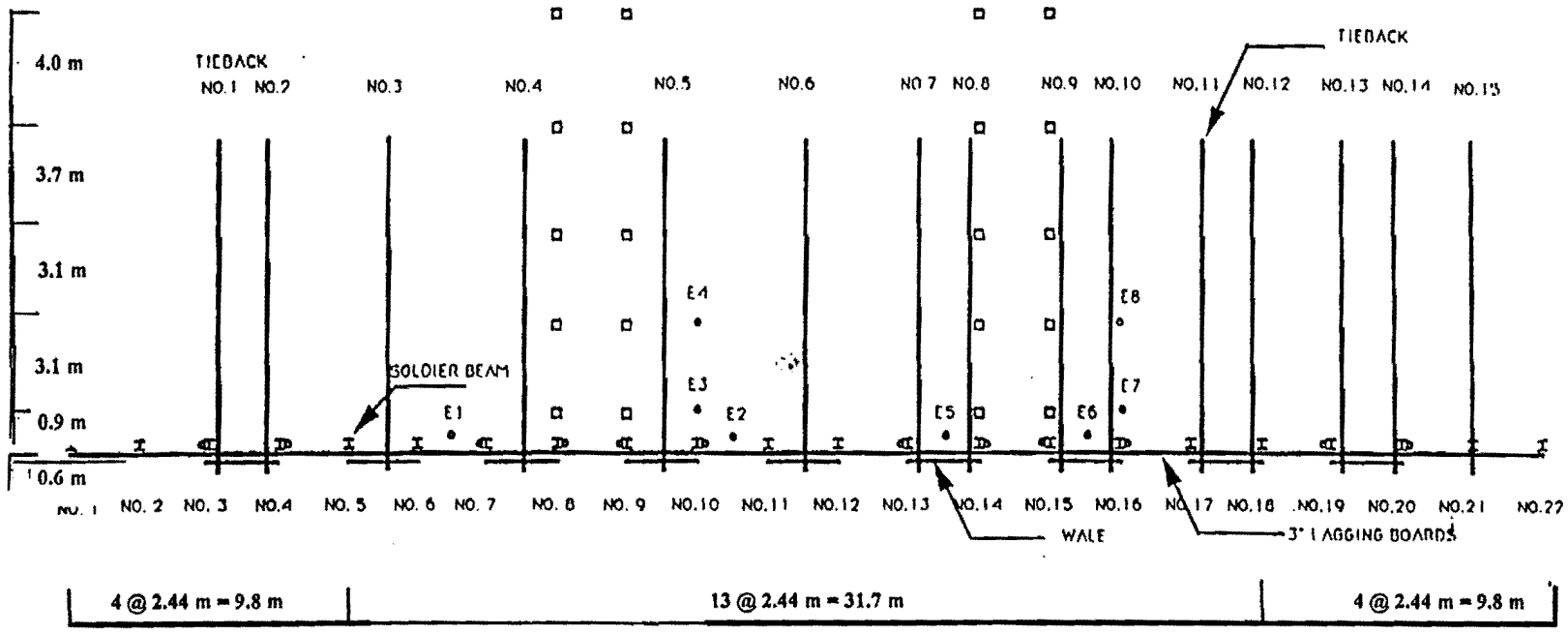

LEGEND

I SOLDIER BEAM
O INCLINOMETER
□ SETTLEMENT POINT

BEAMS NO. 7 & 8 : DRIVEN TWO ROW ANCHORED BEAMS
BEAMS NO. 9 & 10 : DRILLED TWO ROW ANCHORED BEAMS
BEAMS NO. 13 & 14: DRILLED ONE ROW ANCHORED BEAMS
BEAMS NO. 15 & 16 : DRIVEN ONE ROW ANCHORED BEAMS
INCLINOMETERS E1 - E8 POSITIONED BEHIND THE WALL FACE

Figure 48. Full Scale Tieback Wall: Plan View

	Schematic of Construction	Date	Symbol	Event
Stage 1	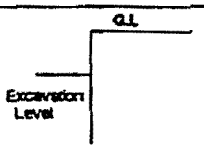	3-7-1991		Excavate wall to 3.1 m
Stage 2	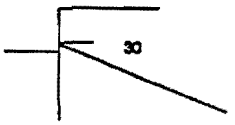	3-13-1991		Stress anchor at 2.7 m
Stage 3		4-3-1991		Excavate wall to 7.6 m

Figure 49. Construction Sequence for the One Row Tieback Wall

	Schematic of Construction	Date	Symbol	Event
Stage 1	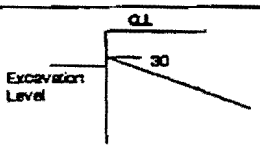	2-26-1991		Excavate wall to 2.4 m
Stage 2		3-8-1991		Stress anchor at 1.8 m
Stage 3	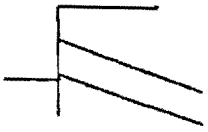	3-20-1991		Excavate wall at 5.2 m
Stage 4		3-26-1991		Stress anchor at 4.9 m
Stage 5		4-3-1991		Excavate wall to 7.6 m

Figure 50. Construction Sequence for the Two Row Tieback Wall

instrumented in the two row anchored section; they are made of the combination of an HP6x25x5/16 beam and two L3x3x5/16 angles. Beams No. 13 to 16 were instrumented in the one row anchored section; they consist of the combination of an HP10x57 section and two L3x3x1/4 angles (Figure 51). The uninstrumented soldier beams were wide flange steel beams HP8x36 and HP12x53 (Figure 52).

The type of soldier beams and their installation are summarized in Table 6. The excavated wall face between soldier beams was lagged with 2.44 m long, 0.3 m high, and 75 mm thick wood boards. They were seated on 127 mm long bolts arc-welded to the face of the soldier beams and fixed with steel plates.

In the one row anchored beams section, the two instrumented driven soldier beams denoted as 15 and 16 on Figure 47 consist of a wide flange section HP10x57 and two angles section L3x3x1/4 to protect the strain gages mounted on the flanges of the beam. For the two instrumented drilled soldier beams denoted as 13 and 14, the same steel HP10x57 sections were placed in 610 mm diameter predrilled holes with concrete backfill. A typical section of the one row tieback wall is presented in Figure 53.

Table 6. Soldier Beam Types

Beam No.	Section Type	Installation Method
1-2	HP 8x36	Driven
3	HP 8x36	Drilled
4	HP 12x53	Drilled
5-6	HP 8x36	Driven
7-8	WF 6x25	Driven
9	WF 6x25	Drilled
10	WF 6x25	Drilled
11-12	HP 8x36	Driven
13	HP 10x57	Drilled
14	HP 10x57	Drilled
15-16	HP 10x57	Driven
17-19	HP 12x53	Driven
20	HP 8x36	Driven
21	HP 10x42	Driven
22	HP 8x36	Driven

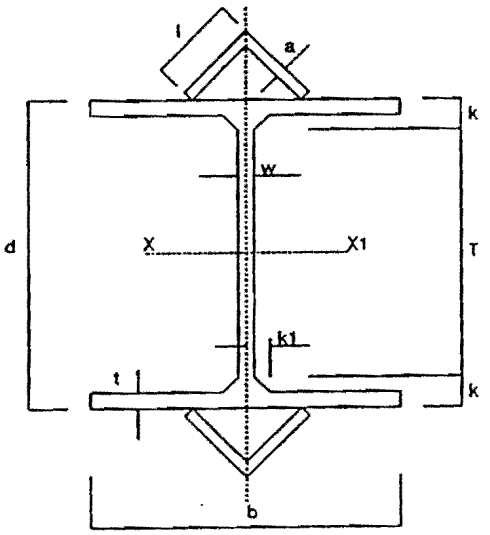

(a) The One Row Tieback Wall Section

Designation	Area	d	T	k	k1	t	b	w	l	a
	(in^2)	(in)	(in)	(in)	(in)	(in)	(in)	(in)	(in)	(in)
HP10x57	16.8	10	$7\frac{5}{8}$	$1\frac{3}{16}$	$1\frac{3}{16}$	$\frac{9}{16}$	$10\frac{1}{4}$	$\frac{9}{16}$		
L3x3x$\frac{1}{4}$	1.44								3	$\frac{1}{4}$

(b) Two Row Tieback Wall Section

Designation	Area	d	T	k	k1	t	b	w	l	a
	(in^2)	(in)	(in)	(in)	(in)	(in)	(in)	(in)	(in)	(in)
W6x25	7.34	$6\frac{3}{8}$	$4\frac{3}{4}$	$\frac{13}{16}$	$\frac{7}{16}$	$\frac{7}{16}$	$6\frac{1}{8}$	$\frac{5}{16}$		
L3x3x$\frac{5}{16}$	1.78								3	$\frac{5}{16}$

Figure 51. Cross Section of Instrumented Soldier Beams

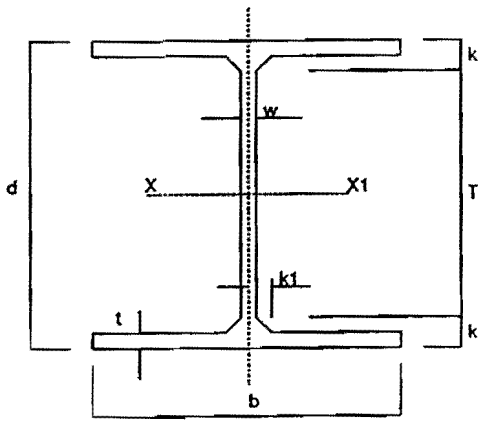

Designation	Area	d	T	k	k1	t	b	w
	(in^2)	(in)	(in)	(in)	(in)	(in)	(in)	(in)
*HP*12x53	15.5	$11\frac{3}{4}$	$9\frac{1}{2}$	$1\frac{1}{8}$	$\frac{7}{8}$	$\frac{7}{16}$	12	$\frac{7}{16}$
*HP*10x42	12.4	$9\frac{3}{4}$	$7\frac{5}{8}$	$1\frac{1}{16}$	$\frac{3}{4}$	$\frac{7}{16}$	$10\frac{1}{8}$	$\frac{7}{16}$
*HP*8x36	10.6	8	$6\frac{1}{8}$	$\frac{15}{16}$	$\frac{5}{8}$	$\frac{7}{16}$	$8\frac{1}{8}$	$\frac{7}{16}$

Figure 52. Cross Section of Uninstrumented Soldier Beams

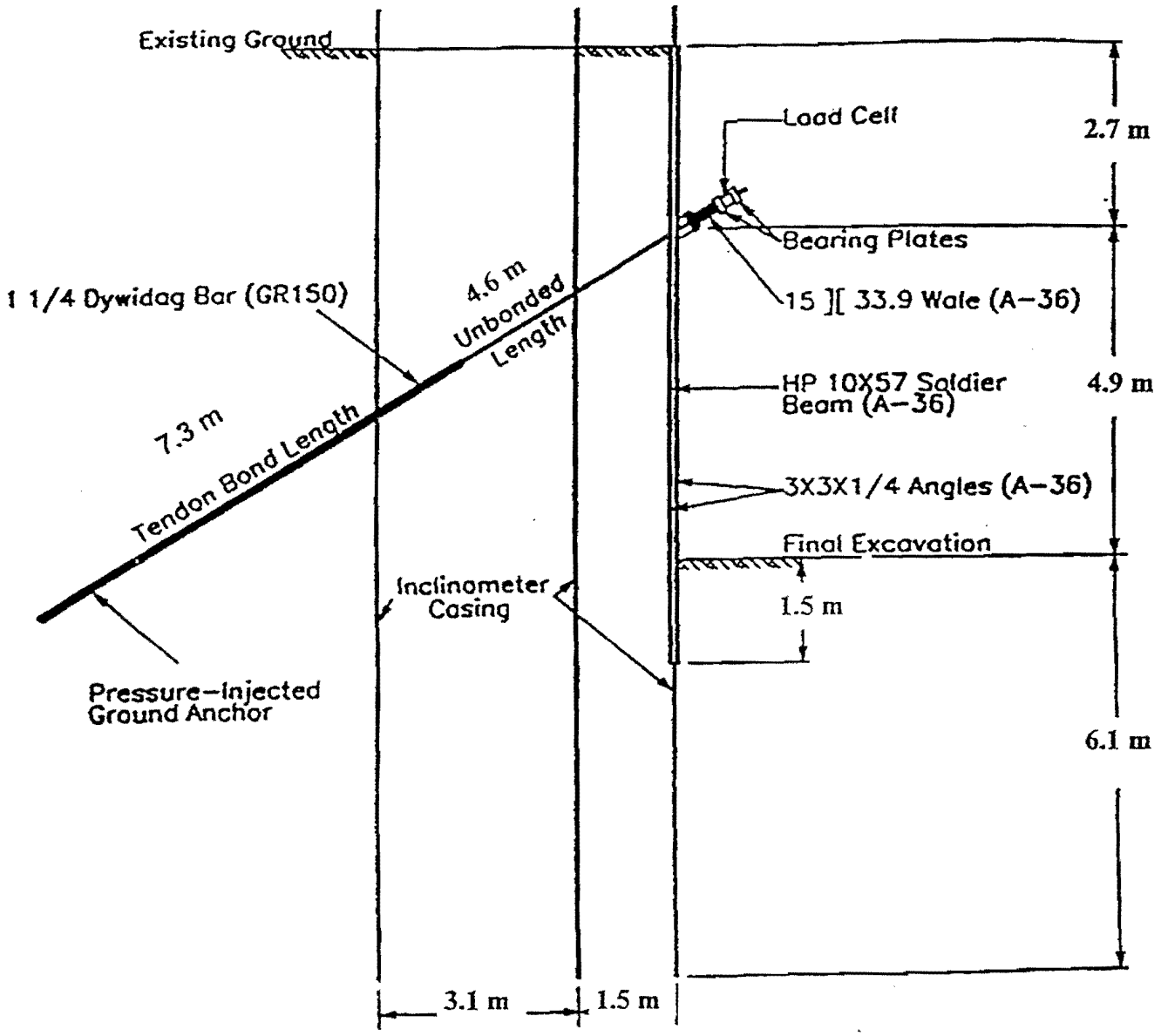

Figure 53. One Row Tieback Wall: Cross Section

In the two row anchored beams section the two instrumented driven beams denoted as 7 and 8 on Figure 47 consist of a beam section of WF6x25 and two L3x3x6/16 angles sections on each side of the flanges. The two instrumented drilled soldier beams denoted as 9 and 10, consist of the same steel sections as the instrumented driven beams; they were placed in 457 mm diameter predrilled holes with concrete backfill. A typical section of the two row tieback wall is presented in Figure 54.

2.3.3.3 Tiebacks

Tieback tendons consisting of a 31.8 mm steel bar (ASTM A-722-75) for the instrumented beams were installed in 89 mm diameter holes filled with high pressure injected cement grout (1.4 to 4.1 Mpa). The tendon consisted of a 7.3 m tendon bond length and 4.6 m to 55 m unbonded length sheathed in plastic with grease between the steel tendon and the plastic sleeve. The anchors were installed at a downward inclination of 30° with respect to the horizontal. For each anchor, performance tests and/or proof tests were carried out before the anchors were locked off. The load and load test information for the anchors are summarized in Table 7.

2.3.4 Construction Sequence

A total of 22 soldier beams, including eight instrumented beams, were installed at a center to center spacing of 2.44 m from the built-up ground level. The driven beams were installed with an impact hammer (model MKT-9B3). For the drilled soldier beams, 610 mm diameter holes for the one row tieback wall section and 457 mm diameter holes for the two row tieback wall section were drilled with a flight auger using a drilling rig. About 6 m deep where the hole would not stand open by itself, casings were vibro-driven in place. Steel casings of 610 mm diameter were vibro-driven for the two row tieback wall section into the corresponding holes using a vibratory hammer. The drill rig then excavated the sand inside the casing using an auger. The soldier beams were lowered in the casing and then filled with concrete while the casing was extracted.

The wall construction was completed on April 3, 1991. The chronological excavation progress is shown in Figure 55. Detailed step-by-step construction and instrumentation procedures are described by Chung and Briaud (1993).

2.3.5 Instrumentation and Data Acquisition

The instrumentation used in the wall consists of strain gages, load cells and inclinometers. The data acquisition system for the strain gages consisted of automated data-loggers and a personal computer. Inclinometer readings were taken using an inclinometer reader (Geokon Model GK-601) and the data files were saved in a personal computer.

A total of 28 vibrating wire strain gages, Geokon Model VSM-4000, was installed every 0.3 m on each side of the soldier beam flanges. A total of 450 gages were installed on the eight instrumented soldier piles. The lowest and topmost strain gages were located 0.3 m from the ends of the soldier beams. Only the second and third strain gages from the top of the beams were placed 0.45 m apart.

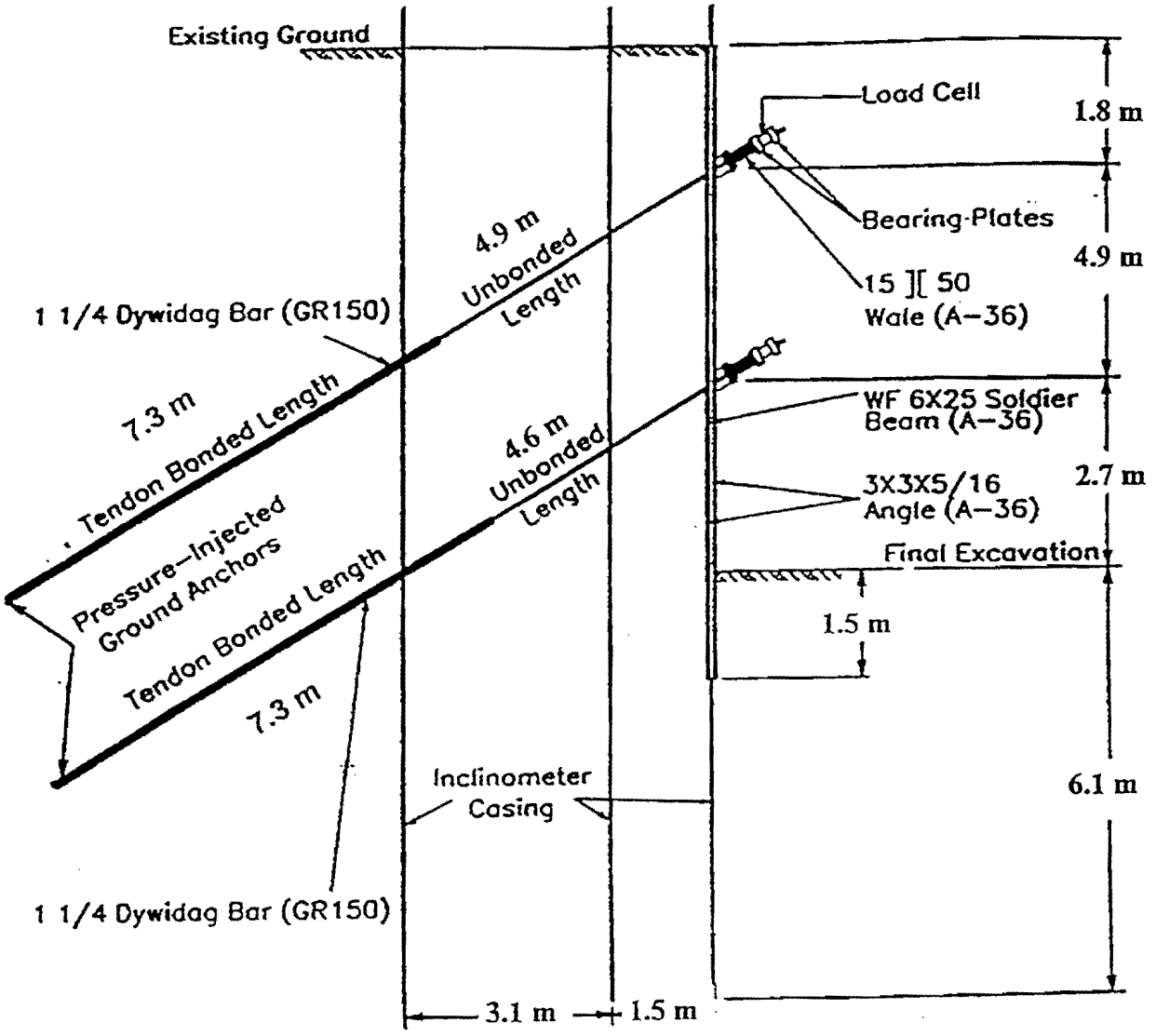

Figure 54. Two-Row Tieback Wall: Cross Section

Table 7. Summary of Anchor Loads and Tests

Anchor No.	Tendon Size (mm)	Design Load (kN)	Test Performed	Lock-Off Load (kN)
1	34.9	113	Proof	85
2	34.9	218	Proof	164
3	31.8	474	Performance	378
4	31.8	474	Proof	378
5	31.8	474	Proof	378
6	31.8	474	Proof	378
7	31.8	400	Performance	300
8	31.8	400	Proof	300
9	31.8	400	Proof	300
10	31.8	400	Proof	300
11	31.8	400	Proof	300
12	31.8	400	Proof	300
13	34.9	218	Proof	164
14	34.9	113	Proof	85
15	31.8	89	Proof	67
16	31.8	427	Proof	320
17	31.8	427	Proof	320
18	31.8	427	Proof	320
19	31.8	427	Proof	320

A total of 16 inclinometer wells were placed on the instrumented soldier beams, between the soldier beams and behind the wall facing, in the embankment.

PVC pipes, 102 mm in diameter, were securely attached to the drilled soldier beams. The soldier beams with the attached PVC pipes were installed in pre-drilled holes. Then the inclinometer casing was installed inside the PVC pipe and secured with grout. For the inclinometer locations associated with the instrumented driven soldier beams and for those placed behind the wall face (embankment), the inclinometer casings were installed in an 89 mm outside diameter, 63.5 mm inside diameter flush-coupled casing driven close ended to a depth of about 13.7 m below the top level of the wall. This was 6.1 m below the excavation level and 4.6 m below the bottom of the soldier piles. At this depth it was assumed that no movement occurred due to the excavation process.

A Sinco Digital Inclinometer Model 50325-E sensor with a Geokon Model GK-601 Inclinometer Reader was used to read the inclinometer wells. The guiding wheels of the inclinometer sensor ride in grooves oriented perpendicular to the wall face in order to measure the horizontal deflection of the wall. The inclinometer readings are taken at 0.61 m intervals from bottom to top and the collected data are dumped to a personal computer.

Geokon Model 4900 vibrating wire load cells were used on each one of the anchors supporting instrumented soldier beams in order to measure the anchor loads. The vibrating wire load cell consists of a hollow steel cylinder with six vibrating wire strain gages located around the circumference of the cell. The readings are taken by a readout box, Geokon Model GK-401 at each one of the six strain gages. The sum of the six readings is computed, then the sum of the zero readings is subtracted, and the difference is multiplied by the load cell factor to obtain the anchor load.

2.3.6 Data Reduction

The data reduction process for the strain gages, load cells, and inclinometers is explained in great detail by Chung and Briaud (1993). However, a summary is given here.

2.3.6.1 Strain Gage Data Analysis

Bending moments and axial forces in the soldier beams were obtained from the measured strains. The strain gages were installed on both sides of each one of the instrumented soldier beams. The measured strains are separated into bending strains and axial strains. By using the theory of elasticity, the bending strains and axial strains give bending moments and axial forces in the soldier beams, respectively.

Figure 56 shows the assumed strain distribution in the cross section of a soldier beam. It is assumed that the strain diagram is linear and that the magnitude of the bending strain is proportional to the distance from the neutral axis. Therefore the bending strains and the axial strains in the soldier beams can be obtained as (Figure 56):

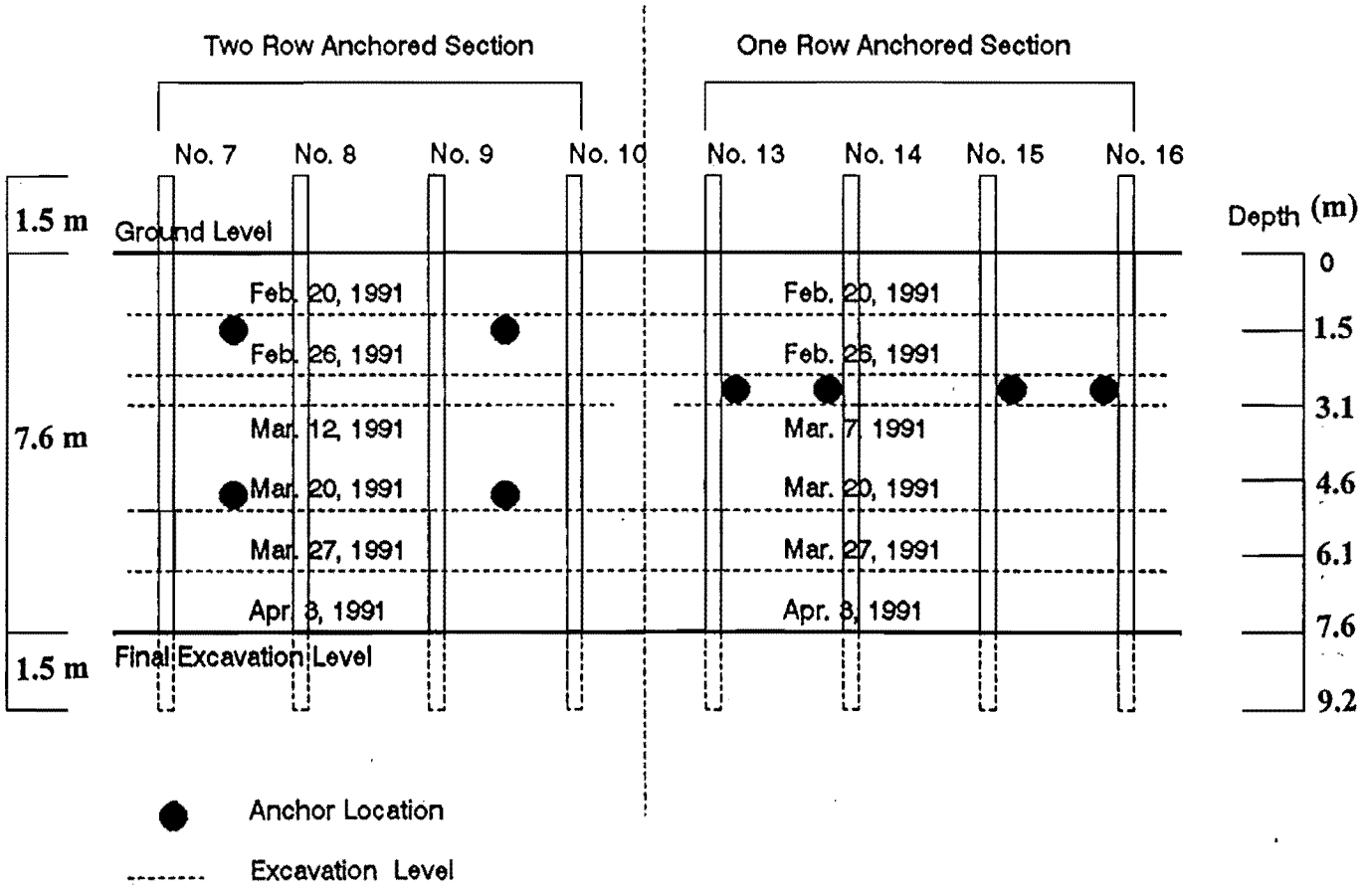

Figure 55. Chronology of the Excavation Process

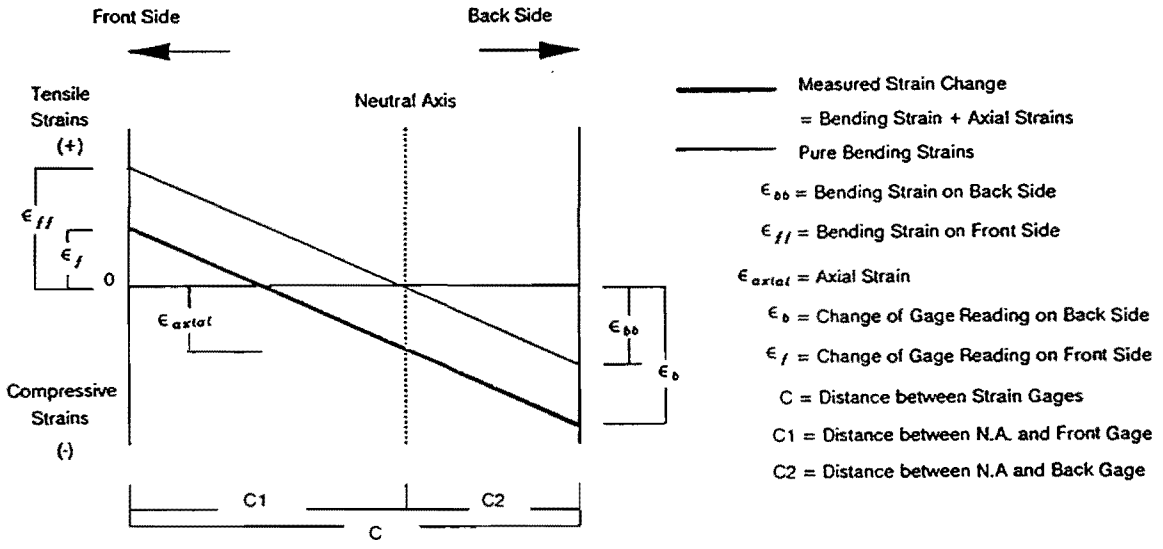

Figure 56. Stress Distribution in Soldier Beams

$$\varepsilon_{bb} = \frac{e_b - e_f}{C} C_2 \tag{13}$$

$$\varepsilon_{axial} = \frac{e_b C - e_b C_2 + e_f C_2}{C} \text{ or } e_b - \varepsilon_{bb} \tag{14}$$

where: ε_{bb} = bending strain on the back side of the beam
ε_b = strain on the back side of the beam
ε_f = strain on the front side of the beam
C = distance between the two gages
C_2 = distance between the neutral axis and the back gage

For the driven soldier beams, the neutral axis lies in the middle of the soldier beam, i.e., $C_2 = ½ C$. Equations 13 and 14 can then be simplified as:

$$\varepsilon_{bb} = \frac{e_b - e_f}{2} \tag{15}$$

$$\varepsilon_{axial} = \frac{e_b + e_f}{2} \tag{16}$$

For the drilled beams special calculations have to be made (next section).

2.3.6.2 Bending Moments Calculation

Using the elastic theory, the stress-strain relationship can be defined as:

$$\sigma = E\varepsilon \tag{17}$$

where, E is the Young's Modulus, and σ is the normal stress in the section at the point where the normal strain is ε. The bending stress, σ_{bb}, in the cross section of the driven soldier beam at the location of the gage on the back side is:

$$\sigma_{bb} = \frac{M}{I} C_2 \tag{18}$$

where M is the bending moment in the beam and I is the moment of inertia of the beam. In this equation M is positive when it produces tension on the back side of the beam, and C_2 is positive when as shown in Figure 56. Combination of Equations 17 and 18 leads to the following equation for the measured bending moment in the driven beams:

$$M = \frac{EI}{C_2} \varepsilon_{bb} \tag{19}$$

The Young's modulus of the steel for the driven beams, denoted in Figure 47 as No. 7, 8, 15, and 16, is 2×10^8 kPa (3×10^7 psi). The moment of inertia of the beam section and the Young's modulus were substituted in Equation 19 in order to calculate the bending moment in the beam. The cross

section of the driven soldier beam is shown in Figure 57. The properties of the driven beam section are presented in Table 8.

The drilled beams were placed in oversized holes and then backfilled with concrete. The concrete on the front side of the drilled beams and above the excavation level was cut out before installing the wood-lagging. The bond between the steel beam and the concrete was assumed to be strong enough to keep the same strain in both materials. Therefore, the drilled soldier beams were analyzed as composite beams. The cross sections of the drilled beams above and below the excavation level are shown in Figures 58 and 59, respectively.

Each composite beam was transformed into an equivalent steel beam. In the transformed section, the steel beam remained unchanged and the width of the concrete portion was reduced by the ratio of Young's moduli, concrete to steel. Young's modulus for concrete was estimated using the following equation:

$$E_{concrete}\,psi = 57000\sqrt{f'c\,(psi)} \tag{20}$$

where f'c is the 28-day compressive strength in psi. The average 28-day compressive strength for the lean-mix fill was 597.7 kPa (86.7 psi) and 32888 kPa (4770 psi) for the structural concrete. Using Equation 20 the Young's moduli was computed to be $3.66\text{x}10^6$ kPa ($5.31\text{x}10^5$ psi) for the lean mix fill and $2.71\text{x}10^7$ kPa ($3.94\text{x}10^6$ psi) for the structural concrete. Table 8 includes the section properties for the composite soldier beams. Bending moments assuming composite behavior for the drilled-in beams were calculated using Young's modulus for steel and the section properties for the composite beams. A detailed discussion regarding this matter is presented in Chung and Briaud (1993).

2.3.6.3 Calculation of Axial Load

The axial forces in the driven beams were obtained from the stress-strain relation as follows:

$$\sigma = \frac{P}{A} = E\,\varepsilon_{axial} \tag{21}$$

where: P = axial force in the section
A = cross sectional area of the beams
ε_{axial} = axial strain obtained from Equation 16

Then the equation for the axial forces in the beam can be written as:

$$P = A\,E\,\varepsilon_{axial} \tag{22}$$

For the drilled beams, the axial forces act on the composite section of the steel beam and the concrete. Equation 21 can be rewritten as:

$$P = (A_s E_s + A_c E_c)\,\varepsilon_{axial} \tag{23}$$

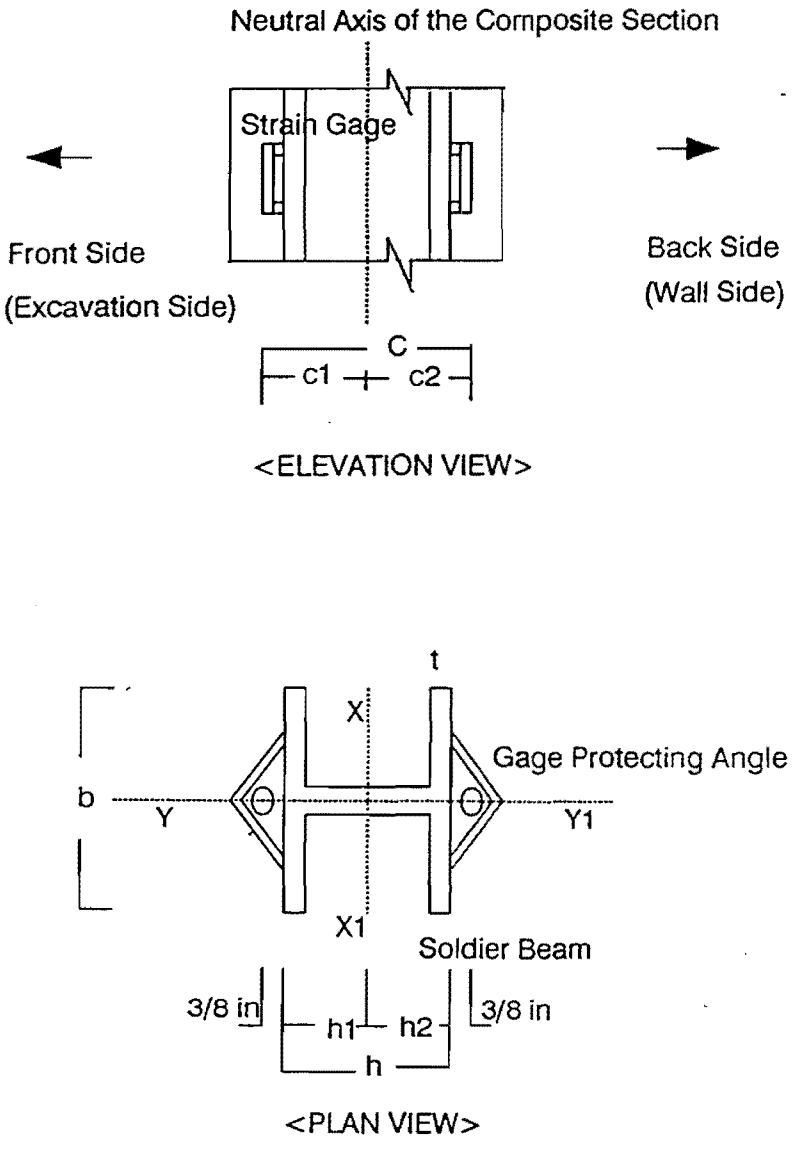

Figure 57. Cross Section of Driven Soldier Beams

Table 8. Properties on the Drilled and Driven Soldier Beams

CATEGORY	DRILLED BEAMS						DRIVEN BEAMS	
	Above Grade		Below Grade					
Beam No.	9 & 10	13 & 14	10	14	9	13	7 & 8	15 & 16
Concrete Used	Lean-mix Backfill		Lean-mix Backfill		Structural Concrete		n/a	n/a
Designation	W 6x25 L 3x3x5/16	HP 10x57 L 3x3x1/4	W 6x25 L 3x3x5/16	HP 10x57 L 3x3x1/4	W 6x25 L 3x3x5/16	HP 10x57 L 3x3x1/4	W 6x25 L 3x3x5/16	HP 10x57 L 3x3x1/4
b (in)	6.0	10.0	6.0	10.0	6.0	10.0	6.0	10.0
d (in)	6.38	9.9	6.38	9.9	6.38	9.9	6.38	9.9
t (in)	0.45	0.6	0.45	0.6	0.45	0.6	0.45	0.6
As (in^2)	10.9	19.68	10.9	19.68	10.9	19.68	10.9	19.68
h (in)	18.0	24.0	18.0	24.0	18.0	24.0	n/a	n/a
c1 (in)	3.94	5.85	3.565	5.325	3.565	5.325	3.565	5.325
c2 (in)	3.19	4.8	3.565	5.325	3.565	5.325	3.565	5.325
c (in)	7.13	10.65	7.13	10.65	7.13	10.65	7.13	10.65
n = Ec/Es	0.0177	0.0177	0.1312	0.1312	0.1312	0.1312	n/a	n/a
I (x-x) (in^4)	164.47	470.6	200.05	606.29	733.35	2198.55	132.94	417.8
Ac (in^2)	171.59	321.33	238.13	426.59	238.13	426.59	n/a	n/a

n = the modulus ratio = Ec/Es
Es = the Young's modulus of steel
I(x-x) = moment of inertia of the composite section about x-x line
Ec = the Young's modulus of concrete
As = the sum of the soldier beam and angle areas
Ac = the area of concrete

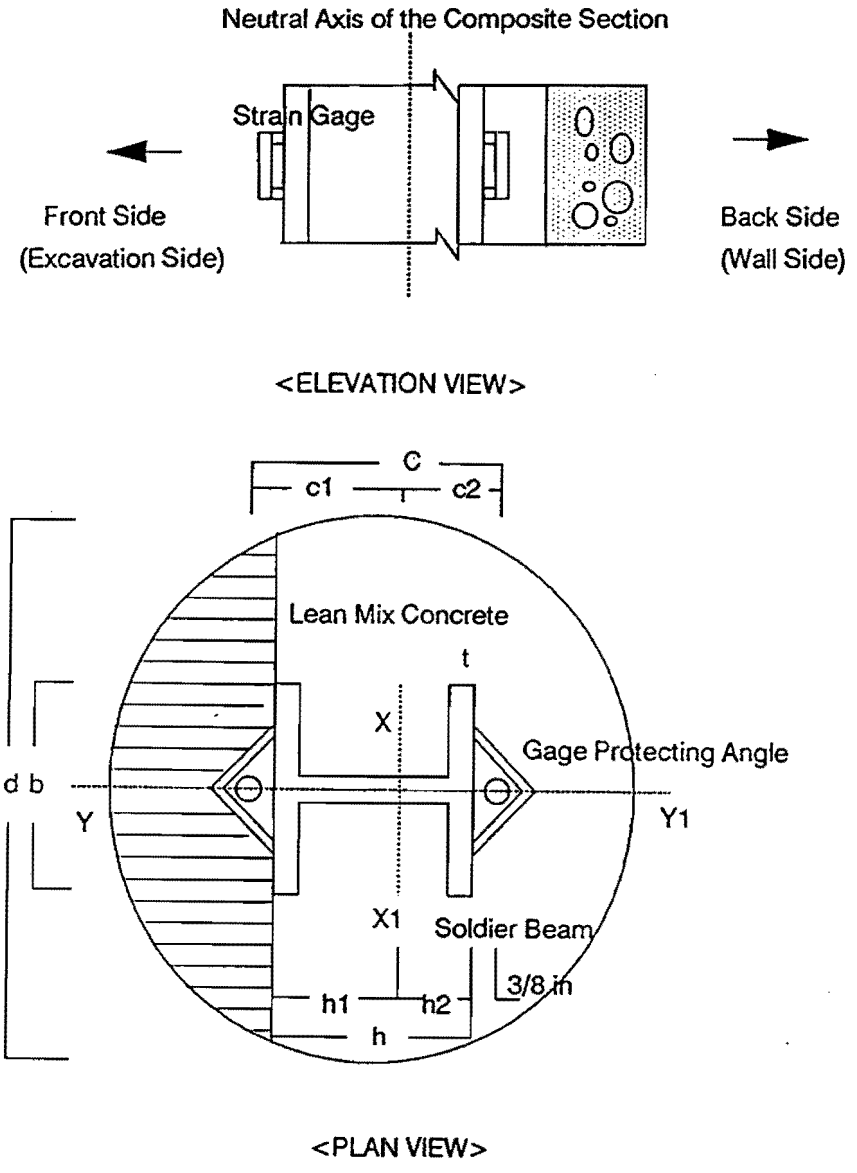

* Shaded area if the drilled beam section is cut off before wood-lagging on soldier beam.

Figure 58. Cross Section of Drilled Soldier Beam Above Final Excavation

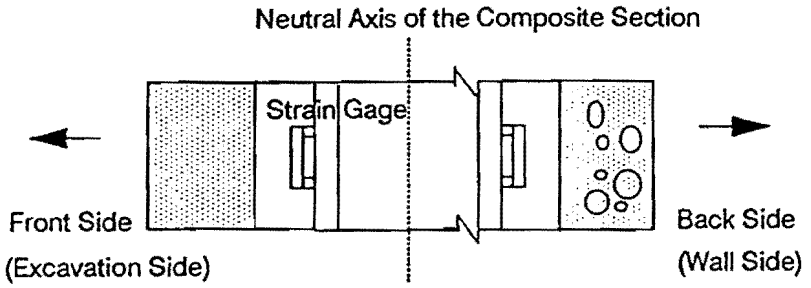

<ELEVATION VIEW>

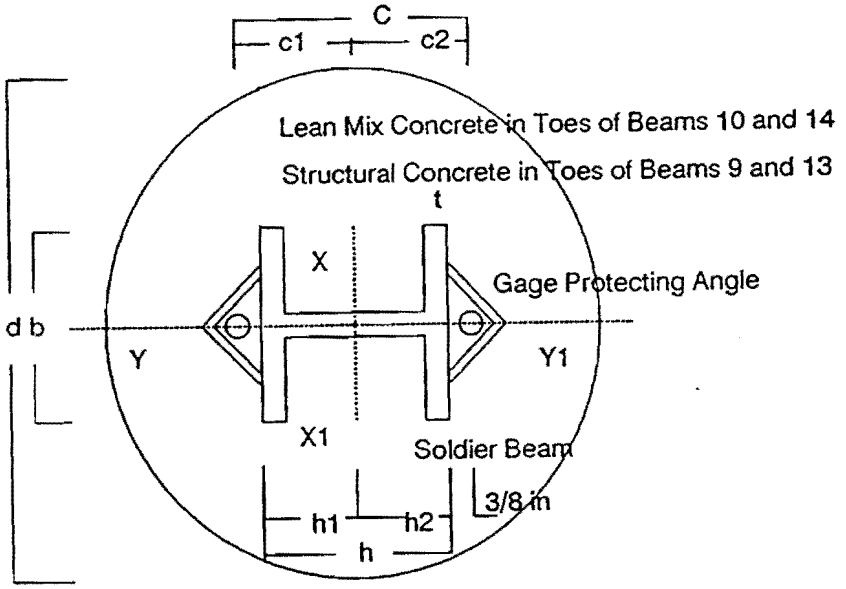

<PLAN VIEW>

Figure 59. Cross Section of Drilled Soldier Beam Below Final Excavation

where: A_s = area of the steel beam section
E_s = the Young's modulus of steel
A_c = area of concrete section
E_c = the Young's modulus of concrete
ε_{axial} = axial strain

2.3.6.4 Data Reduction of the Non-Functioning Strain Gages

Several of the strain gages installed on the H beams were damaged and did not function. The reasons include damage during installation, fabrication of the wale connection, excessive change in curvature at the anchors when stressing the anchors, and the effect of the long time exposure to the weather. The unknown strains for the damaged gages were approximated by correlating to the neighboring strain gage data. The unknown axial (or bending) strain of a single damaged gage was obtained by taking the average of the two strains calculated from the active surrounding gages immediately above and below the damaged gages. When two or more consecutive gages were damaged, corrections were made assuming a logical trend from the closest functional gage measurements. In the case where both strain gages at the back and the front side of the beam were damaged (single row or consecutive rows), the same logical trend was assumed for the most obvious of the two sides. Then, having calculated either the axial or the bending strain, the unknown strain(s) were back-calculated using the combination of Equations 13 and 14.

$$\varepsilon'_{bb} = \varepsilon_b - \varepsilon_{axial} \tag{24}$$

$$\varepsilon'_{ff} = \varepsilon_f - \varepsilon_{axial} \tag{25}$$

where: ε'_{bb} = the unknown bending strain on the back side of the beam
ε'_{ff} = the unknown bending strain on the front side of the beam
ε_b = the measured strain of the back side gage
ε_f = the measured strain of the front side gage
ε_{axial} = the axial strain inferred from the average or trend of neighboring gages

The bending moment was calculated using either Equation 19 or 26:

$$M = \frac{EI}{C_2}\varepsilon_{ff} \tag{26}$$

Table 9 shows an example of data reduction for damaged gages of one of the soldier beams.

2.3.6.5 Inclinometer Data Reduction

The horizontal deflection of the wall was obtained from the measurements made in the inclinometer casings or wells. Deflections were determined in the direction perpendicular to the wall face. The change in slope of the inclinometer casing, measured at 0.61 m intervals and multiplied by the instrument scale factor, gave the absolute deviation of the casing with respect to the initial vertical line.

Table 9. Data Reduction of Strain Gages (Non-Functioning Gages are Enhanced)

BEAM NO. 15, MARCH 1996													
FRONT G	BACK G	FRONT G	BACK G	FRONT	BACK	AX. STRAIN	B STRAIN (Ebb)	B MOMENT (lb-in)	Axial Force (kips)	Depth (ft)	Axial Force (kN)	Depth (m)	B Moment (kN-m)
Mar '96	(Zero readings - 2/91)										Mar '96		Mar '96
-99999	2928	-99999	2991	0.00	-63.20	-0.032	-0.032	-73757	-18.66	-19	-82.99	-0.30	-8.33
3734	2431	3853	2484	-118.70	-52.80	-0.086	0.033	76908	-50.63	-28	-225.21	-0.61	8.69
2573	2397	2628	2479	-54.30	-81.90	-0.068	-0.014	-32210	-40.21	-27	-178.85	-0.91	-3.64
-99999	2249	-99999	2370	-23.55	-120.60	-0.072	-0.049	-113261	-42.55	-26	-189.29	-1.22	-12.80
-99999	2271	-99999	2449	25.90	-178.00	-0.076	-0.102	-237959	-44.90	-25	-199.73	-1.52	-26.89
4132	2507	4092	2761	94.45	-265.50	-0.080	-0.174	-407238	-47.25	-24	-210.17	-1.83	-46.02
2404	2307	2275	2603	128.40	-296.40	-0.084	-0.212	-495758	-49.59	-23	-220.61	-2.13	-56.02
3475	2087	3400	2452	75.70	-364.90	-0.145	-0.220	-514197	-85.37	-22	-379.77	-2.44	-58.10
3914	2057	3758	2439	156.60	-382.00	-0.113	-0.269	-628567	-66.54	-21	-295.99	-2.74	-71.03
2833	2145	2621	2540	212.30	-395.10	-0.091	-0.304	-708860	-53.96	-20	-240.05	-3.05	-80.10
2722	2082	2499	2485	222.80	-402.80	-0.090	-0.313	-730100	-53.14	-19	-236.37	-3.35	-82.50
3154	2206	-99999	2594	216.40	-387.90	-0.086	-0.302	-705242	-50.63	-18	-225.21	-3.66	-79.69
2583	2188	2398	2536	184.90	-347.90	-0.082	-0.266	-621798	-48.12	-17	-214.05	-3.96	-70.26
-99999	2307	-99999	2616	128.77	-308.80	-0.090	-0.219	-510657	-53.15	-16	-236.41	-4.27	-57.70
-99999	2198	2680	2457	61.83	-258.90	-0.099	-0.160	-374308	-58.17	-15	-258.78	-4.57	-42.30
2330	2293	2296	2541	34.50	-248.60	-0.107	-0.142	-330389	-63.20	-14	-281.15	-4.88	-37.33
2414	2577	2468	2716	-54.20	-138.60	-0.096	-0.042	-98498	-56.91	-13	-253.18	-5.18	-11.13
-99999	2551	2364	2605	-125.90	-54.20	-0.090	-0.036	83677	-53.17	-12	-236.50	-5.49	9.46
2082	2746	2310	2685	-228.00	60.60	-0.084	0.144	336807	-49.42	-11	-219.82	-5.79	38.06
2003	2644	2350	2473	-346.40	171.20	-0.088	-2.59	604059	-48.81	-10	-217.13	-6.10	68.26
-99999	2970	2438	2600	-533.70	370.40	-0.082	-0.452	1055120	-48.21	-9	-214.44	-6.40	119.23
-99999	2701	-99999	2482	-370.10	218.70	-0.076	0.294	687153	-44.69	-8	-198.81	-6.71	77.65
-99999	-99999	2402	-99999	-139.50	0.00	-0.070	0.224	522367	-41.18	-7	-183.19	-7.01	59.03
-99999	3167	2309	3077	-217.00	89.40	-0.064	0.153	357581	-37.67	-6	-167.56	-7.32	40.41
2502	4424	2630	4412	-128.10	12.40	-0.058	0.070	163969	-34.15	-5	-151.93	-7.62	18.53
-99999	2556	2533	2540	-129.20	16.00	-0.057	0.073	169454	-33.42	-4	-148.65	-7.92	19.15
2472	2719	2585	2717	-113.00	2.30	-0.055	0.058	134560	-32.68	-2.5	-145.37	-8.38	15.21
-99999	-99999	2570	-99999	-102569	0.00	-0.057	0.043	99665	-33.42	-1	-148.65	-8.84	11.26

Inclinometer casings were positioned 4.57 m deeper than the bottom of the soldier beam. At this depth it was assumed that the casing did not move due to the excavation process. The deflection of the inclinometer casing was obtained by cumulating the calculated deviation at each level from the bottom to the top of the casing. The top of the inclinometer casings was protruding from the ground by 0.61 m to 1.22 m. In some cases the grooves inside the casings were not exactly orthogonal to the wall. Stick up lengths and skew angles of the inclinometer casings were measured and taken into account in the calculations in order to plot the horizontal deflection curves of the wall in the direction perpendicular to the wall face.

Data reduction was done using a program (INC) developed by Chung and Briaud (1993) and Kim and Briaud (1994). Inclinometer casing length, stick-up length and skew angles are required inputs to obtain inclinometer profiles.

During the monitoring process performed in April 1996, just seven out of 16 inclinometer casings were found functional. The rest were either clogged or excessively bent to let the inclinometer sensor pass through the casings and measure the horizontal deflection. The majority of the non-functioning casings were those that are located on the embankment in between soldier beams, and the ones that are located beside the two row anchor soldier beams, where the largest deflections were measured in 1991.

It was also found that the excavation height had decreased by approximately 1 m to 1.5 m, showing an average height of 6.5 m, as measured in April 1996.

2.3.6.6 Load Cell Data Reduction

Vibrating wire load cells were used to measure the loads at the heads of the tieback anchors. The sum of the six strain readings in each load cell was subtracted from the initial value (zero reading). Then the difference was converted into the anchor load by multiplying by the manufacturer gage factor.

2.3.7 Observed Short-Term Performance (1991)

The short-term behavior of the one row and two row tieback walls is summarized in this section (from Chung and Briaud, 1993). In this report, the short-term performance will be considered as the performance three months after the wall was completed. The bending moments and axial forces in the soldier beams, the variation of anchor loads, and the horizontal deflections of the wall were observed at different times during and after the wall construction.

2.3.7.1 One Row Tieback Wall

The one row tieback wall consists of a drilled beam section and a driven beam section. Each section has two instrumented soldier beams: beams 13 and 14 for the drilled soldier beam section and beams 15 and 16 for the driven soldier beam section (Figure 47).

In the driven soldier beams, the maximum bending moment for the driven one row anchored wall was 161 kN-m and occurred at the anchor location of soldier beam No. 15 and at the final construction stage. The moment is positive and produces tension on the back side of the beam. At the end of the construction stage when excavation proceeded to 7.6 m, drastic changes in axial forces and horizontal deflection movements occurred. They are assumed to be due to the downward movement of the soil mass (downdrag) and to the vertical component of the anchor force. The axial forces developed along the soldier beams are compression forces. The vertical component of the tieback lock-off load was 150 kN or about 50% of the maximum axial load in the beam. The maximum lateral movement of the driven beams was 20 mm at the top of the wall. At the final construction stage, the wall moved out towards the excavation side 10 mm at the top of the wall and 7.6 mm at the tieback location. All the maximum values of bending moment, axial force, and horizontal deflection on the driven one row tieback wall were observed on soldier beam 15.

In the drilled soldier beams the maximum bending moment in the drilled beams was 187 kN-m or about 20% larger than the maximum bending moment in the driven soldier beams. The axial force is again due partly to the downdrag of the soil mass behind the wall and to the vertical component of the anchor force. Large variations in axial forces and lateral wall movement were observed during the final construction. The maximum horizontal deflection of 33 mm was observed at the top of the wall. The horizontal deflections between the soldier beams were measured from readings in the inclinometer casing E5 for the drilled beam section and E6 for the driven beam section. The horizontal movements of inclinometers E5 and E6 indicate that the zone of the wall between the soldier beams deflected with the same trend and the same magnitude as the soldier beams themselves. Inclinometer casings E7 and E8 allowed to measure the horizontal ground movement behind the wall face. Inclinometer E8, which is located 4.57 m behind the wall indicates a movement of 5 mm towards the excavation at a depth of 2.65 m below the top of the wall. This point corresponds to the beginning of the bonded anchor zone.

Tiebacks number 7 and 8 were installed in the soldier drilled beams section while tiebacks 9 and 10 were installed in the driven soldier beams. The tiebacks were locked-off at 300 kN or 75% of the design anchor load of 400 kN. The anchor loads increased during the excavation and were comparably constant for the following 75 days after excavation. The increase varied from 3.7% to 19.5%. The maximum increase was recorded in tieback 8 (soldier beam 14) and was 14% during the excavation and 5% for the next 75 days after the excavation.

2.3.7.2 Two Row Tieback Wall

The two row tieback wall is made of four instrumented soldier beams. Beams 7 and 8 are driven beams while beams 9 and 10 are drilled beams (Figure 47).

In the driven soldier beams, a maximum bending moment of 90 kN-m was observed at the upper anchor location (soldier beam No. 7 and at the final construction stage). Drastic changes in axial forces were induced at each excavation levels. The vertical component of the anchor forces was recorded as 175 kN for the upper anchor and 160 kN for the lower anchor. The inclinometer casing number 7 (soldier beam 7) became clogged near the excavation level and could not be read after March 26, 1991. The maximum horizontal deflection in the driven two row anchored beams was 38 mm at

the top of the wall. During the final construction stage, the wall moved out 20 mm at the ground level, 10 mm at the excavation level, and 2.5 mm at the bottom of the soldier beams.

In the drilled soldier beams, at the end of the final construction stage, the bending moment in the soldier beams reached a maximum value of 70 kN-m at the topmost anchor location and was zero at the excavation level. The change in axial forces at the topmost anchor location could not be known because some gages were damaged. The excavation process induced large deformations in the wall. During the final stage of the excavation the wall deflected out towards the excavation 15 mm at the top of the wall, 7.6 mm at the excavation level, and 2.5 mm at the bottom of the soldier beams. The maximum horizontal deflection of the wall throughout the excavation was 30.5 mm in Beam 10 at the top of the wall. Inclinometer casings E1 and E2 (Figure 48) were located between the driven soldier beams and the drilled soldier beams, respectively. The observed movements at the end of the construction stage for both Inclinometer casings were very similar, with Inclinometer casing E2 showing a slightly higher lateral deflection of 31 mm. The lateral movement of inclinometer casings E3 and E4, located 1.5 m and 4.5 m behind the wall face, respectively, reveals that the horizontal deflection 4.5 m behind the wall is about one-third of the horizontal movement at the wall face.

The anchor loads in the two row tieback wall decreased in the driven beams and increased in the drilled beams. This comparison was made considering the initial anchor loads as the one measured at the beginning of the wall construction. The final measurement of this period was taken on June 27, 1991. Some readings were taken at each significant construction stage and after the wall completion. The load decreased by 0.6% and 17% for the driven soldier beams and increased by 11% and 21% for the drilled soldier beams. Most of the variation took place during construction.

The reason for the difference in behavior of the two types of soldier beams is believed to reside in the beams settlement. For the drilled soldier beams which have larger sections (cement grout and steel) and stronger point resistance, the settlement is expected to be small. If the settlement of the soldier beam is small, the horizontal movement of the wall is reduced because very little rotation takes place around the tendon bonded length of the anchor. On the contrary, for the driven beams which have smaller cross section areas, the settlement is expected to be larger. In this case more rotation takes place around the tendon bonded length of the anchor; this, in turn, induces additional lateral movement. The anchor loads are tied to the deflections.

2.3.8 Monitoring after Construction

After the final excavation, the time-dependent behavior of the wall was observed for 85 days. Three sets of measurements taken on April 3, May 17, and June 27, 1991, were used in order to study the short-term behavior.

The one row tieback wall presented variation with time of the bending moments, axial forces, horizontal deflections, and axial loads. The increase varied from 5% to 25% for the bending moments and from 4% to 20% in the axial forces. The increase of horizontal deflection at the top of the wall face ranged from 4% to 18%. These variations were calculated from the measurements taken on June 27, 1991, with respect to the corresponding values measured at the end of excavation (April 3, 1991). The maximum values were recorded for soldier beam No. 13. The time-dependent movement could

be attributed to the mass movement of the ground behind the wall after the final excavation. On the other hand, the anchor loads were comparatively constant with time.

The two row anchored wall also presented some variation with time. The bending moment increased anywhere from 0% to 32% and the axial forces increased anywhere from 5% to 15% with respect to the values taken at the end of excavation. The average increase in horizontal deflection at the top of the two row tieback wall for 85 days was 27%. The anchor loads remained comparatively constant with time.

The readings of inclinometer casing No. 4 indicate that the soil mass located 4.57 m behind and 5.4 m below the ground level moved 3.1 mm toward the excavation. Since this point corresponds to the beginning of the bonded anchor zone and the anchor loads remained constant, this movement is attributed to the soil movement.

As in the case of the one row tieback wall, most of the variation in the two row tieback wall behavior took place for the first 45 days. The variation after that was comparatively small.

2.3.9 Experiment on Release of Anchor Load

Ninety-nine days after the wall was completed (July 11, 1991), the anchor loads on tiebacks 4 (top anchor between the two row anchor soldier beams 7 and 8) and 9 (one row anchor supporting soldier beam 15) were reduced to a fraction of their design loads which were 472 kN and 400 kN respectively, in order to observe the effect of the load reduction on the wall behavior. The load in tieback No. 4 was reduced from a lock-off load of 378 kN to 107 kN and the load in tieback No. 9 was reduced from a lock-off load of 300 kN to 126 kN. Readings on the instrumentation were taken before (June 27, 1991) and after (July 17, 1991) the load in the anchors were reduced.

Some variations in bending moments, axial forces, horizontal deflections, and loads were observed after the reduction of the load on the mentioned anchors. In soldier beam No. 15, the result was a decrease in bending moment at the anchor location from 171 kN-m to 105 kN-m. The axial forces in the soldier beam were uniformly reduced; the maximum axial force decreased from 320 kN to 198 kN. The increase of horizontal deflection of the beam at the anchor location was 4.3 mm, although no significant change took place at the top of the wall.

The reduction of the anchor load in tieback No. 9 supporting soldier beam No. 15 did not cause any significant change in adjacent beams. It was found that load reduction in a tieback has an influence only on the corresponding beam and the time-dependent behavior is minimal.

One week after reduction of the load on tieback No. 4 (top anchor between soldier beams 7 and 8), the maximum bending moment in beam No. 8 decreased from 67 kN-m to 36 kN-m, and the maximum axial force decreased from 276 kN to 228 kN. The wall moved towards the excavation 4.6 mm at the upper anchor location and about 2 mm at the top of the wall. The variation in the behavior of soldier beam No. 7 is questionable since many damaged and non-functioning strain gages in that beam made a reasonable analysis of the strain gage data impossible.

As in the case of tieback No. 9, the reduction of anchor load in tieback No. 4 was found to have no influence in the neighboring soldier beams. The anchor load reduction caused a change only in the corresponding soldier beam which was supported by that anchor and the time-dependent behavior was minimal.

2.3.10 Observed Long-Term Performance of the Wall

The long-term performance of the tieback wall was evaluated from readings on the strain gages (bending moments and axial forces), inclinometer casings (horizontal deflections), and load cells (anchor loads). The last set of measurements was taken in April 1996, five years after the wall construction was completed.

The reference date for making a valid comparison about the long-term behavior of the tieback wall was selected to be July 1991, which corresponds to the first set of measurements taken after the anchors load reduction experiment took place. Measurements taken in July 1991 will be considered as the beginning of the long-term evaluation.

Three sets of measurements were taken at different dates during this period to evaluate the long-term behavior of the tieback wall: July 1991, December 1991, and April 1996.

2.3.10.1 One Row Tieback Wall - Driven Soldier Beams

In April 1996, the bending moments measured at the anchor location for the driven one row anchored soldier beams were 119 kN-m and 140 kN-m for soldier beams 15 and 16, respectively. The load of the anchor supporting soldier beam No. 15 had been previously reduced to about 30% of the design load in July 1991, or 38% of its previous load (measured in June 1991). Bending moment profiles, Figures 60 and 61, show that the bending moment at the anchor location in beam 15 increased by 14.3 kN-m over the five-year period (from 104.9 to 119.2 kN-m or 13.6% increase). For the case of beam 16, the bending moment at the anchor location decreased by 25 kN-m (from 164.7 to 139.7 kN-m), which represents a decrease of 15.2%. These moments are both positive and produce tension on the back side of the beam.

However, the maximum negative bending moments, measured in the curvature zone between the anchor and the excavation level have both increased, making the curvature more prominent. The maximum negative bending moments, as measured in April 1996, were -82.5 kN-m, an increment of 17.5 kN-m representing a variation of 26.8% in beam 15, and -85.4 kN-m, an increment of 14 kN-m and a variation of 19.7% in beam 16.

Substantial changes in axial forces were observed, being more noticeable in soldier beam 15, as can be seen in Figures 62 and 63. They are assumed to be due to the downward force of the soil mass (downdrag), induced by the anchor load reduction which allowed the wall to deflect and hence allowed the ground to move toward the excavation. The vertical component of the anchor force is also part of the axial force. The axial forces developed along the beams are compression forces.

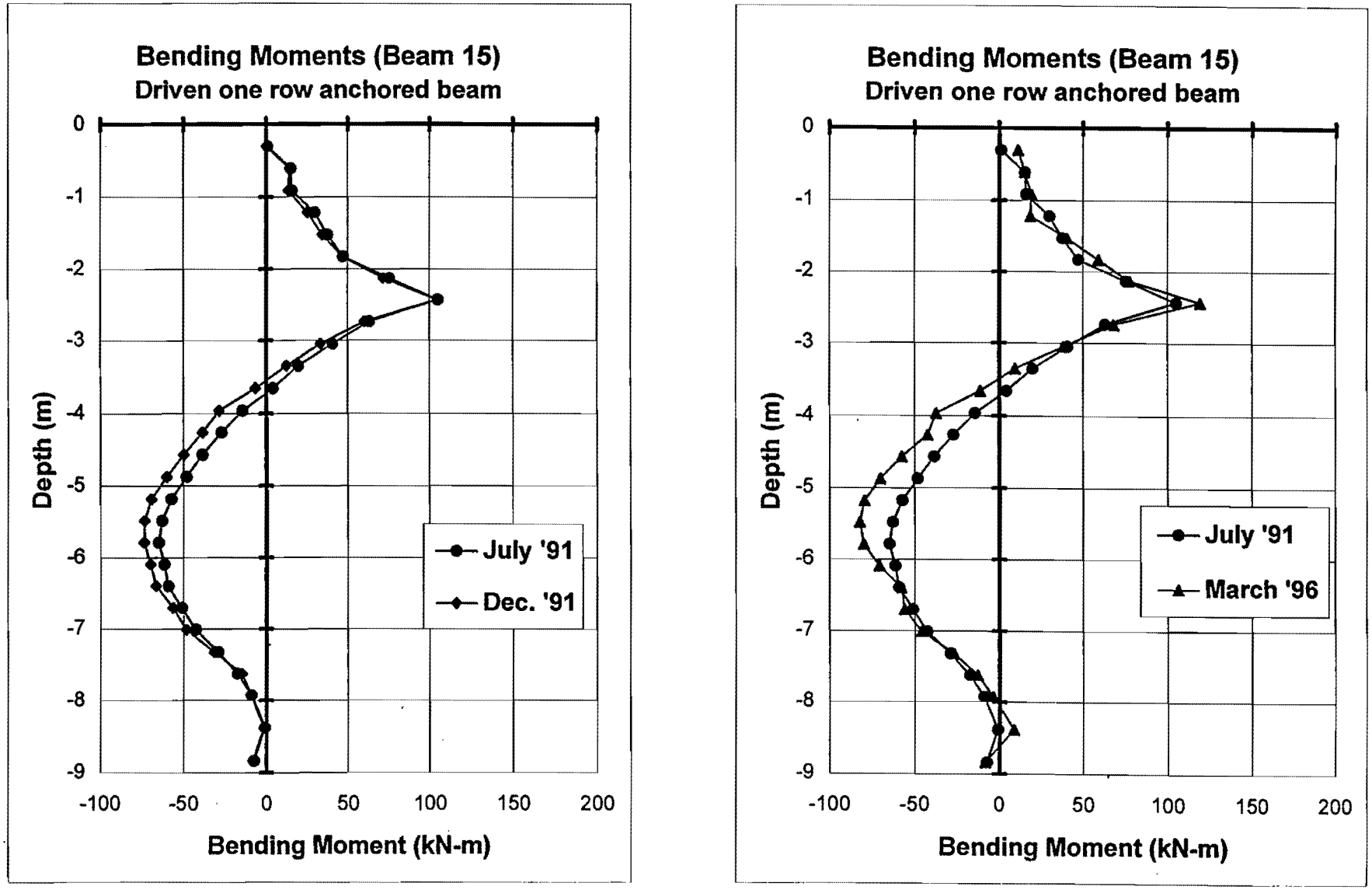

Figure 60. Bending Moments Comparison - Beam 15

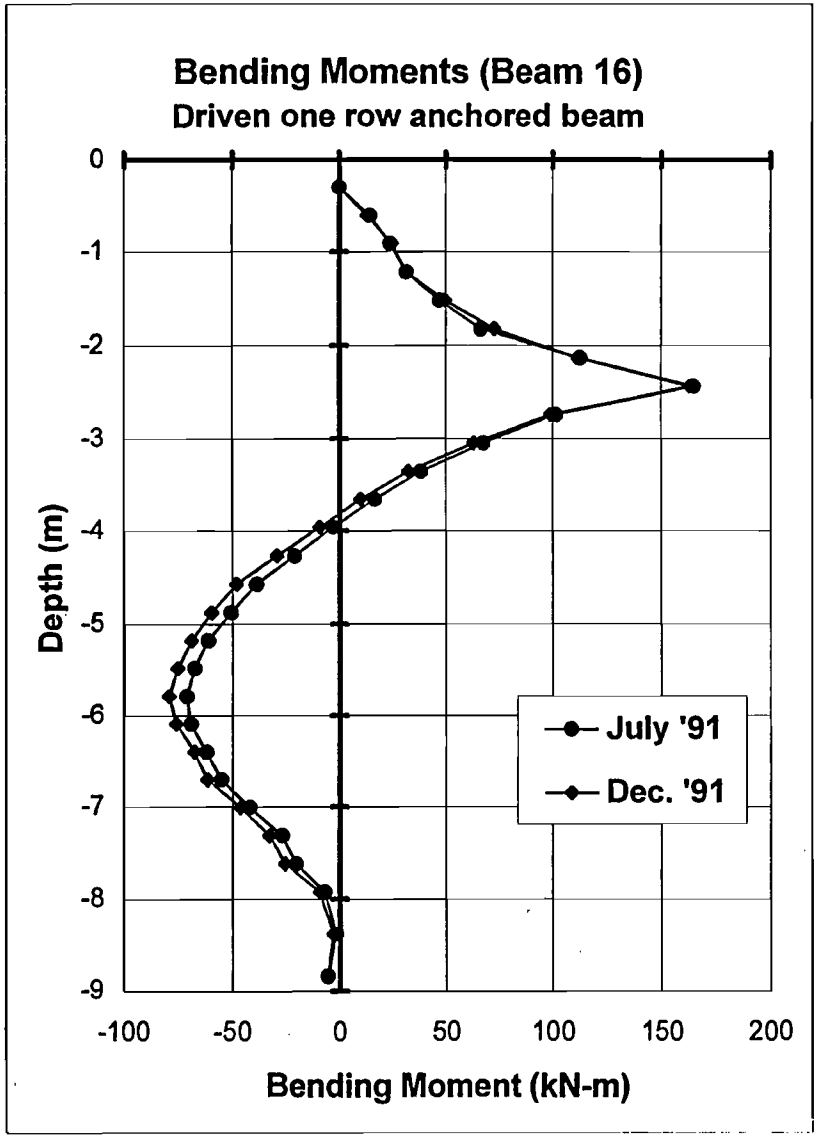

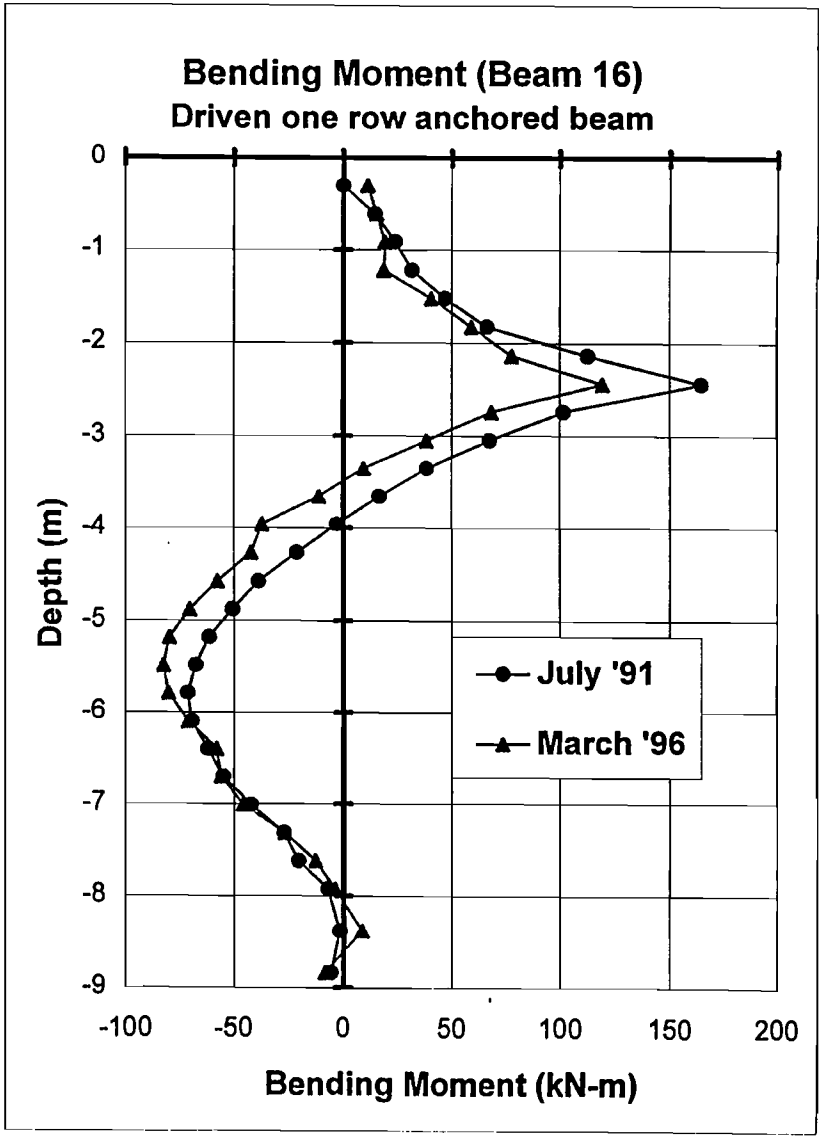

Figure 61. Bending Moments Comparison - Beam 16

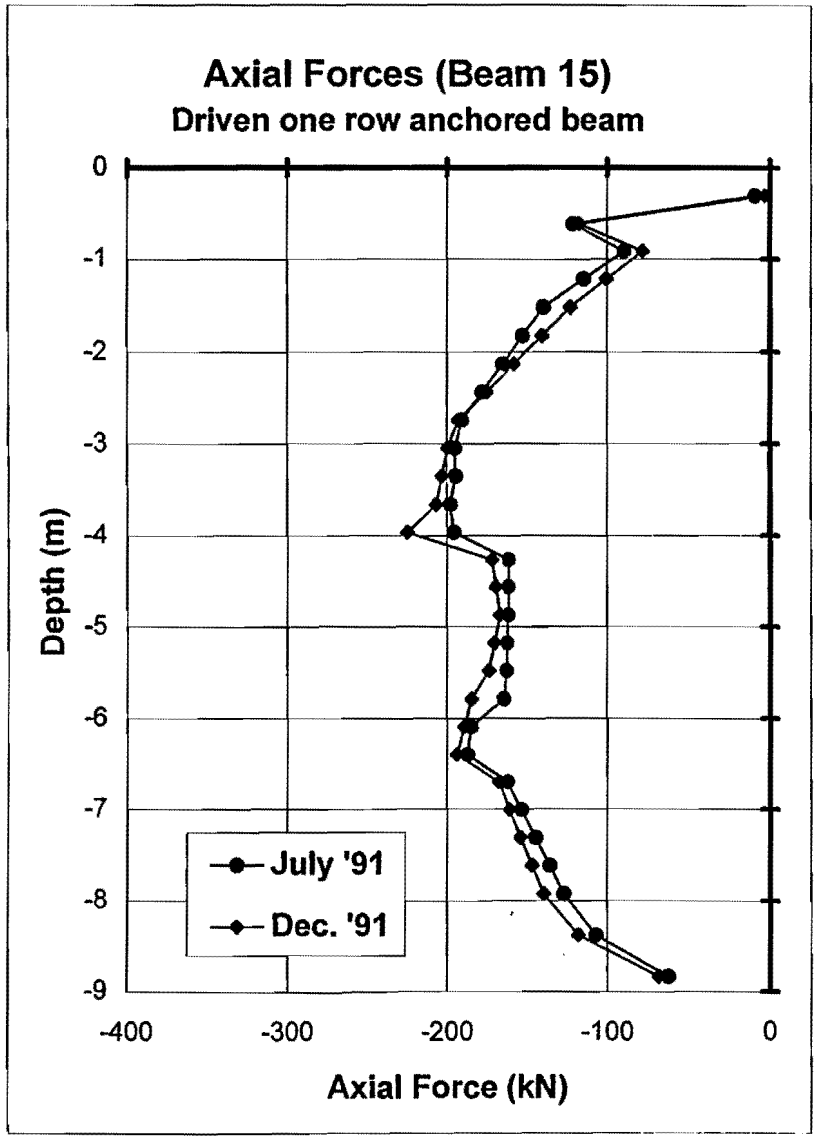

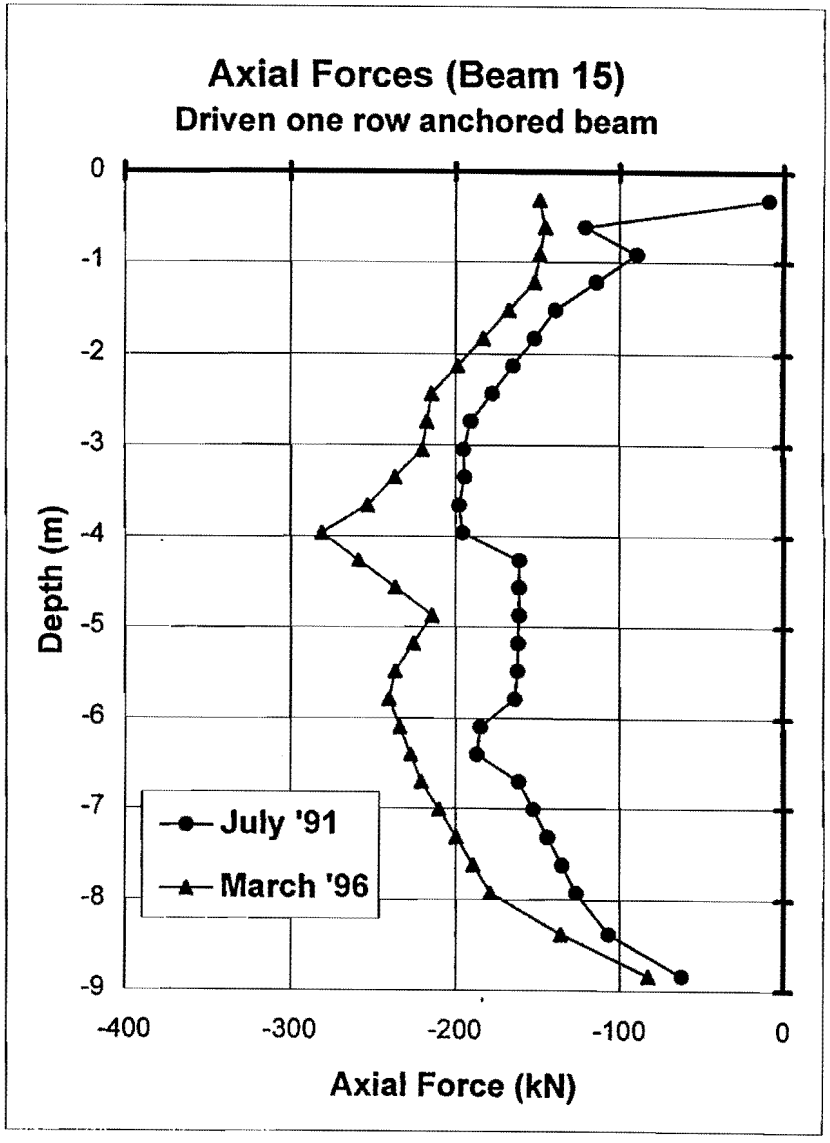

Figure 62. Axial Forces Comparison – Beam 15

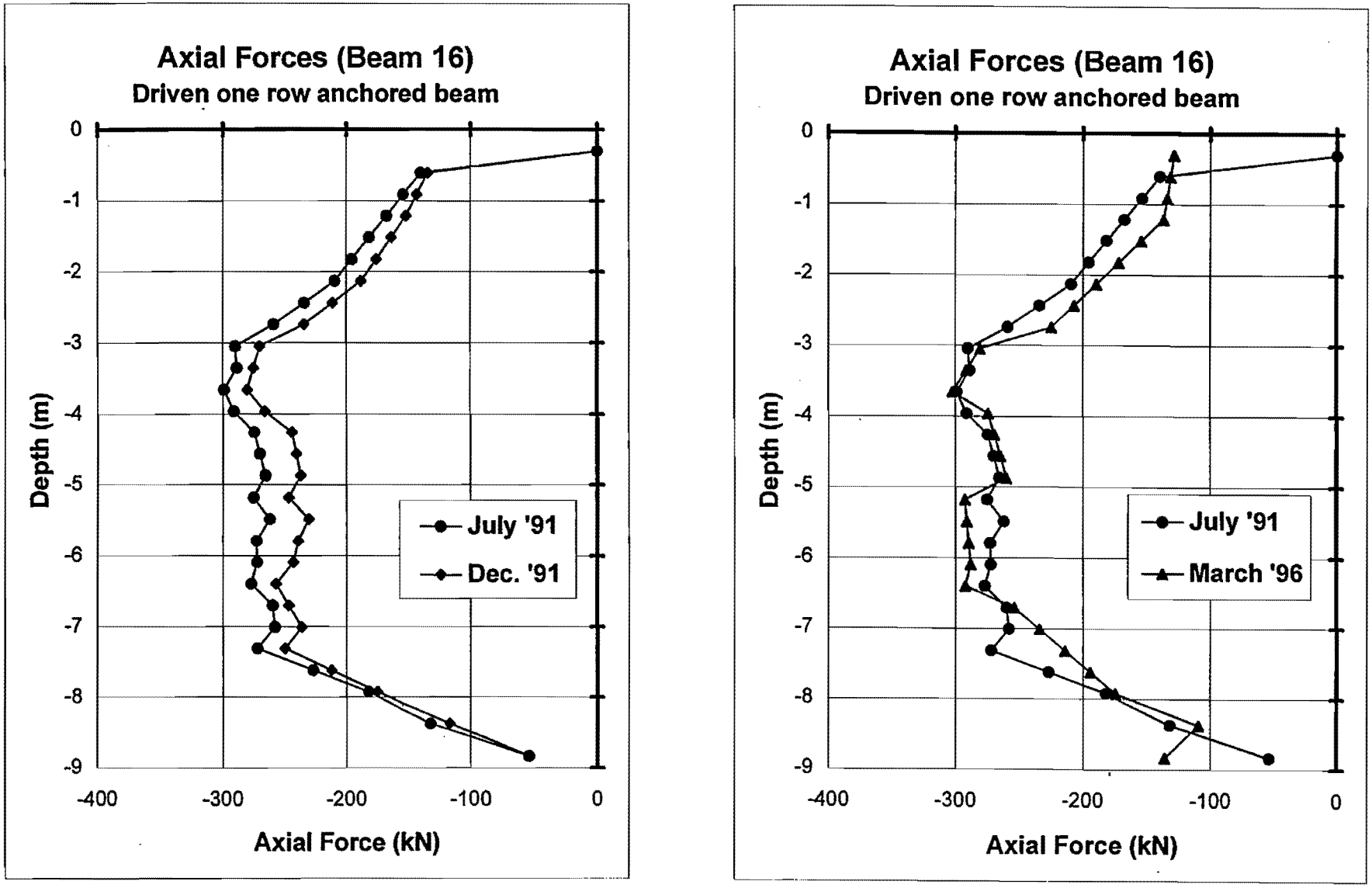

Figure 63. Axial Forces Comparison - Beam 16

The vertical component of the soldier beam 15 tieback load was about 67 kN by July 1991, or about 50% of the measured axial load in the anchor. The anchor has gained 61 kN in load as part of a load redistribution effect. The ground movement over the five-year period contributed to increasing the axial force by a maximum of -83.3 kN, which represents a positive increment of 42%. The maximum axial force increment magnitude (83.3 kN) is comprised of 30 kN from the anchor load gain, and 53 kN from the downdrag. From these measurements it is observed that downdrag is causing most of the axial forces increment. The significant increase in downdrag is induced by the effect of the load reduction on tieback 9, the anchor supporting soldier beam 15. Load reduction allowed the wall to deflect and hence allowed the ground to move toward the excavation. However, it was observed that shortly after the anchor load decreased, downdrag decreased as well, at least temporarily. This behavior is due to the temporary reduction in natural earth pressure and friction as the horizontal component of anchor load is reduced. After a while, when the ground progressively moves and presses more on the beam, downdrag increases until reaching the observed values at the end of the period. For the case of soldier beam 16 there was practically no change in axial forces, showing a very small increment of 1% over the five-year period. Axial force performances are very consistent with the behavior of the anchor loads in the past.

Anchor loads on soldier beams 15 and 16 gained 69 kN and 18 kN, representing a variation of 55% and 6%, respectively (Figure 64). This behavior is a clear evidence of a load redistribution effect. This behavior suggests that the end of anchor 15 is properly bonded to the soil to allow this kind of load recovery.

The maximum lateral movement of the one row driven beams, as measured in April 1996, was 30 mm at the top of the wall, as observed in soldier beam 15 (Figures 65 and 66). At this location, the wall moved out toward the excavation a maximum of 10 mm since June 1991. The average deflection along the excavation height was 23.5 mm, showing an average increment of 9 mm with respect to the deflection measured in July 1991. This movement represents a positive increment of 60% over the five-year period.

Inclinometer casing E7 allowed to measure the horizontal ground movement behind the wall face. The profile for inclinometer E7 (Figure 67), which is located 1.5 m behind beam 16, shows a maximum deflection of 25 mm near the top of the wall, a movement of 9 mm out towards the excavation since July 1991. The average deflection along the excavation height was measured as 16.9 mm, an average increment of 6.2 mm over the five-year period, representing an increment of 59%.

The maximum variation percentages of bending moments (positive and negative), axial force, and horizontal deflection on the driven one row tieback wall sub-section were observed on soldier beam 15.

The overall performance of this sub-section of the wall is caused by the time-dependent behavior and, to a lesser extent, by the load redistribution effect developed within the wall elements to compensate for the variations induced by the anchor load reduction. The slight influence of the reduction in load on anchor 9 (beam 16) on the behavior of soldier beam 16 is probably due to the fact that both anchors are connected by the same wale.

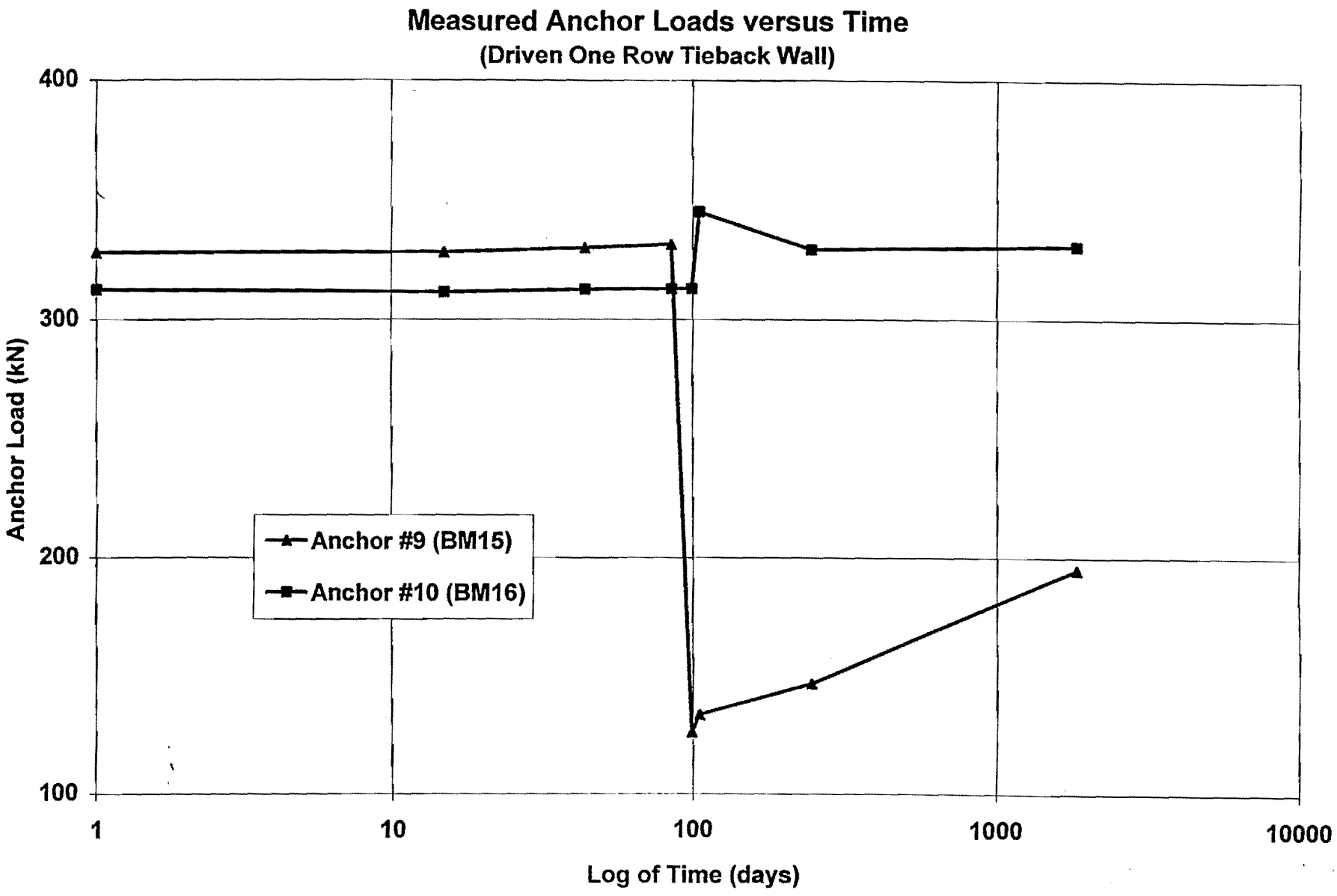

Figure 64. Anchor Loads vs. Time (Driven One Row Section)

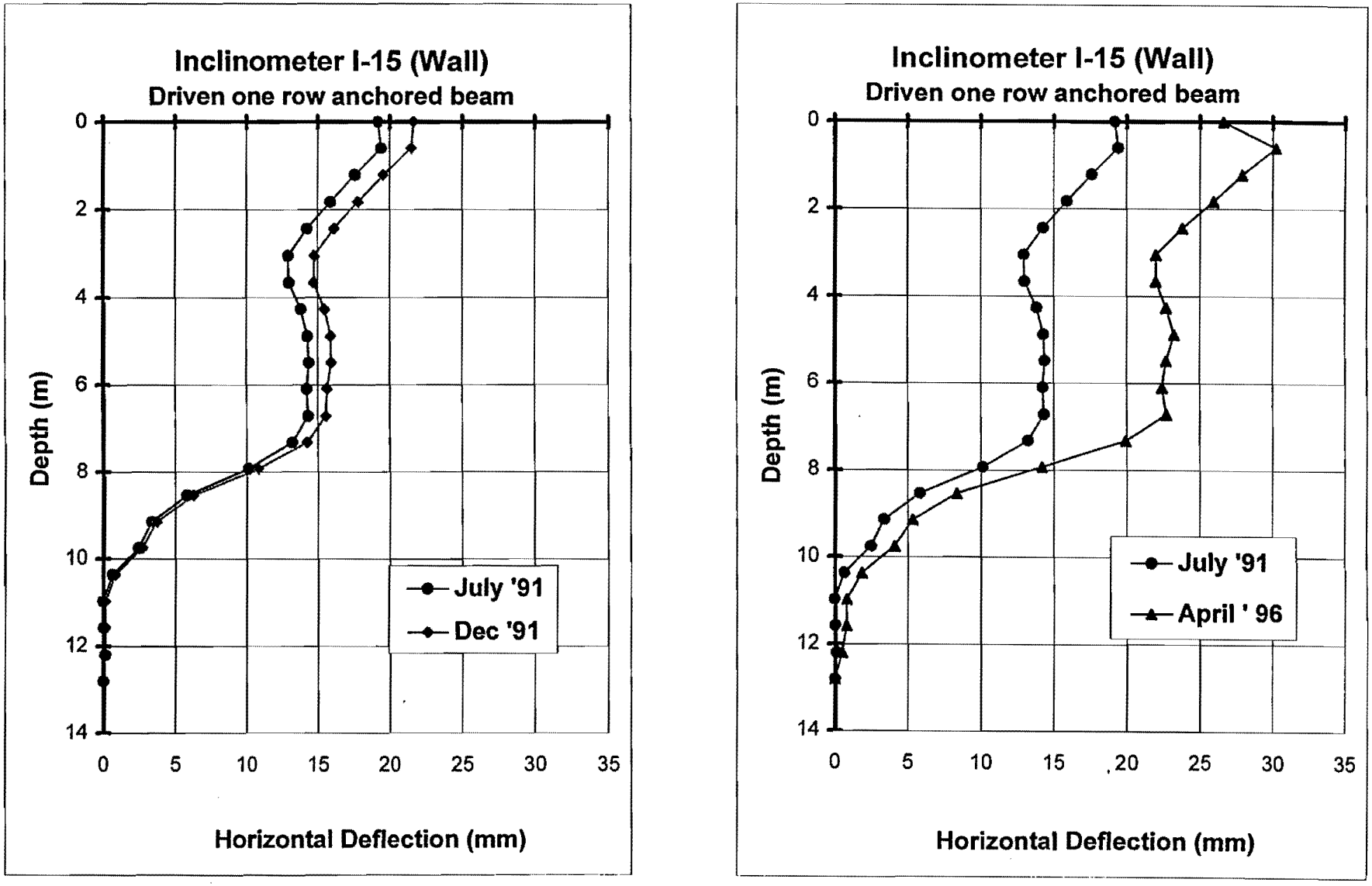

Figure 65. Horizontal Deflection Comparison – Casing I-15

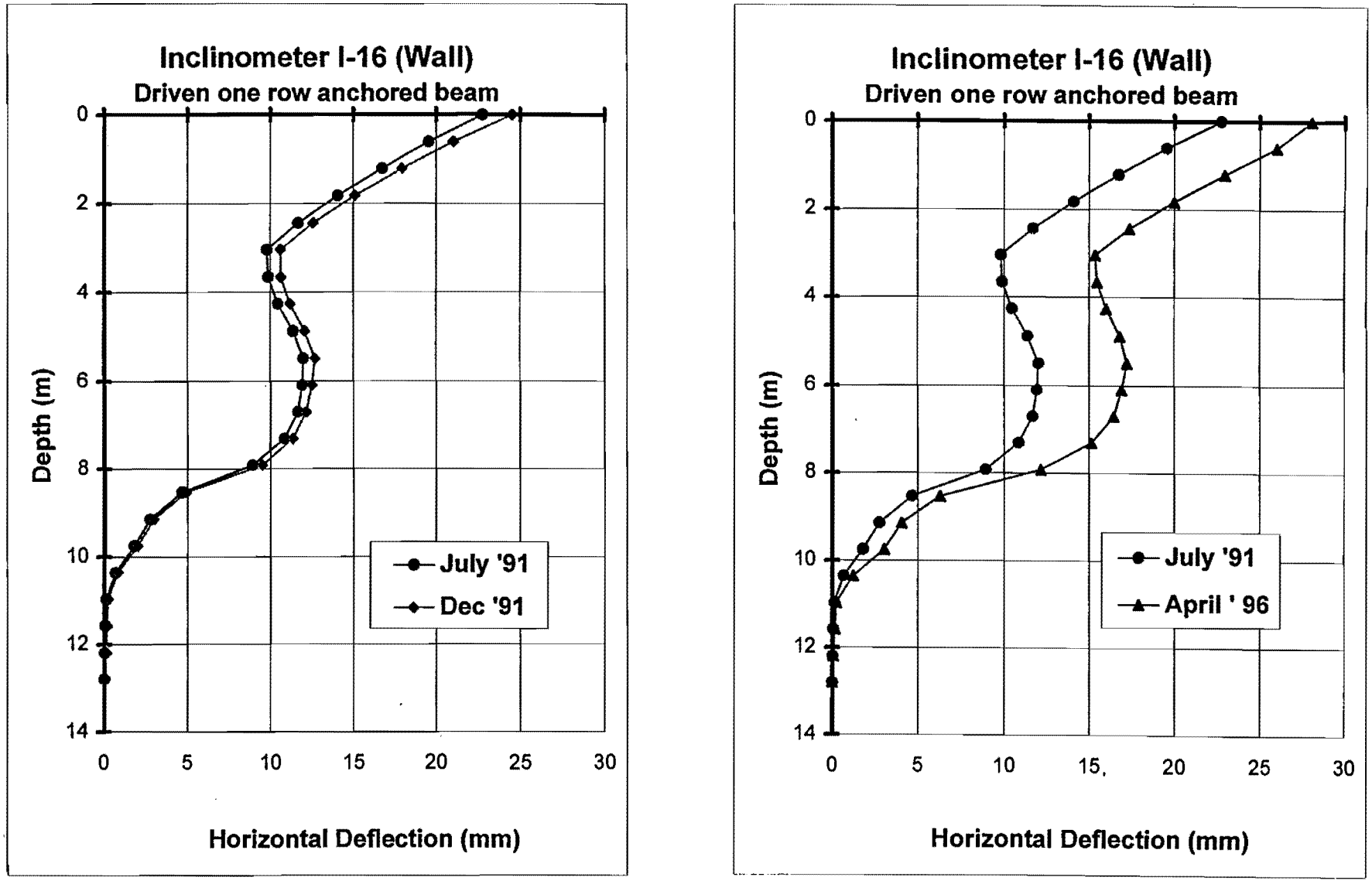

Figure 66. Horizontal Deflection Comparison – Casing I-16

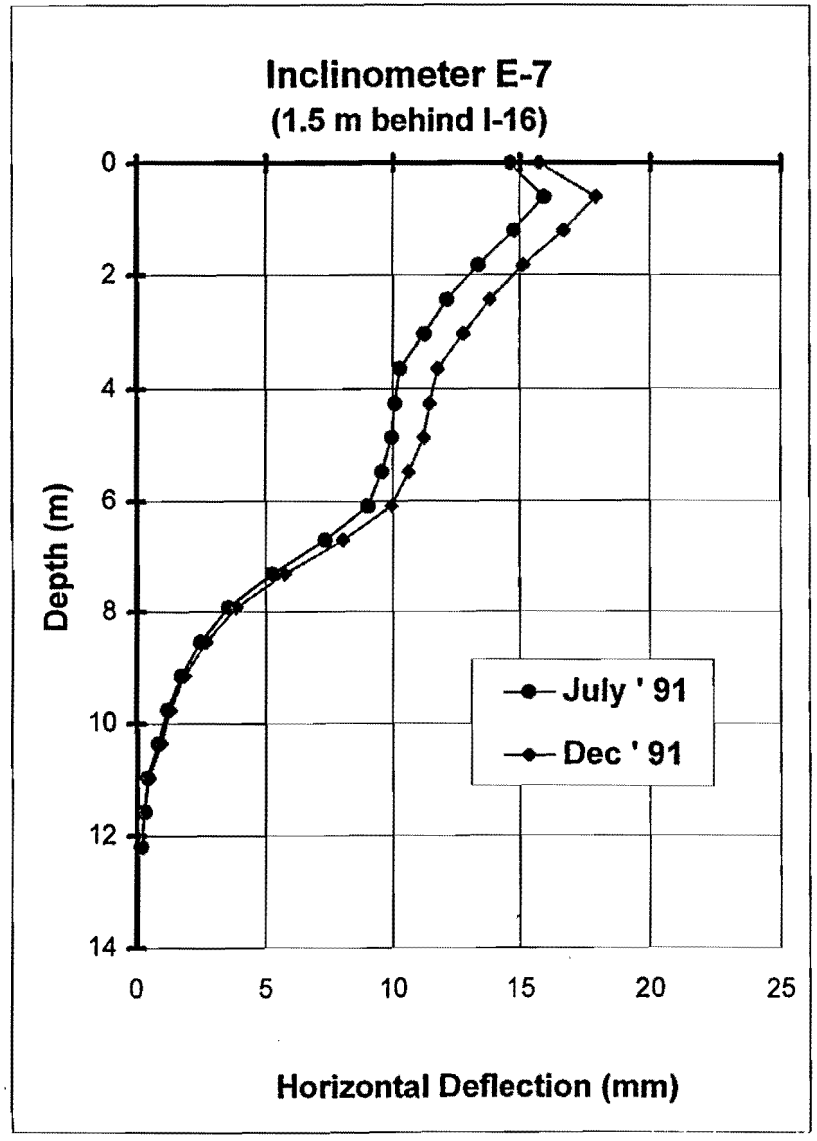

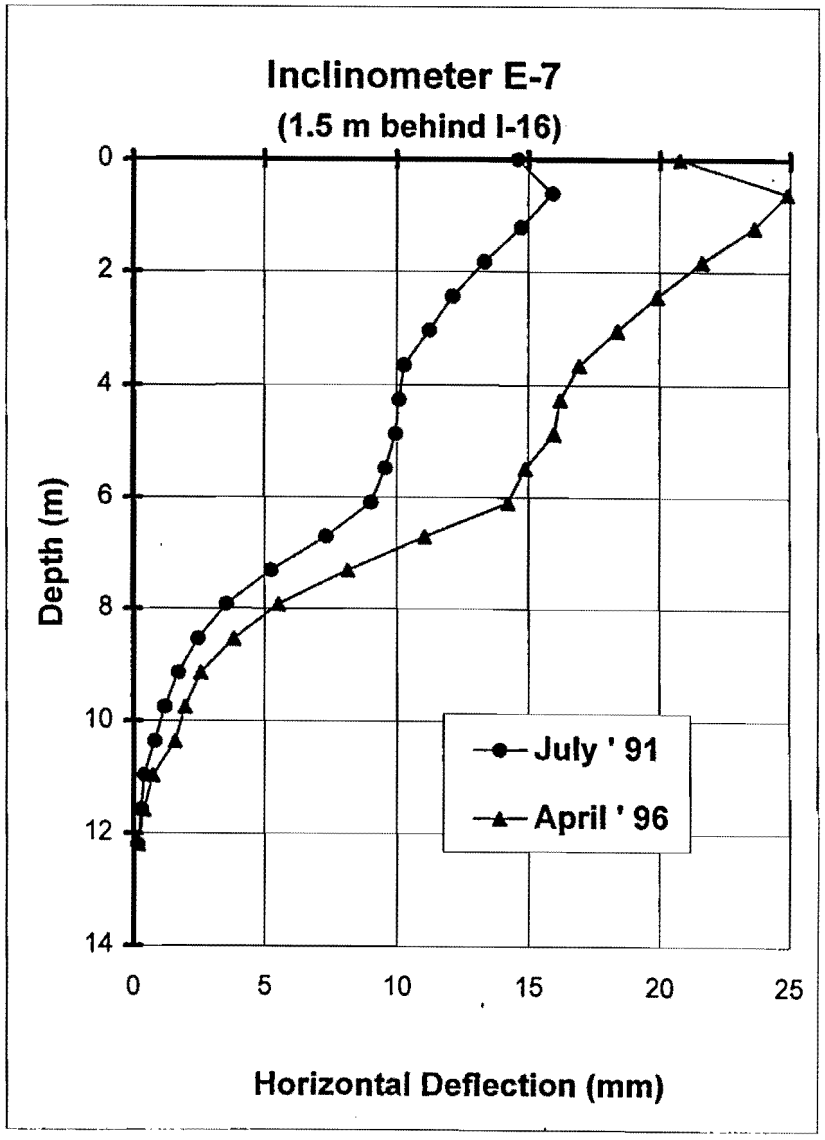

Figure 67. Horizontal Deflection Comparison - Casing E-7

2.3.10.2 One Row Tieback Wall - Drilled Soldier Beams

In April 1996, the bending moments measured at the anchor location for the drilled one row anchored soldier beams were 161 kN-m and 152 kN-m for beams 13 and 14, respectively. The maximum bending moment in the drilled beams was 161 kN-m or about 15% larger than the maximum bending moment in the driven beams as can be seen in Figure 68. Bending moment profiles (Figures 69 and 70) show that the bending moment at the anchor location on soldier beam 13 was reduced by 41.5 kN-m over the five-year period (from 199.2 kN-m to 160.8 kN-m), which represents a negative variation of 20.5%. For the case of soldier beam No. 14, the bending moment at the anchor location has decreased 45 kN-m (from 197.5 kN-m to 152.5 kN-m), which represents a decrease of 24%. These moments are both positive and produce tension on the back side of the beam. However, the maximum negative bending moments measured in the curvature zone between the anchor and the excavation level have both increased, making the curvature more prominent. The maximum negative bending moments, as measured in April 1996, were -73.6 kN-m in soldier beam 13 showing an increment of 15.5 kN-m, a variation of 26.7%, and -105 kN-m, showing an increment of 29.6 kN-m, a variation of 39.2% in soldier beam 14.

Since the inclinometer casing next to soldier beam 13 was not functional at the time of the readings, the lateral movement of the drilled beams was measured only in the inclinometer casing located next to soldier beam 14. The maximum deflection, as measured in April 1996, was 30.4 mm at the top of the wall, as can be seen in Figure 71. At this location, the wall moved out toward the excavation a maximum of 4.3 mm. The average deflection along the excavation height was measured as 19.4 mm, showing an average increment of 4.9 mm with respect to the deflection measured in July 1991. This movement represents a positive increment of 33% over the five-year period.

Anchor loads have remained remarkably constant over the five-year period, showing a maximum variation of 9 kN, as observed in soldier beam 14. This represents only a decrease in load of 2.4%. Anchor load behavior of this section is shown in Figure 72.

Although the axial forces could not be calculated and deflections were only measured at soldier beam 14, the performance of this section of the wall is probably due to the time-dependent behavior. No signicant influence of reduction of load on soldier beam 15 was observed in this sub-section of the wall.

2.3.10.3 Two Row Tieback Wall - Driven Soldier Beams

Many damaged and non-functioning strain gages were found in soldier beam 7. This condition made a reasonable analysis of the strain gage data almost impossible. However, a major effort was expanded in reducing the data of the instrumentation of this soldier beam and identifying the variation in behavior. In April 1996, the maximum positive bending moments were measured at the topmost anchor location. The magnitude of bending moments was 49.4 kN-m and 18.1 kN-m for soldier beams 7 and 8, respectively. The load of the top anchor supporting soldier beams No. 7 and 8 had been previously reduced to about 22% of the design load, or 30% of its previous load in July 1991. Bending moment profiles (Figures 73 and 74) show that the bending moment at the anchor location of beam 7 has remained very steady over the five-year period. For the case of soldier beam No. 8, the bending

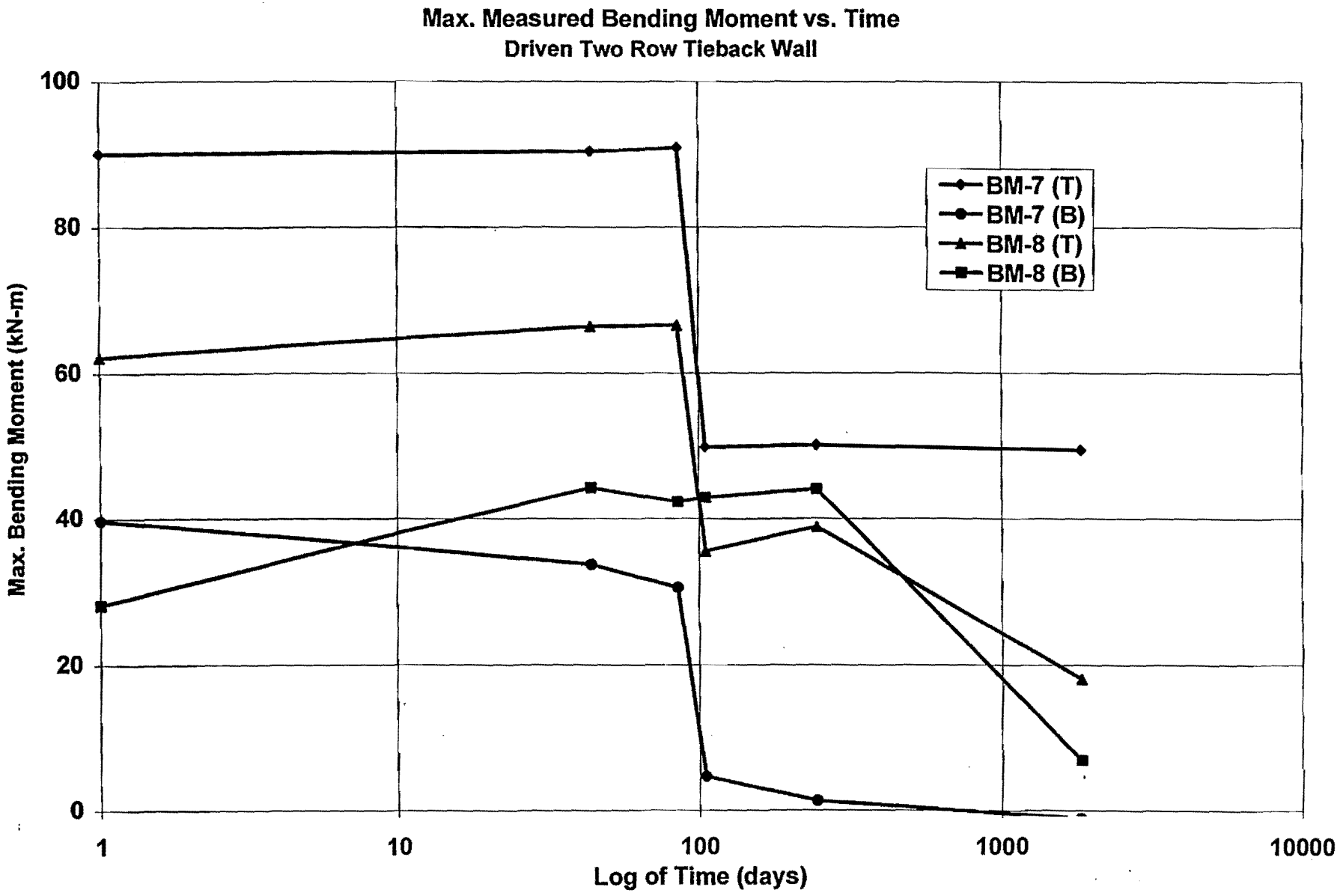

Figure 68. Maximum Bending Moment vs. Time (Driven One Row Section)

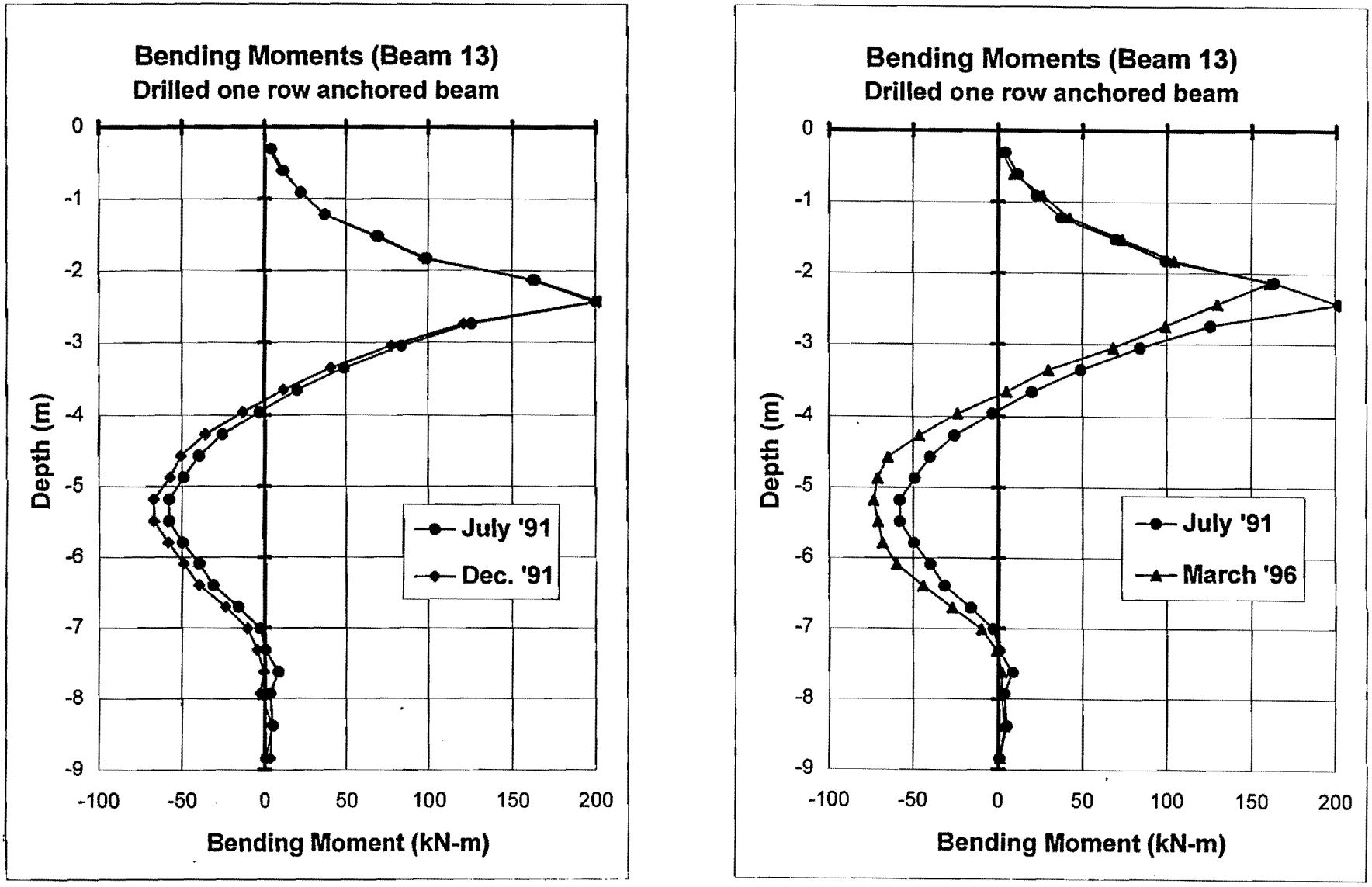

Figure 69. Bending Moment Comparison – Beam 13

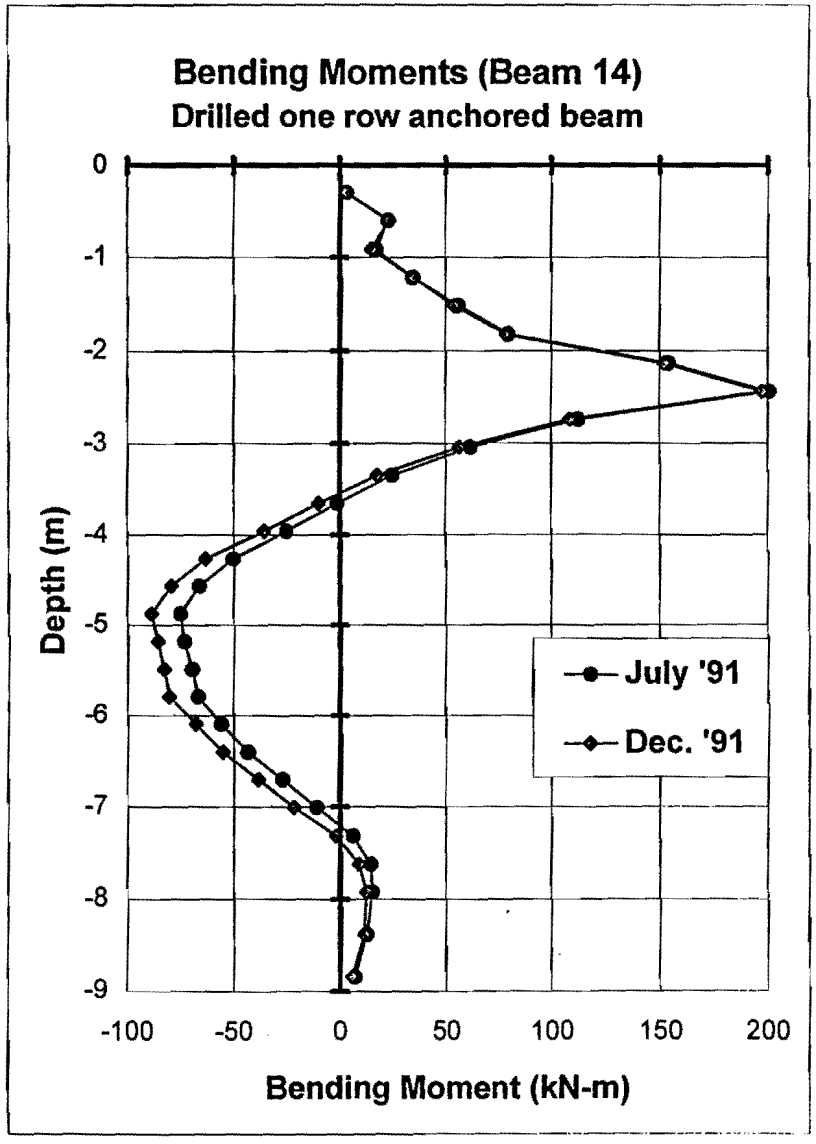

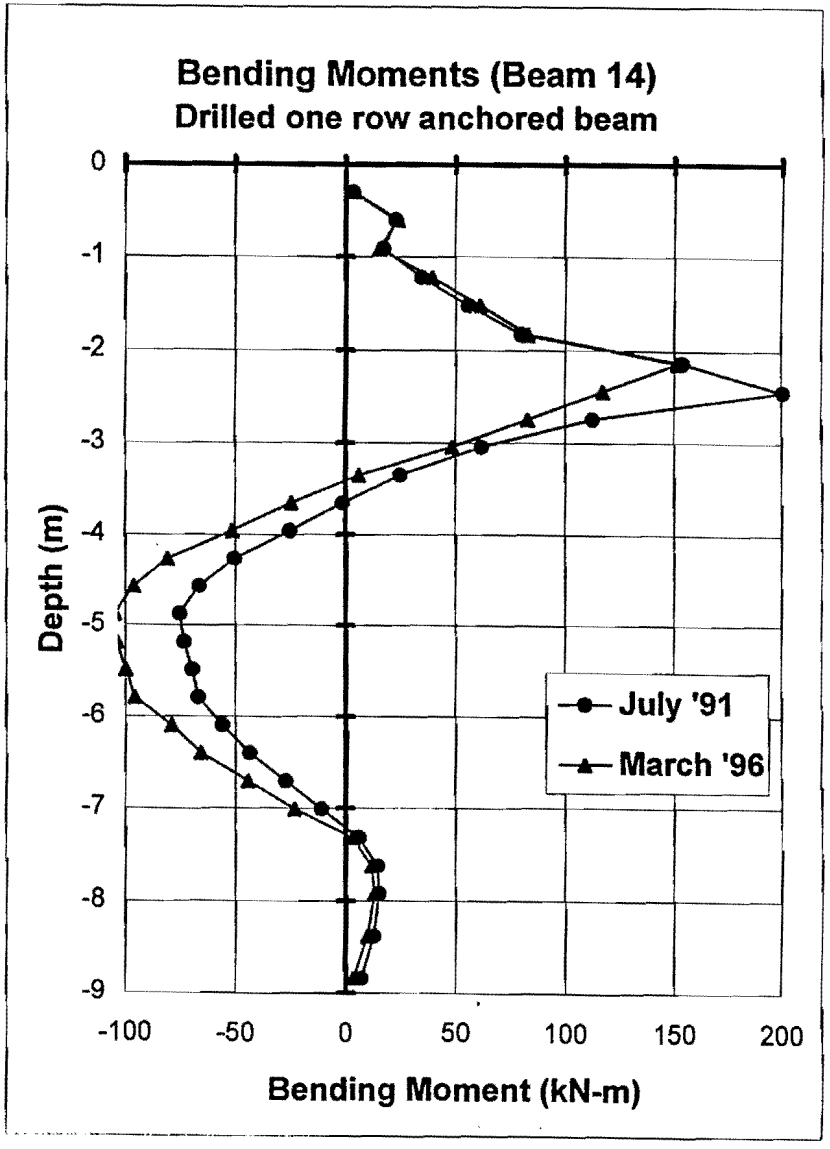

Figure 70. Bending Moment Comparison – Beam 14

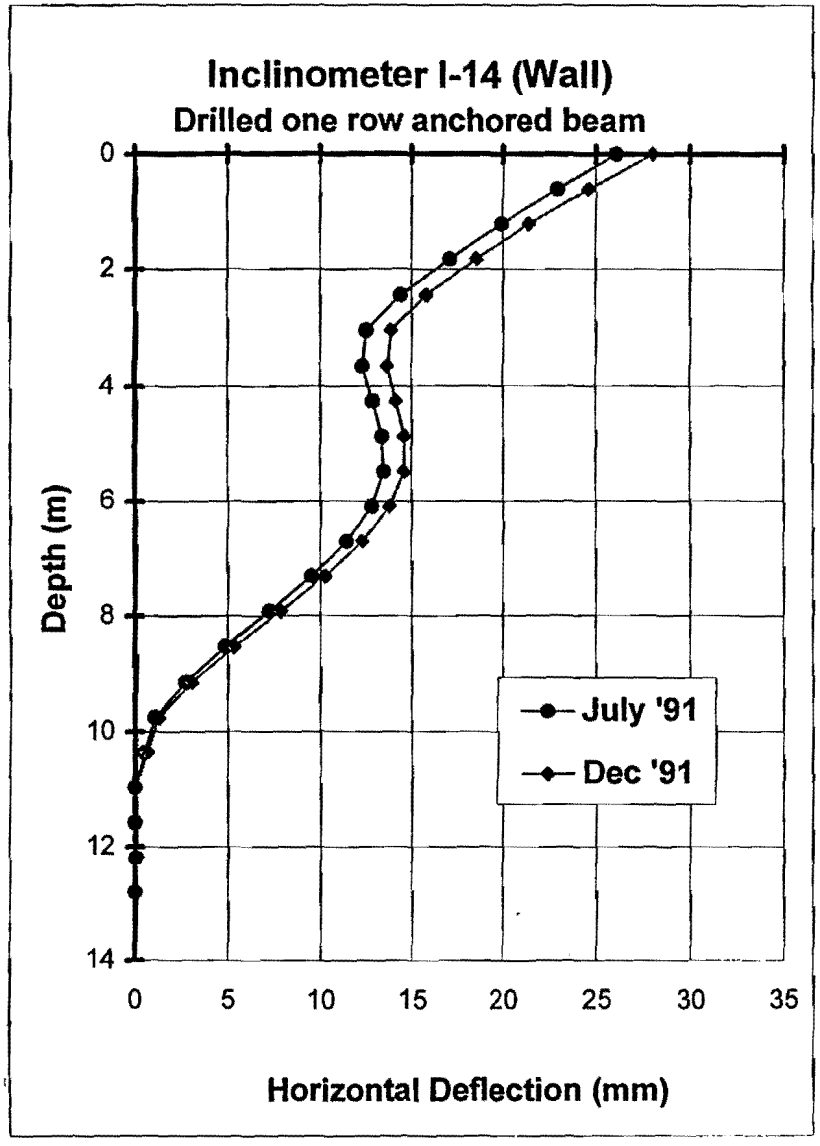

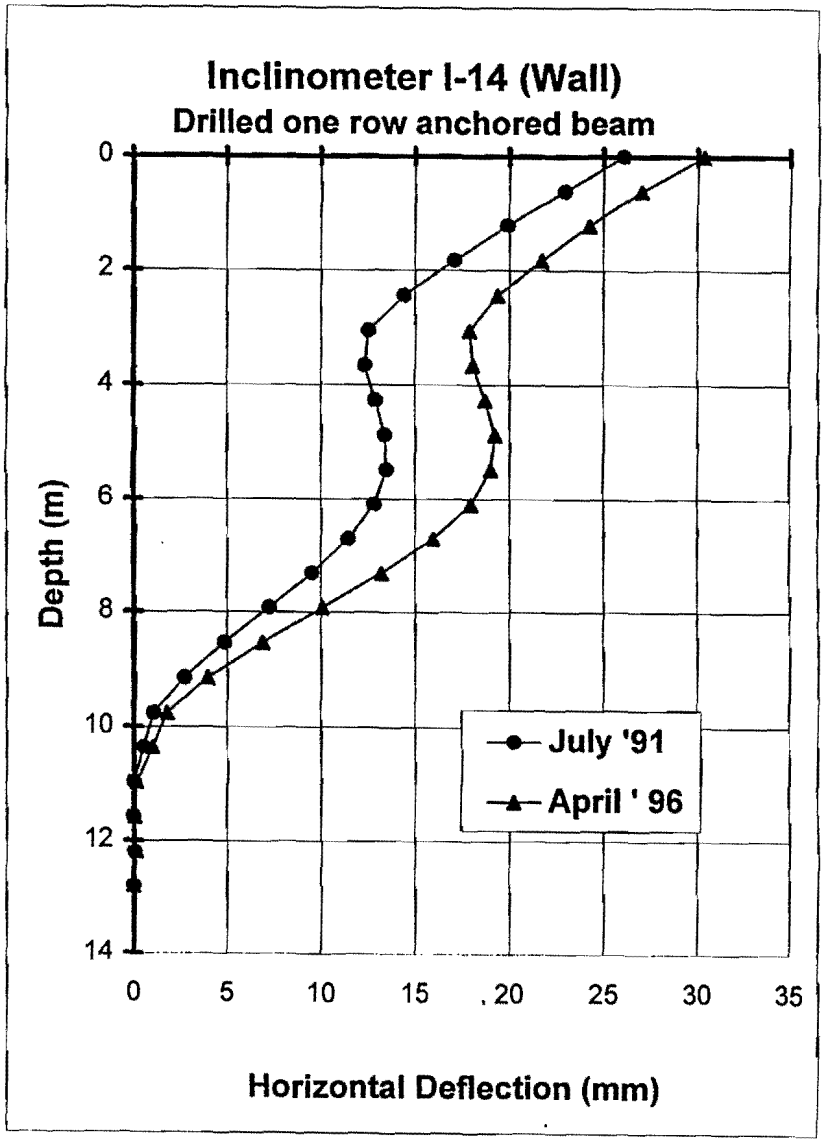

Figure 71. Horizontal Deflection Comparison – Casing I-14

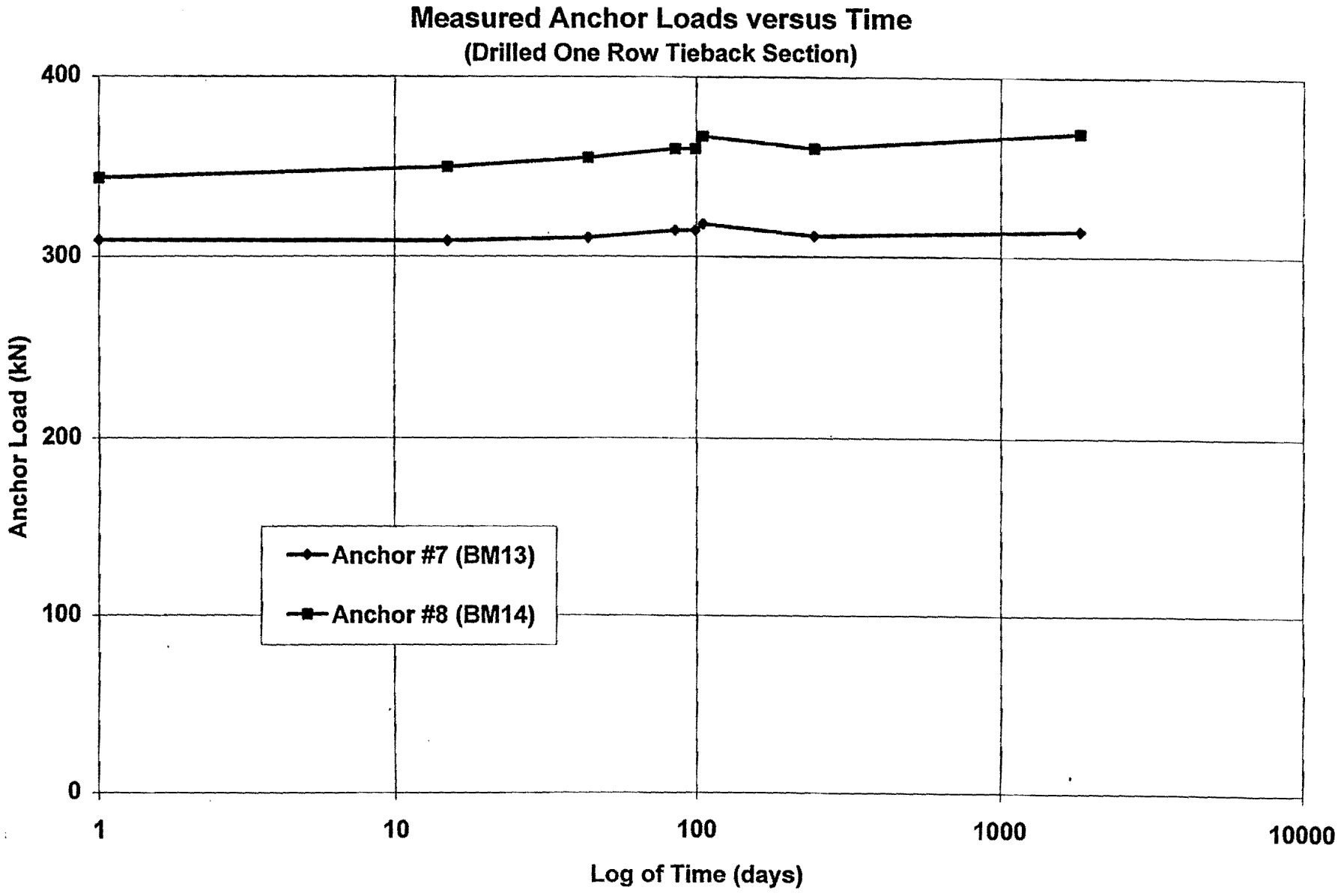

Figure 72. Anchor Load vs. Time (Drilled One Row Section)

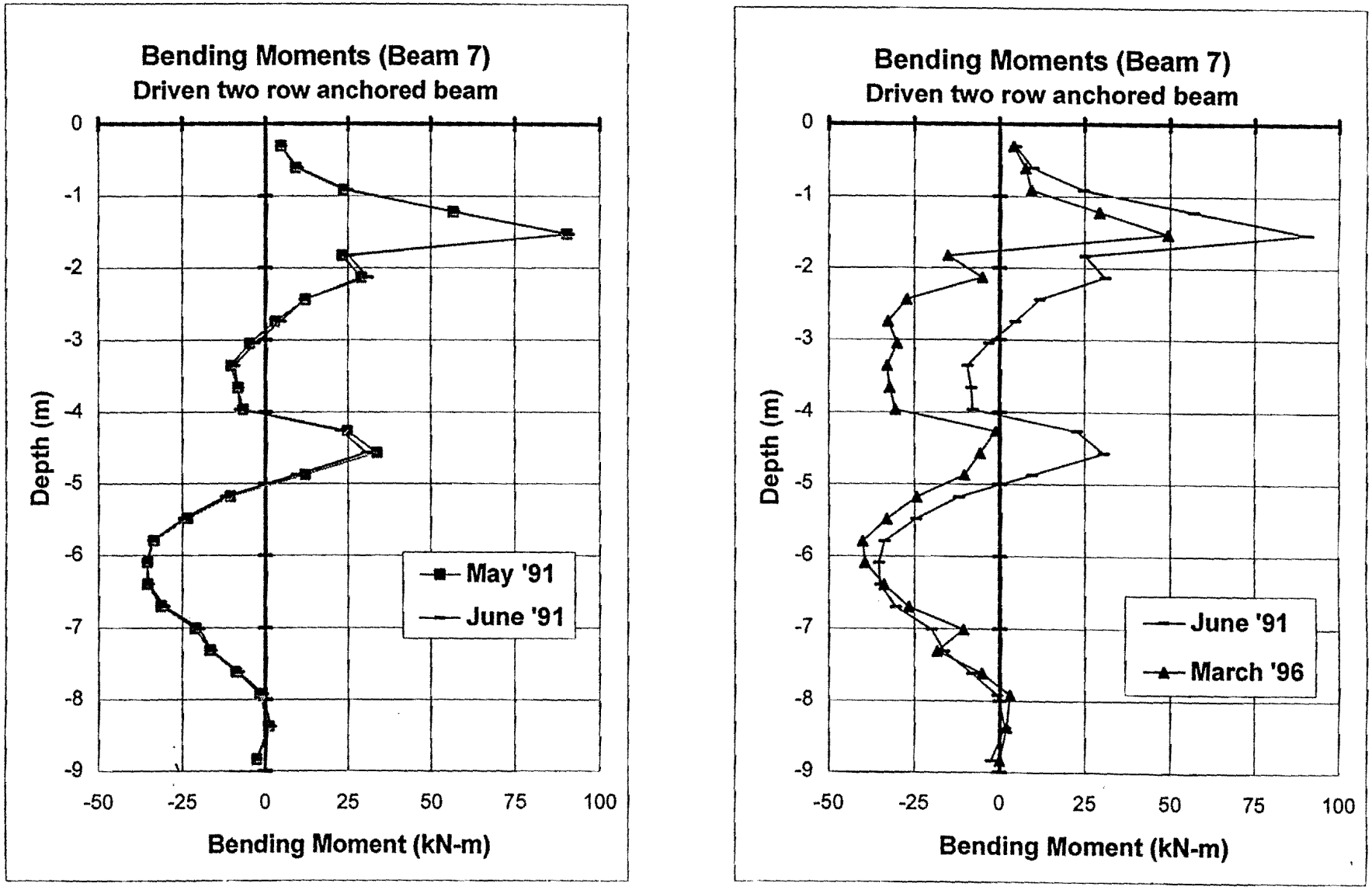

Figure 73. Bending Moment Comparison - Beam 7

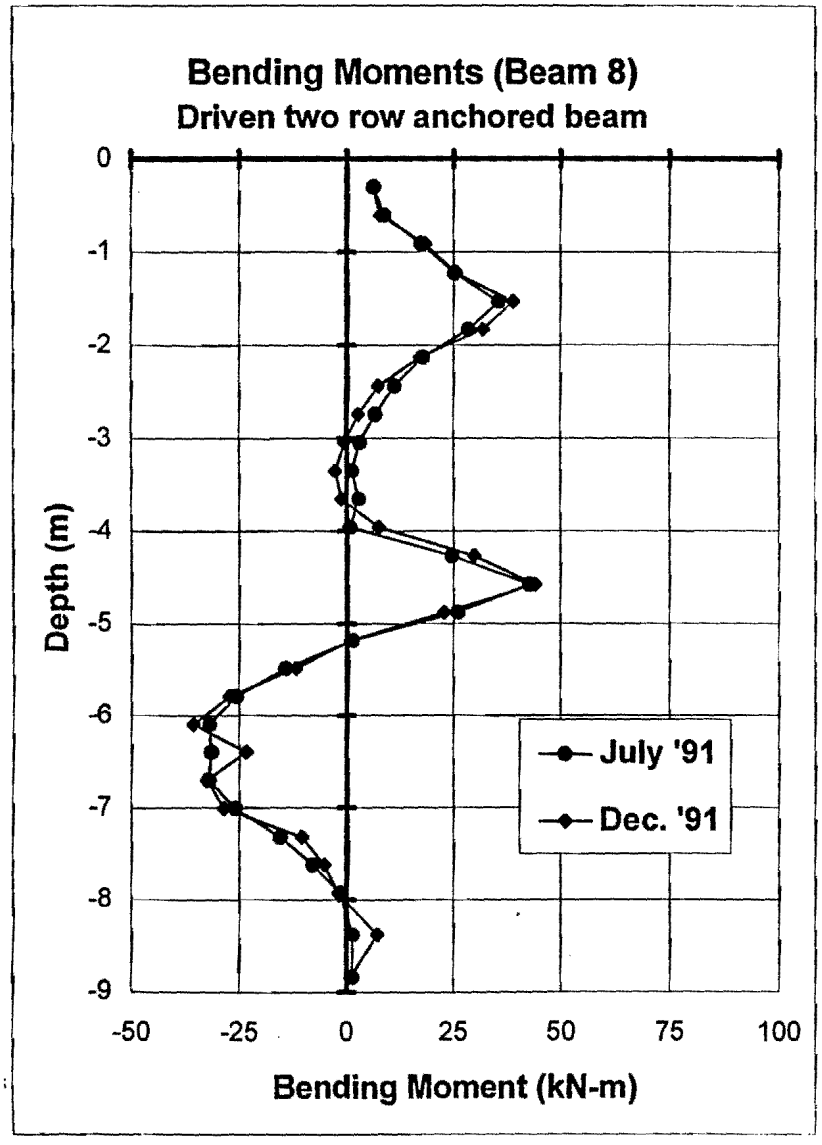

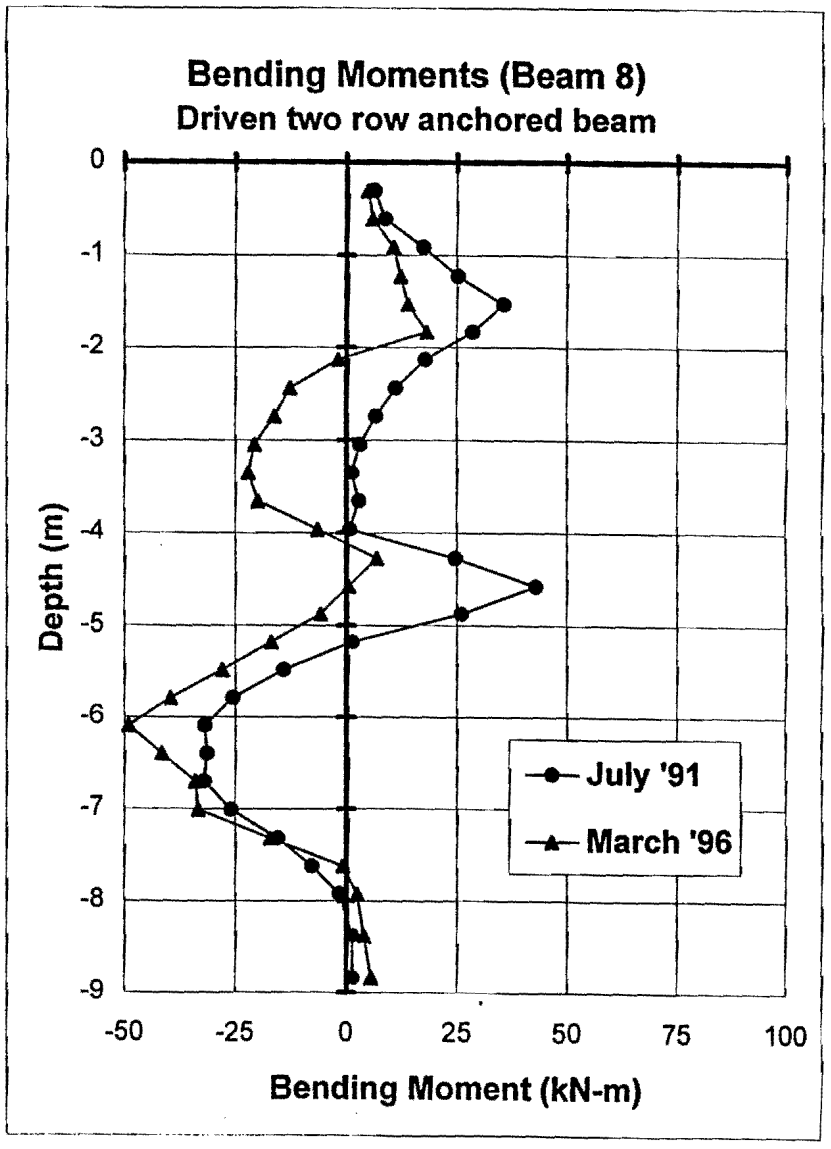

Figure 74. Bending Moment Comparison – Beam 8

moment at the topmost anchor location has been reduced by 17.4 kN-m (from 35.5 kN-m to 18.1 kN-m), which represents a decrease of 49% as can be seen in Figure 75. These moments are both positive and produce tension on the backside of the beam. The maximum negative bending moments located in the curvature zones between anchors and between the anchor and the excavation level have both increased, making the curvatures more prominent. The variation of maximum negative bending moments in soldier beam 8 were 23 kN-m and 17 kN-m for the top and bottom curvature, as measured in April 1996. For the case of beam 7, no information was obtained from the first set of readings, therefore no comparison was possible.

Axial forces were measured just in beam 8, again due to the damaged strain gages in beam 7 that made the data interpretation impossible. Substantial changes in axial forces were observed in soldier beam 8 (Figure 76). The maximum measured axial force showed an increment of 72 kN, from -228.4 kN in July 1991 to -300 kN in April 1996, representing a positive variation of 31% over the five-year period. The maximum measured axial force increment magnitude in beam 8 (72 kN) is comprised of approximately 14 kN from anchors load redistribution, and the remaining 56 kN from downdrag. As can be observed from these measurements, downdrag is causing most of the axial forces increment. This significant increase in downdrag is induced by the effect of the load reduction on tieback 4, the top anchor supporting soldier beams 7 and 8. This load reduction allowed the wall to deflect and, hence, allowed the ground to move toward the excavation.

The anchor loads have drastically changed over the five-year period, as can be seen in Figure 77. The top anchor supporting soldier beams 7 and 8 has gained 80 kN, representing a load increment of 75%. On the contrary, the load in tieback 17, the bottom anchor supporting soldier beams 7 and 8, has decreased by 52.5 kN, near 20% of its previous load. This behavior clearly represents a load redistribution effect in the vertical direction.

The maximum lateral movement of the two row driven soldier beams were not measured because the inclinometer casings were non-functional at the time of the measurements. The inclinometer casing next to beam 7 became clogged near the excavation even before the completion of the wall.

The overall performance of this section of the wall is due to the time-dependent behavior and to the force redistribution effect developed within the wall elements to compensate for the variations induced by the reduction in load of the top anchor supporting soldier beams 7 and 8.

2.3.10.4 Two RowTieback Wall - Drilled Soldier Beams

In April 1996, the maximum positive bending moments were measured at the topmost anchor location for the drilled two row anchored soldier beams. The magnitude of the positive bending moments observed at the topmost anchor locations were 48.2 kN-m and 56.7 kN-m for soldier beams 9 and 10, respectively (Figures 78 and 79). However, these values as well as the ones observed at the bottom anchor locations show a decrease in bending moment ranging from 15 kN-m to 40 kN-m, representing changes of 30% to 70%, respectively. Bending moment losses are more noticeable in soldier beam 9, as seen in Figure 80. The maximum bending moment in the two row anchored drilled beams section was 56.7 kN-m or about 15% larger than the maximum bending moment measured in

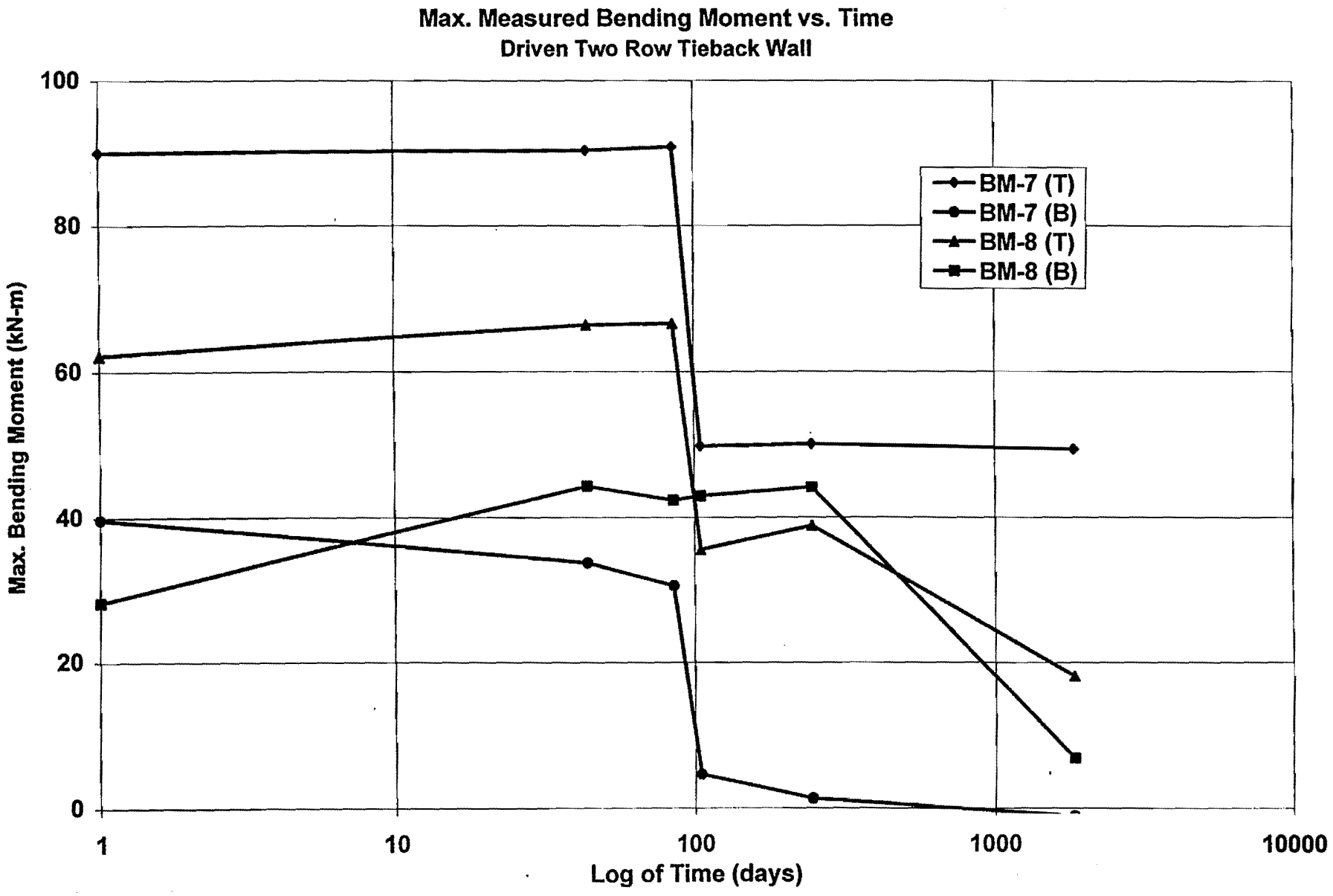

Figure 75. Maximum Bending Moment vs. Time (Driven Two-Row Section)

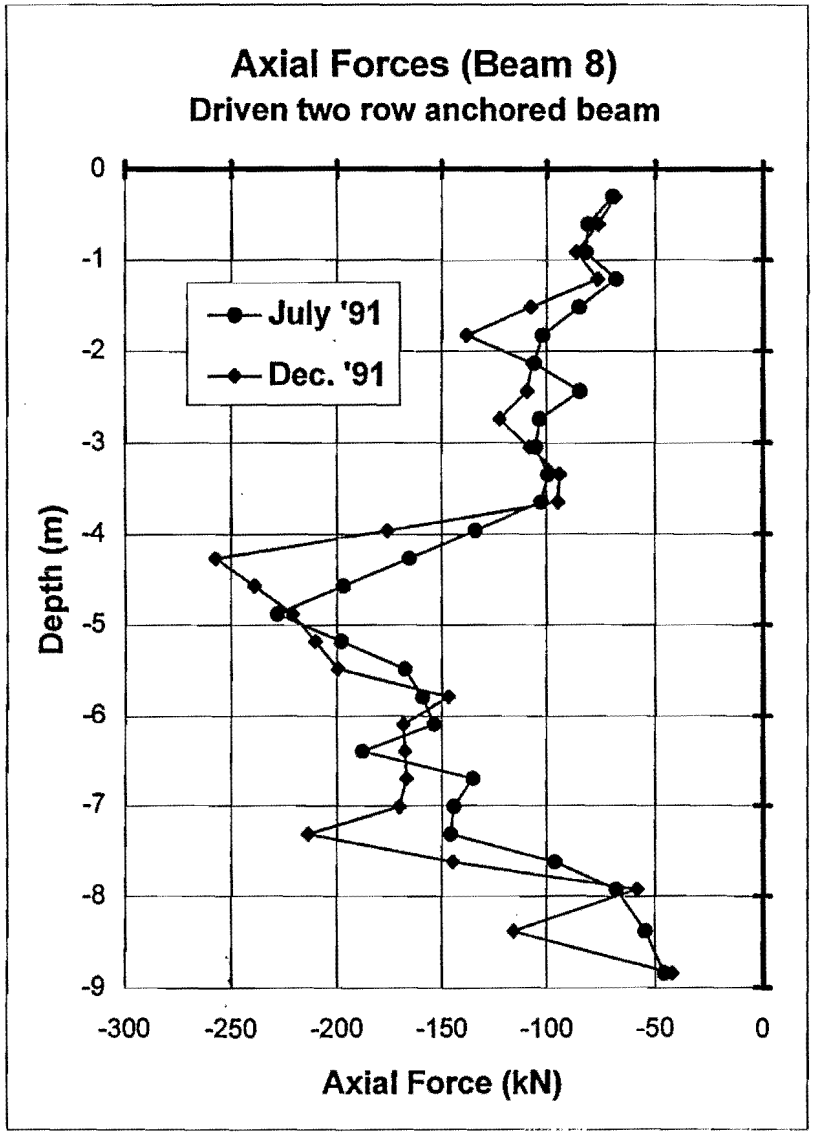

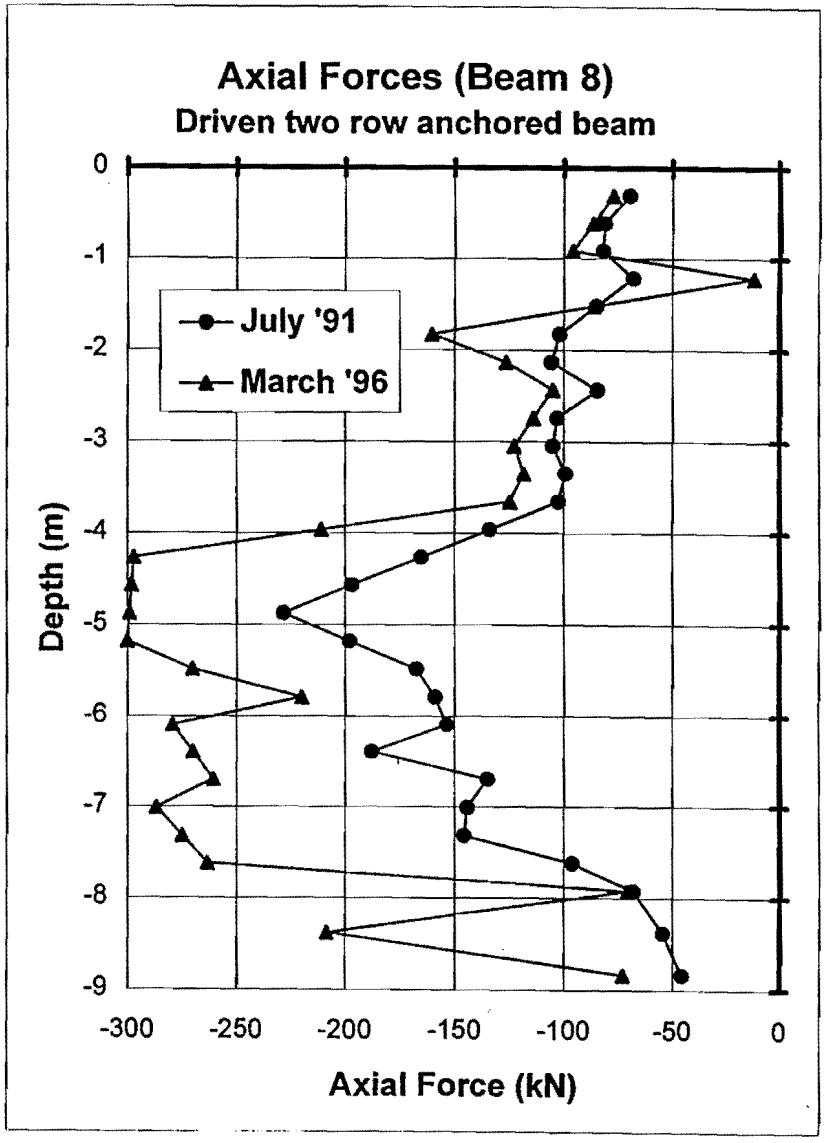

Figure 76. Axial Force Comparison – Beam 8

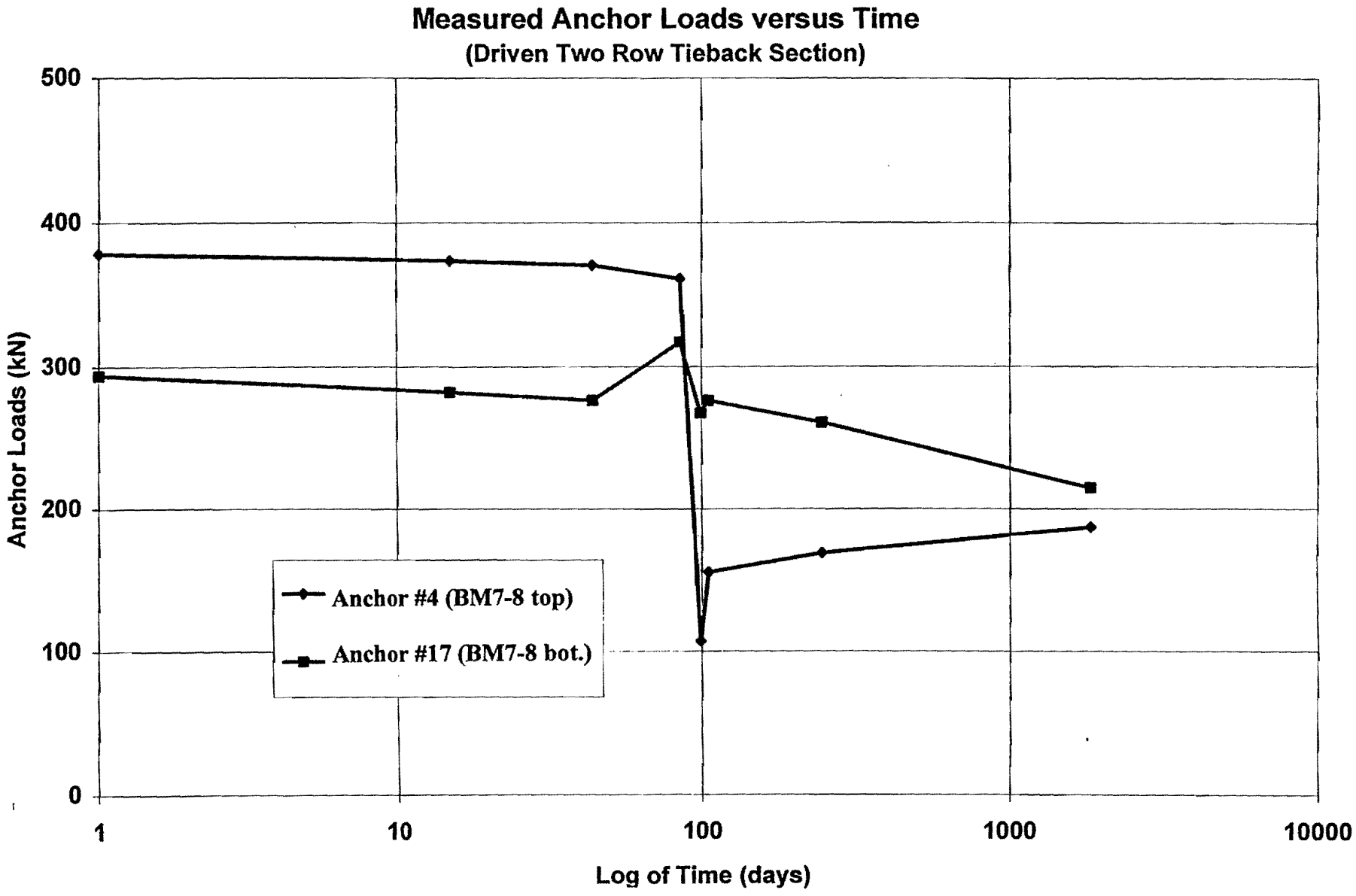

Figure 77. Anchor Load vs. Time (Driven Two Row Section)

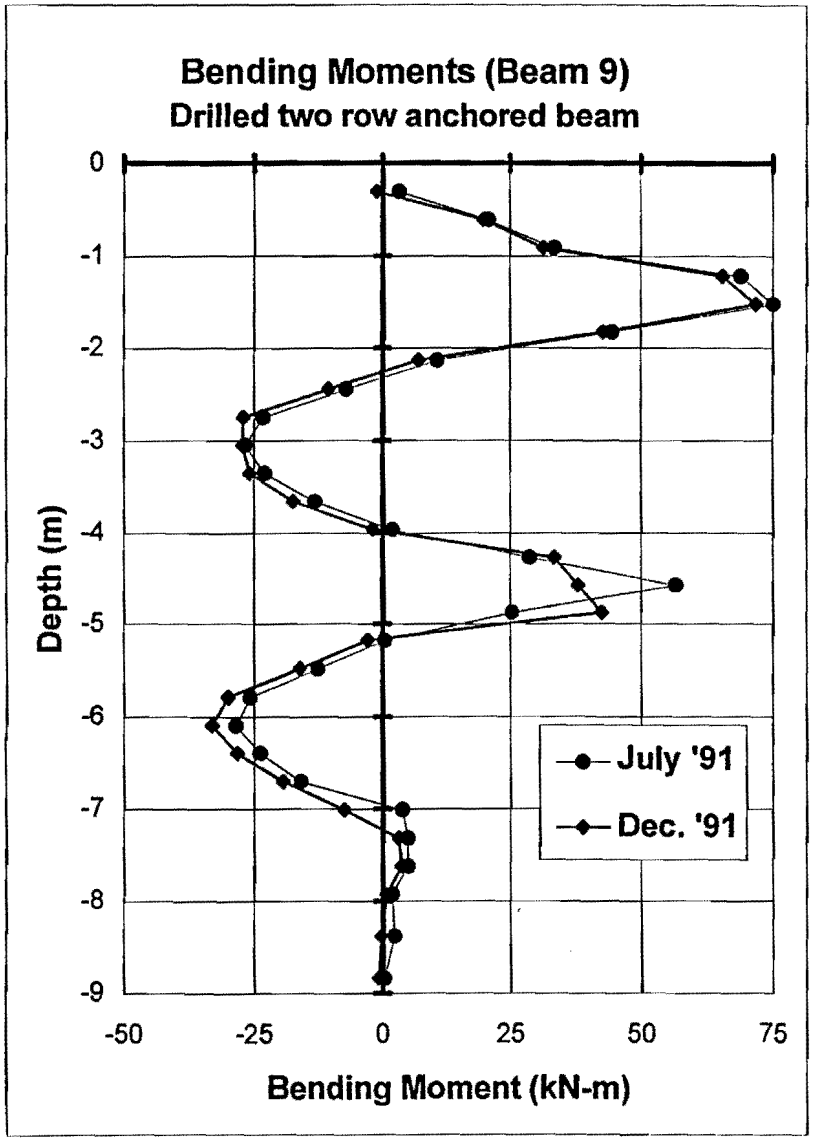

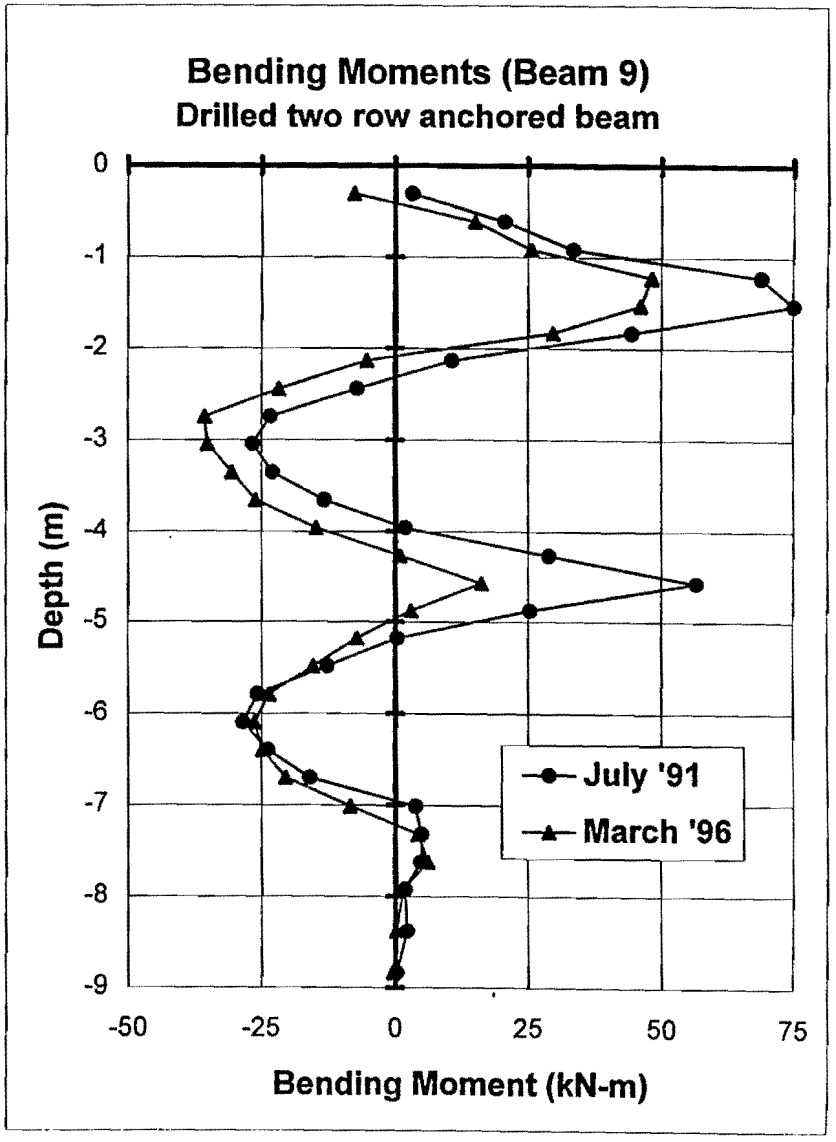

Figure 78. Bending Moment Comparison – Beam 9

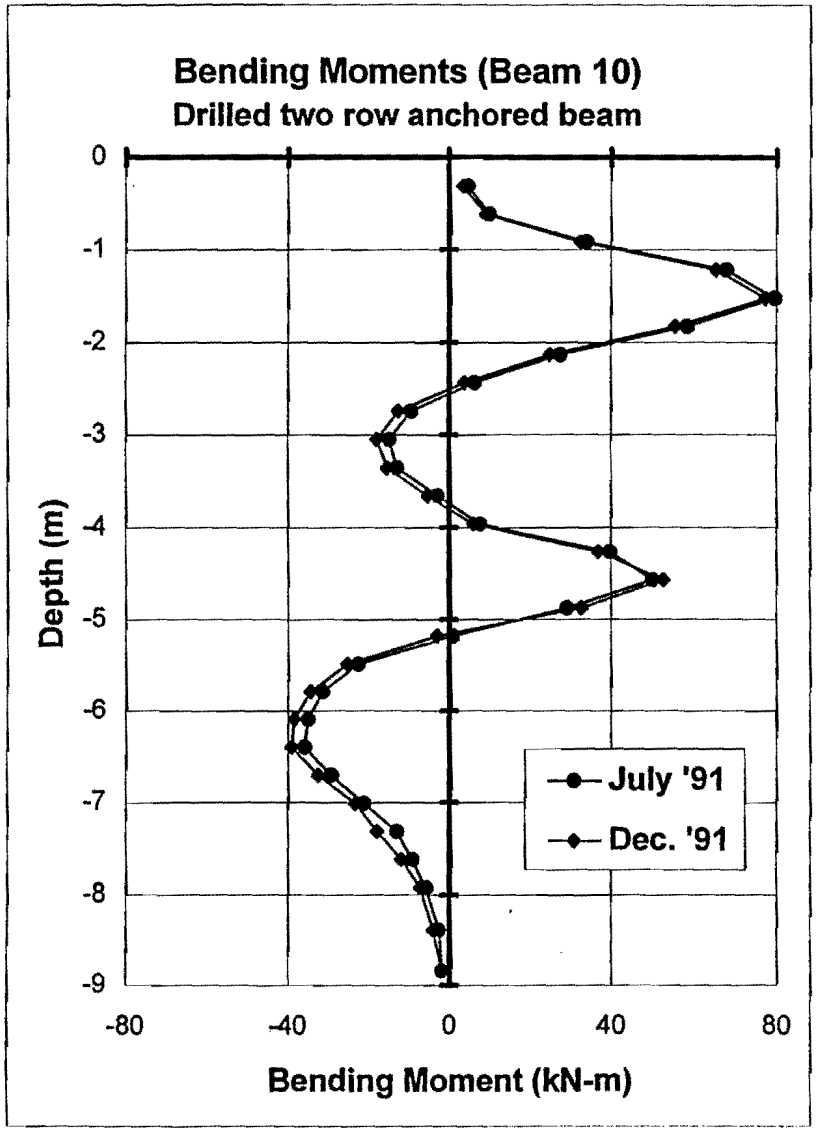

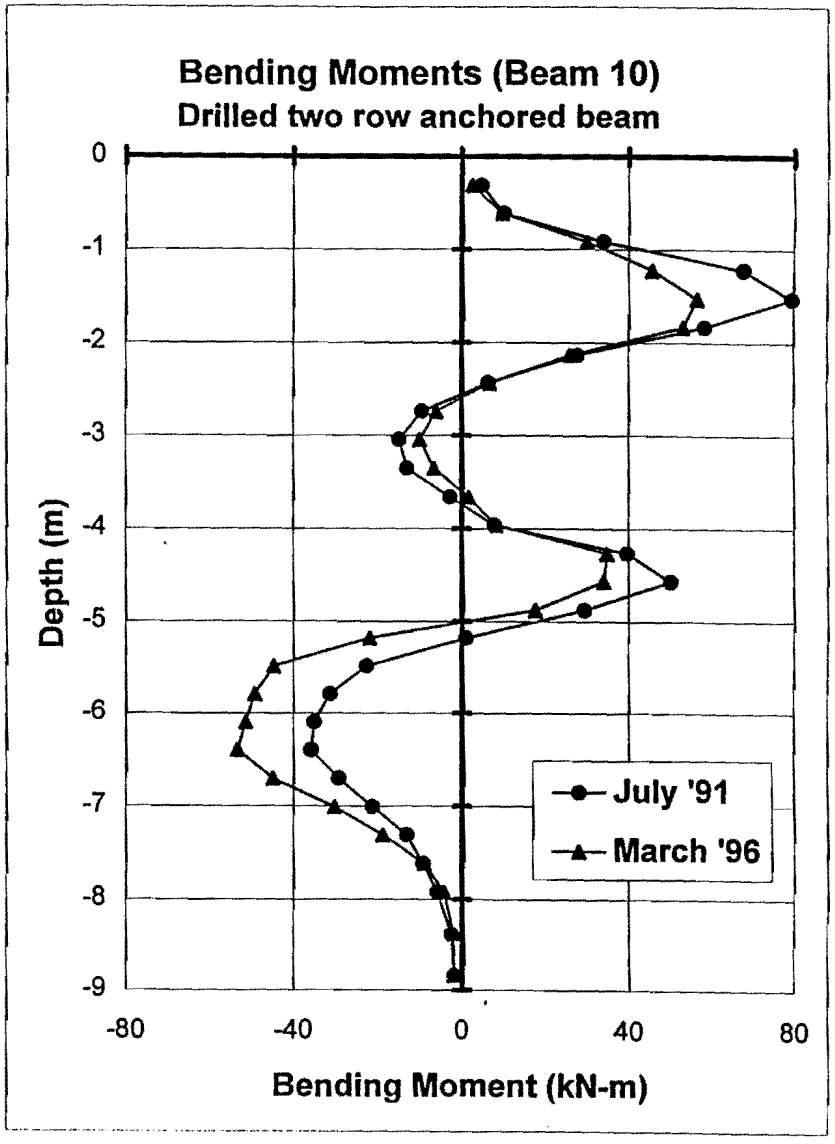

Figure 79. Bending Moment Comparison – Beam 10

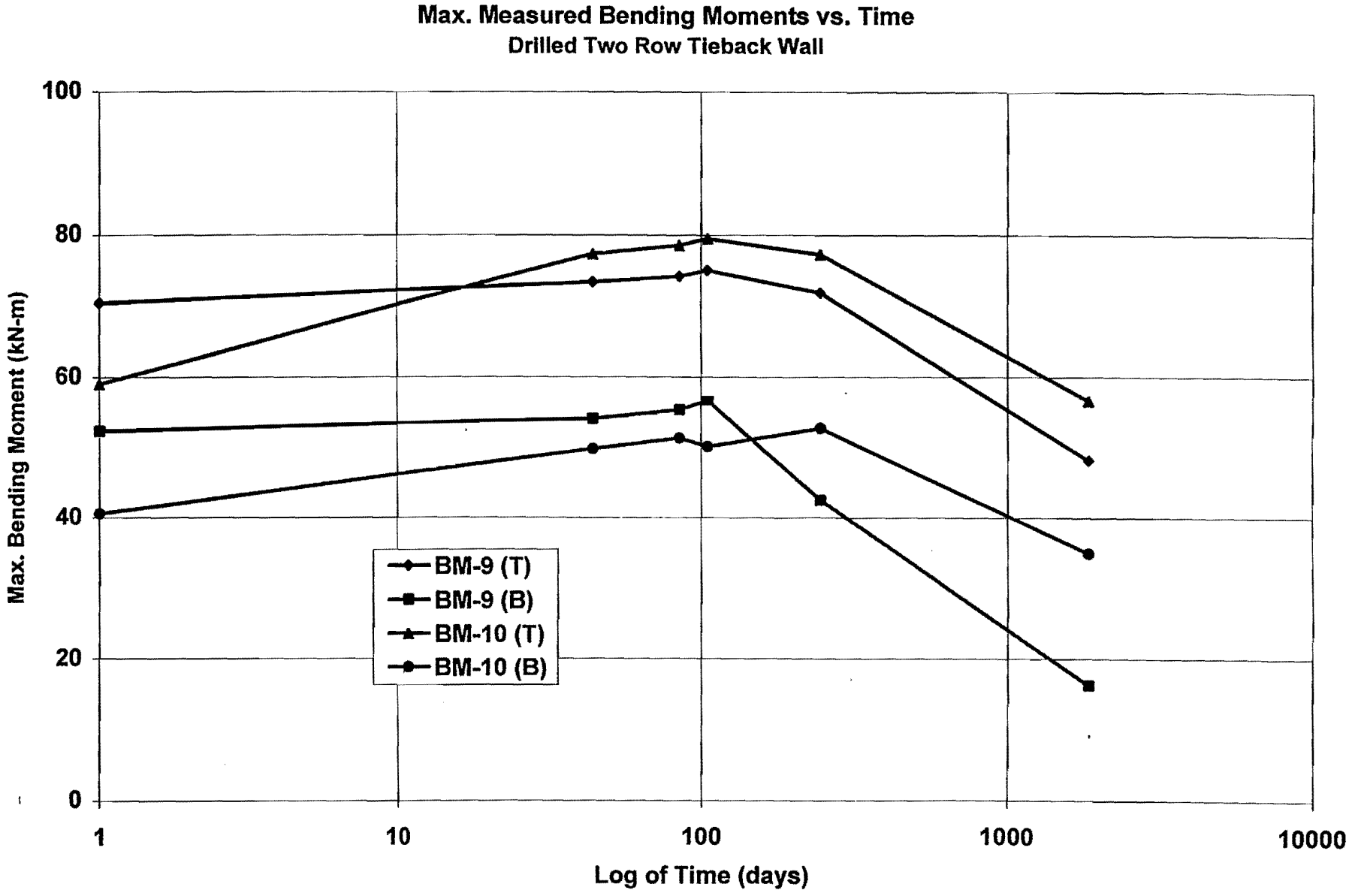

Figure 80. Maximum Bending Moment vs. Time (Drilled Two-Row Section)

the two row anchored driven soldier beam section. Variations in negative bending moments are somewhat erratic, not showing a consistent trend, ranging from 5 kN-m and -16.6 kN-m.

Since the inclinometer casing next to soldier beam 10 was not functional at the time of the readings, the lateral movement of the drilled beams section was measured only using the inclinometer casing located next to soldier beam 9. The maximum deflection, as measured in April 1996, was 34 mm at the top of the wall (Figure 81). The average deflection along the excavation height was calculated to be 23.8 mm, showing an average increment of 5.7 mm with respect to the average deflection in July 1991, representing a positive increment of 31.2%.

The lateral movement of the inclinometer casings E3 and E4 located on the embankment, 1.5 m and 4.5 m behind beam 10 respectively, were also measured. The maximum deflections were found in the order of 49 mm and 37 mm respectively, significantly larger than the rest of the measurements (Figures 82, 83, and 84).

The average deflection along the excavation height was measured as 32 mm in casing E-3 and 20 mm in casing E-4. Variations in average deflections were positive representing an increment of movement toward the excavation of 40% and 45%.

Anchor loads have remained relatively constant over the five-year period, showing a maximum variation (reduction) of 65 kN as observed at the location of tieback 5, top anchor supporting soldier beams 9 and 10 (Figure 85). This represents a decrease in load of 14.6%. The bottom anchor has lost just 6.2 kN, which is a load decrease of less than 2%.

Although the axial forces could not be calculated and deflections were only measured at the location of soldier beam 9, the performance of this section of the wall is probably due to the time-dependent behavior. Very little evidence of forces redistribution effect was observed in this subsection, induced by the reduction of the load of tieback 4, the top anchor supporting soldier beams 7 and 8. From this observation it can be inferred that load redistribution effect is more noticeable in the vertical direction than in the horizontal direction.

2.3.11 Lift-Off Tests

On August 29, 1996, lift-off tests were conducted on tiebacks 4, 17 (top and bottom anchors supporting soldier beams 7 and 8), and 7 (anchor supporting soldier beam 13) installed on the tieback wall at the sand site (Figure 47). The results provide information about the load carried by the anchors. Also, lift-off tests can help in determining the validity of the load cell readings. The actual magnitude of the lock-off load variation or long-term load variation can be also determined by simple comparison to previous recorded loads.

The lift-off consisted of reattaching the jack to the anchor, increasing the jack pressure until a visually perceptible sudden movement or separation (lift-off) occurred between the anchor head and the bearing plate above the load cell, as indicated by the dial gage. At that moment the pressure gage was read and registered. Then the jack pressure was released and the test equipment was removed.

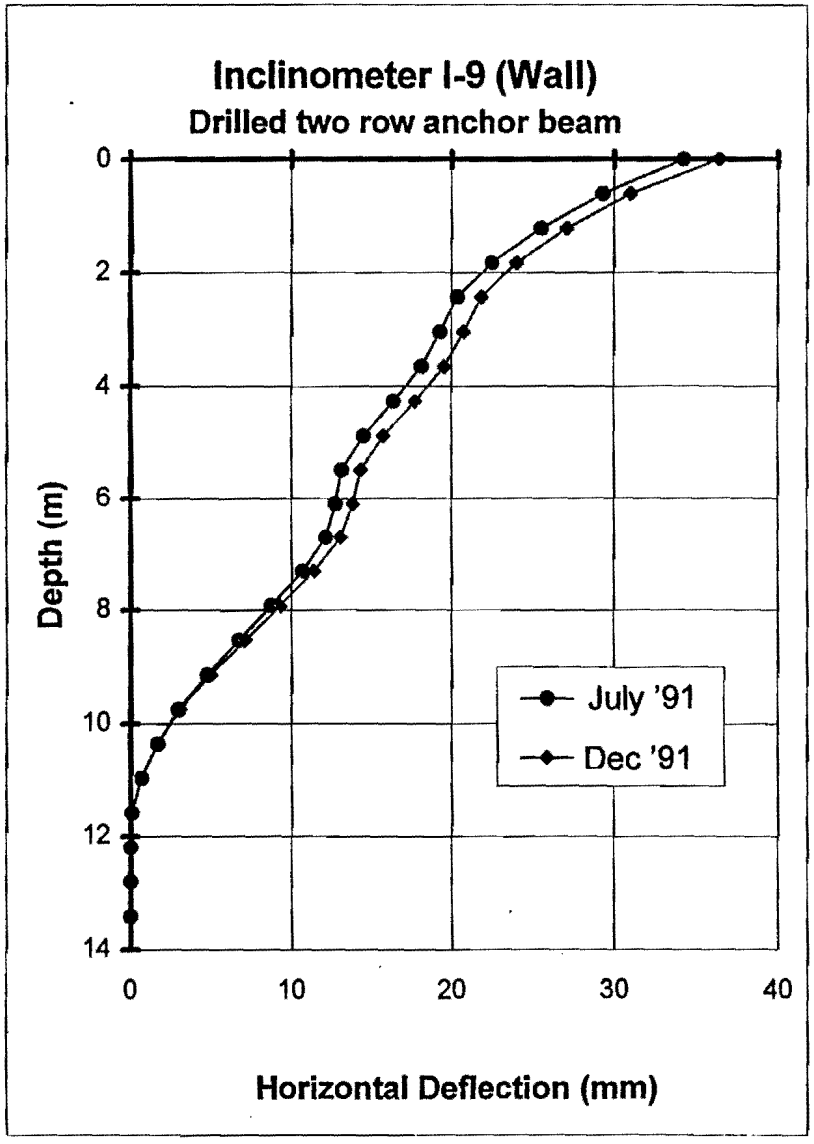

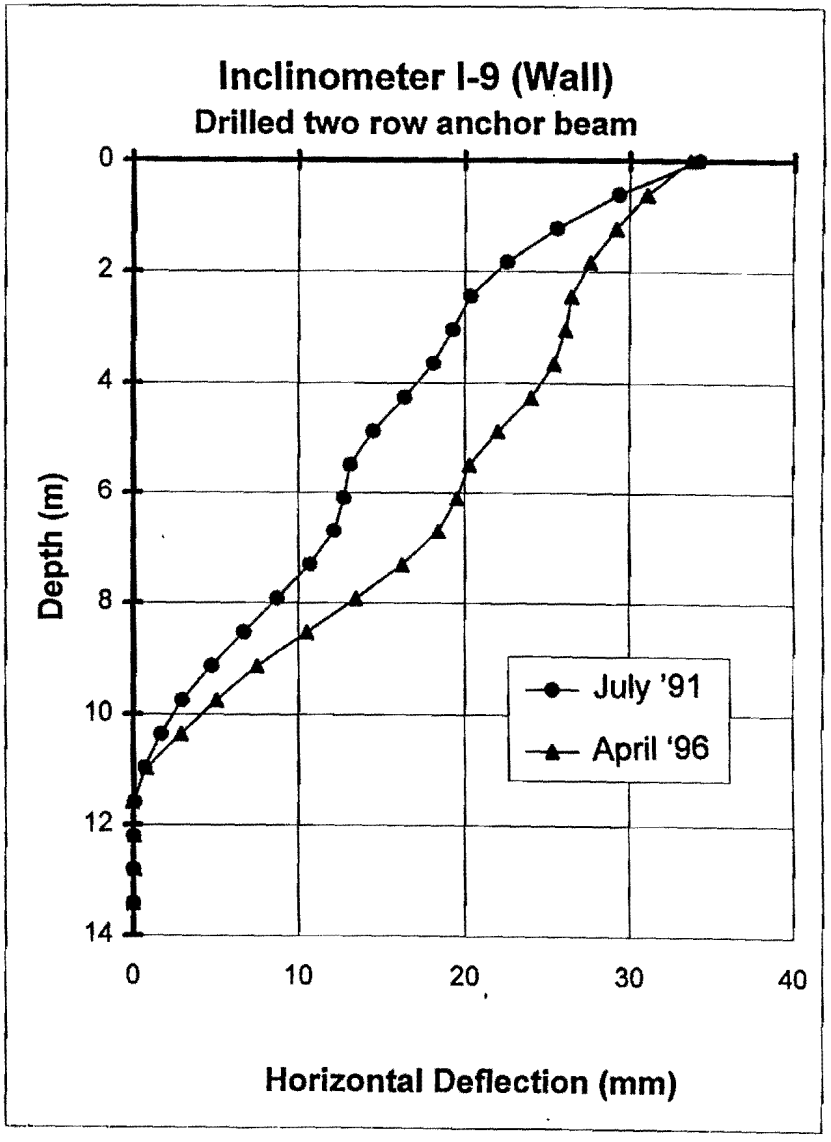

Figure 81. Horizontal Deflection Comparison - Casing I-9

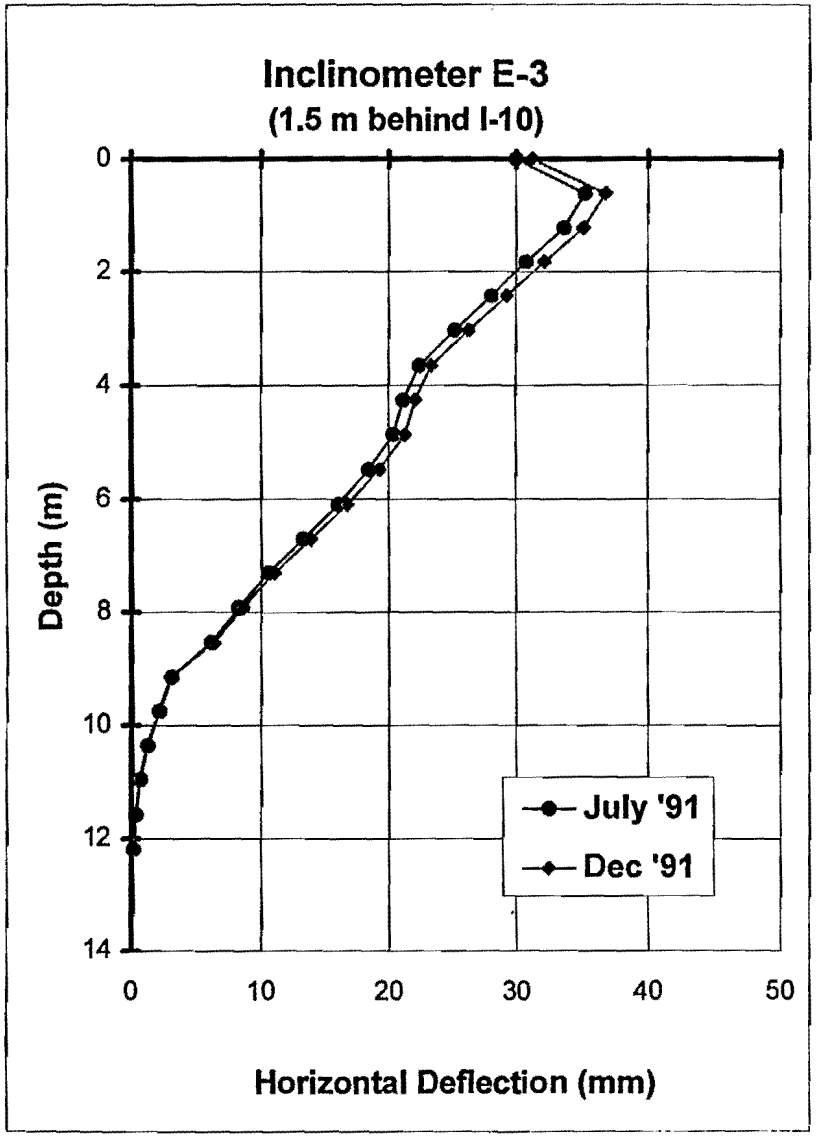

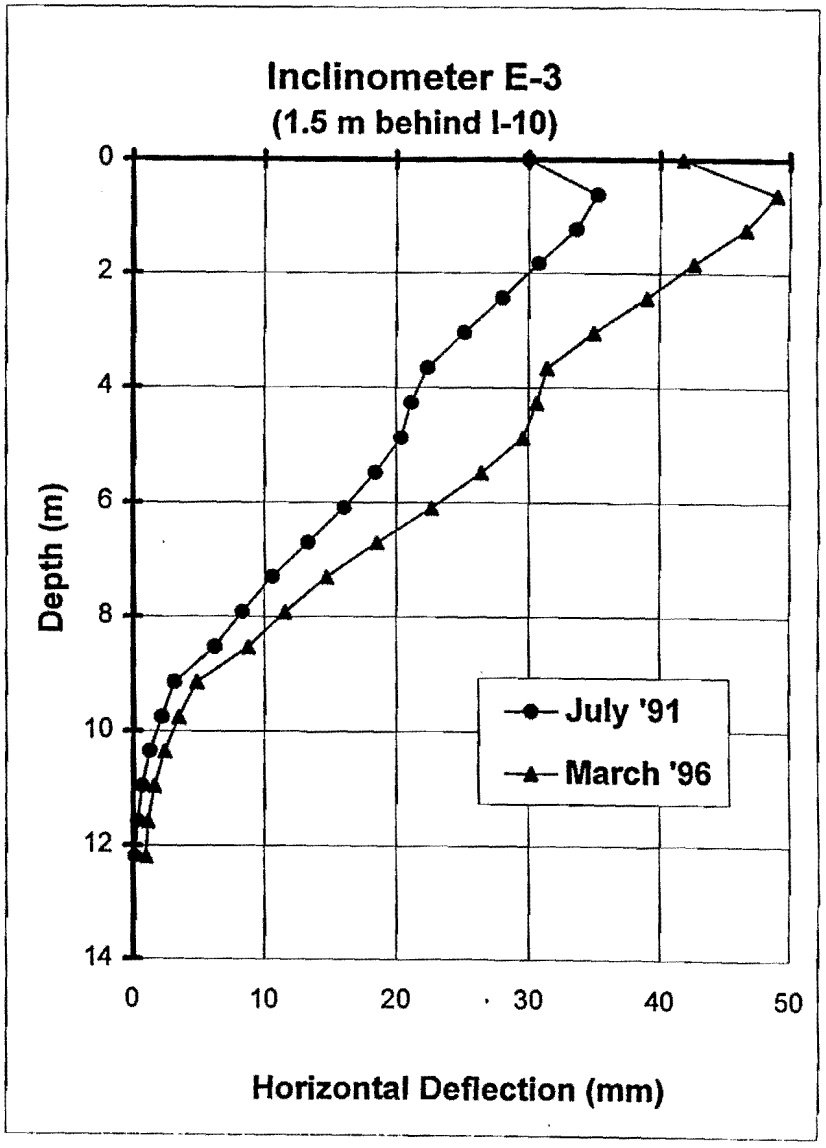

Figure 82. Horizontal Deflection Comparison - Casing E-3

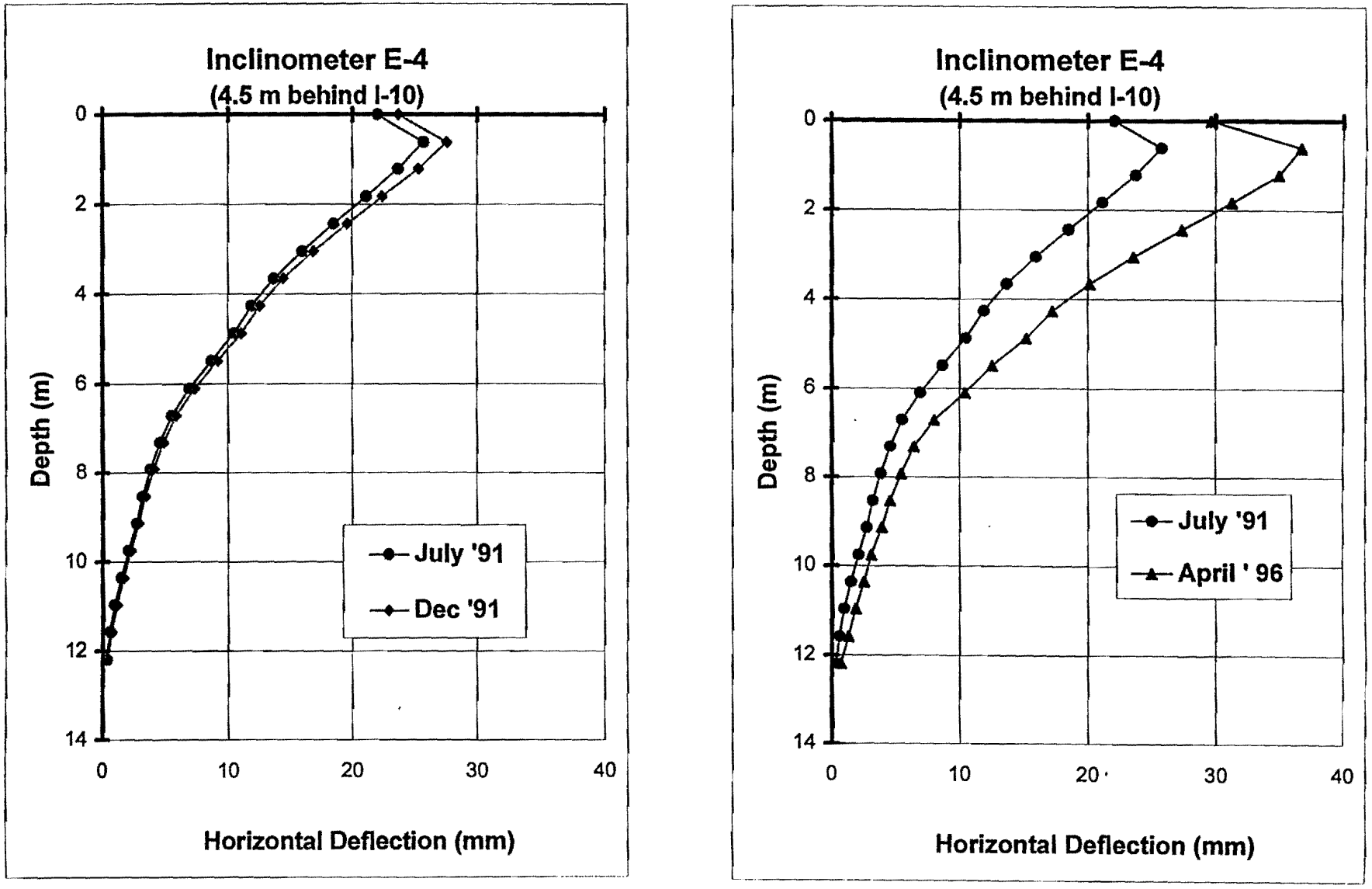

Figure 83. Horizontal Deflection Comparison – Casing E-4

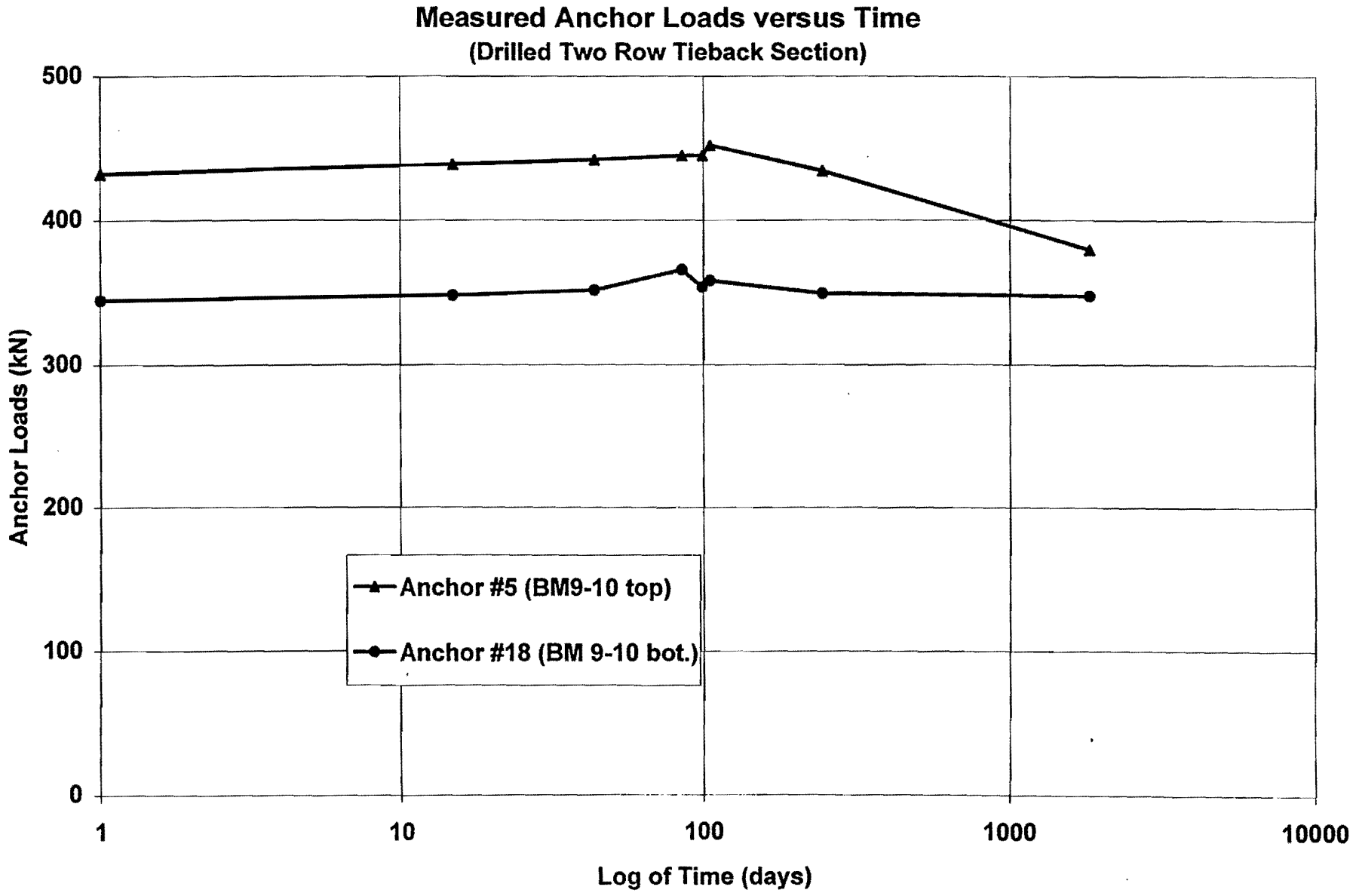

Figure 84. Maximum Deflection vs. Time (Casings in Embankment)

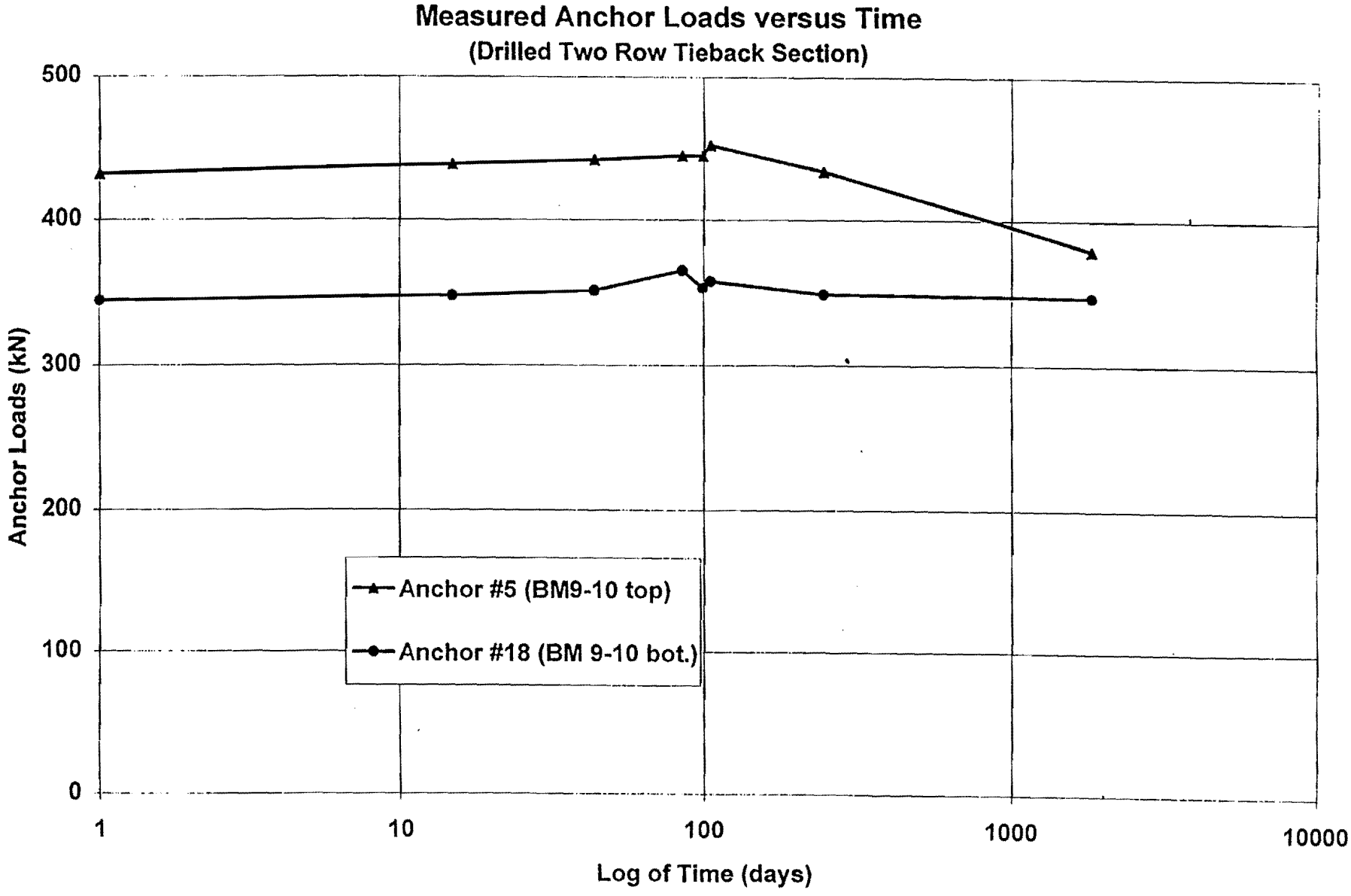

Figure 85. Anchor Loads vs. Time (Drilled Two Row Section)

Three tiebacks were selected to perform lift-off tests on the wall: tiebacks No. 4 and No. 17 (top and bottom anchor supporting soldier beams 7 and 8) were selected because they had shown great variability in load between July 1991 and April 1996, and tieback No. 7 (anchor supporting soldier beam 13) was selected because it had been holding the load very steadily over the same period. Comparisons between the lift-off loads and the load cell readings are shown in Figure 86.

The difference found between the load cell readings and the lift-off tests is small, differing at most by 10%. This difference may well be within the limits of error, considering that the jack readings are crude. From the results of lift-off tests, a conclusion is that vibrating wire strain gauge load cells are functioning very well after five years. The anchor load comparison between July 1991 and April 1996, according to the load cells, is shown in Figure 87. This figure indicates that very little change in anchor load took place over this five-year period except around anchors where the load had been significantly modified.

2.4 FEM SIMULATION OF NGES WALL

2.4.1 Background

Most commonly, tieback walls are designed on the basis of a simple pressure diagram (Terzaghi and Peck, 1967) used to calculate the anchor loads and the bending moment profile in the piles. There is a growing trend in practice to design tieback walls by using the beam-column approach (Halliburton, 1968; Matlock et al., 1981). This computer-based solution is used to predict the bending moment, the axial load, and the deflection profiles of the piles after the anchor loads have been chosen. Compared to the simple pressure diagram approach, the beam-column approach leads to deflection predictions and to improved bending moment profiles; however, the predicted deflections are not as reliable as the bending moments because the model ignores the mass movement of the soil. The Finite Element Method (FEM) represents another level of sophistication which comes very close to modeling all the components involved (Clough, 1984). The drawback is that the FEM approach is very time consuming; therefore, it is generally performed at the research level or for very large projects.

A study on the use of the beam-column approach (Kim and Briaud, 1994) led to detail recommendations on how to best use that method. It also identified the inability of predicting reliable displacement profiles with this method because the model ignores mass movement. The FEM study described in this article was undertaken after the beam-column study to better simulate the deformation process and to evaluate the influence of various factors on the wall deflections. These factors include the location of the first anchor, the length of the tendon unbonded zone, the magnitude of the anchor forces, the embedment of the soldier piles, and the stiffness of the wood-lagging and of the piles (Lim and Briaud, 1996).

2.4.2 Mesh Boundaries: How Far Is Far Enough?

One of the first steps in any numerical simulation is to determine where to place the boundaries so that their influence on the results will be minimized. The boundary effect was studied while using a linear elastic soil. The bottom of the mesh is best placed at a depth where the soil becomes notably harder. If D is the distance from the bottom of the excavation to the hard layer, a value of D equal

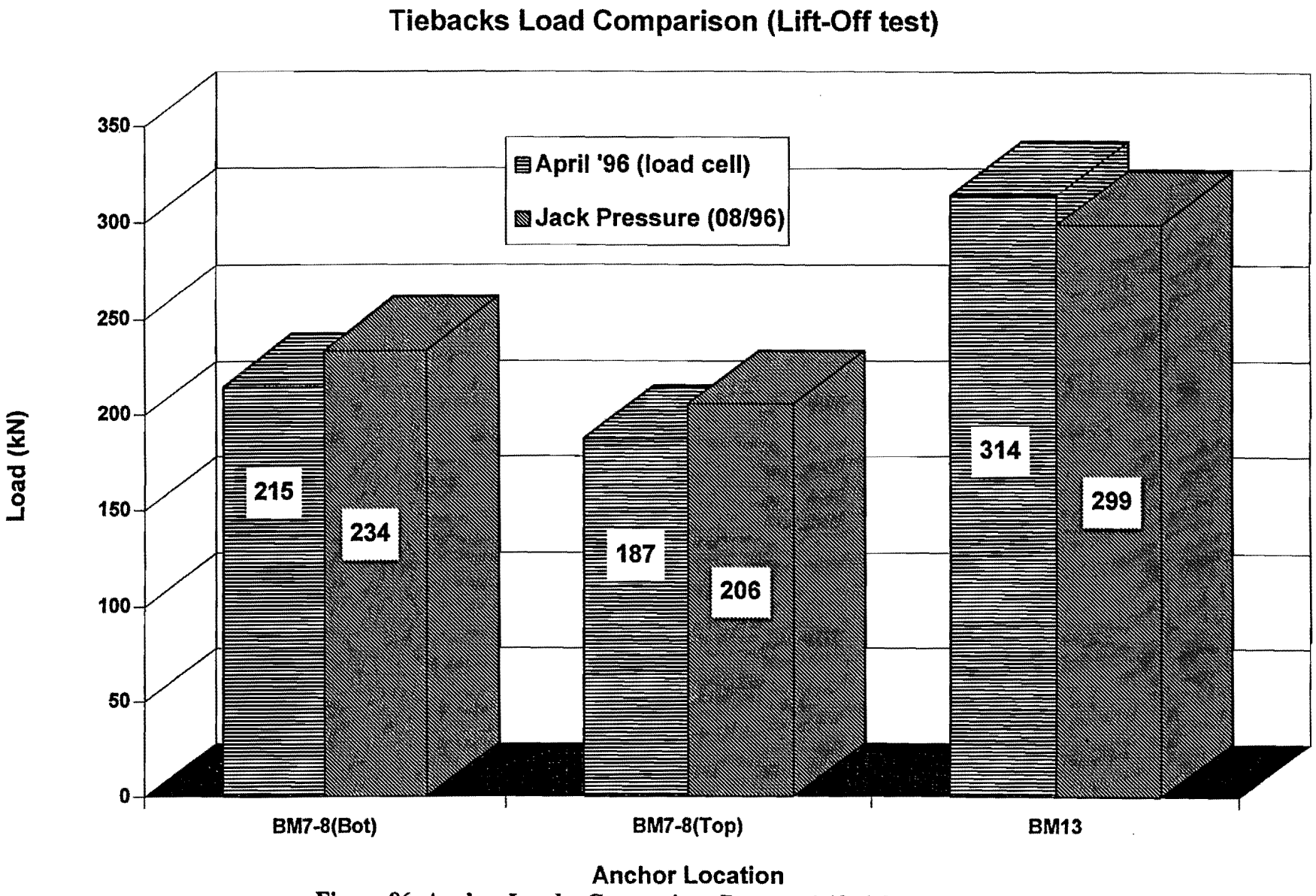

Figure 86. Anchor Loads: Comparison Between Lift-Off and Load-Cell

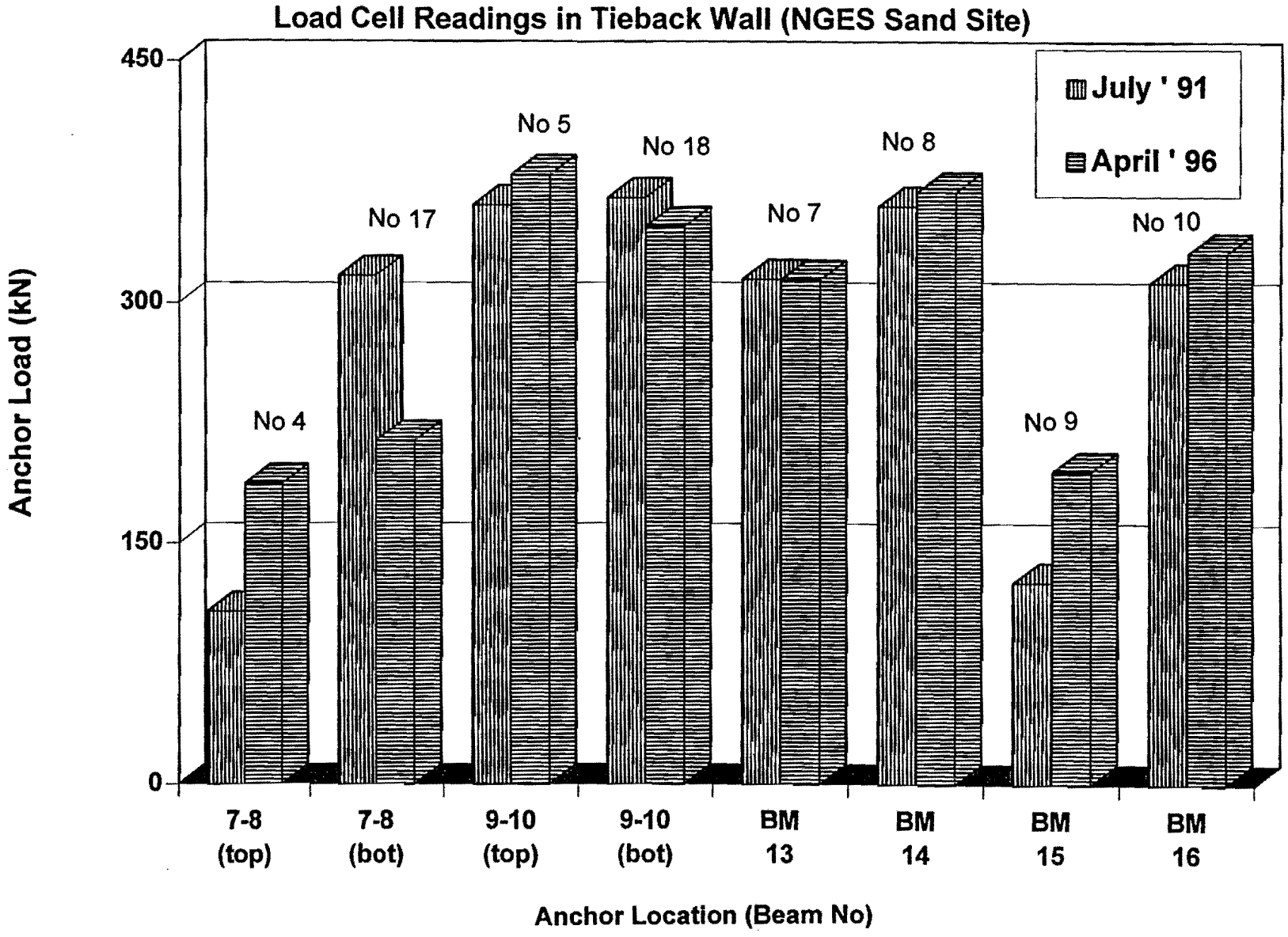

Figure 87. Anchor Load Comparison (July '91-April '96)

to 9 m was used for nearly all analyses. This value of *D* came from the instrumented case history chosen to calibrate the FEM model because of the hard shale layer existing at that depth. It was shown (Lim and Briaud, 1996) that when using a linear elastic soil in the simulation, D has a linear influence on the vertical movement of the ground surface at the top of the wall but comparatively very little influence on the horizontal movement of the wall face.

Considering the parameters H_e, W_e, B_e, and D as defined in Figure 88, it was found in a separate study (Lim and Briaud, 1996) that $W_e = 3D$ and $B_e = (H_e + D)$ were appropriate values for W_e and B_e; indeed beyond these values, W_e and B_e have little influence on the horizontal deflection of the wall due to the excavation of the soil. This confirms previous findings by Dunlop and Duncan (1970). For the instrumented wall to be simulated, H_e was 7.5 m, D was 9 m, B_e was 66 m or 4 m (H_e + D) and W_e was 10 m. The small value of W_e was chosen because the U-shape excavation for the case history was 20 m wide.

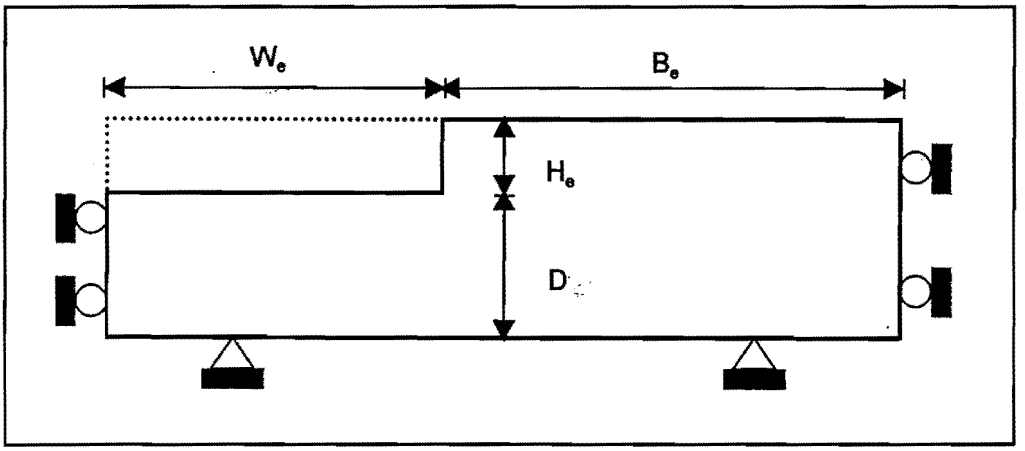

Figure 88. Definition of H_e, W_e, B_e, and D

2.4.3 Simulated Wall Section

It would be possible to simulate the entire width of the bridge in three dimensions. However, the size of the mesh would be prohibitively large. Instead, a repetitive section of the wall was chosen for the simulation. It was found that the best section (Figure 89) would include one vertical pile at the center of the section, one stack of inclined anchors attached to the soldier pile and penetrating back into the soil, and the soil mass. The width of the mesh was equal to the pile spacing or 2.44 m for the case history. Special moment restraints were required on the vertical edge boundaries of the wall in order to maintain a right angle in plan view between the displaced wall face and the sides of the simulated wall section. The final mesh is shown on Figure 90.

2.4.4 Soil and Structural Element Model

The general purpose code ABAQUS (1992) was used for all the runs. The soldier piles and the tendon bonded length of the anchors were simulated with beam elements; these are 1D elements which can resist axial loads and bending moments. The stiffness for the pile elements was the EI and

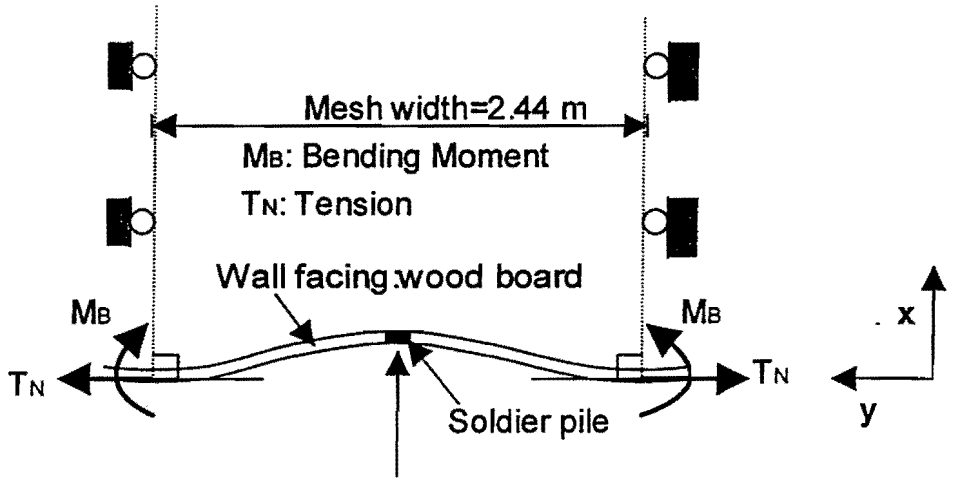

(a) Force and boundary condition requirements: Plan view

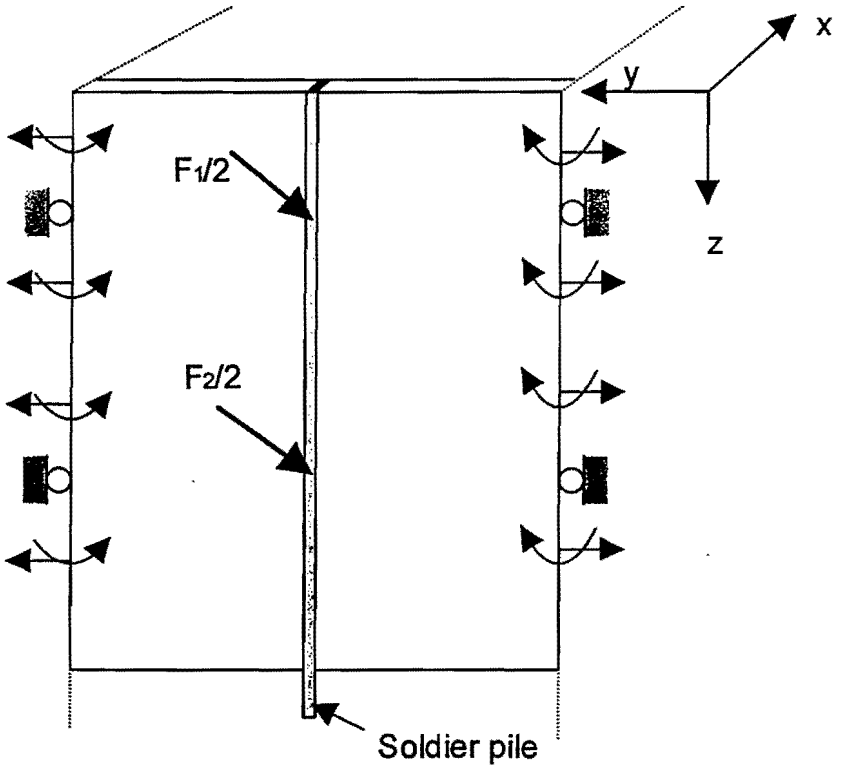

(b) Force and boundary condition requirements: Front view

Figure 89. Simulated Repetitive Wall Section

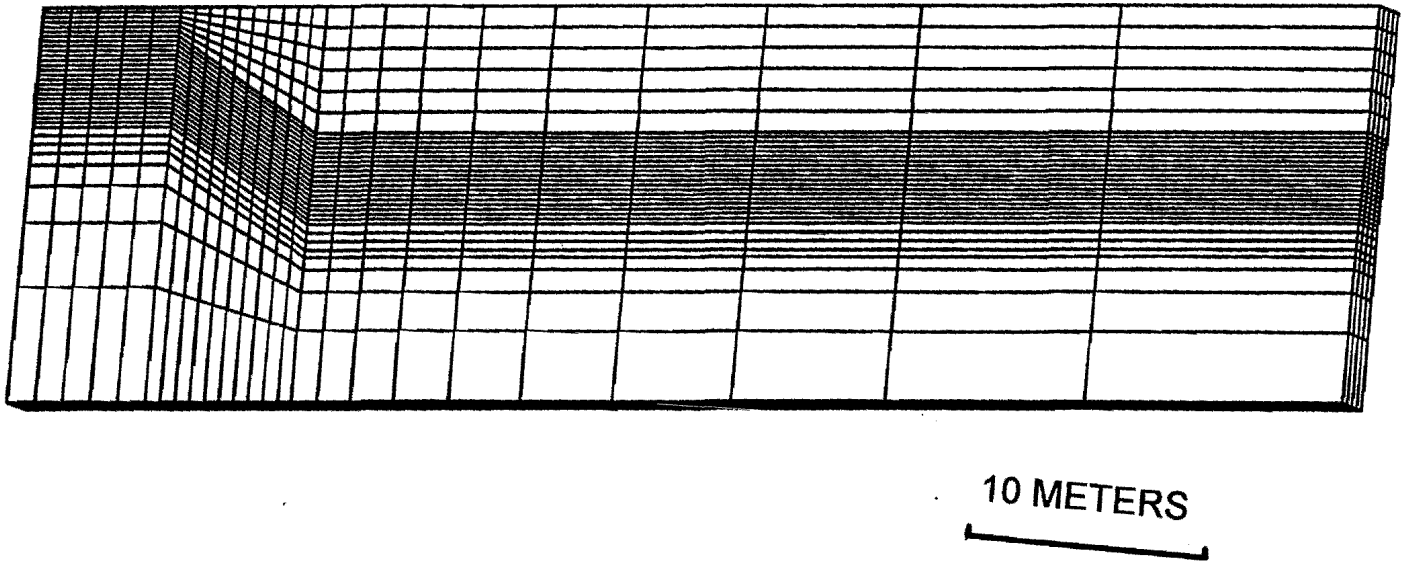

Figure 90. Finite Element Mesh

AE values of the soldier piles in the case history. The tendon bonded length was treated as a composite steel/grout section in order to get the EI and AE stiffness; a reduced grout modulus equal to 40% of the intact grout modulus was used to account for grout cracking; 40% was an educated guess. The wood-lagging facing was simulated with shell elements; these are 2D elements which can resist axial loads and bending moments in the two directions. The shell elements were given the thickness of the wooden boards and the modulus of wood. The steel tendon in the tendon unbonded length of the anchor was simulated as a spring element; this is a 1D element that can only resist axial load. This element was given a spring stiffness K equal to the initial slope of the load-displacement curve obtained in the anchor pull-out tests.

The soil was simulated with three-dimensional eight noded brick elements. The soil model was a modified Duncan-Chang hyperbolic model (Duncan et al., 1980). This model is a nonlinear model which includes the influence of the stress level on the stiffness, on the strength, and on the volume change characteristics of the soil. With this soil model it was also possible to simulate the hysteresis of the soil by unloading and reloading the soil along a path different from the loading path. The parameters necessary for the soil model included seven parameters to describe the loading path tangent Young's modulus E_t, plus two parameters to describe the Poisson's ratio v_t, plus one parameter to describe the unloading-reloading path modulus E_{ur}. The seven parameters for E_t included the unit weight γ, the coefficient of earth pressure at rest K_o, the initial tangent modulus factor K, the stress influence exponent n for the tangent Young's modulus, the failure ratio R_f, the effective stress friction angle φ, and the effective stress cohesion c. The two additional parameters for v_t were the bulk modulus factor K_B and the stress influence exponent n_B for the bulk modulus. The additional parameter for E_{ur} was the unload-reload modulus factor K_{ur}.

The tangent Young's modulus E_t is defined as the instantaneous tangential slope of the triaxial stress strain curve:

$$E_t = \frac{\partial(\sigma_1 - \sigma_3)}{\partial \varepsilon_1} \tag{27}$$

where σ_1 and σ_3 are the major and minor effective principal stresses in a soil element, and ε_1 is the major principal strain for that same soil element. The expression that gives E_t for the hyperbolic model is:

$$E_t = \left(1 - \frac{R_f (1 - \sin\varphi)(\sigma_1 - \sigma_3)}{2(c\cos\varphi + \sigma_3 \sin\varphi)}\right)^2 K p_a \left(\frac{\sigma_3}{p_a}\right)^n \tag{28}$$

where σ_1 and σ_3 have initial values of γz and $K_o \gamma z$ (z = depth) and are updated as the loading and unloading take place in increments, and p_a is the atmospheric pressure. The unload-reload modulus E_{ur} is given by:

$$E_{ur} = K_{ur} p_a \left(\frac{\sigma_3}{p_a}\right)^n \tag{29}$$

The tangent Poisson's ratio v_t is defined as:

$$v_t = 0.5 - \frac{E_t}{6B_t} \tag{30}$$

where the tangent bulk modulus B_t is given by:

$$B_t = K_B p_a \left(\frac{\sigma_3}{p_a} \right)^{n_B} \tag{31}$$

This hyperbolic model was coded in FORTRAN and implemented into ABAQUS as a user-defined subroutine UMAT.

2.4.5 Simulating the Excavation Sequence

The excavation sequence was simulated step-by-step as shown in Figure 91. The first step (Figure 91) was to turn on the gravity stresses in that parallelepiped which was 76 m long, 16.5 m high, and 2.44 m wide. The second step was to install the piles; this consisted of activating the beam elements and allowing them to be stressed by the next steps. Therefore driving stresses were not simulated. The third step was to excavate the first lift (2.4 m in the case history). This step induced initial deflections and a change in stress. The fourth step was to install the wood-lagging and to install the first row of anchors. This step consisted of activating the shell elements simulating the wood-lagging, activating the beam elements simulating the tendon bonded length of the anchor, and allowing them to be stressed by the next steps. The fifth step was to stress the anchor. This was simulated by applying the same force F, but in the opposite direction at the top of the tendon bonded zone. The sixth step consisted of activating the spring element simulating the unbonded tendon length. The seventh step was the excavation of the next lift. The following steps were repetitions of steps three to five to simulate additional excavation lifts and anchor stressing. The final step was an excavation step to final grade below the last rows of anchor. Each run required about six hours of CPU time on the Texas A&M University Super Computer (SGI Power Challenge 10000 XL). A total of about 100 runs were performed for a dollar value of $18,000.

Each excavation was simulated by applying on each element along the n^{th} excavation boundary a stress vector $\Delta\vec{\sigma}_n$ in opposite direction to the stress vector which existed on that boundary at the end of the $(n-1)^{th}$ excavation step. The stress vector $\Delta\vec{\sigma}_n$ was found by iteration until that vector and the stress vector existing on that boundary at the end of the previous step added to zero all along the n^{th} excavation boundary. All elements above the n^{th} excavation boundary were then deactivated.

2.4.6 Calibration of Model Against Case History

The TAMU two row anchor tieback wall was used to calibrate the FEM model (Figure 92). The H piles were replaced with pipe piles of equivalent stiffness (AE and EI) because the H piles created some numerical instabilities. For the anchors, the grout annulus with a modulus equal to 0.4 times the intact modulus of grout was included with the steel tendon to compute the stiffness AE and EI of the tendon bonded length. The 10 parameter hyperbolic model was used for the soil.

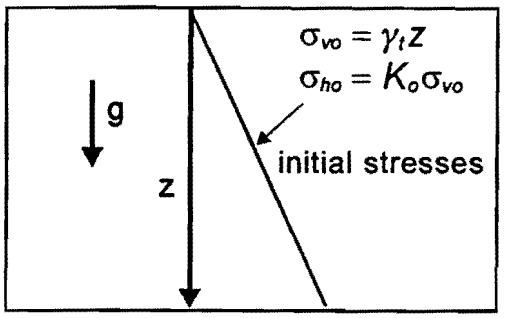

STEP 1. Specify initial geostatic stress condition, and apply gravity load to the mesh and check equilibrium.

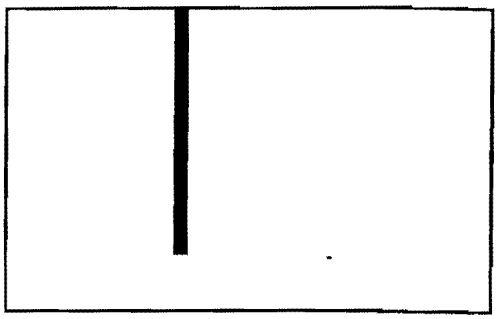

STEP 2. Install piles by activating the corresponding elements.

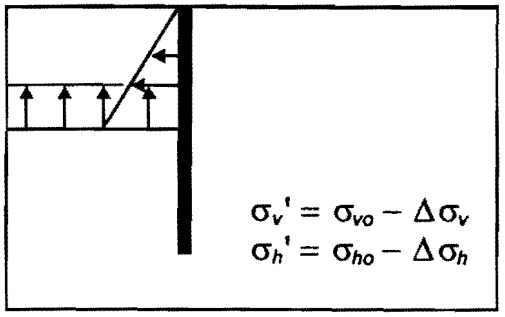

STEP 3. Excavate to the first excavation level

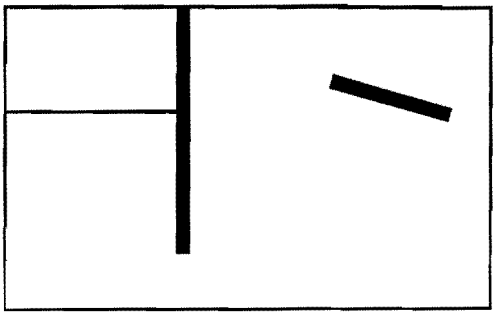

STEP 4. Install tendon bonded zone of the anchor, wall facing.

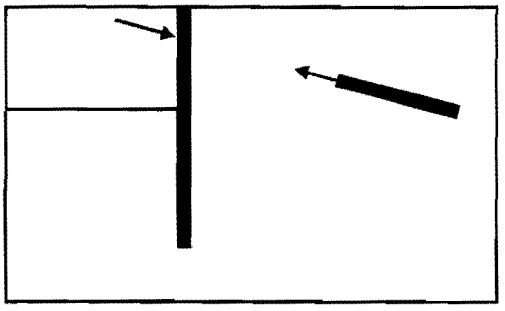

STEP 5. Apply lock-off load.

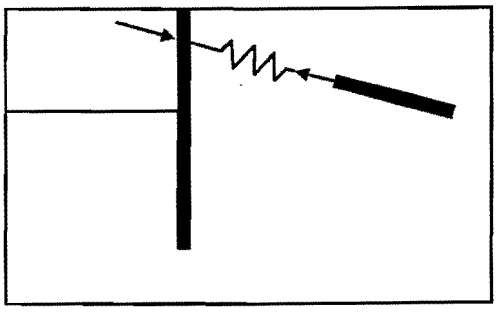

STEP 6. Activate spring simulating tendon unbonded length.

Figure 91. Simulation of the Excavation Sequence

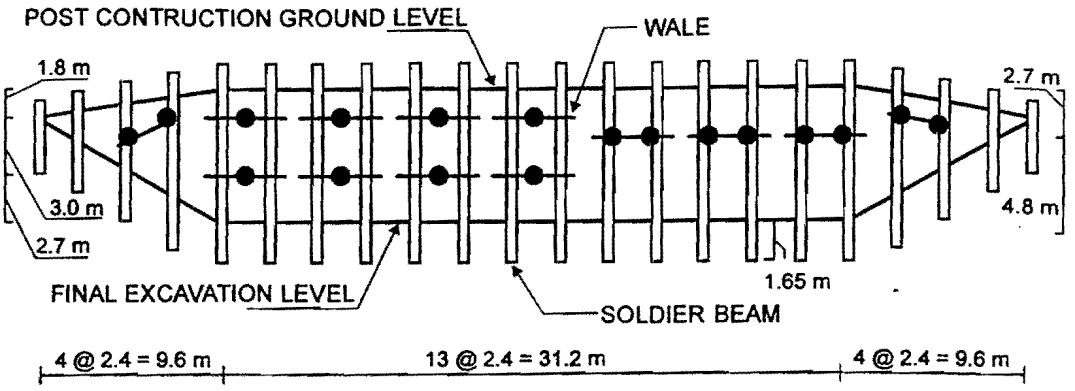

(a) Elevation View

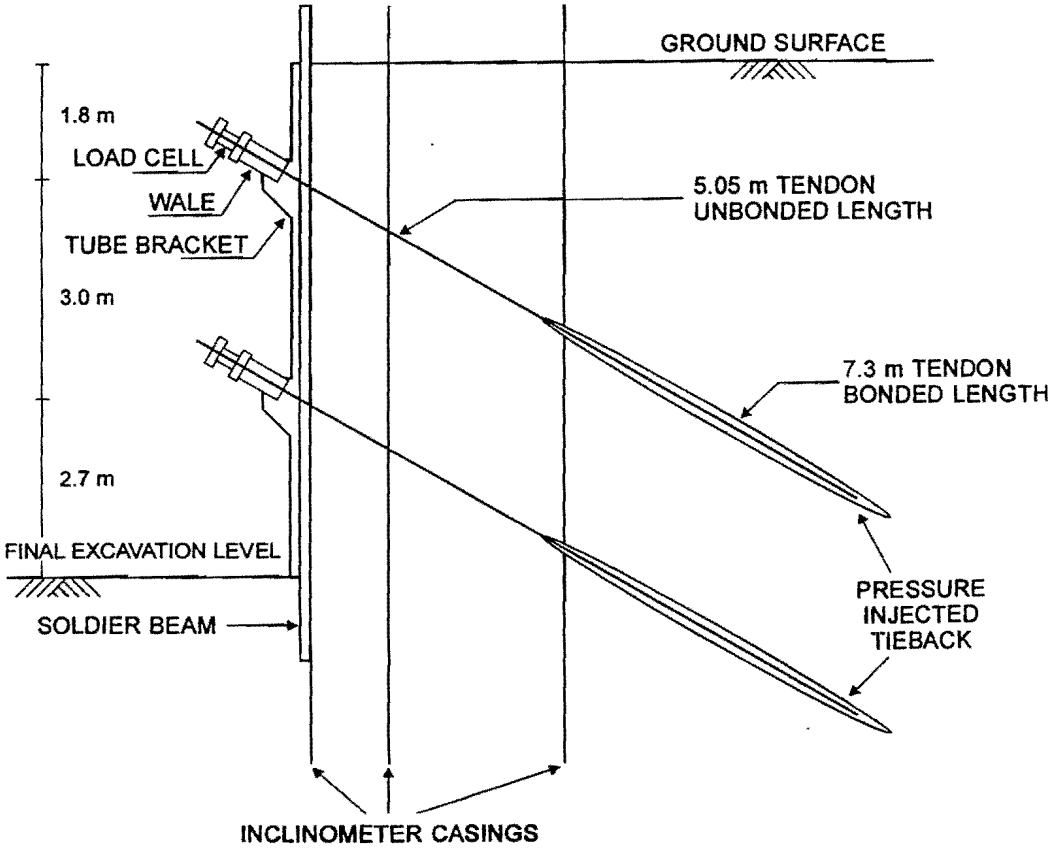

(b) Two Row Anchored Wall - Section View

Figure 92. The Texas A&M University Tieback Wall

The calibration process consisted of finding the set of those 10 parameters which led to the best match between the measured and calculated deflection u, bending moment M, and axial load Q profiles of the soldier piles. It was found that the most influential parameters were K and K_o for the bending moment, γ_t for the axial load including the downdrag load. All other parameters had a relatively small impact on the calculated values.

The comparison between measured and calculated u, M, and Q profiles is shown on Figure 93. The final model parameters are presented in Table 10.

2.4.7 Parametric Analysis

A number of factors were varied from the initial values of the case history in order to evaluate their influence on the design. These factors were the location of the first anchor, the length of the tendon unbonded zone, the magnitude of the anchor force, the embedment of the soldier piles, the stiffness AE and EI of the wood lagging, and the stiffness AE and EI of the soldier piles.

The location of the first anchor was varied from 0.6 m to 1.8 m below the top of the wall. The second anchor was kept 3 m below the first anchor. The results show (Figure 94) that a position of 1.2 m to 1.5 m leads to lower deflections and lower bending moments with a 25% reduction in u and M compared to the 1.8 m anchor position. The results also show that the position of the first anchor has very little influence on the axial load distribution including the downdrag load.

The length of the tendon unbonded zone L_u was about 5 m for the case history. This length L_u was varied from 1.375 m to 16.2 m while keeping the tendon bonded length constant and equal to 7.3 m. The results show (Figure 95) that L_u only has a small influence on the bending moment and the axial load in the soldier piles as long as the beginning of the tendon bonded zone is outside the failure wedge. The unbonded length L_u has a significant influence on the deflection at the top of the wall u_{top}; when L_u was three times longer than in the case history, the deflection at the top of the wall u_{top} was equal to 0.57 times the value of u_{top} for the case history. It was found that L_u had no influence on the deflection at the bottom of the wall which remained equal to 10 mm. It was also found that increasing L_u for the first anchor alone was much more effective to reduce deflection than increasing L_u for the second anchor.

The magnitude of the anchor force was varied. The sum of the horizontal components of the anchor forces divided by the frontal area of the wall is the average pressure p corresponding to a constant pressure diagram against the wall. The ratio of p over γH_t is the earth pressure coefficient K; γ is the effective soil unit weight and H_t is the total height of the wall. The value of K was varied in the parametric analysis from 0.02 to 1.1 by varying the anchor loads correspondingly, and the deflection at the top of the wall u_{top} was calculated by the FEM. Case histories were also collected to obtain measured values of K and corresponding measured values of u_{top}. The Boston case history was obtained from Houghton and Dietz (1990), the Bonneville case history was obtained from Munger et al. (1990), the Lima case history was obtained from Lockwood (1988), and the Texas A&M University case history was obtained from Chung and Briaud (1993). The relationship between K and (u_{top} / H_t) is in Figure 96. The relationship between K and (u_{mean} / H_t) is shown in Figure 97. The parameter u_{mean} is the mean deflection of the wall face. These figures show that for the common value of K equal to

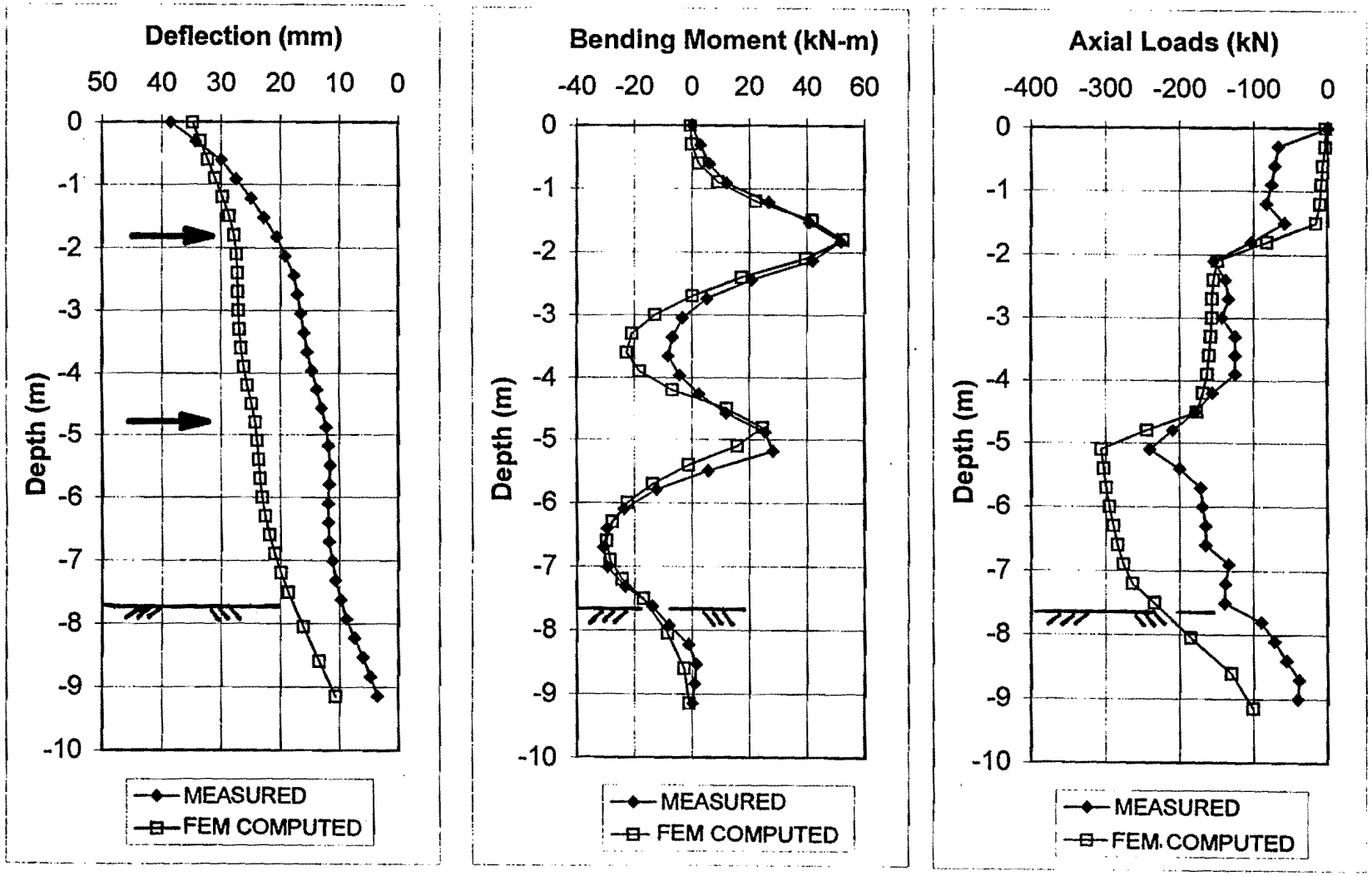

Figure 93. Measured and Calculated Displacements, Bending Moments, and Axial Loads

Table 10. Parameters Used for the FEM Simulation

Soil Data	Initial tangent modulus factor, K	300
	initial tangent modulus exponent, n	0.85
	Strength ratio, R_f	0.93
	Friction angle, φ	32°
	Cohesion, c	0
	Unloading-reloading modulus number, K_{ur}	1200
	Bulk modulus number, K_B	272
	Bulk modulus exponent,n_B	0.5
	Unit weight, γ_s	18.5 kN/m^3
	At rest earth pressure coefficient, K_0	0.65
Anchor Data	Tendon unbonded length	5.05 m
	Tendon bonded length	7.3 m
	Lock-off load - row 1	182.35 kN
	Lock-off load - row 2	160.0 kN
	Tendon stiffness - row 1	19846 kN/m
	Tendon stiffness - row 2	19479 kN/m
	Angle of Inclination, β	30°
Wall Facing Data	Wall height	7.5 m
	Thickness of wall facing	0.1 m
	Elastic modulus of wood board	1.365x10^6 kN/m^2
Soldier Pile Data	Length of soldier pile	9.15 m
	Embedment	1.65 m
	Diameter of pipe pile	0.25 m
	Thickness of pipe pile	0.00896 m
	Horizontal spacing of piles	2.44 m
	Elastic modulus of steel pipe pile	2.1x10^8 kN/m^2
	Flexural stiffness, EI	11620 kN-m^2
	Axial stiffness, AE	1.47x10^6 kN

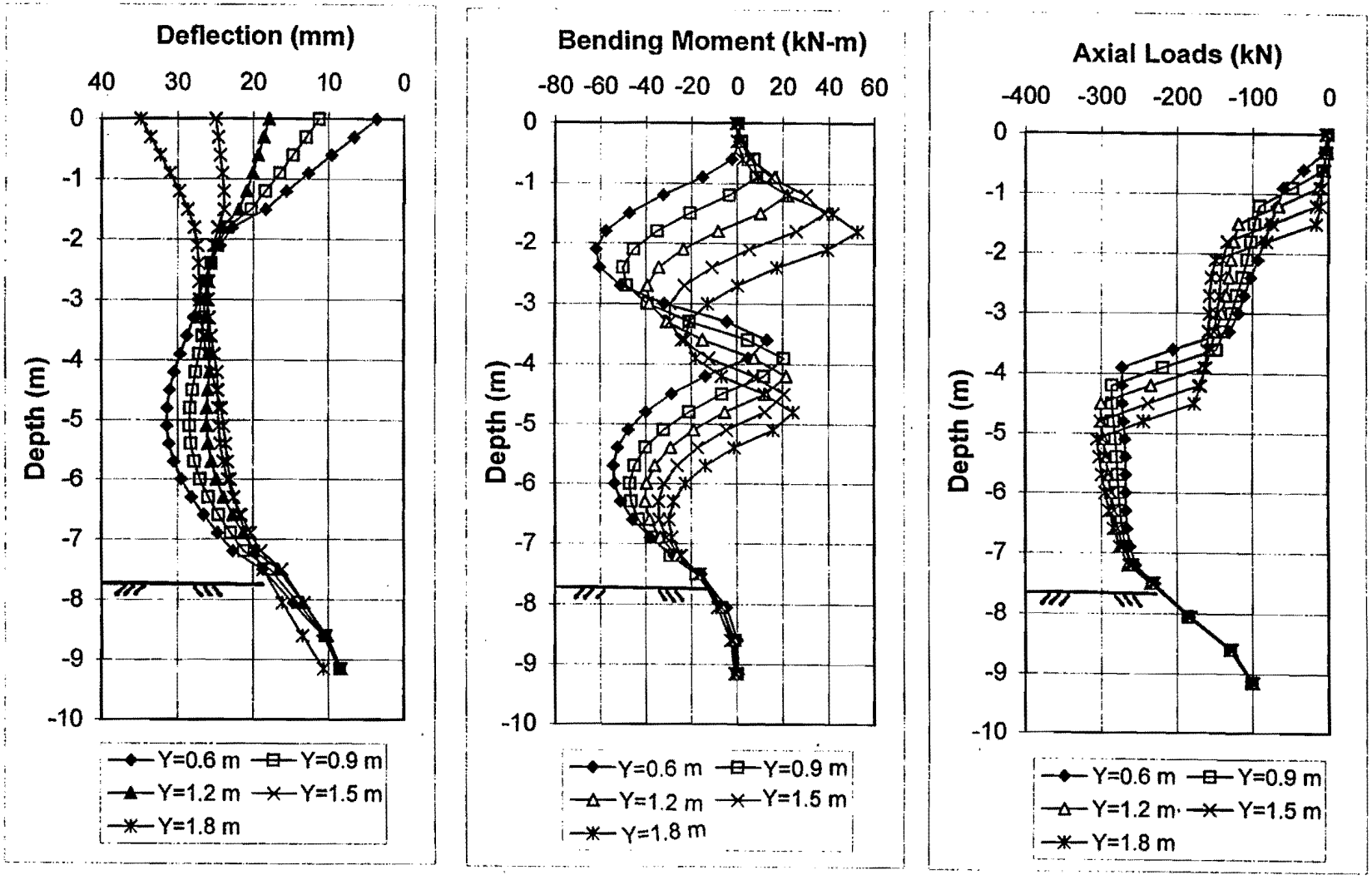

Figure 94. Influence of First Anchor Location

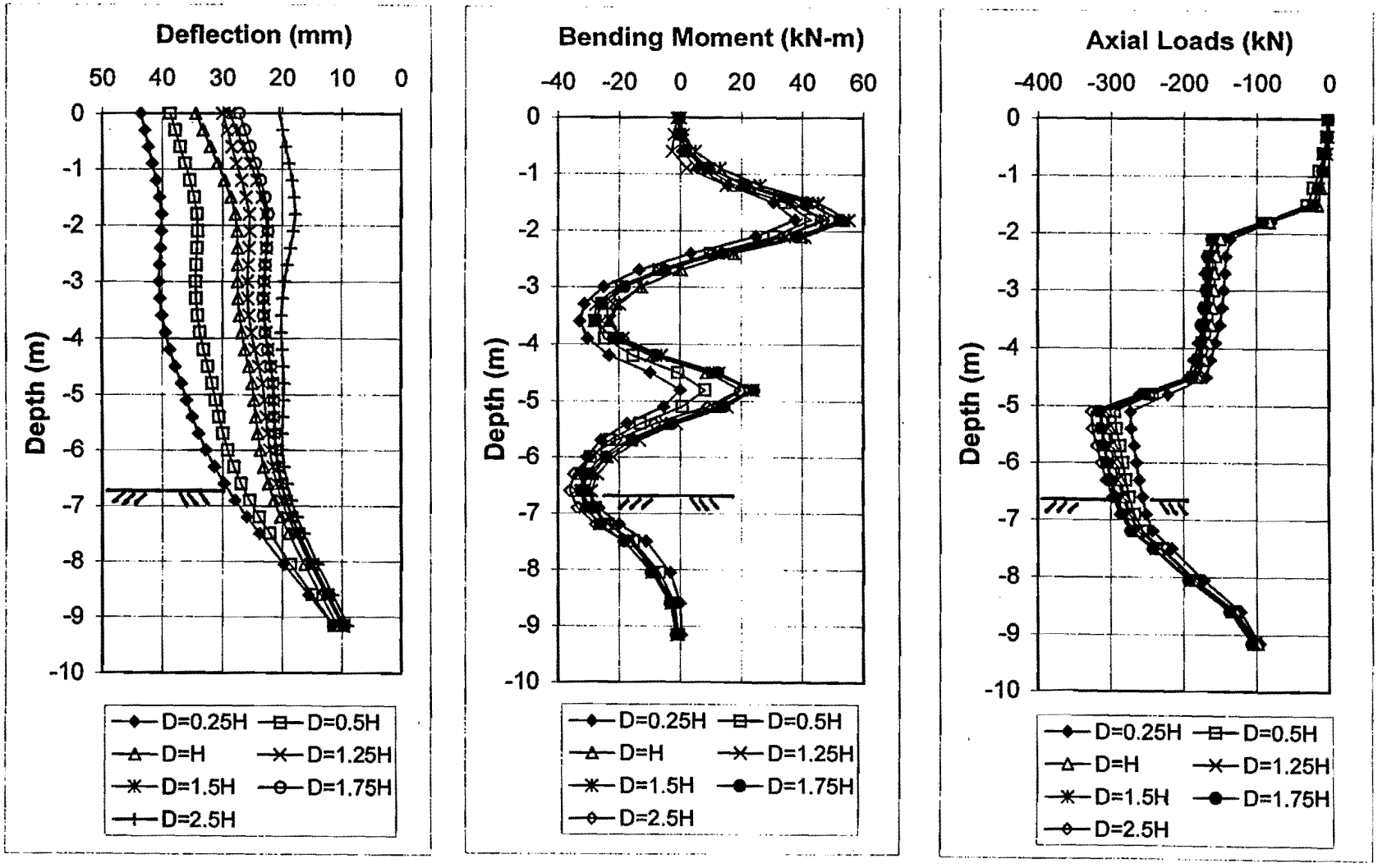

Figure 95. Influence of Tendon Unbonded Length

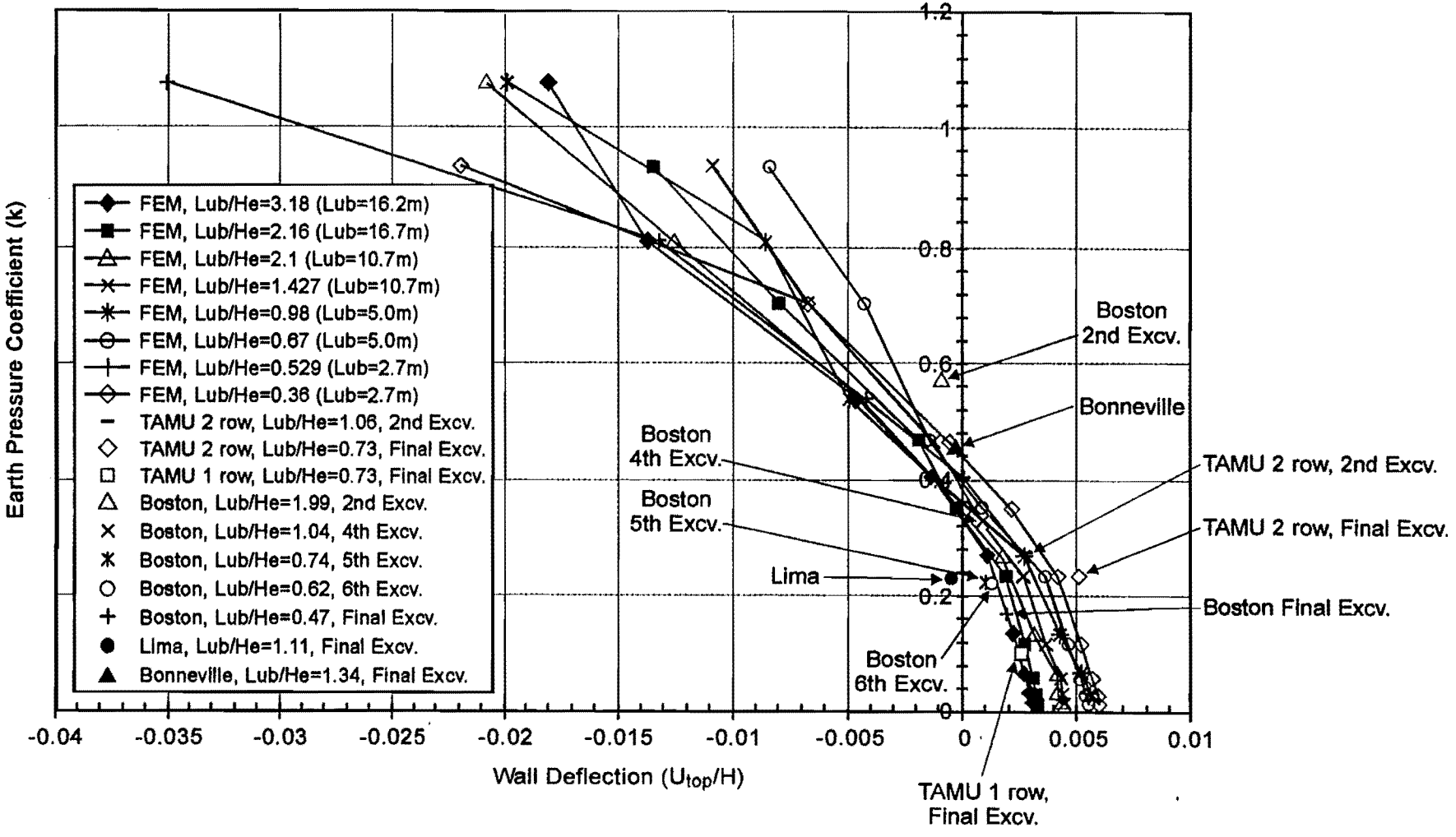

Figure 96. Influence of Anchor Force on the Top Wall Deflection

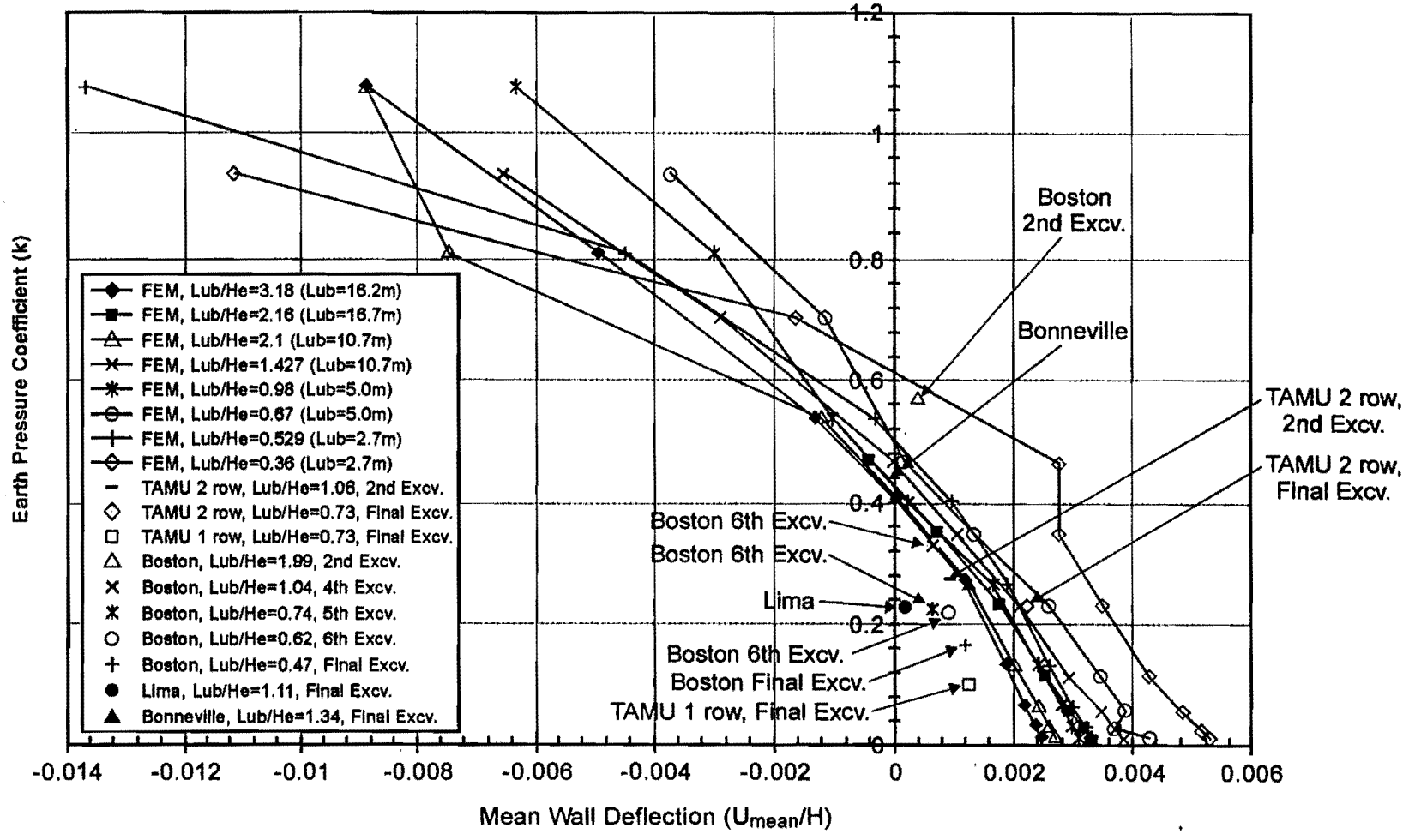

Figure 97. Influence of Anchor Force on the Mean Wall Deflection

0.65 K_a used in design, the ratio (u_{top} / H_t) varies from 1/500 to 1/225 depending on a number of factors including L_u. For the same value of K, the ratio (u_{mean} / H_t) varies from 1/1000 to 1/300. The figures also show that for K values of about 0.4, the deflections are close to zero and that for K values higher than 0.4, the wall moves inward.

The embedment of the soldier piles was varied from 0 m to 10 m. The results show that u_{top} decreases with increasing embedment (Figure 98), that the bending moment profile does not change significantly, but that the downdrag load increases significantly with increasing embedment.

The modulus of the wood-lagging E_{wood} was varied. With the E_{wood} value equal to the wood modulus, the wooden boards bow between the soldier piles and the center of the wooden boards deflects more than the piles. As E_{wood} increases, the boards become more rigid and the boards and soldier piles tend toward a common deflection; as a result the piles deflection increases. The bending moment also increases but the axial load is relatively unaffected. Varying the stiffness of the soldier piles has only a small influence on the deflections, bending moments, and axial loads.

2.5 RECOMMENDATIONS

2.5.1 Laboratory Testing

The following recommendations are based on 34 Constant Rate of Displacement triaxial tests (CRD) and 12 Constant Load Increment triaxial tests (CLI).

1. The Constant Load Increment (CLI) triaxial tests performed on a low plasticity clay led to undrained shear strength and initial stiffnesses which were slightly higher than the ones obtained in Constant Rate of Displacement (CRD) triaxial tests. This is an indication that it is somewhat conservative to use CRD tests for predicting the behavior of anchors which are usually subjected to CLI tests.

2. The power law model ($s/s_1 = (t/t_1)^n$) where s and s_1 are the displacements after a time t and t_1 respectively fits the triaxial CLI test data well and the exponent n increases linearly with the stress level in the sample. This is one more indication that this model can be used to predict the long-term movements in soils. At zero stress level the n value is zero while at failure the n value generally varies from 0.02 for stiff clays to 0.08 for soft clays, and from 0.01 for dense sands to 0.03 for loose sands.

3. A delayed failure occurred in some CLI triaxial tests when the stress level was above a delayed failure threshold. This threshold seems to be equal to the yield stress of the soil.

2.5.2 Field Testing of Anchors

The following observations are based on the load testing of 10 full-scale low pressure grouted anchors in a stiff to very stiff clay and on the analysis of the results. The anchors were 0.3 m in diameter and 13.8 m long, were installed dry with a hollow stem auger, and were grouted under 0.7 MPa of pressure.

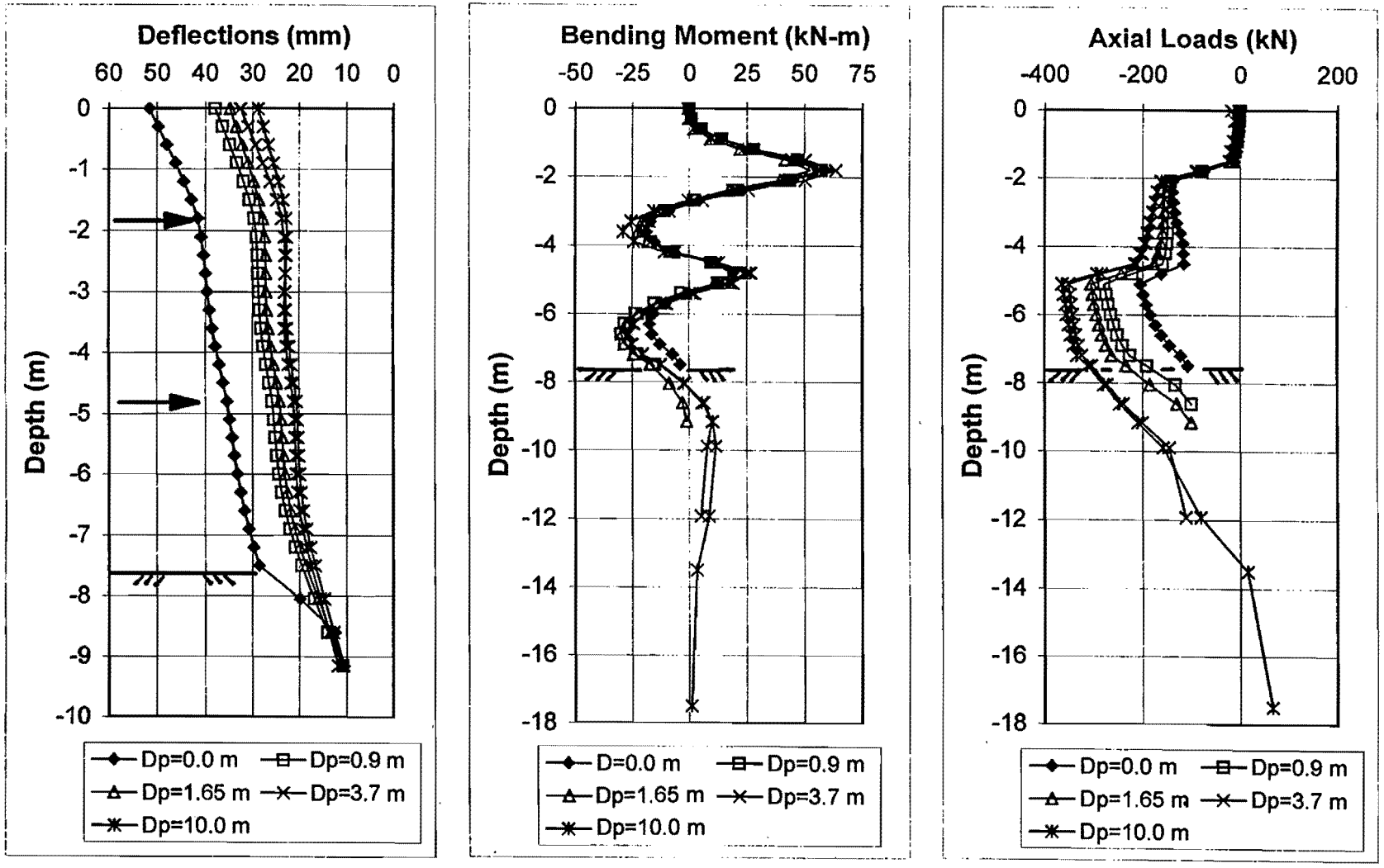

Figure 98. Influence of Soldier Pile Embedment

1. The load distribution in the anchor is illustrated for the three elements involved: soil, grout, and steel tendon. At working loads, it shows that stresses in the soil are concentrated near the boundary between the bonded and the unbonded zone.

2. In the very stiff clay, the shear strength of the soil-grout interface f_{max} (kPa) averaged over the length of each anchor was related to the average soil properties by the following relationships:

$$\frac{f_{max}}{s_u} = 0.52, \quad \frac{f_{max}}{q_c} = 0.016, \quad \frac{f_{max}}{p_L} = 0.043, \quad \frac{f_{max}}{N} = 2.9$$

3. The ultimate soil resistance Q_u was found to be 23% larger for the anchors with a short bonded length (4.6 m) than for the anchors with a long bonded length (9.2 m).

4. The anchor failure load Q_f corresponding to a creep rate of 2 mm per log cycle of time was found to be equal to 0.86 times the soil ultimate load Q_u on the average.

5. The creep load threshold Q_t corresponding to the load at which the creep movement starts to accumulate much faster was clearly defined in most cases and corresponded to 0.7 times the soil ultimate load Q_u on the average.

6. Since the anchor design load Q_d is at most equal to 0.75 times Q_f, the following minimum factors of safety exists against Q_t, Q_f, and Q_u.

$$Q_d \leq \frac{Q_u}{1.54} = \frac{Q_f}{1.33} = \frac{Q_t}{1.09}$$

7. The creep movement at the design load Q_d was 2.8 times less for the anchors with the short tendon bond length (4.6 m) than for the anchors with the long tendon bond length (9.6 m).

8. The creep rate under the design load averaged 0.9 mm and 0.22 mm per log cycle of time for the anchors with the long and short tendon bond lengths respectively. This corresponds to 6.9 mm and 1.7 mm in 100 years.

9. The creep rate decreased drastically upon reloading. A typical case would be 0.2 mm per log cycle of time for the first loading and 0.1 mm per log cycle of time for the reloading. Retesting using the same creep failure rate should not be allowed until the load-history effects are better understood.

10. It was found that the current creep model which consists of a straight line on a creep movement vs. log time plot fits the data well only for loads between 50% and 80% of the

ultimate load Q_u. This range, however, covers the range of test loads and lock-off loads for most anchors.

11. The load loss of four anchors locked-off for 70 days at a load Q equal to about one-half Q_u averaged 0.9% of Q per log cycle of time. This corresponds to less than 7% of Q in 100 years.

12. For the same overall length the grouted anchors with a short tendon bond length had the following advantages over the grouted anchors with a long tendon bond length: higher ultimate load, lower creep rate, brings the soil stresses back further away from the wall, and lower time-dependent load loss. For tieback walls, it is essential to ensure that the anchor bond length L_a is adequate (Equation 2 and Figure 99) to support design and proof test loads without transferring axial force into the active failure zone. This study seems to indicate that, given L_a, the tendon bond length L_b should be as short as required to safely transfer the load from the steel tendon to the grout column (Figure 99). Further testing to evaluate these findings would be valuable.

13 The minimum required tendon bond length L_6 is usually not calculated in practice so that no guidelines exist for those calculations. Instead, minimum recommended values of L_6 are used. For common cases, those minimum values are 3 m to 4.5 m for bar tendons and 4.5 m to 6 m for strand tendons.

14. The power law model $(s/s_1 = (t/t_1)^n)$ where s and s_1 are the total displacements at the anchor head after a time t and t_1 respectively for the anchor load test data well. For the anchors tested, the n values typically range from 0.002 to 0.015 with the lower values applying to the anchors with a short tendon bond length.

2.5.3 Long-Term Observation on NEGS-TAMU Tieback Wall

1. Over a period of five years the percent increase in deflection at the top of the wall was between 0% and 37% and averaged 18.5% for the beams located away from the anchors which were released.

2. The deflection at the top of the wall after construction (July 1991) varied between 20 mm and 35 mm averaging 27 mm. The deflection at the top of the wall five years later varied between 28 mm and 48 mm and averaged 34 mm. The power law model $(s/s_1 = (t/t_1)^n)$ where s and s_1 are the deflections at the top of the wall after a time t and t_1 respectively seems to fit the data reasonably well. The n values however are closer to the ones obtained in soils tests (triaxial test, pressurementer test) than those obtained in anchor load tests.

3. The horizontal deflection profile of the wall seems to be made of two components: the horizontal deflection profile of the wall due to the soil pressure behind it and the horizontal deflection profile of the wall due to a general rotation of the anchor-soldier beam system. This rotation takes place when the soldier beam settles and the anchor-

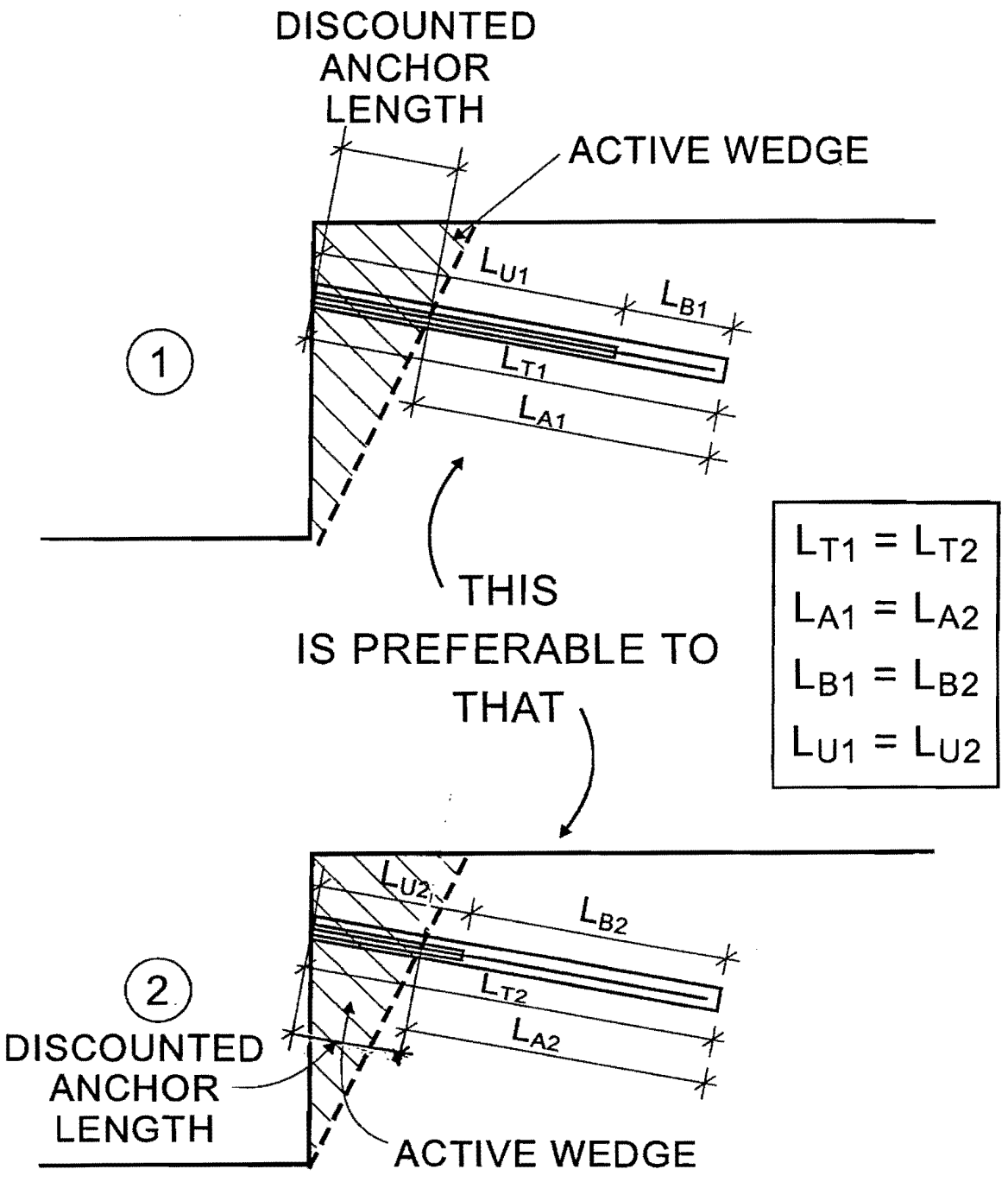

Figure 99. Grouted Anchors Should Have Short Tendon Bond Length

soldier beam system rotates around the anchor tendon bond length. The settlement of the soldier beam is due to the downdrag imposed by the soil on the wall facing. A soldier beam rotation of only 1° can lead to a horizontal top deflection of 131 mm for a 7.5 m high wall. Therefore in order to limit the horizontal deflection due to rotation, it is important to design soldier beams which can resist the downdrag load without much settlement.

4. The maximum positive bending moments M_{mp} (backside in tension) occur at the anchor locations. Over the five-year period, M_{mp} decreased significantly in all instances except one where the anchor load after having been decreased, increased over time. As an example, the decrease in M_{mp} averaged 29% over five years for the section of the one row anchor wall where no anchor was released.

5. The maximum negative bending moments M_{mn} occur between anchor loactions or between the last anchor and the excavation level. Over the five-year period, M_{mn} increased by an amount similar to the decrease M_{mp}. In essence the bending moment profile shifted towards the negative bending moments.

6. Over the five-year period, the anchor load for the anchors located away from the anchors which were released changed very little (± 10%). The load on the anchors which were released to about 30% of their lock-off load, increased over the five-year period back to about 55% of that lock-off load while the load on adjacent anchors tended to decrease.

7. The minimum axial load induced by the downdrag of the soil and the vertical component of the anchor force stayed about the same for the beams where the anchor force was not released, but increased somewhat for the beam where the anchor load was released.

2.5.4 FEM Simulation of Tieback Walls

The following observations and recommendations are based on the data from four case histories, on a detailed three dimensional nonlinear Finite Element Method simulation of one of the case histories and on an extensive FEM parametric analysis. The application of these recommendations is limited by the range of parameters studied.

1. The best position for the first anchor appears to be between 1.2 m and 1.5 m below the top of the wall. In current practice the first anchor tends to be placed deeper than that; significant deflections can accumulate during this step and it is very difficult to eliminate them by further construction. By comparison in soil nailing, the first nail is placed at a much shallower depth. A vertical spacing of 3 m between anchor rows below the first anchor appears to work well.

2. The length of the unbonded length proposed by Cheney (1988) seems to work well. Longer unbonded zones particularly for the first anchor lead to somewhat smaller deflections.

3. The magnitude of the anchor loads is the most important factor influencing all variables. It has a direct influence on deflections and bending moments. In the case of mechanically stabilized earth walls and soil nailed walls, deflections are largely uncontrolled. In the case of tieback walls, the engineer can now use the proposed K vs. (U_{top} / H_t) relationship to select anchor loads which will approximately generate a chosen deflection. Zero deflection can be reached for a constant pressure diagram with a pressure intensity equal to $0.4\gamma H_t$. This pressure is approximately two times larger than Terzaghi and Peck intensity of $0.65 K_a \gamma H$.

4. Providing no embedment for the soldier piles is not recommended even if bottom heave and slope stability are not a problem. No embedment leads to larger deflection. An embedment of 1.5 m decreased the top deflection significantly in this study.

3. CORROSION ISSUES

3.1 BACKGROUND AND FUNDAMENTALS OF CORROSION

This portion of the report describes findings regarding the corrosion of permanent ground anchors. It includes a discussion of the mechanisms of corrosion, current protection systems used for ground anchors, and a series of laboratory tests performed to establish a direct correlation between the corrosion rate and various soil characteristics.

3.1.1 Aqueous Corrosion

Corrosion is defined as the deterioration or destruction of a material caused by reaction with its environment, which, for metals is generally an electrochemical reaction. The discussion is focused on the corrosion of metals, although corrosion in general can be noted in a wide variety of materials, including ceramics, plastics, and composite materials.

Corrosion in metals occurs when the overall free energy of the system is lowered. For most metals of engineering interest, the thermodynamically stable condition is for the metal to exist in a nonmetallic (oxide, sulfide, etc.) form. An example is rust, a corrosion product that forms on steel under atmospheric conditions, which is thermodynamically more stable than the steel. Table 11 (Jones, 1996) lists the standard potentials (EMFs) for common metals and cathodic reactions. The active metals are toward the bottom of the table, while the more noble metals are towards the top of the table. For example, in a deaerated acidic environment, under standard conditions, all of the metals below hydrogen will tend to dissolve, while those above hydrogen will not dissolve. This table is for equilibrium conditions and does not indicate anything about the kinetics of a particular reaction.

For aqueous corrosion to occur, there are three requirements: 1. Potential difference, 2. Electrolyte, and 3. Connecting path (Fontana, 1986). An example of this is given in Figure 100. The potential difference enables an anode and cathode to develop. They can be two separate pieces of metal or the anode and cathode may develop on the same piece of metal. The larger the potential difference, the greater the driving force, and for many systems a higher corresponding corrosion rate. However, this may not necessarily be true because of the importance of kinetic factors, which the potentials do not take into consideration. This will be discussed later. The electrolyte is a solution that contains ions. Seawater, for example, is an excellent electrolyte, while fresh oil would not be considered an electrolyte because of its lack of ions. The connecting path allows the current to flow and complete the circuit. At the anode, oxidation takes place and electrons are given off, while at the cathode, reduction takes place and electrons are consumed. The connecting path may be a physical wire connecting the anode and cathode or it may be a single material that uses its internal structure as the connecting path.

In the case of iron, when refined iron or steel is exposed to a moist oxygen-rich environment, the iron oxidizes and the oxygen in the air supports the cathodic reaction (Uhlig and Revie, 1985). The result of this exchange is hydrated iron oxide, commonly known as rust. If the iron is exposed for a long enough period of time, it deteriorates into a component which no longer has the original

Table 11. Standard Table of EMFs (Jones, 1996)

	Reaction	Standard Potential, e° (volts vs. SHE)
Noble	$Au^{2+} + 3e^- = Au$	+1.498
	$Cl_2 + 2e^- = 2Cl^-$	+1.358
	$O_2 + 4H^+ + 4c^- = 2H_2O$ (pH 0)	+1.229
	$Pt^{2+} + 3e^- = Pt$	+1.118
	$NO^- + 4H^+ + 3e^- = NO + 2H_2O$	+0.957
	$O_2 + 2H_2O + 4e^- = 4OH^-$ (pH 7)*a*	+0.82
	$Ag^+ + e^- = Ag$	+0.799
	$Hg_2^{2+} + 2e^- = 2Hg$	+0.799
	$Fe^{1+} + e^- = Fe^{2+}$	+0.771
	$O_2 + 2H_2O + 4c^- = 4OH^-$ (pH 14)	+0.401
	$Cu^{2+} + 2e^- = Cu$	+0.342
	$Sn^{1+} + 2e^- = Sn^{2+}$	+0.15
	$2H^- + 2c^- = H_2$	0.000
	$Pb^{2+} + 2e^- = Pb$	-0.126
	$Sn^{2+} + 2e^- = Sn$	-0.138
	$Ni^{2+} + 2e^- = Ni$	-0.250
	$Co^{2+} + 2e^- = Co$	-0.277
	$Cd^{2+} + 2e^- = Cd$	-0.403
	$2H_2O + 2e^- = H_2 + 2OH^-$ (pH 7)[2]	-0.413
	$Fe^{2+} + 2e^- = Fe$	-0.447
	$Cr^{1+} + 3e^- = Cr$	-0.744
	$Zn^{2+} + 2e^- = Zn$	-0.762
	$2H_2O + 2e^- = H_2 + 20H^-$ (pH 14)	-0.828
	$Al^{3+} + 3e^- = Al$	-1.662
	$Mg^{2+} + 2e^- = Mg$	-2.372
	$Na^+ + e^- = Na$	-2.71
Active	$K^+ + e^- = K$	-2.931

° Not a standard state but included for reference.
Source: *Handbook of Chemistry and Physics*, 71st ed., CRC Press, 1991.

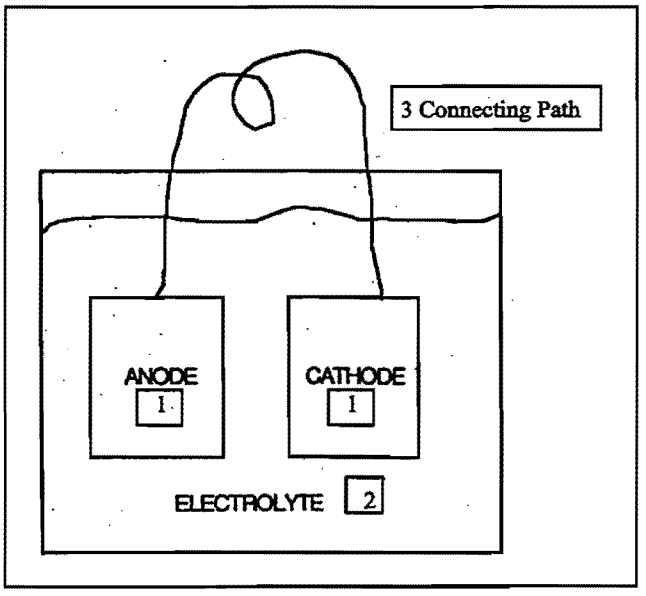

Figure 100. Schematic Representation of the Corrosion Process

material's desirable physical and mechanical properties, and failure may occur. The rate of the corrosion, which is often tabulated as mils per year of penetration (mpy), is dependent upon the type of corrosion occurring, factors in the environment, and the materials involved. The following paragraphs will discuss in more detail the various anodic and cathodic reactions, corrosion rates, and different types of corrosion.

3.1.1.1 Thermodynamics

The majority of metals are thermodynamically unstable at room temperature and atmospheric pressure. That is, pure Fe and Al, are not in their state of lowest free energy (Uhlig and Revie, 1985; Fontana, 1986; *Corrosion*, 1987). Energetically, they would prefer to be oxides or some other compound. It requires energy to win (separate) metals from their ores, and it requires care to use them successfully in their pure or alloyed state. Although much useful information can be obtained from thermodynamics, there is no kinetic information contained in equilibrium thermodynamics. Thermodynamics will tell us whether a reaction may proceed in one direction or the other, but thermodynamics provides no information about the rate of the reaction. See Example 1 where the standard state free energy is given for the reaction of Mg, Cu, and Au in aerated H_2O. The Mg and Cu reactions are thermodynamically able to proceed, while the Au reaction is not. In fact, Cu is considered corrosion resistant under atmospheric conditions. The architecturally attractive green patina that forms on the surface protects the copper from further atmospheric corrosion occurring.

Example 1. Thermodynamics

$$Mg + H_2O(l) + \tfrac{1}{2}\, O_2(g) \rightarrow Mg(OH)_2(s)$$
$$\Delta G^\circ = -598 \text{ kJ/mol}$$

$$Cu + H_2O(l) + \tfrac{1}{2}\, O_2(g) \rightarrow Cu(OH)_2(s)$$
$$\Delta G^\circ = -120 \text{ kJ/mol}$$

$$Au + H_2O(l) + \tfrac{3}{4}\, O_2(g) \rightarrow Au(OH)_3(s)$$
$$\Delta G^\circ = +66 \text{ kJ/mol}$$

The free energy is linked to the EMF through the relationship given below:

$$\Delta G^\circ = -nFE^\circ \tag{32}$$

where,

ΔG° is the Gibb's free energy in the standard state,
n is the number of electrons,
F is Faraday's constant (96 500 C/mol), and
E° is the standard state EMF in volts.

Nernst showed that the electrochemical potential of a cell could be ascribed to E° and the activities of the chemical species involved in the cell reaction (Uhlig and Revie, 1985; Fontana, 1986). The Nernst equation is given below:

$$E = E^{\circ} - (RT/nF)\,[\ln (a_{products}/a_{reactants})] \qquad (33)$$

where,

R is the gas constant,
T is the temperature (K), and
a's are the activities.

The results from the Nernst equation can be summarized in a Pourbaix diagram as shown in Figure 101 for Fe (Pourbaix, 1973). The two dashed lines on the diagram labelled a and b correspond to the evolution of H_2 and O_2 respectively. Between those lines water is stable. Since the Pourbaix diagram represents thermodynamic data, there is no kinetic information available. However, it certainly can indicate the likely phases present under various environmental conditions. For example in Figure 101, there is a broad range where Fe is immune below -650 mV (SHE) and between a pH of -2 to about 9. Similarly for potentials more positive than -600 mV and pH's between -2 and about 7, Fe^{2+} exists as the stable species.

3.1.1.2 Corrosion Reactions

There are several basic corrosion reactions (Uhlig and Revie, 1985; Fontana, 1986). The anodic or oxidation reaction is given below. This dissolution reaction is seldom rate limiting, and therefore, providing additional cathodic reactions that will consume electrons can accelerate the corrosion process.

Anodic dissolution reaction (oxidation):

$$M \longrightarrow M^{n+} + ne^{-}$$

There are five basic cathodic or reduction reactions and these are given below.

(1) Hydrogen reduction in an acid solution:

$$2H^{+} + 2e^{-} \longrightarrow H_2$$

(2) Oxygen reduction in an acid solution:

$$O_2 + 4H^{+} + 4e^{-} \longrightarrow 2H_2O$$

(3) Oxygen reduction in a neutral or basic solution:

Primary reaction

$$O_2 + 2H_2O + 4e^{-} \longrightarrow 4(OH)^{-}$$

Secondary reaction at very negative potentials

$$2H_2O + 2e^{-} \longrightarrow 2(OH)^{-} + H_2$$

(4) Metal ion reduction:

$$M^{n+} + e^{-} \text{ ---> } M^{(n-1)+}$$

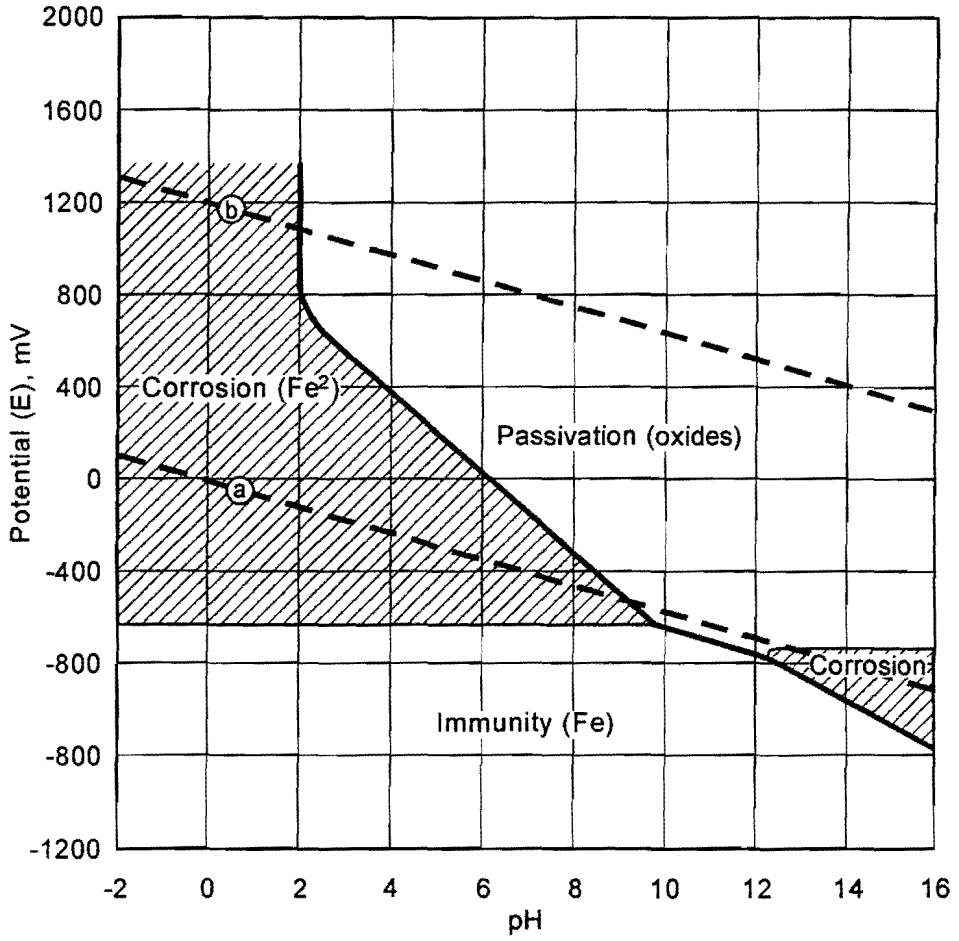

Figure 101. Pourbaix Diagram for Iron (Pourbaix, 1973)

(5) Metal deposition:

$$M^+ + e^- \text{---> } M$$

With these basic reactions, the majority of corrosion situations may be understood. For example, it becomes clear that adding oxygen to a deaerated solution may well increase the overall corrosion reaction. It is possible to have more than one reaction taking place at any given time. For example, in an aerated acid solution, both cathodic reactions 1 and 2 may take place simultaneously. However, depending on the particular circumstance, one reaction may dominate. See D. A. Jones (1996) or M. Fontana's (1986) textbook on corrosion for additional details.

3.1.1.3 Polarization

Under equilibrium conditions the potentials of pure metals are given by the emf series and can be predicted by the Nernst equation for changes in solution concentration and temperature. However, once a metal or an alloy is placed into a solution where corrosion can occur, the system is no longer under equilibrium conditions, and there is a change in the potential as measured at the surface of the metal. This process is called polarization and is what controls the kinetics of corrosion. There are two primary types of polarization: 1) activation or charge transfer, and 2) concentration or mass transport.

For activation polarization, the rate of the process is controlled by the slowest step in some reaction sequence (Uhlig and Revie, 1985; Fontana, 1986; Atkinson and Van Droffelaar, 1982; Jones, 1996). A schematic polarization curve for a system under activation polarization is shown in Figure 102. Under activation polarization the relationship between the voltage and the current can be expressed for the anodic reaction as

$$\Delta\varphi_a = E_{corr} - (E_e)_a = \beta_a \log (i_a / i_{o,a}) \tag{34}$$

For the cathodic reaction, the relationship can be expressed similarly as:

$$\Delta\varphi_c = E_{corr} - (E_e)_c = \beta_c \log (i_c / i_{o,c}) \tag{35}$$

where

φ_a and φ_c are the overpotentials (volts),
β_a and β_c are the Tafel constants,
E_{corr} is the freely corroding potential,
$(E_e)_a$ and $(E_e)_c$ are the equilibrium potentials,
$i_{o,a}$ and $i_{o,c}$ are the exchange current densities, and
i_a and i_c are the measured currents.

The intersection of the two polarization curves gives the freely corroding potential, E_{corr}, and the corrosion current, i_{corr}. At the intersection of the two curves, the total oxidation equals the total reduction. Faraday showed that the current was related to the loss of material and the corrosion rate may be determined from i_{corr} using the following relationship (Uhlig and Revie, 1985; Atkinson and Van Droffelaar, 1982).

$$\text{Corrosion Penetration Rate (mm / y)} = 0.00327\ (k\ i_{corr} / \rho) \qquad (36)$$

$$\text{For mpy (mils / y)} = 0.129\ (k\ i_{corr} / \rho)$$

where

k is the equivalent weight [(At. Wt.) / n],
i_{corr} is the corrosion current density ($\mu A/cm^2$),
ρ is the density (g/cm^3), and
n is the number of electrons.

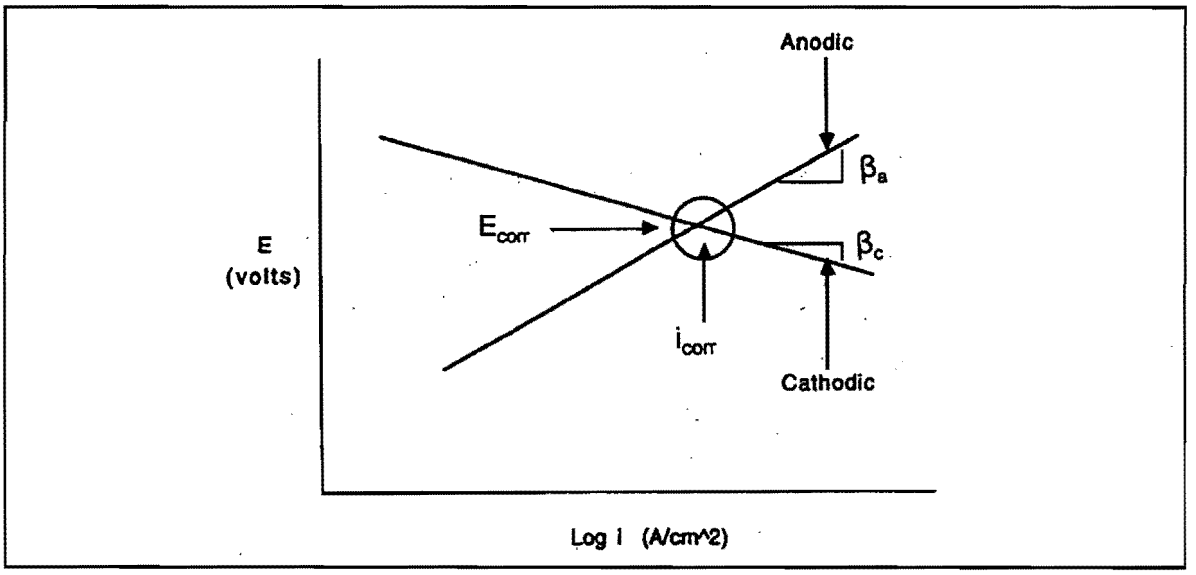

Figure 102. Schematic Representation for Activation or Charge Transfer Polarization

For mass transport or concentration polarization, the cathodic reaction achieves some limiting current density which is a function of the temperature, velocity, and the concentration of the reactive species. Under these conditions, the maximum achievable corrosion rate is given by (Uhlig and Revie, 1985; Fontana, 1986):

$$i_L = (i_{corr})_{max} = n\ F\ D_O\ C_O^b / \delta \qquad (37)$$

where

i_L is called the limiting current density,
D_O is the diffusion coefficient,
C_O^b is the concentration of the reduced species, and
δ is the diffusion distance.

A schematic polarization curve is shown in Figure 103, for an anodic reaction under charge transfer or activation control and a cathodic reaction under mass transport or concentration control. The freely corroding potential and corrosion current are given by the intersection of the two polarization curves.

3.1.1.4 Corrosion Rate Measurements

Through the use of a potentiostat, E_{corr} and i_{corr} can be determined. A schematic for a potentiostatic setup is shown in Figure 104. The potentiostat controls the voltage and measures the current, and from these data potentiodynamic polarization curves may be developed (Atkinson and Van Droffelaar, 1982; EG&G Princeton Applied Research, 1982).

Using a mild steel test specimens, the difference between activation and mass transport control may be demonstrated in concentrated HCl solutions compared to dilute HCl solutions. The corrosion of mild steel in concentrated solutions is controlled by the reduction of hydrogen (activation control), while in the dilute solutions the corrosion is controlled by the reduction of oxygen (mass transport control).

3.1.1.5 Linear Polarization Resistance

Another means of determining the corrosion rate is to measure the linear polarization resistance of the metal or alloy in the solution. This can be performed using the potentiostat, and examining the potential-current relationship within ± 10 or 15 mV of E_{corr}. Consider the encircled region shown in Figure 102. When the data are plotted as voltage vs. current, a straight line exists, as shown in Figure 105. The slope of the line is called the polarization resistance, and can be used to determine the corrosion current. The Stearn-Geary equation is an approximation which shows that i_{corr} is inversely related to the polarization resistance, R_p (Fontana, 1986).

$$i_{corr} = (1/R_p)\,(b_a * b_c) / (2.3)\,(b_a + b_c) \qquad (38)$$

Once i_{corr} has been determined, the corrosion rate may be found from Equation 36.

3.1.1.6 Cathodic/Anodic Reactions

Anodic reactions occur when there is a production of electrons, which creates a more negative immediate locale. Cathodic reactions are the consumption of electrons and result in a more positive site. Conservation of charge will not allow for a net production or consumption of charge in these reactions; thus, at the freely corroding potential, E_{corr}, the cathodic and anodic reactions occur at the same rate, which is determined by the slower of the two reactions. An example of these reactions is illustrated by the reaction of zinc in hydrochloric acid (Fontana, 1986). As shown in Figure 106a, the zinc loses electrons when immersed in the solution, creating positive zinc ions and free electrons: an anodic reaction. At the same instant, the positive hydrogen ions in the solution (Figure 106b) bond with the newly freed electrons and form hydrogen gas on the surface of the zinc. The negative chlorine ions in the solution are not active in the reaction (that is, their presence is not needed for the reaction to occur) and only combine with zinc ions when the solubility limit is exceeded. Using the anodic reaction and the cathodic reaction 1 (Section 3.1.1.2) listed earlier, the overall reactions are as follows:

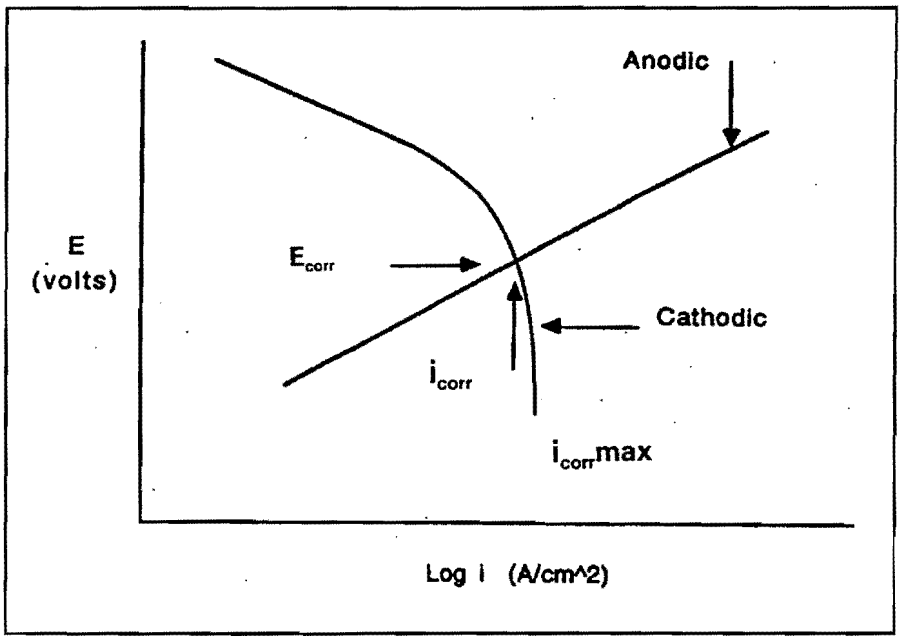

Figure 103. Schematic Polarization Curve Representing Mass Transport or Concentration Polarization

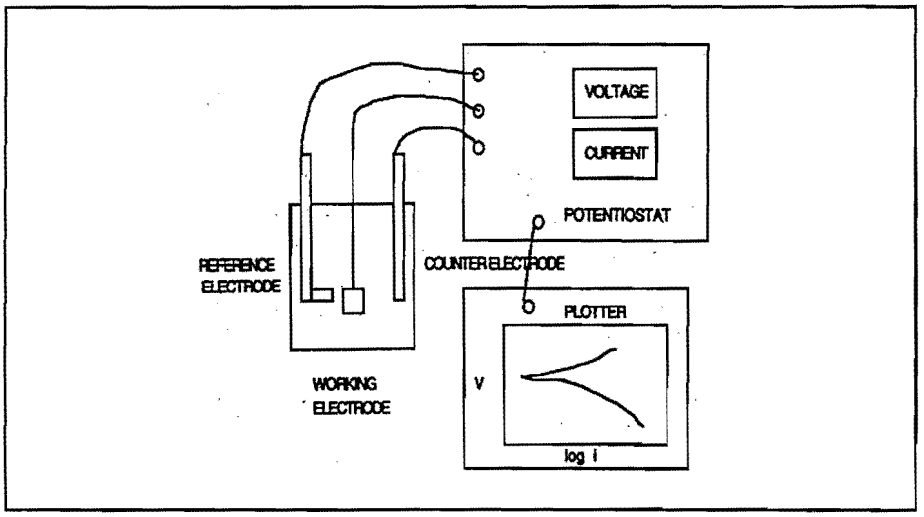

Figure 104. Schematic Representation of the Use of a Potentiostat to Measure Polarization Behavior

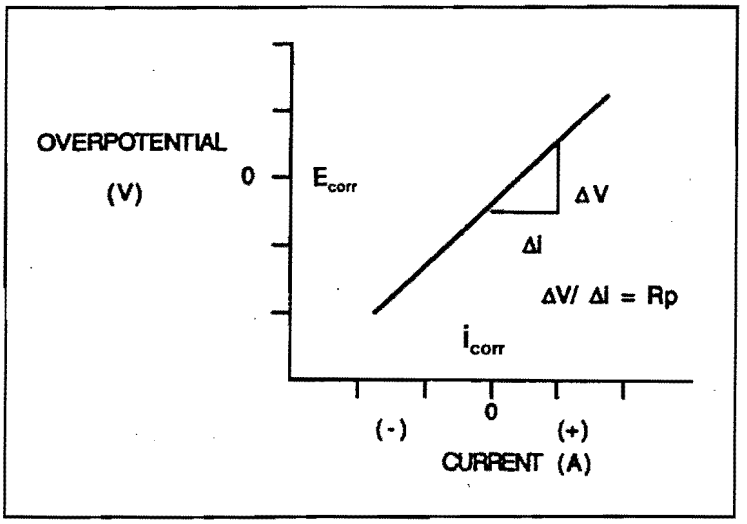

Figure 105. Linear Polarization Resistance

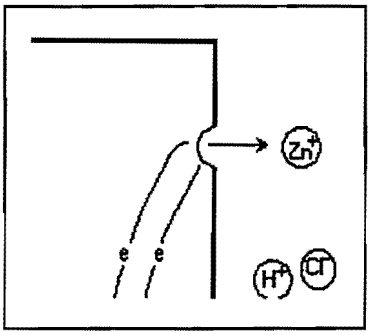

Figure 106a. Anode

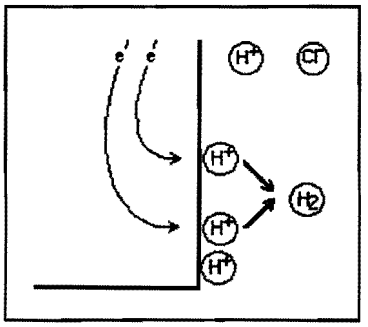

Figure 106b. Cathode

Anodic: $Zn \rightarrow Zn^{+} + 2e^{-}$
Cathodic: $2H^{+} + 2e^{-} \rightarrow H_2$
Overall: $Zn + 2H^{+} \rightarrow Zn^{2+} + H_2$

3.1.1.7 Differential Aeration Cells

The presence of oxygen is one of the key factors in the corrosion of steel, and the concentration of oxygen in the solution directly affects the rate of the metal corrosion. If a structure such as a ground anchor passes through soils of different oxygen concentrations, a cathodic region forms in the metal at the higher concentration while an anodic region forms at an area of lower oxygen concentration (Figure 107). The higher concentration of oxygen at the cathode polarizes that region, and causes the potential to become nobler than the lower oxygen concentration region of the anode. This juxtaposition of the cathode and anode forms a differential aeration corrosion cell. Another example would be for a metal to be partially under a concrete or asphalt roadway or runway.

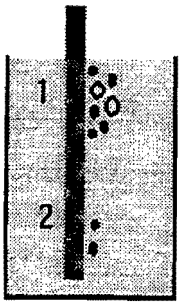

Figure 107. Region 1 Indicates a High Oxygen Concentration (Cathodic Region). Region 2 Indicates a Lower Concentration (Anodic Region).

3.1.1.8 Differential Concentration Cells

Differential concentration cells can form where ionic concentration varies, not just oxygen concentration. An example of such variation can be indicated by pH, since pH is a measure of the concentration of hydrogen ions. If circumstances arise in which one region of soil has an acidic pH, while at a lower depth the pH is basic, the variance of hydrogen concentration creates the macro cell in which one region serves as the cathode and the other as the anode. Although acidic conditions indicated by a low pH are sufficient cause, it should be noted that pH alone is not an exclusive indicator of possible corrosion in soil. Steel passing through different types of soils can result in the development of anodic and cathodic regions. This certainly has been a problem for pipelines that are not cathodically protected.

3.1.2 Types of Corrosion

Corrosion can be broken down into several broad categories. These are uniform, localized, and environmental cracking types of corrosion. Table 12 lists the more specific types that fall into these broad categories.

Table 12. Specific Types of Corrosion

General Category	Specific Type of Corrosion
Uniform	Uniform
	General
Localized	Pitting
	Crevice
	Galvanic
	Intergranular
	Erosion
	Fretting
	Weld Decay
Environmental Cracking	Stress Corrosion Cracking
	Hydrogen Embrittlement
	Hydrogen Attack
	Corrosion Fatigue
	Liquid Metal Embrittlement
Microbiologically Influenced Corrosion	This type can contribute to several of the above types.

3.1.2.1 Uniform Corrosion

Uniform corrosion is the most common form of corrosion. It is caused by electrochemical reactions that proceed uniformly over the entire metal surface. The metal loss due to the uniform corrosion can be estimated by several methods. As uniform corrosion proceeds, the metal becomes thinner and eventually fails by perforation or fracture. For uniform corrosion, the corrosive environment should have the same access to all parts of the metal surface, and the metal itself must be metallurgically and compositionally uniform. For example given a corrosion rate of 5 mpy, then after 20 years of exposure there will be a reduction in thickness of 100 mpy or 0.1 in. Uniform attack can be prevented or reduced by (1) proper coating materials, (2) inhibitors, or (3) cathodic protection (Fontana, 1986). Uniform corrosion is preferred from a technical viewpoint because it is predictable and thus acceptable for design. Yet other forms, particularly localized corrosion, are more insidious and difficult to predict and control.

3.1.2.2 Localized Corrosion

Only the types relevant for ground anchors will be discussed in this section, and that will be pitting, crevice, and galvanic corrosion. One of the major difficulties with localized corrosion is the difficulty in predicting when and where it will occur. Once initiated, it is still difficult to predict the rate of attack and to measure its growth.

3.1.2.2.1 Pitting Corrosion

Pitting is a form of localized attack that aggressively attacks relatively small regions in the metal. The pitting process is random in nature and difficult to predict. Generally, there is a statistical distribution in the depth of pits. Unfortunately, only one deep pit may be sufficient to initiate failure. During the initiation of a pit, the local environment becomes different from the bulk environment, and all of the anodic current gets concentrated in a small or local region. Pitting corrosion is so destructive and insidious that it may cause components to fail suddenly with a small weight loss of the entire structure. It is of particular concern with prestressing steels, such as anchor tendons since they are subjected to high stresses and have small cross sectional areas (Weatherby, 1982). If the reduction in area at a pit continues, it may lead to failure of the stressed member. It is difficult to detect pits and measure them quantitatively due to their small size and the varying depths and numbers of pits. The corrosion rate and lifetime of a component subject to pitting is difficult to predict.

For steels a pit is formed at an area where chloride ions locally weaken the passive film that protects the steel (Figure 108). The anode is established where the passive film is destroyed and the surrounding steel becomes cathode. Also, the presence of Cl^- encourages the hydrolysis process which lowers the local pH within the pit.

Pitting generates small holes in the surface of the metal, often undetectable through the products of corrosion that are produced. The severity of pitting is difficult to detect, even under laboratory conditions, because the weight loss due to corrosion is small. The formation of pits is statistical in nature, and the initiation stage is usually the slowest step in the process. Initiation and

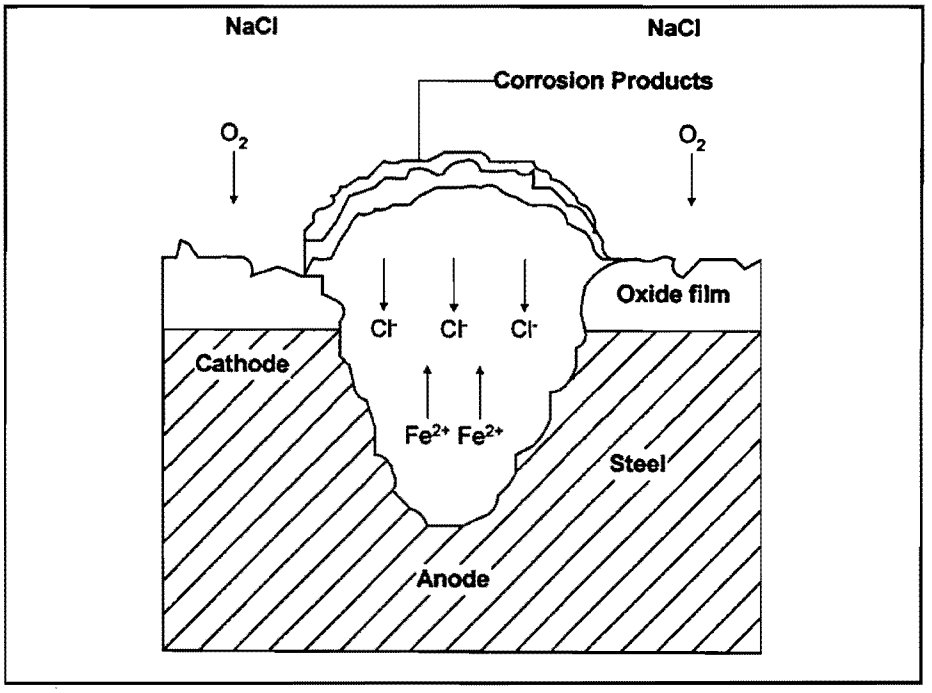

Figure 108. Schematic Model for Pitting and Crevice Corrosion

growth of pits varies, even under identical conditions: days, months, or longer may pass before pitting is detectable on one specimen, while an identical specimen shows signs of pitting in half the time.

3.1.2.2.2 Crevice Corrosion

Crevice corrosion is another form of localized corrosion that is important. This is similar to pitting corrosion except that it lacks the statistical nature of pitting. Crevices provide a location where the corrosion may initiate. Bolt heads, flanges, rivets, washers, and deposits are some of the locations that provide a site for crevice corrosion. The crevice needs to be thin enough that the solution can become stagnant. When this results, it is possible for the local environment within the crevice to become more acidic. The corrosion initiates within the crevice where the anodic reaction continues. The cathodic reaction initially occurs within the crevice but, as the cathodic species is consumed, the cathodic reaction continues outside of the crevice and, in fact, protects that area from corrosion. The process once initiated is similar to that shown in Figure 108. Crevice corrosion is tougher on alloys that pitting because of the crevice. Even though an alloy is resistant to pitting, it may not be resistant to crevice corrosion. If an alloy is resistant to crevice corrosion, it will be resistant to the formation of pits.

Crevice corrosion can be modeled with two steps: initiation and propagation. Even with the presence of the crevice the initiation stage is the slowest step in the process. However, since the corrosion occurs in a covered location, it is difficult to observe and locate. As in pitting corrosion, there is not much metal lost due to the corrosion. Crevice corrosion can be the initial step in a failure sequence that may lead to attack by some form of environmental cracking. A particularly aggressive ion is chlorine. The presence of high levels of chlorine can accelerate crevice corrosion. There are

several locations in ground anchors that could be susceptible to the effects of crevice corrosion. These would be the grout steel bond, the anchor head region, and portions of the unbonded regions.

3.1.2.3 Galvanic Corrosion

When two dissimilar alloys are coupled in the presence of a corrosive electrolyte one of them is preferentially corroded while the other is protected from corrosion due to the potential difference. Any alloy (anodic) will be preferentially corroded when coupled to another alloy with a more noble potential in the Galvanic Series. At the same time, the nobler alloy (cathodic) is protected from corrosion. One desirable form of galvanic corrosion is in the form of a dry cell or battery. In this situation, the corrosion of the anode supplies the current that is drained from the battery. An example of a carbon-zinc dry cell is shown in Figure 109. Another application of galvanic corrosion is in the process of cathodic protection where a more active metal is coupled with a less active metal. The more active metal corrodes, while the less active metal is protected from corrosion. An example of this is galvanized steel, which is steel with a layer of zinc on the outside. The zinc corrodes and protects the steel.

Another good example of this type of corrosion involves riveted copper and steel plates (Fontana, 1986). The copper plates are joined by steel rivets, while the steel plates use copper rivets. The plates are then submersed into seawater for an extended period of time. Compared to steel, copper is more noble than steel in seawater, thus steel is the anode and copper is the cathode. As the seawater attempts to corrode the copper plates, the copper draws the necessary electrons from the steel, causing the steel to corrode faster. In the case of the steel plates (copper rivets), the copper has a substantially smaller surface area and requires fewer electrons to remain protected. Therefore, although the steel is still anodic with respect to the copper, the small size of the cathodic area compared to the large size of the anodic area means that there will not be much corrosion of the steel. However, in the case of the copper plates (steel rivets) the copper has a large area compared to the steel. In this case, the copper must draw a large number of electrons from the steel to preserve its state. As a result, the steel corrodes at an extremely accelerated rate. After 15 months the steel rivets were completely corroded. For galvanic corrosion, it is poor practice to have a large cathodic area and a small anodic area.

3.1.2.4 Environmentally Induced Cracking

Environmentally induced cracking is defined as brittle fracture of a ductile material due to the effect of the corrosive environment (*Corrosion*, 1987). It includes stress corrosion cracking (scc), corrosion fatigue cracking (cf), and hydrogen embrittlement (he).

3.1.2.4.1 Stress Corrosion Cracking

Stress corrosion cracking occurs in alloys under tension in the presence of a specific corrosive medium. Generally, scc occurs in metals in environments where the metal is almost corrosion resistant. As Figure 110 indicates, scc (crosshatched region) requires a susceptible material, a specific environment, and a tensile stress. Type 304 and 316 austenitic stainless steels are susceptible to scc in the presence of warm Cl^- containing water and a tensile stress.

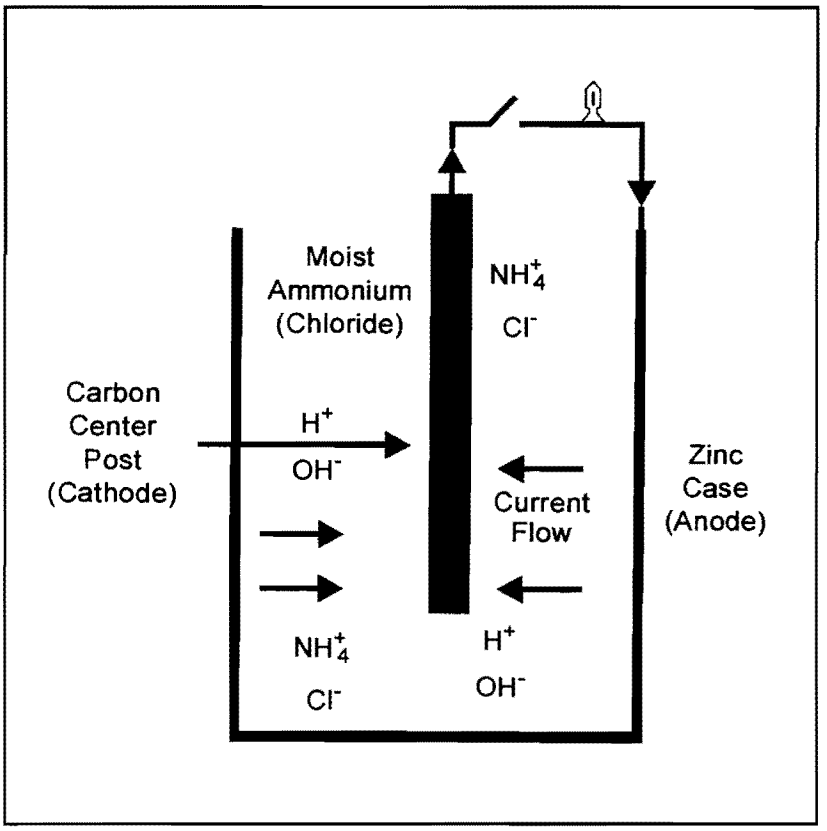

Figure 109. Carbon-Zinc Dry Cell

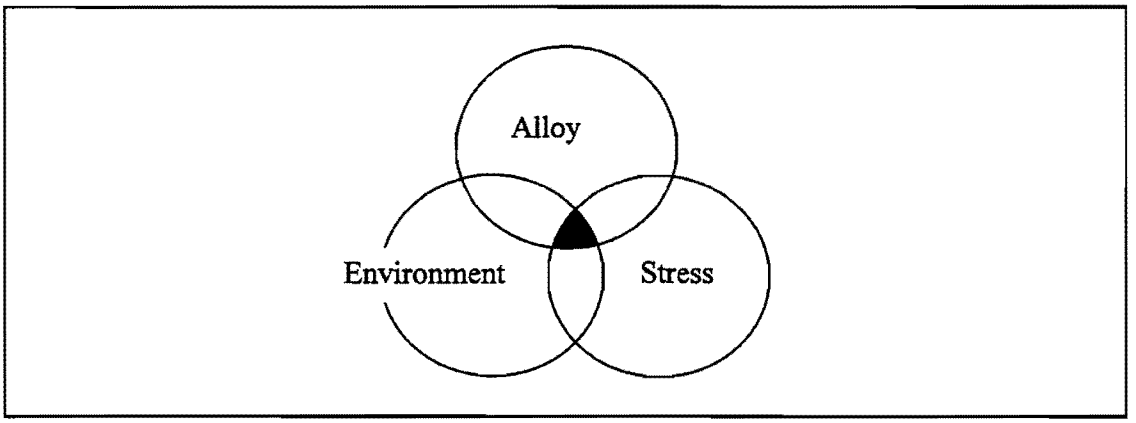

Figure 110. Intersection of Three Requirements for Stress Corrosion Cracking

This cracking is an anodic corrosion process with the crack developing at anodic sites. The initiation site is often a pit or crevice that has formed. During stress-corrosion cracking, the metal is virtually unattacked over the surface, while fine cracks propagate through it. The cracking phenomenon has serious consequences because it can occur at stresses within the range of typical design stress. Therefore, it is important to examine a wide range of tensile stresses and environments in studying stress corrosion cracking behavior. The initiation stage is generally the slowest step in the process, and a pit or crevice can shorten the time for initiation. SCC may be of concern for ground anchors because of the high stress levels and the possibility of developing some form of localized corrosion.

3.1.2.4.2 Corrosion Fatigue

Corrosion fatigue cracking occurs under repeated cyclic stresses in a corrosive environment. In general fatigue failures occur at stress levels below the yield point and after many cyclic applications of this stress. This type of environmental cracking is probably not as critical for permanent ground anchors as the others because of the difficulty in having an anchor loaded cyclically.

3.1.2.4.3 Hydrogen Embrittlement or Cracking

Hydrogen-induced cracking or embrittlement results from the diffusion of hydrogen into the alloy, where it interacts with different defect sites and may induce cracking. The source of the hydrogen that enters the lattice makes no difference. During the hydrogen evolution reaction, atomic hydrogen may be produced at the surface during corrosion and, if conditions are right, the hydrogen may enter the lattice. Atomic hydrogen diffuses easily in steel at room temperature, and often the hydrogen will collect at defects, inclusions, and grain boundaries. The penetration of atomic hydrogen into the metal structure can decrease the ductility and tensile strength of the alloy. There are a variety of mechanisms for producing cracking and failure. As a result of hydrogen embrittlement, high local stresses occur, cracks develop, and brittle fracture results. Hydrogen may be removed from an alloy by a high temperature vacuum anneal. Typically, this type of embrittlement is found in high-strength steels. Many of the early ground anchor failures appear to be hydrogen embrittlement related. This type of failure was avoided when better steels were selected and more careful heat treatments were employed. In addition, hydrogen can attack ductile materials and cause a decrease in an alloy's elongation at failure. Even some austenitic stainless steels (UNS30400) have exhibited decreased ductility in the presence of absorbed hydrogen. Generally, hydrogen-induced cracking is distinguished from stress-corrosion cracking by the interactions with applied currents. Hydrogen-induced cracking is accelerated by the hydrogen evolution reaction, whereas the anodic dissolution process accelerates stress corrosion cracking.

3.1.2.5 Microbiologically Induced Corrosion

Microbiolically induced corrosion (MIC) is an indirect bacterial attack (Pope and Morries, 1995). The most common form of bacteria to participate in this attack is sulfate-reducing bacteria (SRB). Found in anaerobic conditions, such as sulfate bearing clays or organic soils below the water

table, SRB do not attack the metal directly, and in fact pose little threat to the metal itself. However, the by-products of these bacteria can cause serious damage (Pope, 1986). The job of these microbes is to attack sulfate and in the process produce sulfide ions. The sulfide ions slow hydrogen evolution by the cathodic regions and cause acceleration of the dissolution of anodic regions of the metal, creating metal sulfides. By accelerating the dissolution of the anodic regions, the rate of corrosion is increased. Other types of corrosion-inducing bacteria include sulfur oxidizing and iron bacteria (Fontana, 1986). However, the conditions for the presence of these two later bacteria are currently beyond the guidelines for soils supported by tieback anchors.

MIC may not lead to failure, but it can provide a starting point for localized corrosion where the time for initiation is shortened because of the effect of the bacteria. In principle, the ground anchors would be protected from bacteria by the grout or other coating that may be in place.

3.2 SURVEY OF FAILURES

Permanent tieback anchors have been installed routinely since the 1960s and they have performed well in a variety of environments. The majority of these tiebacks used cement grout for protection over their anchor length. It is reported that where the tendon is encased in cement grout, there is no evidence of a failure of tieback anchor. The following are nine cases of anchor failures reported by Nernberger (1980).

3.2.1 Case Histories Reported by Nernberger (1980)

3.2.1.1 Case 1

Forty-two permanent tiebacks were installed in 1959 in West Germany. They were installed in an underground power station. Corrosion protection for the tendon in the unbonded length consisted of a cold applied coating and a wrapping of gauze-like material impregnated with hot bitumen. The anchor head was not protected from corrosion. The steel was stressed to 1,068 N/mm^2 at lock-off. It was postulated that bending and tension caused the tendon to be stressed above its ultimate strength in the region near the anchor head.

Ten months after lock-off, it was discovered that 17 tendons were broken, 10 were probably broken, eight were damaged, and seven were still functioning. All the tendons broke within the unbonded length with 30% breaking at the anchor head, and 43% breaking within 500 mm of the anchor head. The report concluded that the failure was due to localized corrosion, which led to the formation of stress cracks.

3.2.1.2 Case 2

Tiebacks were installed along the Rhine River in Germany. These tiebacks were installed using 8 mm wires having an ultimate strength of 1,470 MPa. The tendons were encased with grout. After a few years, three tiebacks failed. Eighty-five percent of the ruptured wires failed in the vicinity of the anchor head. In this area only a thin coating of grout covered the tendons. It was assumed that failure was caused by stress corrosion cracking due to groundwater containing

industrial pollutants. Insufficient grout coverage near the anchor head was given as the primary reason for the initiation of corrosion.

3.2.1.3 Case 3

The tendons were fabricated from 152 mm bars having an ultimate strength of 1372 MPa. The first tendon failed days after lock-off. Other tendons failed between 99 and 100 days. The failure mechanism was postulated to be fatigue failure resulting from bending.

3.2.1.4 Case 4

Failure occurred in the United States in 1971. Here, four tiebacks supporting a sheet pile wall failed six weeks after lock-off. The tendons were fabricated from 32 mm, hot-rolled, drawn, and stress relieved bars. No corrosion protection was provided over the unbonded length of the tendon, which was located in a railway embankment. The soil at the site was acidic and moist in the vicinity of the tendon. Failure of the tendon was postulated to be a result of stress corrosion cracking.

3.2.1.5 Case 5

In this application, temporary tiebacks failed four weeks after lock-off. The tendons had no corrosion protection in the unbonded zone and they were installed in a moist soil with a low pH. Stress corrosion was suspected as the cause of the failure.

3.2.1.6 Case 6

Corrosion failure of several tiebacks occurred eight years after installation. The tendons were fabricated from 5 mm diameter wires. After removing corrosion products from the wires, heavy pitting was observed. It was postulated that stress corrosion had caused the failure.

3.2.1.7 Case 7

Case 7 involved tiebacks fabricated using 5 mm diameter wires. These were temporary soil tiebacks, but they were required to function for an extended period of time. Two 15-wire tendons failed. The wires were heavily pitted and some of the pits had cracks emanating from their roots.

3.2.1.8 Case 8

The tendons were fabricated from 5 mm wire, and they were used to support a retaining wall. The tendons failed within a year of lock-off. In some areas, deep pits were visible. Some of the failed wires still had grout covering a portion of the tendon. In these areas, the steel was more or less free of corrosion. On the sites where the grout was absent, heavy corrosion occurred. Analysis of the corrosion products showed a 0.63% sulfate content. The fractures emanated from pits, and the breaks were purely brittle. The cause of these brittle breaks is surmised to have been a result of

combined stresses due to bending and tension. The tendons were bent as a result of backfill settlement behind the retaining wall.

3.2.1.9 Case 9

Temporary tiebacks fabricated from 32 mm hot-rolled, and threaded bars were used to support a sheet pile. The unbonded length was covered by a pipe, and no corrosion protection was provided at the anchor head. Two of the tiebacks failed between 16 and 17 weeks after lock-off. The first tieback failed 50.8 mm behind the anchor head. The second failed in the middle of the unbonded length.

The first tieback failed in a brittle fracture at a relatively large corrosion pit. The pit was located in the unprotected area near the anchor head. It is postulated that localized high stresses developed at the pit, and bending could have over-stressed the tendon. The second failure was attributed to hydrogen embrittlement. Corrosion could have been caused by stress concentration, the lack of corrosion protection, and the use of a corrosion susceptible steel.

3.2.2 **The Joux Dam (France)** (Portier, 1974))

Failure of several 1,300-ton capacity anchors occurred after a few months in use. Portier (1974) concluded that the corrosion under tensile stresses was responsible for the anchor failure. The stress level in the tendons was about 67% of the failure value.

3.2.3 **The World Trade Center** (Feld and White, 1974)

Some of the tendons at the World Trade Center showed corrosion activity, and a cathodic protection system was installed (Feld and White, 1974). It was found that the groundwater was corrosive due to the formation of sulphuric acid.

3.2.4 **FIP Report** (1986)

The 35 case histories of failure by tendon corrosion were collected and reported by the FIP in 1986. Of these cases, 24 related to permanent anchors protected or unprotected and 11 were temporary anchors without protection.

In this survey corrosion failure is associated frequently with certain anchor components. Nineteen failures occurred at or within 1m of the anchor head, 21 failures took place in the unbonded length, and only two occurred in the bonded length.

In terms of duration of service, nine failures occurred within six months, 10 between six months to two years, and the remaining 18 between two years and up to 31 years.

Causes of anchor head failure were a) lack of protection, b) incomplete protection, and c) damage to the protective filler. Exposure of the anchor head to the atmosphere contributes to the corrosion risk and increases corrosion potential.

Reports of failure in the unbonded length were caused by the following reasons:

a. Overstressing tendon due to ground movement initiating pitting corrosion or corrosion fatigue.
b. Absences of cement grout or inadequate grout cover in tendons.
c. Disruptions of bitumen cover.
d. Poor choice of protective materials.
e. Poor storage conditions on site.
f. Poor execution of the protection.

In the case of bonded length, inadequate grouting of the tendon bond length caused the two failures involving the bonded anchor length. In one case, this lack of protection exposed 3 m of tendon to aggressive groundwater containing chlorides and sulfides.

3.3 EXAMINATION OF ANCHORS

3.3.1 Tieback Anchors Along I-90 in Mercer Island, Washington

The site was located along I-90 in Mercer Island between MP 4.67 and 5.70 (Kramer, 1993). To construct the westbound lanes of lanes of I-90, a tied back soldier pile wall of up to about 12 m high was constructed. The wall was constructed with tiebacks typically installed at four levels. The anchor tendons were required to meet the ASTM standards for 1034 MPa threaded prestressing rod or seven-wire, 1862 MPa prestressing strands. Anchor tendons were required to have double corrosion protection.

The observations of anchor tendon corrosion were notable for the lack of significant corrosion. Of the 569 anchor tendons evaluated, no corrosion was observed in 560 (98.4%). Evidence of mild corrosion was observed on only nine (1.6%) anchor tendons, and significant corrosion was not observed on any anchor tendon. In general, the corrosion protection systems employed along the anchor tendon appeared to have been very effective. Figure 111 shows the observed results of anchor tendon corrosion.

In order to investigate the potential for corrosion in the anchor head zone, they observed the grease leakage from the trumpet. Grease leakage observations were attempted on 995 tiebacks. Because of inaccessibility for proper examination observations could not be made on 148 of these. As a result of field observation, no evidence of grease leakage was observed for 451 (53.2%) of the remaining 847 tiebacks. Mild or significant grease leakage was observed for 274 (32.3%) and 122 (14.4%), respectively. The rate of leakage observed was correlated to the level of disturbance. In general, the amount of leakage at undisturbed tiebacks was small, but was significant at several locations.

3.3.2 Tieback Anchors in the I-820-Glenview/Pipeline, Ft. Worth

This site is located at the intersection of the I-820 and Glenview/Pipeline in Ft. Worth, Texas. The tieback anchors (single-bar anchors) were installed between concrete piers supporting vertical reinforced concrete walls around bridge abutments. These anchors were installed in 1983.

No significant corrosion was observed on one of the anchor bars that could be observed in the field. Examination with a stereo microscope could not find any evidence of corrosion in the unbonded length as well the bonded length. Mechanical properties of the anchor bars are listed in Table 13.

Table 13. Results of Tensile Testing for Anchor Tendon

Properties of Material	Specimen 1	Specimen 2	Average Value
Elastic Modulus (10^7)	1.787	2.931	2.359
Yield Stress (MPa)	846.05	887.57	866.81
Ultimate Tensile Stress (MPa)	1052.63	1082.16	1067.40
Breaking Stress (MPa)	770.63	808.89	789.76
Ductility	51.04%	50.63%	51.33%

3.3.3 Clay Site at National Geotechnical Experimental Site

On July 31, 1996, a section of 1.33 m length was removed from an exposed section of a tendon at the clay site. This tendon, as all others in this project, had been exposed to the elements of nature for approximately five years. The section consisted of a fully exposed portion of the tendon, 1 m, and a greased, sheathed section, 0.33 m in length at one end (Figure 112). The tendon itself is composed of seven twisted strands. A 100 mm portion was removed from both the fully exposed section and the protected section, as indicated on the figure, to view the damage incurred to the tendon over the time span. Upon removing the sheath from its respective 100 mm portion, it was discovered that the protective grease was still in reasonable condition. Examination of sections from the seven strands with a microscope revealed no evidence of corrosion, and the grease in this length of the tendon was declared effective. Visual examination of the 100 mm section exposed to the air showed clear evidence of corrosion on the exterior surfaces. When the strands were separated, it was noted that the lines of contact within the strands were not as corroded, although the evidence was still clearly visible to the naked eye. Microscopic examination showed possible signs of pitting, although the most prevalent type was uniform or general corrosion. Further examination of the remaining tendon revealed problems with the grease. The top 50 mm of the sheath was removed to examine the extent of the corrosion of the original exposed portion. Upon removal, it was discovered that no grease was present, although evidence suggests that grease had originally filled the annular space. This once grease-protected section showed definite signs of corrosion, though not as severe as the original fully exposed section. Removal of several more

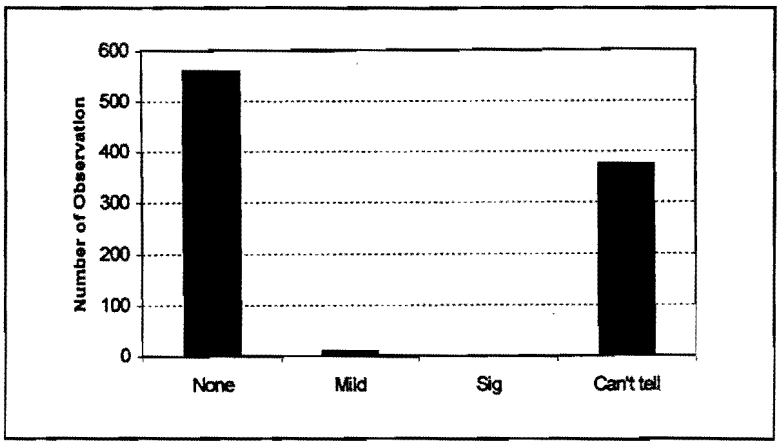

Figure 111. Observations of Anchor Tendon Corrosion

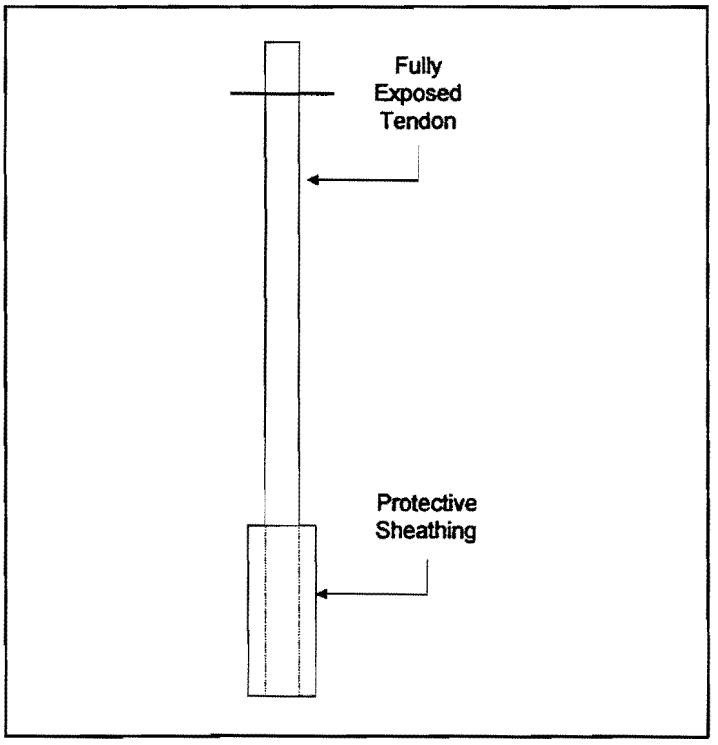

Figure 112. A Section of a Tendon at the Clay Site

centimeters of sheathing revealed grease in a tacky, thick state, apparently in the process of drying out. This supported the suggestion that the grease on the previous section had indeed dried into an unprotective state; nonetheless, corrosion is no longer apparent by the end of this region, approximately 70 mm to 80 mm into the sheathing. The grease is first noted in the original, moist state approximately 120 mm into the sheathing.

3.4 SOIL CORROSION PREDICTORS

3.4.1 Soil Characteristics

Corrosion of metals in soil is established by a combination of factors, not one of which will singularly indicate the degree of corrosivity. The overall aggressivity of the soil is marked by the soil's electric resistivity, pH, water concentration, concentration of chloride, and degree of aeration. Table 14 contains the design practices of the United States, United Kingdom, France, and Germany based on soil properties (Elias, 1990).

3.4.2 Corrosion of Ground Anchors

Corrosion attack of steel tendons in ground anchors is a serious problem in maintaining the long-term performance. Generally soil conditions are inhomogeneous, and the ground strata have unknown characteristics; incidents of corrosion along the anchor tendon can occur if the tendon is unprotected.

This chapter is intended to provide criteria to guide design engineers in evaluating corrosion of ground anchors and in determining construction damage losses. Case histories of tieback anchor failures documented in several reports are also included in this chapter.

3.4.2.1 Factors Controlling Anchor Corrosion

Among the factors that effect the corrosion rate of steel embedded in soil are (1) soil resistivity, (2) soil pH, (3) water content, (4) soluble salts, (5) redox potential, and (6) aeration. Each of these factors may affect the anodic and cathodic polarization characteristics of a metal in a soil (Tomashov and Mikhailovsky, 1959). These parameters are interrelated but may be measured independently. These soil properties can be combined into a great number of different soil environments, each causing different corrosion rates for the metal in the soil. Table 15 contains the design practices of the United States, United Kingdom, France, and Germany based on soil properties.

3.4.2.1.1 Soil Resistivity

Resistivity, which is inversely proportional to conductivity, is recognized as an important parameter in soil aggressiveness (Romanoff, 1957). Soil resistivity expressed in units of ohms/cm is a measure of the ability of the soil to resist ionic current flow. If the soil solution as an electrolyte in any place has lower resistivity, the magnitude of ionic current flow can be larger and then the

Table 14. Electrochemical Limits of Select Backfills Used in Conjunction with Galvanized Steel Reinforcements (Elias, 1990)

Property	U.S. (FHWA)	France	United Kingdom	Germany
Resistivity O/cm	>3,000	>1,000 dry[1] >3,000 wet[2]	>5,000[3]	>3,000
pH	>5 <10	>5 <10	>6 <9	>5 <9
Chloride Content PPM	<200	<200 dry <100 wet	<500	<50
Sulfate Content PPM	<1,000	<500 wet <1,000 dry	<500	<500
Sulphides PPM	— —	<300 dry <100 wet	— —	— —
Organic Content	— —	100 PPM	— —	— —
Biochemical Need of Oxygen	— —	Minimal	— —	— —
Redox Potential + mV	— —	— —	200-400	100-200

[1] "dry" is an upland structure

[2] "wet" is structure repeatedly or permanently submerged

[3] measured insitu

Table 15. Electrochemical Limits for Select Backfills (after Elias, 1990)
(Galvanized Steel Reinforcement)

Property	U.S. (FHWA)	France	U.K.	Germany
Resistivity (Ohm/cm)	>3000	>1000 dry >3000 wet	>5000	>3000
pH	5-10	5-10	6-9	5-9
Chloride Content (PPM)	<200	<200 dry <100 wet	<500	<50
Sulfate Content (PPM)	<1000	<1000 dry <500 wet	<500	<500
Redox Potential (mV)			200-400	100-200

corrosion rate of the embedded steel also should be higher as a result of electrochemical reactions at the metal surface. Table 16 gives guidance for the effect of resistivity on corrosion.

Table 16. The Effect of Resistivity on Corrosion (after King, 1977)

Aggressiveness	Resistivity in ohm/cm
Very corrosive	< 700
Corrosive	700 ~ 2,000
Moderately corrosive	2,000 ~ 5,000
Mildly corrosive	5,000 ~ 10,000
Non-corrosive	> 10,000

The amount of dissolved inorganic anions and cations in the soil solution is proportional to the electrolytic conductivity (Elias, 1990). The electrolytic conductivity of the soil solution is the sum of all the individual equivalent ionic conductivities times their concentration. Soil resistivity governs the effectiveness of the ionic current pathway. Despite all the criteria engineers have used to rank the degree of corrosivity among soils, resistivity is still the most commonly used parameter for assessing soil corrosion characteristics (Miller et al., 1981).

Soil resistivity can be measured by several techniques. As an insitu method, a standard test method for field measurement of soil resistivity is the Wenner four-electrode method (ASTM G 57-95a) which has been adapted for field use in predicting soil corrosivity. Soil resistivity may also be determined by measuring the electrical conductivity of the soil solution in the laboratory. In this method resistivity is dependent on the water content in soil because the ionic current flows through the liquid phase.

3.4.2.1.2 Soil pH

The pH of soil is known to be a good indicator of the corrosivity of a soil environment. It has been used as a measure of the influence of hydrogen on corrosion rate. Extremely acidic (<4.0) or very strongly alkaline (>10) soils are generally associated with significant corrosion rates. Fontana (1986) showed the influence of soil pH on carbon steels. Below pH 5, cracked and incomplete films of $Fe(OH)_2$ and $Fe(OH)_3$ form, and result in higher corrosion rate. Hydrogen ions act as reactants in the cathodic portion of corrosion reactions:

$$2H^+ + 2e^- \rightarrow H_2 \tag{38}$$

Reduction of other species such as oxygen is usually much more important at the pH values normally associated with soils. Elias (1990) suggests that the allowable pH range may be between 4.5 and 9.5 in soils.

There are two different types of pH measurement for soil. One is the standard test method for pH of soils (ASTM D 4972-89) and the other is the standard test method for measuring soil pH for use in corrosion testing (ASTM G 51-95).

3.4.2.1.3 Moisture Content

In general, resistivity decreases as the water content increases and drops drastically as the water content increases from 0% to 20% (Elias, 1990). A maximum corrosion rate in soil usually occurs at intermediate moisture content (65% saturation). At low moisture contents, there is insufficient water to support the corrosion reaction. At high moisture contents, oxygen is excluded and limited from the metal surface and corrosion rates are low.

Escalante and Cohen (1980) observed the effect of moisture on the corrosion of steel. The specimens were initially exposed in a dry sand mixture and moisture saturated sand mixture. As the response of the corrosion as function of time, specimens placed in the saturated condition did not corrode, while the specimens in the dry condition corroded as moisture was introduced. Escalante's report suggested that the degree of moisture played an important role in the corrosion rate of steel embedded in soil.

3.4.2.1.4 Soluble Salts

Since soluble salts decrease the resistivity of the soil and affect the electrochemical reaction at the metal surface, it is generally recognized that soluble salts are detrimental. As the primary agents in the promotion of corrosion, chlorides and sulphates have been identified.

3.4.2.1.5 Redox Potential

The redox potential, referred to as oxidation-reduction potential, is used to give information on the type of corrosion mechanism such as anaerobic bacterial corrosion. Elias (1990) reported that a low value of the redox potential tends to indicate susceptibility to microbial attack, while a high value shows the presence of oxygen supported corrosion. Redox potential measurement may allow estimating the likelihood of development of macrocells, in which a steel member runs through two different types of soils. Table 17 shows the range of redox potential for soil corrosiveness using hydrogen electrode.

3.4.2.1.6 Aeration

Since a porous soil tends to have an optimum aeration and moisture content for a long time, this will increase the initial corrosion rate. Corrosion products formed in an aerated soil may be more protective than those formed in an unaerated soil. However, localized corrosion, which is

usually observed in an unaerated soil, is significantly more damaging to a steel member in soil than a higher overall corrosion rate occurring uniformly (Uhlig and Revie, 1985).

Table 17. Range of Redox Potential for Soil Corrosiveness (after King, 1977)

Corrosiveness	Redox Potential (HE)
Very corrosive	< 100
Corrosive	100 - 200
Moderately corrosive	200 - 400
Mild and non-corrosive	> 400

3.5 LABORATORY TESTING OF CORROSION RATES

3.5.1 Potentiodynamic Polarization Measurements

In order to determine how the variations of soil pH and soil conductivity affect the corrosion of tieback anchors in a retaining wall, potentiodynamic polarization measurements were performed in the laboratory on soil samples collected from the National Geotechnical Experimental Site. The specific objectives were: (1) generation of data on the effect of soil pH and soil conductivity on corrosion rates of bare steel specimens in sand or clay and (2) identification of field conditions for which such corrosion is likely to be a problem.

3.5.2 Background and Electrochemical Principles

When a metal specimen is immersed in a corrosive medium, typically the metal specimen corrodes and the medium is reduced. At this time both anodic and cathodic currents occur on the specimen surface. When these currents are exactly equal in magnitude, which implies a steady state condition exists, the corrosion potential (E_{corr}) can be measured.

At a potential more positive than E_{corr}, the anodic current dominates relative to the cathodic current due to the polarization characteristics. However, at the potential more negative than E_{corr}, the cathodic current dominates relative to the anodic current. The polarization characteristics can be explained by plotting the current response as a function of given potential (Figure 113).

The corrosion current, i_{corr}, and corrosion potential, E_{corr}, can be determined from the interaction of the two polarization curves as shown in Figure 113. Based on this curve, the

relationship between the voltage difference and the current can be expressed for the anodic reaction as:

$$\Delta\varphi_a = \beta_a \log(i_a / i_{corr}) \tag{39}$$

For the cathodic reaction, the relationship can be expressed similarly as:

$$\Delta\varphi_c = \beta_c \log(i_c / i_{corr}) \tag{40}$$

where

$\Delta\varphi_a, \Delta\varphi_b$ = the overpotentials in volts,
β_a, β_c = the Tafel coefficients,
E_{corr} = the corrosion potential,
i_{corr} = the corrosion current , and
i_a, i_c = the measured current.

The measured current can be written as:

$$i_{measured} = i_a - i_c = i_{corr}(10^{\varphi/\beta_A} - 10^{-\varphi/\beta_C}) \tag{41}$$

Expressed as series,

$$10^{(\varphi/\beta)} = 1 + 2.3(\varphi/\beta) + \frac{(2.3(\varphi/\beta))^2}{2!} + \cdots \tag{42}$$

If $\Delta\varphi/\beta_c$ and $\Delta\varphi/\beta_a$ are small, higher term can be neglected and Equation 42 can be approximated by

$$i_{measured} = 2.3 i_{corr} \Delta\varphi \left(\frac{1}{\beta_c} + \frac{1}{\beta_a} \right) \tag{43}$$

If from Equation 43 the corrosion current can be obtained as follows:

$$i_{corr} = \frac{\beta_a \beta_c}{2.3(\beta_a + \beta_c)} \frac{i_{measured}}{\Delta\varphi} \tag{44}$$

The intersection of the two polarization curves gives the corrosion potential, E_{corr} and the corrosion current, i_{corr}. At the intersection of the two curves, the total oxidation equals the total reduction. The corrosion rate can be determined from i_{corr} using the above equation (Fontana, 1986). And if E_{corr} and/or β_a or β_c is known, then i_{corr} can also be determined.

3.5.2.1 Polarization Resistance Measurements

The linear polarization resistance (LPR) test performs a potentiodynamic scan, which changes the potential and then measures the corresponding current. This experiment was performed on the steel specimens to determine the polarization resistance, which in turn determines the influence of the chemical and physical factors that limit the corrosion rate. Once the system reaches a steady state, the polarization resistance measurement can measure absolute corrosion rates in less than 10 minutes.

When a metal is exposed to a given corrosive environment, it develops a certain corrosion potential, E_{corr}, where the anodic current density is numerically equal to cathodic current density, and corresponds to the corrosion current density (i_{corr}). Thus, the current measured with an external device will be zero. If a potential differing from E_{corr} is applied to such an electrode, a net current will be observed due to the difference of anodic and cathodic current. The measurement of this difference results in the polarization curve as measured with a potentiostat.

A polarization resistance measurement is performed by scanning through a potential range, ±20 mV, about E_{corr}. Figure 114 shows the plot for measuring polarization from a best fit line on the potential difference relative to E_{corr} versus current curve. Polarization resistance (R_p) can be determined from the polarization curve slope within the above potential range (Equation 45).

$$R_P = \Delta\varphi/\Delta i = \frac{\beta_a \cdot \beta_c}{2.3(i_{corr})(\beta_a + \beta_c)} \tag{45}$$

where

$\Delta\varphi/\Delta i$ = the slope of the polarization resistance plot,
β_a, β_c = the anodic and cathodic Tafel constants determined from a Tafel plot, and
i_{corr} = the corrosion current.

The corrosion current (i_{corr}) can be obtained from the polarization resistance shown in Equation 46.

$$i_{corr} = \frac{\beta_a \beta_c}{2.3R_p(\beta_a + \beta_c)} \tag{46}$$

Since the corrosion current is directly related to the absolute corrosion rate, it can be obtained the through Faraday's relationship (see Equation 36).

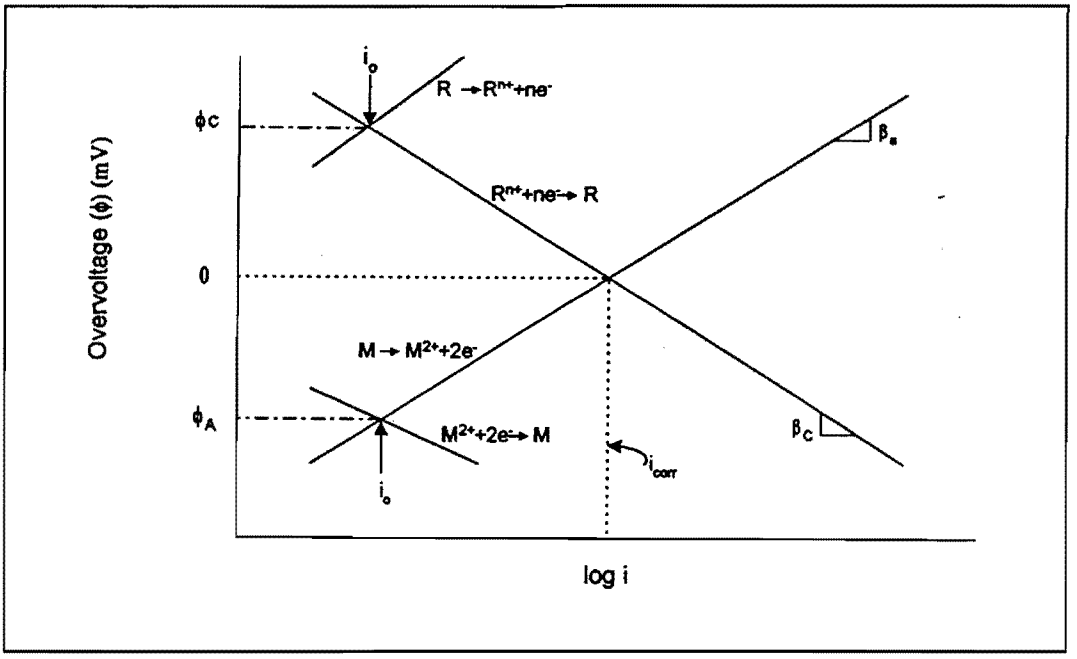

Figure 113. Potential-Current Relationship for a Mixed Electrode System

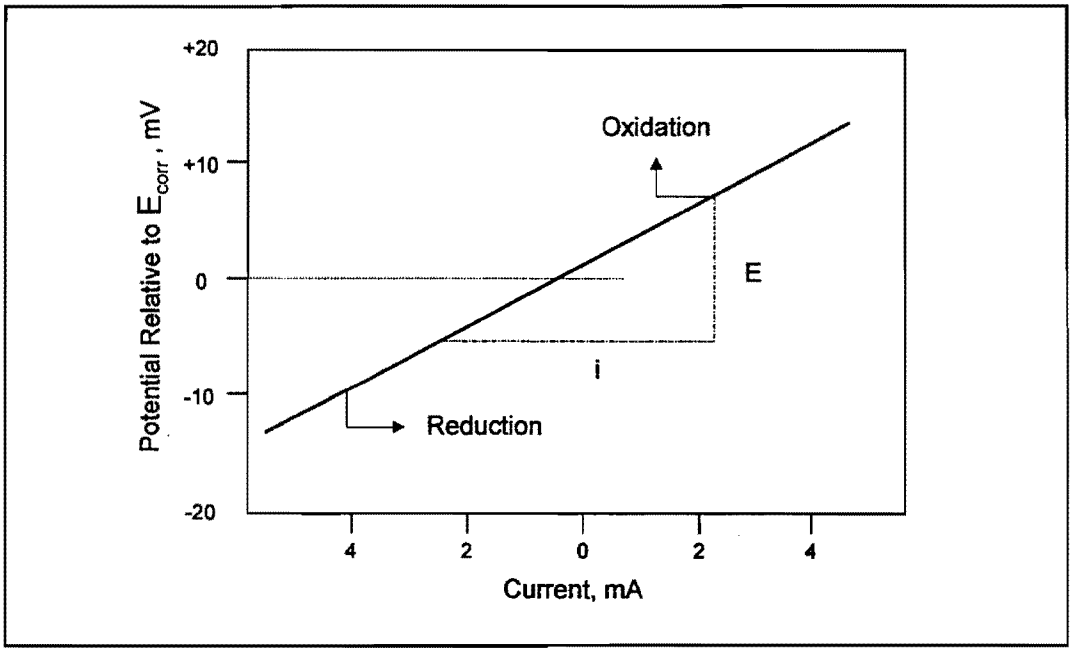

Figure 114. The Plot is Used to Determine the Polarization Resistance

3.5.2.2 Tafel Extrapolation

The Tafel extrapolation method is used to determine the corrosion rate using data obtained from cathodic and anodic polarization measurements. In order to develop the polarization curves, the steel specimen is termed the working electrode, and current is supplied to it by means of a counter electrode. The potential of the working electrode is measured with respect to a reference electrode by a potentiostat. The setup is shown in Figure 115.

The potentiostat measures the corrosion potential of steel specimens with respect to a reference electrode. Figure 116 illustrates the polarization curve for a steel specimen in terms of the potential and logarithm of applied current. The potentiostat measures the difference between the anodic and cathodic currents and near E_{corr} the measured current goes to zero. However, at high currents the relationship between voltage and the logarithm of current becomes linear and this region of linearity is referred to as the Tafel region. The measured anodic and cathodic polarization curves are superimposed as dashed lines and shown in Figure 116. In order to determine the corrosion rate from polarization measurement, the Tafel region is extrapolated to the corrosion potential (E_{corr}). At the intersection of the corrosion potential and the corrosion current density (i_{corr}), the rate of reduction is equal to the rate of dissolution (oxidation), and i_{corr} can be obtained (dotted lines).

The Tafel extrapolation is not valid when concentration polarization occurs and IR drops are sufficiently large to reduce the linear region to a region where extrapolation to i_{corr} is difficult. This is illustrated in Figure 116 by the dashed line marked oxygen reduction.

3.5.3 Measurement of Soil pH

The pH is defined as the logarithm of the hydrogen ion concentration and expressed as $-\log[H_3O^+]$. Following the procedure given in ASTM Standard D-4972-89, the pHs of the soil samples were measured. Table 18 summarizes the pH values as measured in the laboratory.

Table 18. Variation of pH with Solution Addition

Measured pH Value		
Clay (NGES)	**Sand (NGES)**	**Porcelain Clay**
4.4	4.7	4
6.2	5.2	5
7.3	6.2	6.7
8	7	8.2
10.2	9.7	9.6

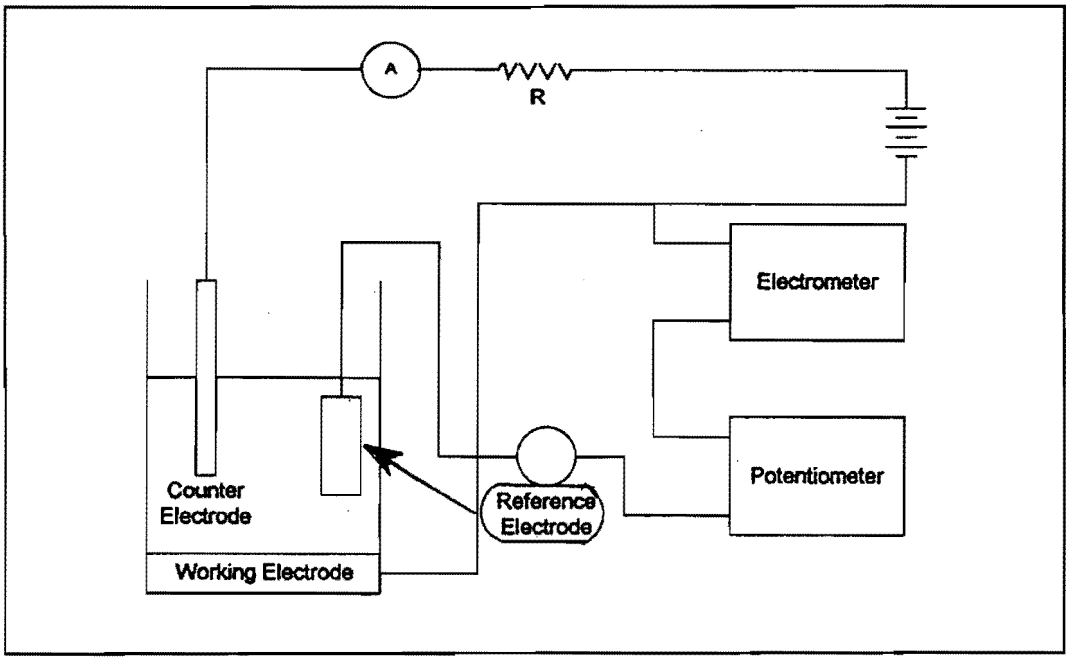

Figure 115. Electric Circuit for Polarization Measurements

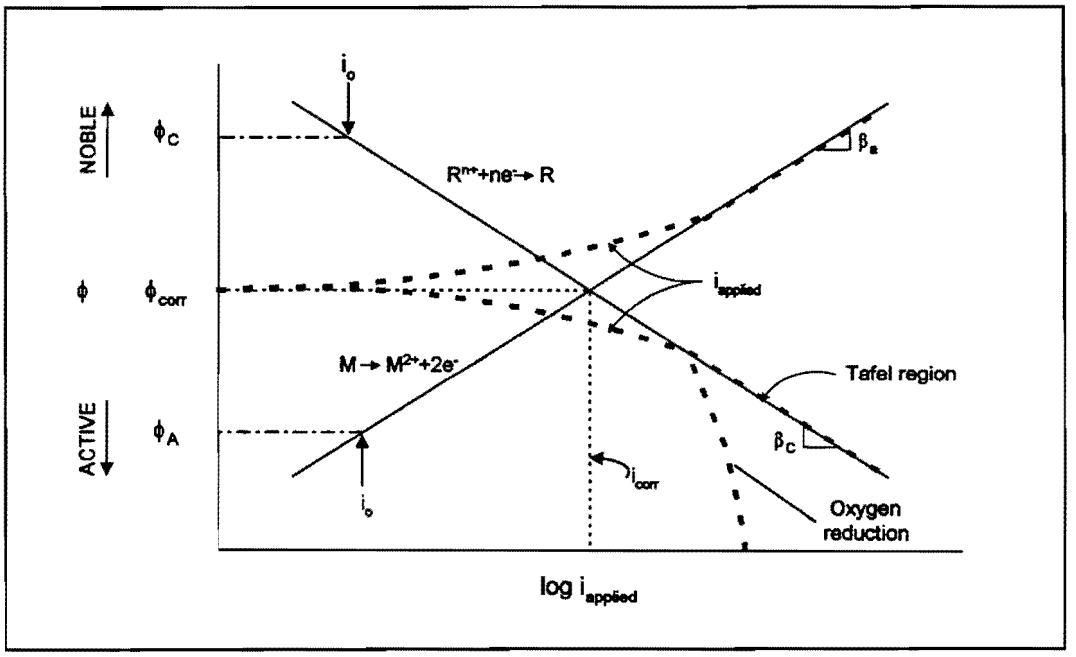

Figure 116. Polarization Curve of a Corroding Metal (Tafel Extrapolation)

3.5.4 Measurement of Soil Electrical Conductivity

Conductivity measurements indicate the relative ability of a medium to carry electrical currents. Soil electrical conductivity tests were performed in accordance with a procedure developed by Bredenkemp and Lytton (1994). The test procedures are described below:

1. Take 5 grams soil and dry soil in the room temperature.
2. Break up soil lump.
3. Mix the dry soil with distilled water (solid:water = 1.5 in weight).
4. Shake the containers for 4 hours to mix homogeneously.
5. Calibrate the conductivity meter.
6. Measure the conductivity in milliSiemens (mS).

Table 19 shows the electrical conductivity of the soils as well as the soil pH.

Table 19. Electrical Conductivity of Soils

Clay (NGES)		Sand (NGES)		Porcelain Clay	
pH	Conductivity (mS)	pH	Conductivity (mS)	pH	Conductivity (mS)
4.4	2.09	4.7	0.2	4	0.67
6.2	0.73	5.2	0.19	5	0.17
7.3	0.35	6.2	0.2	6.7	0.21
8	0.51	7	0.07	8.2	0.49
10.2	1.02	9.7	0.35	9.6	0.45

3.5.5 Soil Chemical Analysis

Chemical contamination is known to be one of the major contributors to corrosion of steel embedded in soil environment. Table 20 illustrates the chemical properties of clay in NGES.

Table 20. Soil Chemical Analysis

Soil Test Ratings (PPM element)

K	Ca	Mg	Zn	Fe	Cu	Na	S	Cl
84	1669	260	0.12	6.73	0.25	102	40	32
Low	High	High	Low	High	High	Low	High	

3.5.6 Test Conditions: Soil and Steel Plates

A series of soil samples (porcelain clay, clay, and sand from the NGES site) were prepared for potentiodynamic polarization measurements called DC-corrosion rate testing. In order to vary the soil pH, NaOH and HCl solutions were added to the natural soil samples to adjust the pH.

ASTM 1018 steel plates were chosen because they are representative of the ground anchor steel and their availability. The steel plates were 150 mm × 100 mm in size and 5 mm in thickness. The steel arrived with a light coat of grease from the manufacturer to protect it from corrosion while in storage and transit. For this reason, the steel surfaces were degreased using acetone and then sanded using 400 grit sandpaper.

3.5.6.1 Test Methods and Procedures

These experiments were designed to provide a comparison of the corrosiveness of steel in different soils. Linear polarization resistance measurement (LPR) and Tafel extrapolation (TE) require the application of a potential and the simultaneous measurement of the current. In the case of LPR the collected data was used to calculate the polarization resistance, and to estimate the corrosion rate of the steel specimens. As a result of polarization over a larger potential range, TE can be used to measure the corrosion current by extending the line in the Tafel region to the corrosion potential.

The laboratory procedures to obtain measurements are as follows:

1. Place calomel reference electrode in the soil sample in the environment cell, insuring that the electrode is not in contact with the steel specimen.
2. Place the counter electrode (platinum wire) in the soil sample near the reference electrode.
3. Connect red wire of voltmeter to reference electrode.
4. Connect green and black wires to working electrode.
5. Measure the corrosion potential at equilibrium condition.
6. Scan the potential and measure the applied current at each potential.

The effects of soil environment on the ground anchor steel were determined by measuring the corrosion current (i_{corr}), corrosion rate, and corrosion potential for five different pH conditions in the soil. The data from the experiment were automatically monitored and analyzed during the exposure time using a computerized data acquisition system. A schematic of the test cell is shown in Figure 141.

3.5.6.2 Data Reduction and Results

Linear polarization resistance measurements (LPR) and Tafel extrapolation methods (TE) were used to determine corrosion rates for all the different soil-pHs specified in Table 18. Variations of corrosion potential, corrosion current, polarization resistance, and corrosion rate of the test specimens for different soils as a function of soil pH are shown in Figures 117 through 135. Table 21 shows the results of polarization resistance measurements.

3.5.6.2.1 Clay (NGES), Variations of Soil pH

Figures 117 through 120 provide information on the corrosion characteristics for mild steel specimen samples embedded in clay with pH 4.4, 6.2, 7.3, 8, and 10.2. The corrosion rate estimated for pH 4.4 samples' was 0.53 mm/y from LPR and 0.261 mm/y from TE. For pHs greater than 6.2 the corrosion rate sharply dropped to 0.031 mm/y (LPR) and 0.048 mm/y (TE) and remained relatively constant over the pH range tested. Below a pH of about 6, the corrosion rate increases as the pH decreases. The natural pH of clay in NGES is 7.3; this suggests a low corrosion rate under field conditions.

Figure 117 shows the corrosion potential of the samples embedded in clay as a function of pH. The observed E_{corr} values for clay samples showed values between -586 mV and -722.5 mV. The variations of corrosion current density (i_{corr}) are shown in Figure 119. As can be seen, i_{corr} values are inversely proportional to the soil pH on a semilogarithm plot. An increase in the soil pH in clay gives rise to a lower corrosion rate.

3.5.6.2.2 Sand (NGES), Variations of Soil pH

Figures 121 through 124 present information on the corrosion characteristics of sand samples with variations of soil pH. As can be seen, the trend of sand samples is similar to that of clay samples. The data also indicate the extremely acidic soil create high corrosion rates of steel specimens. The measured corrosion rates at pH 4.7 were 0.31 mm/y (LPR) and 0.376 mm/y. The natural state of sand (pH 6.2) indicated the lowest corrosion rate (0.0054 mm/y) when using the Tafel extrapolation method. When using the Tafel extrapolation method shown in Figure 133, the corrosion rates in sand samples are generally greater than those in clay samples. This result indicates that the contact between the relatively pervious sand and the steel specimen was well oxygenated.

Figure 121 summarizes the corrosion potential values of steel specimens embedded in sand. The E_{corr} values in sand for steel specimens showed them to be generally greater than for the clay samples. The E_{corr} values were deterined to be in the range of –487 mV and –632.8 mV.

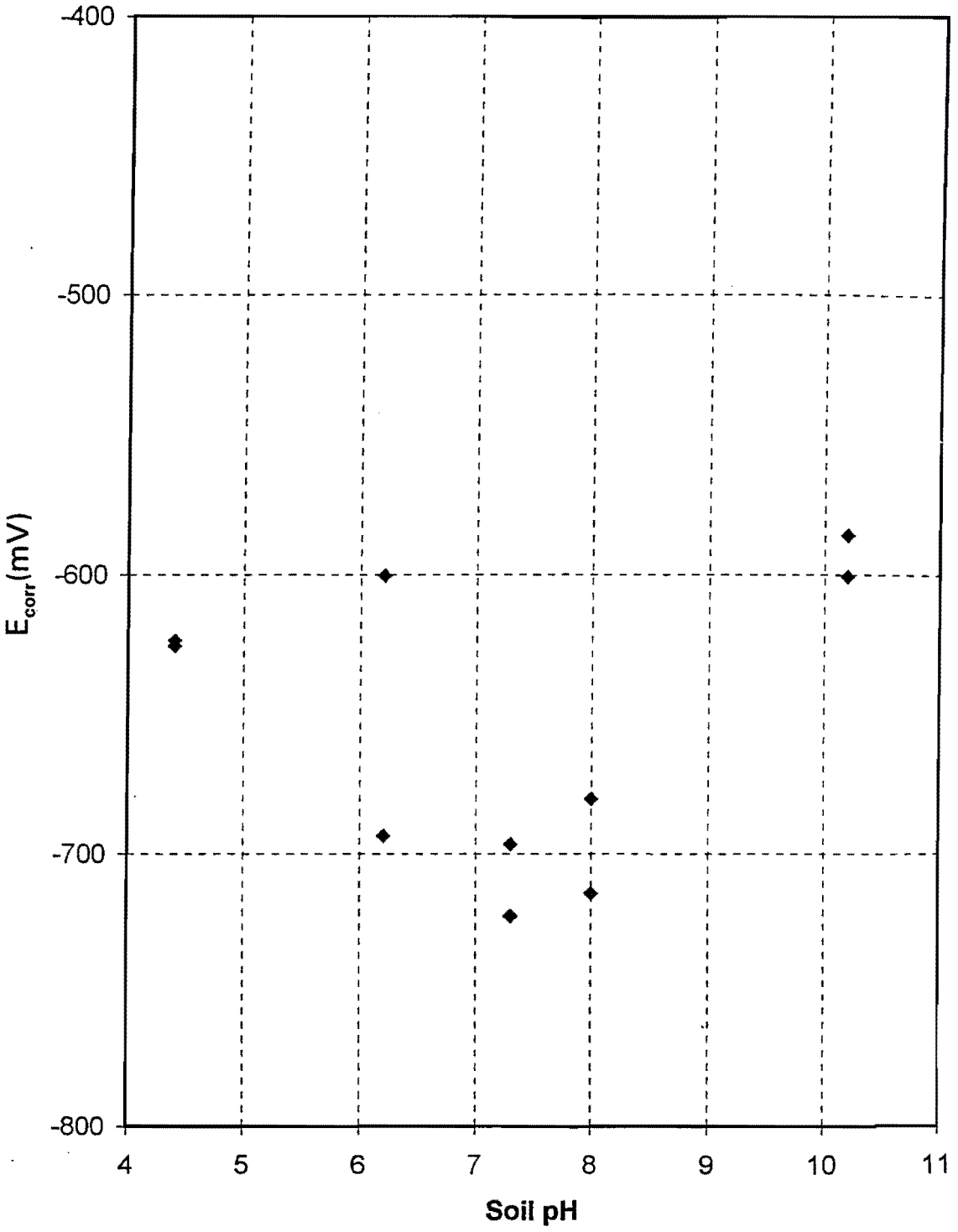

Figure 117. Corrosion Potential with Variations of Soil pH (Clay Sample)

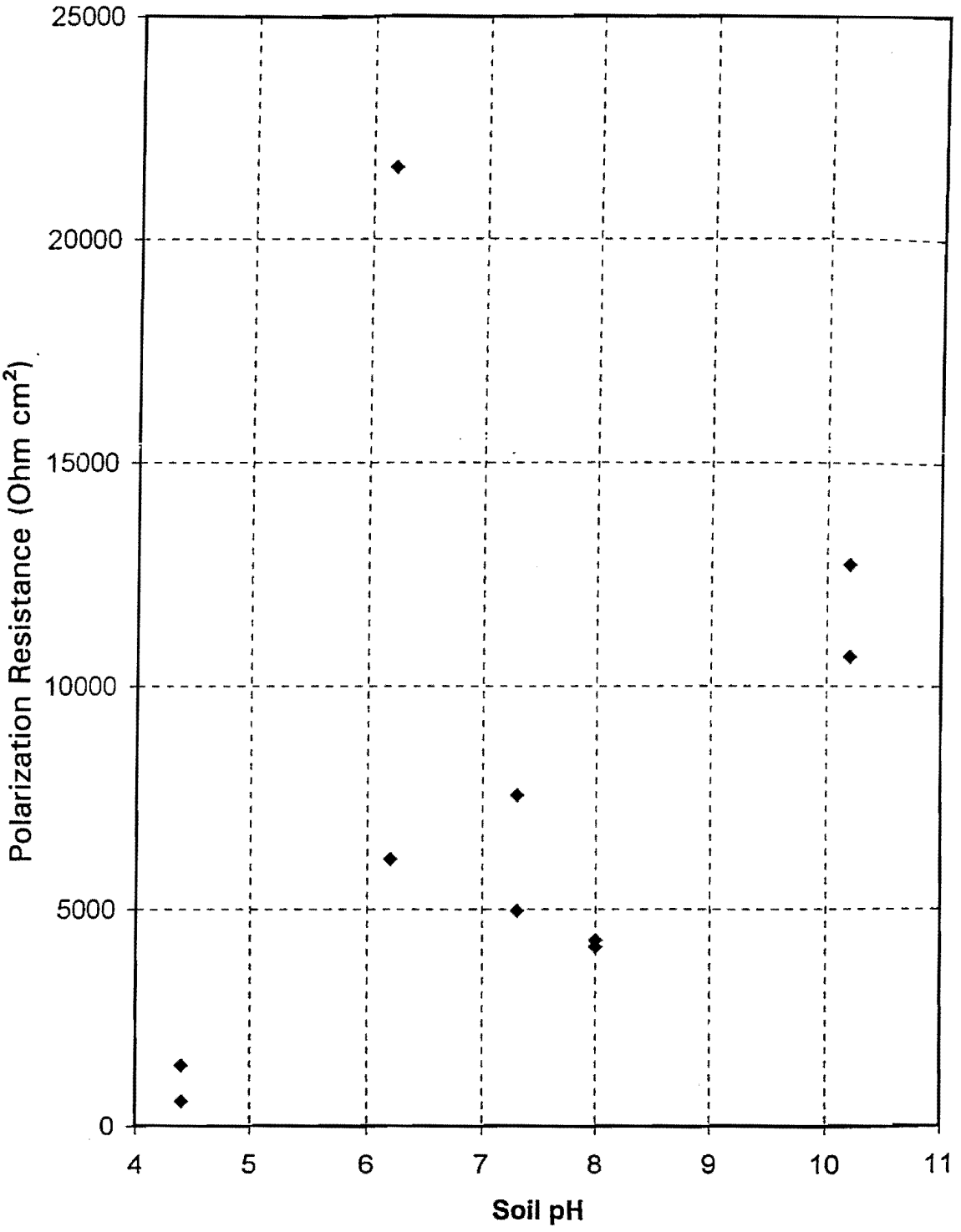

Figure 118. Polarization Resistance with Variations of Soil pH (Clay Sample)

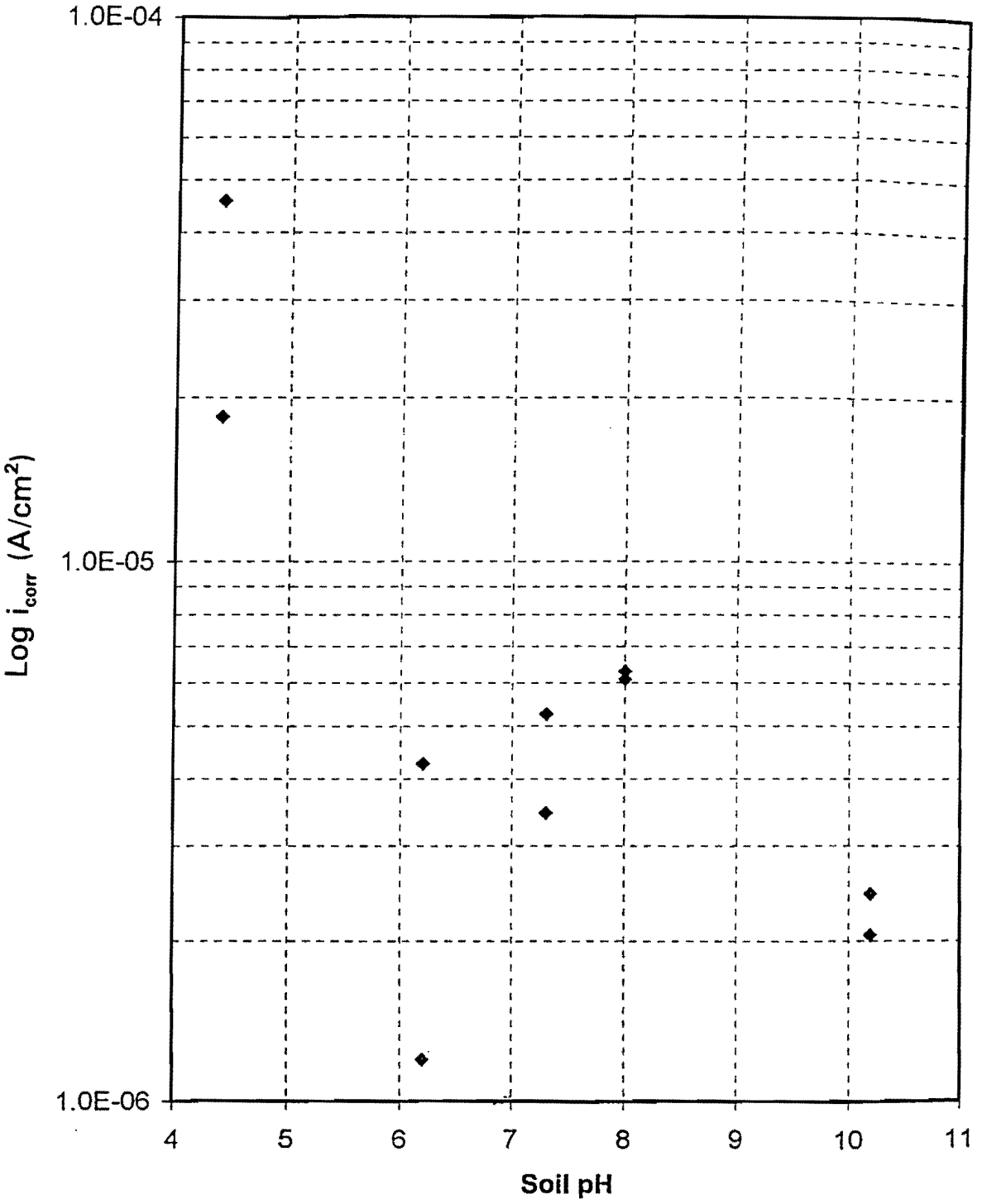

Figure 119. Corrosion Current Density with Variations of Soil pH (Clay Sample)

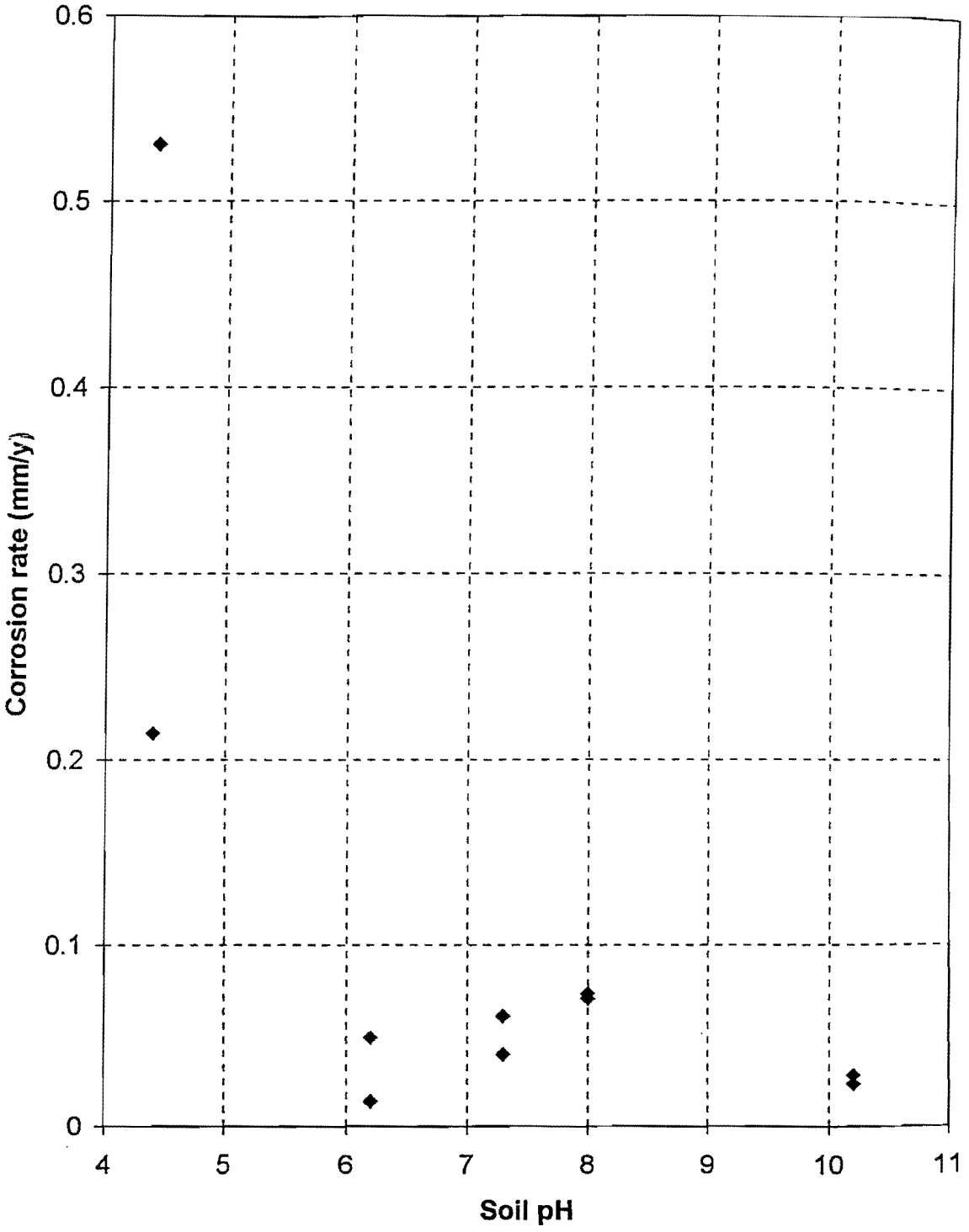

Figure 120. Corrosion Rate with Variations of Soil pH (Clay Sample)

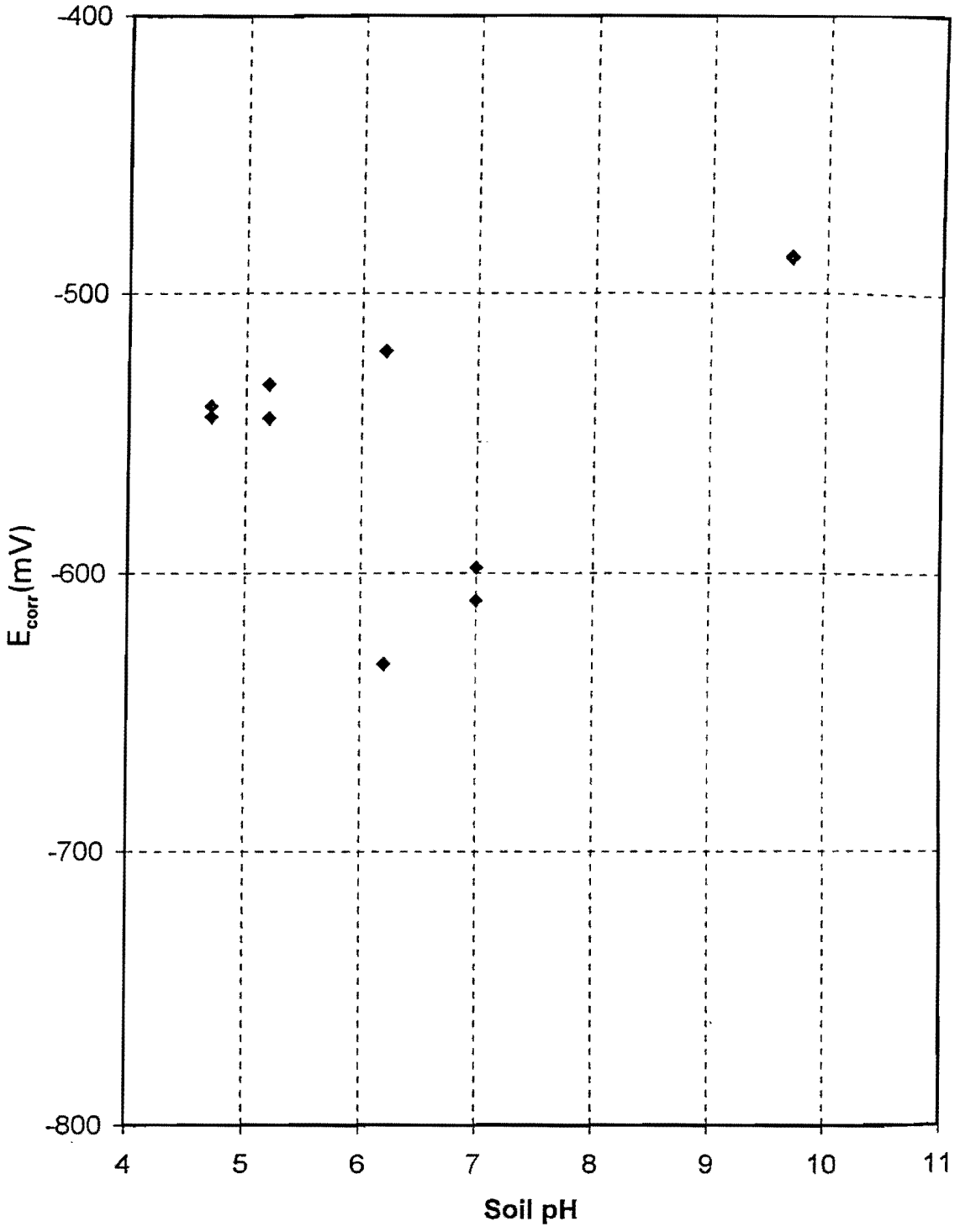

Figure 121. Corrosion Potential with Variations of Soil pH (Sand Sample)

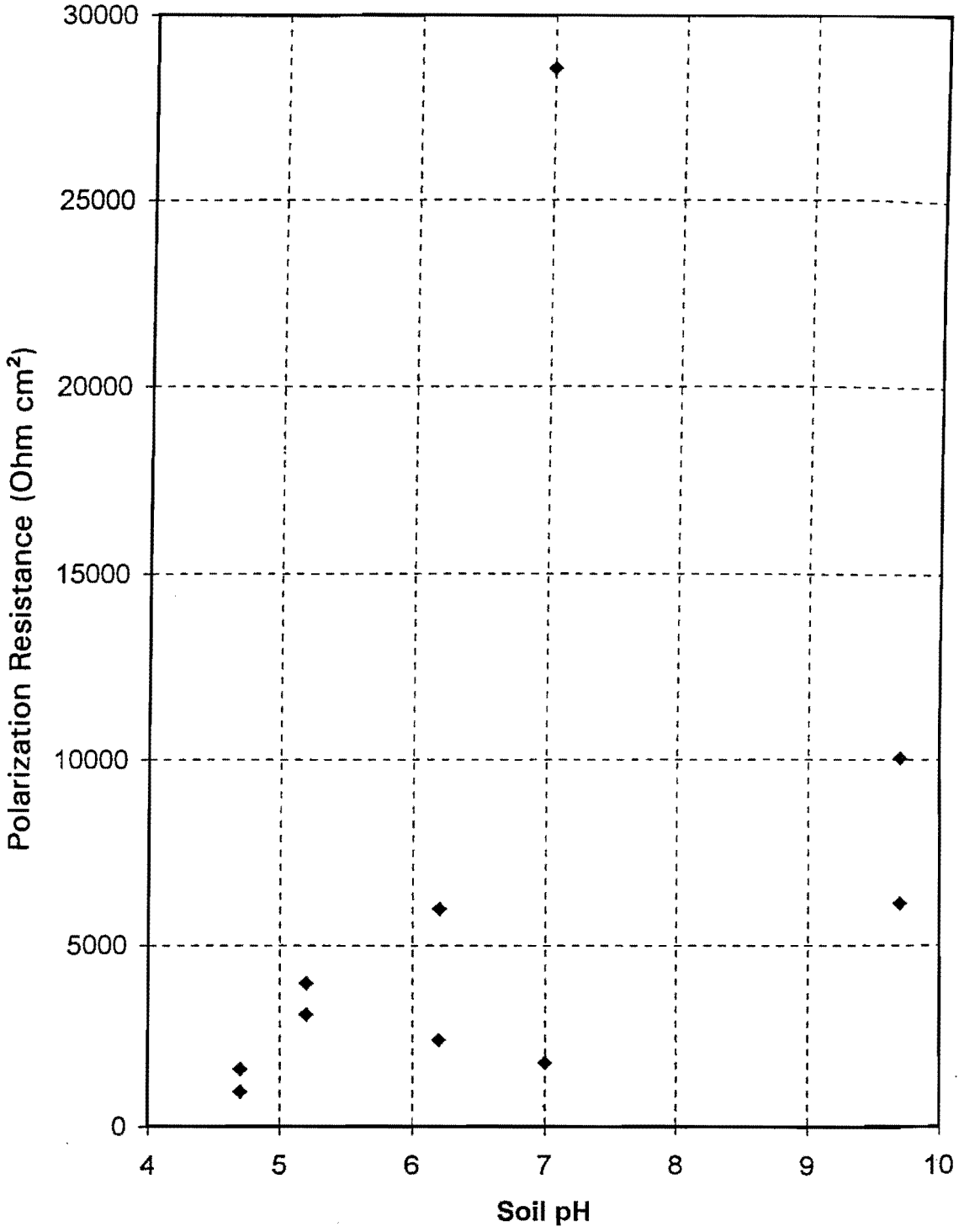

Figure 122. Polarization Resistance with Variations of Soil pH (Sand Sample)

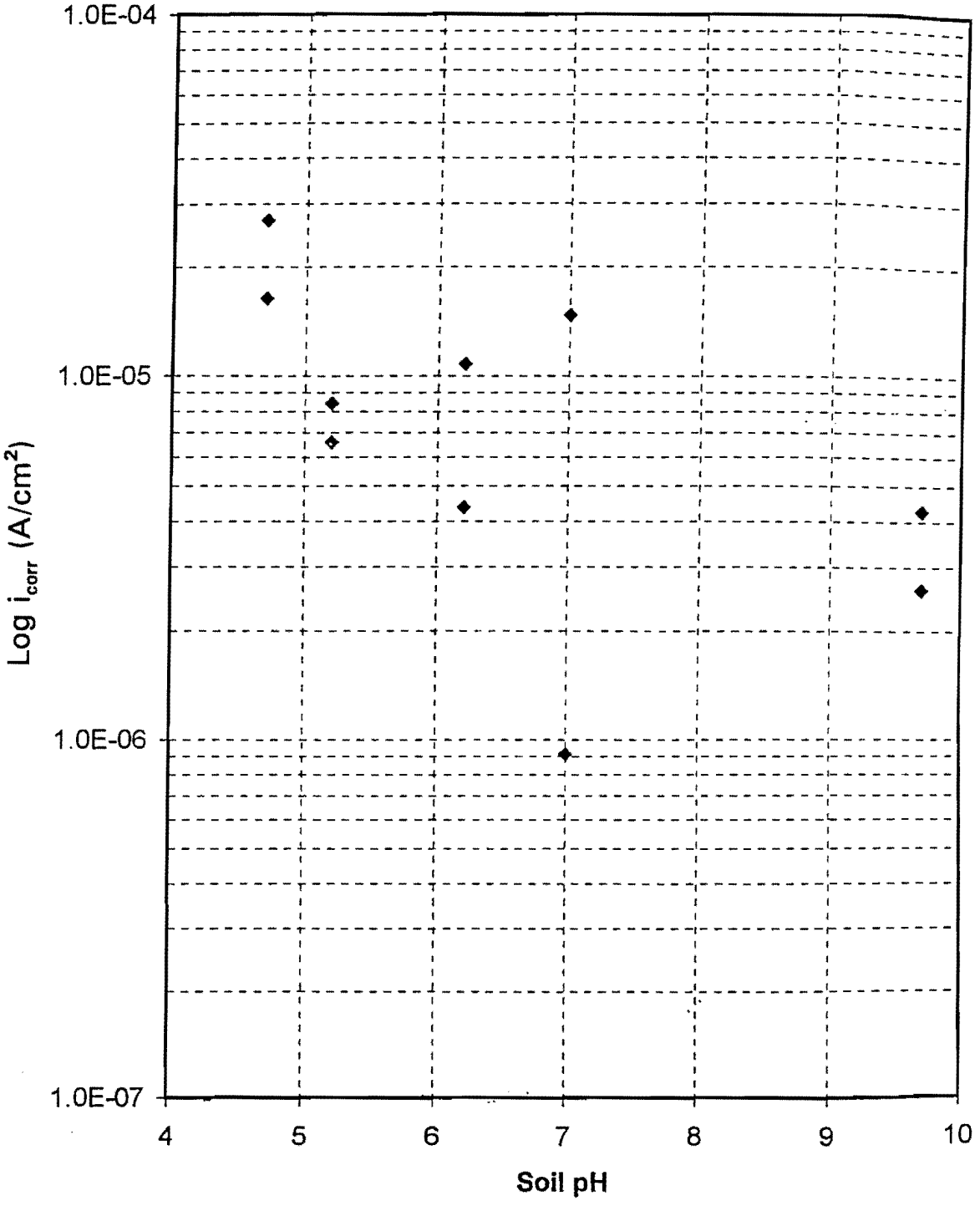

Figure 123. Corrosion Current Density with Variations of Soil pH (Sand Sample)

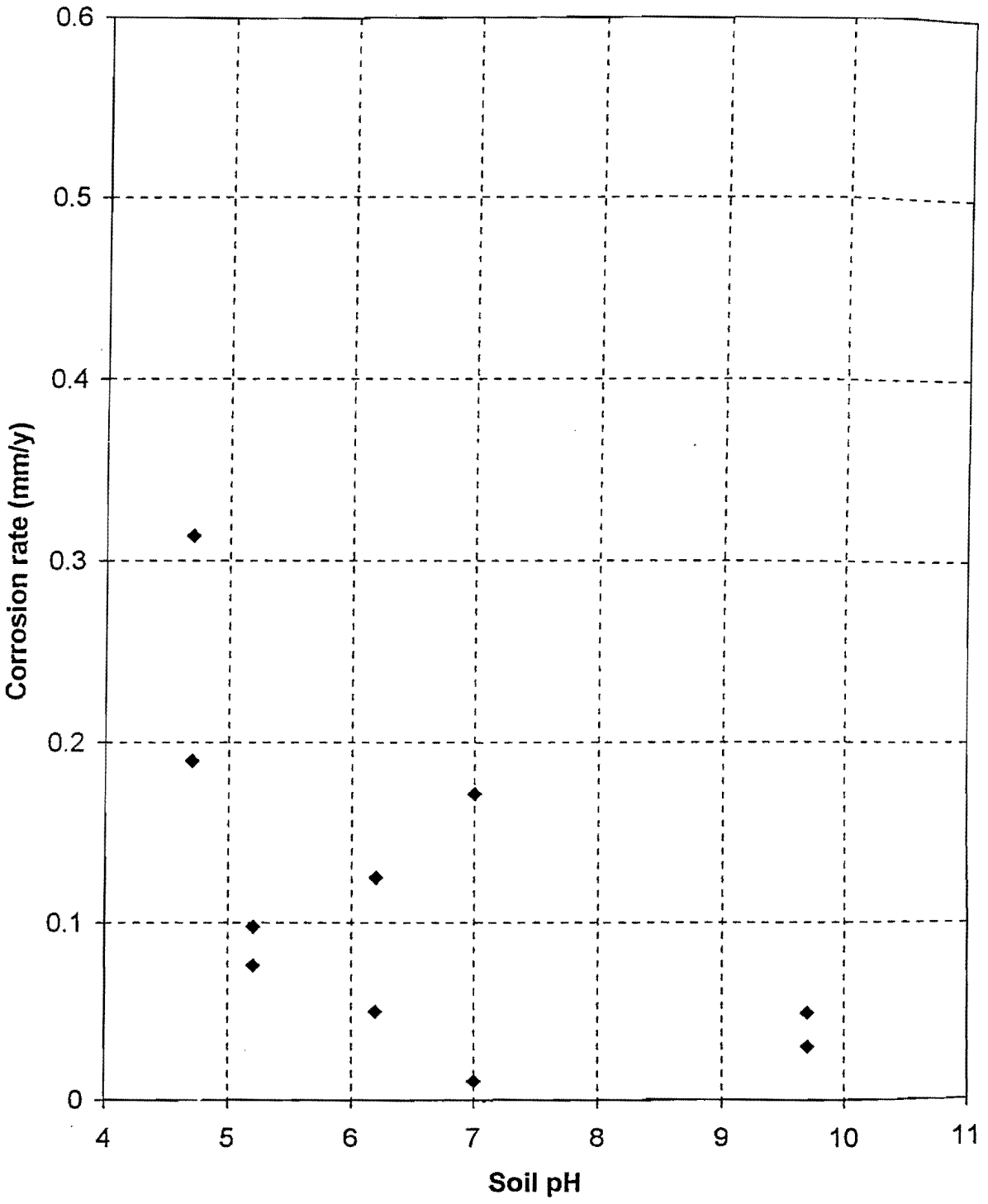

Figure 124. Corrosion Rate with Variations of Soil pH (Sand Sample)

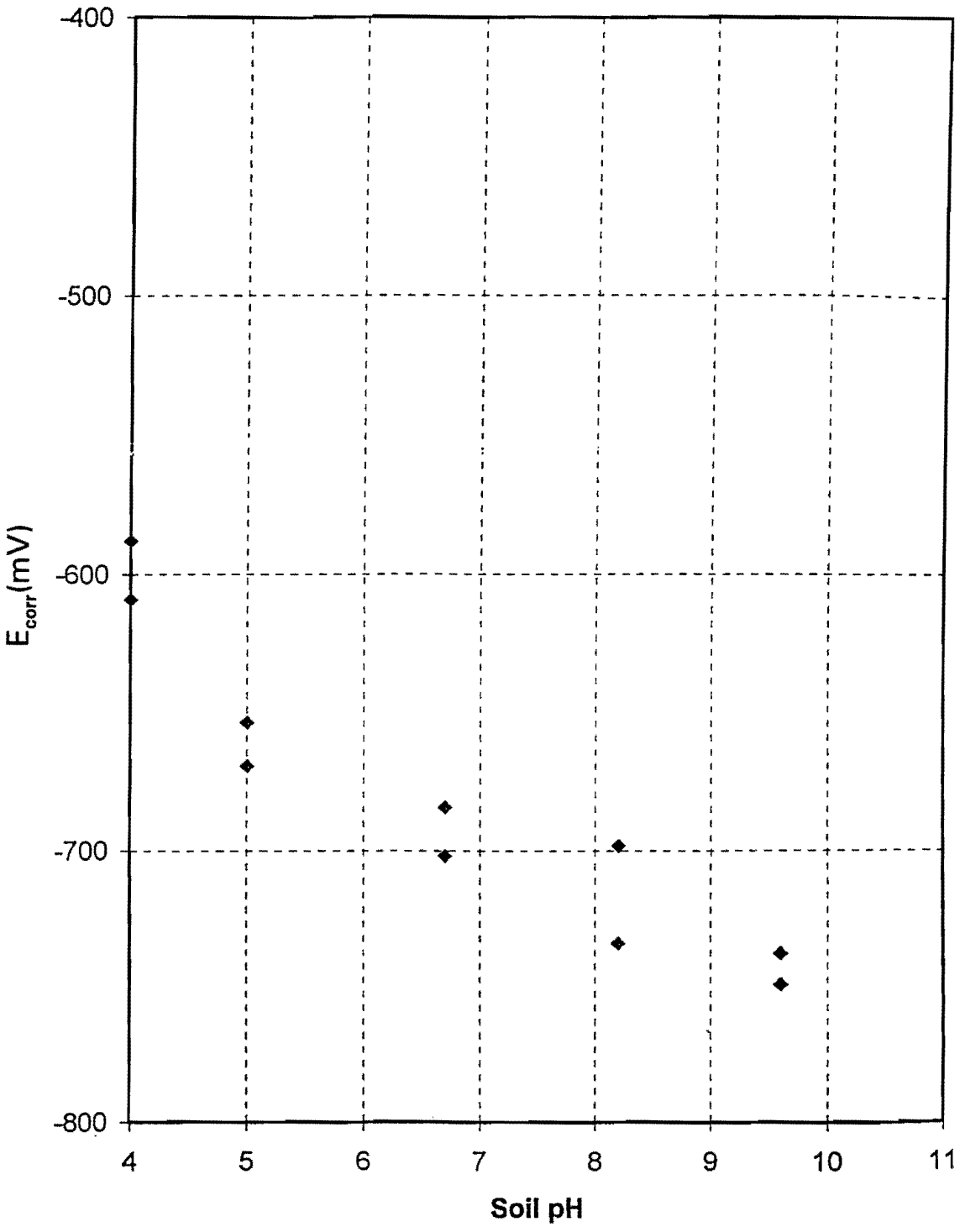

Figure 125. Corrosion Potential with Variations of Soil pH (Porcelain Clay Sample)

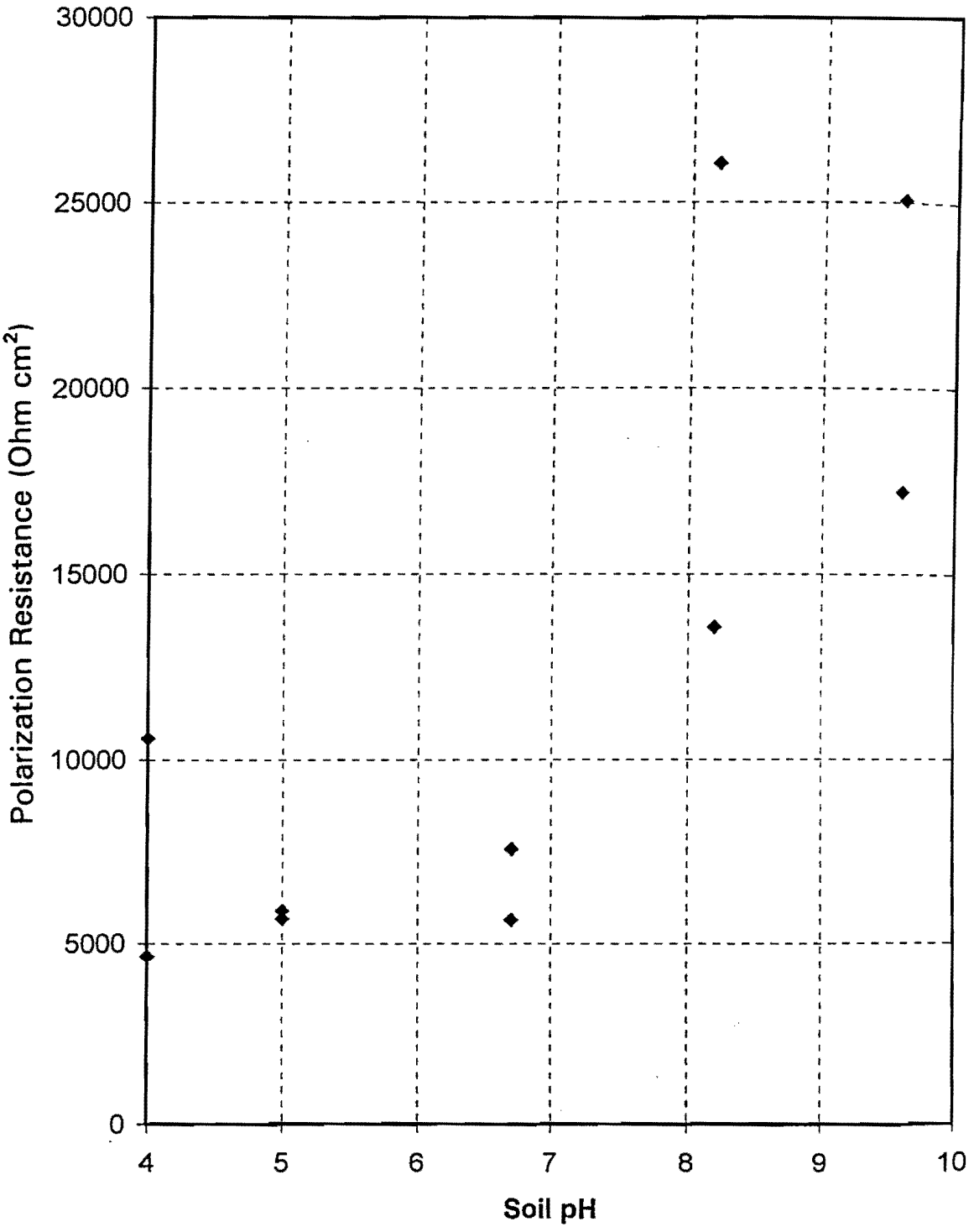

Figure 126. Polarization Resistance with Variations of Soil pH (Porcelain Clay Sample)

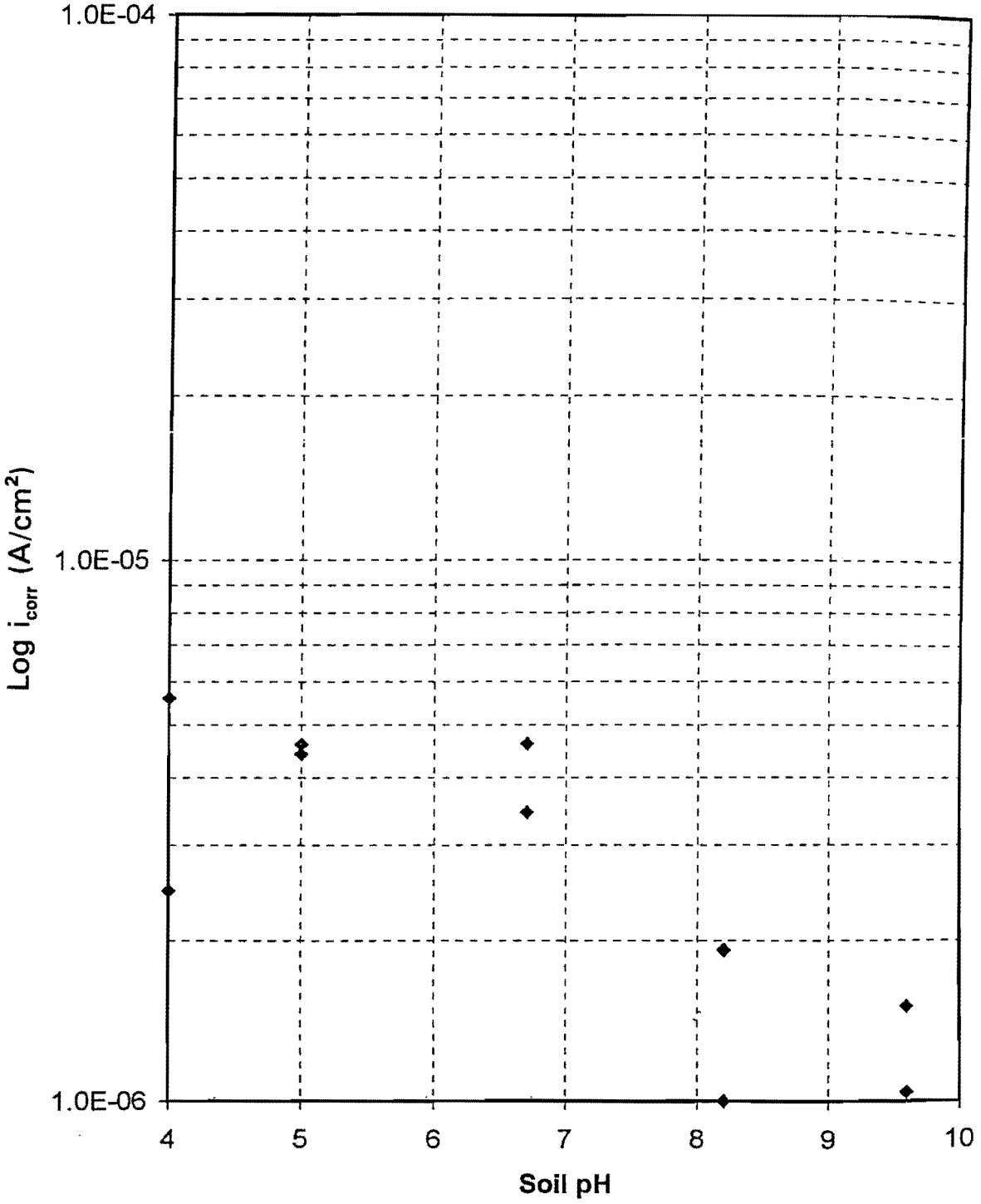

Figure 127. Corrosion Current Density with Variations of Soil pH (Porcelain Clay Sample)

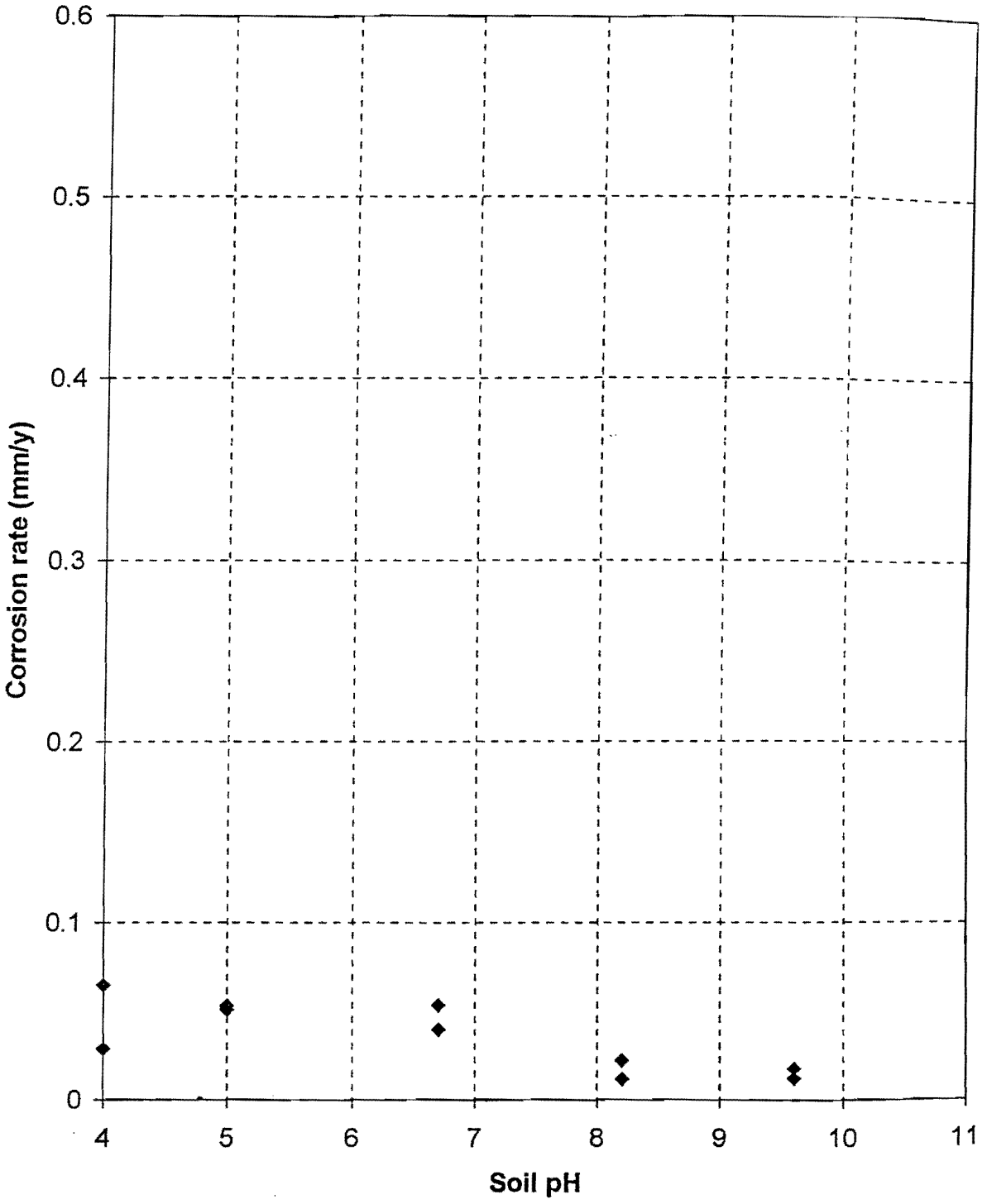

Figure 128. Corrosion Rate with Variations of Soil pH (Porcelain Clay Sample)

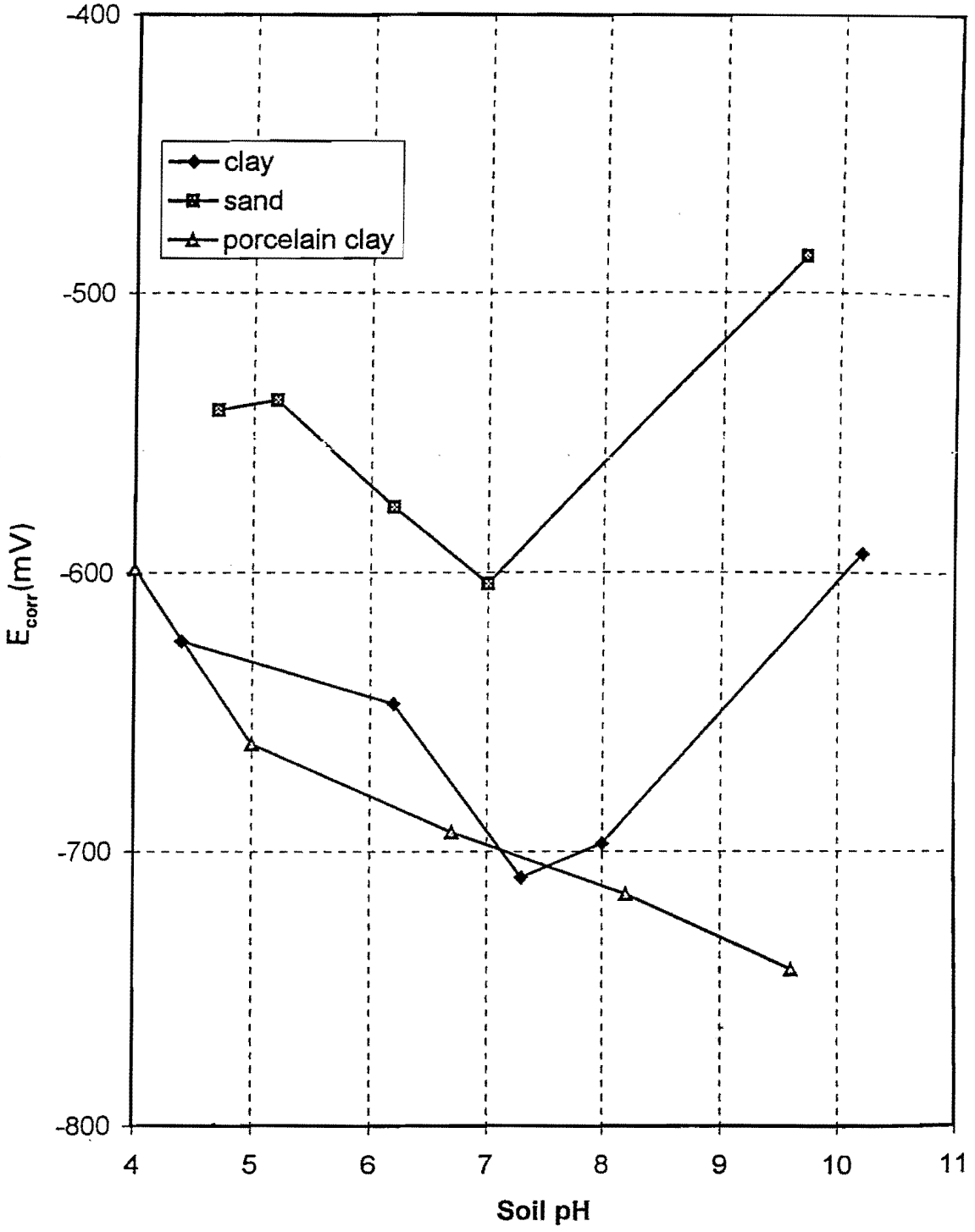

Figure 129. Comparison of Corrosion Potential with Variations of Soil pH

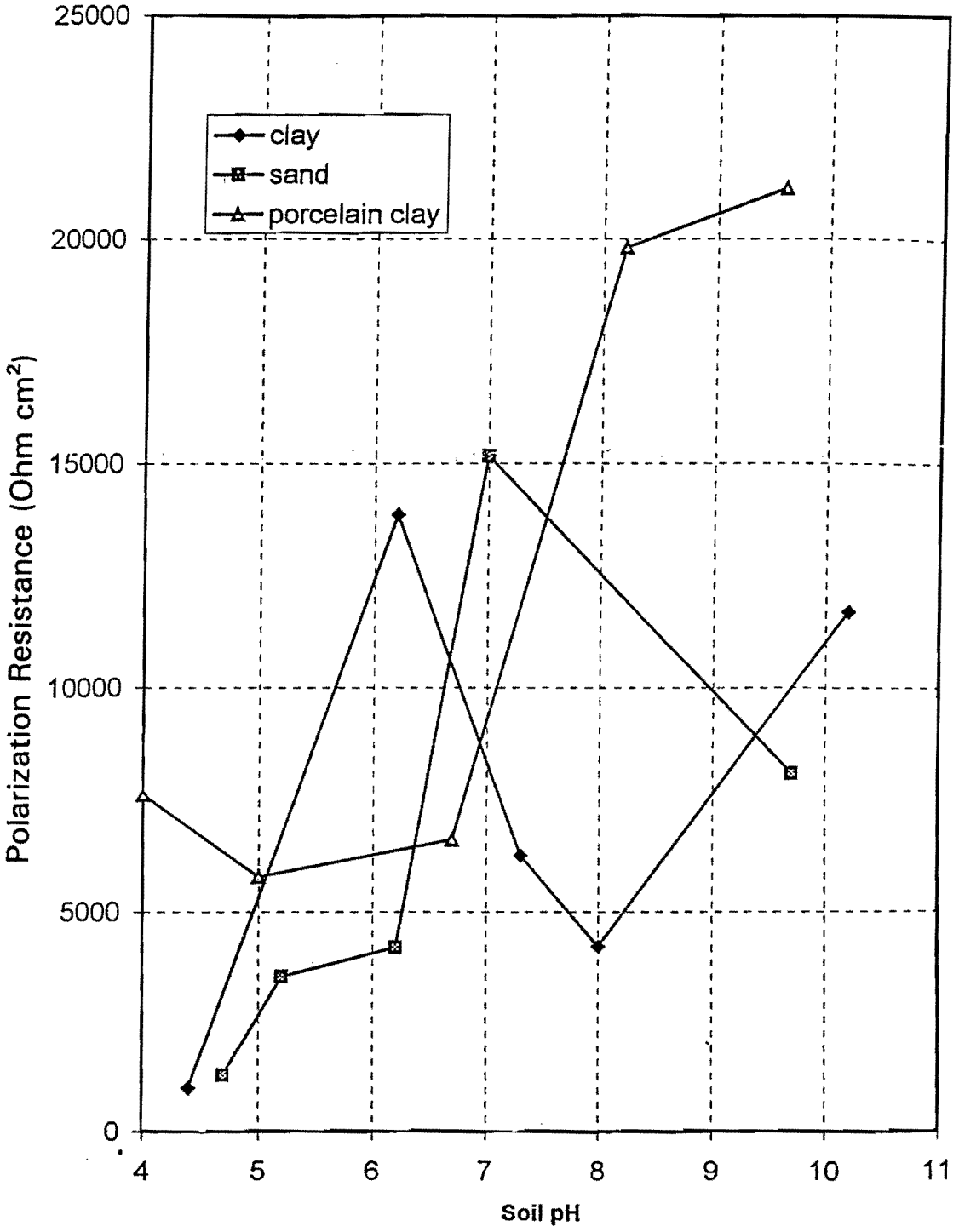

Figure 130. Comparison of Polarization Resistance with Variations of Soil pH

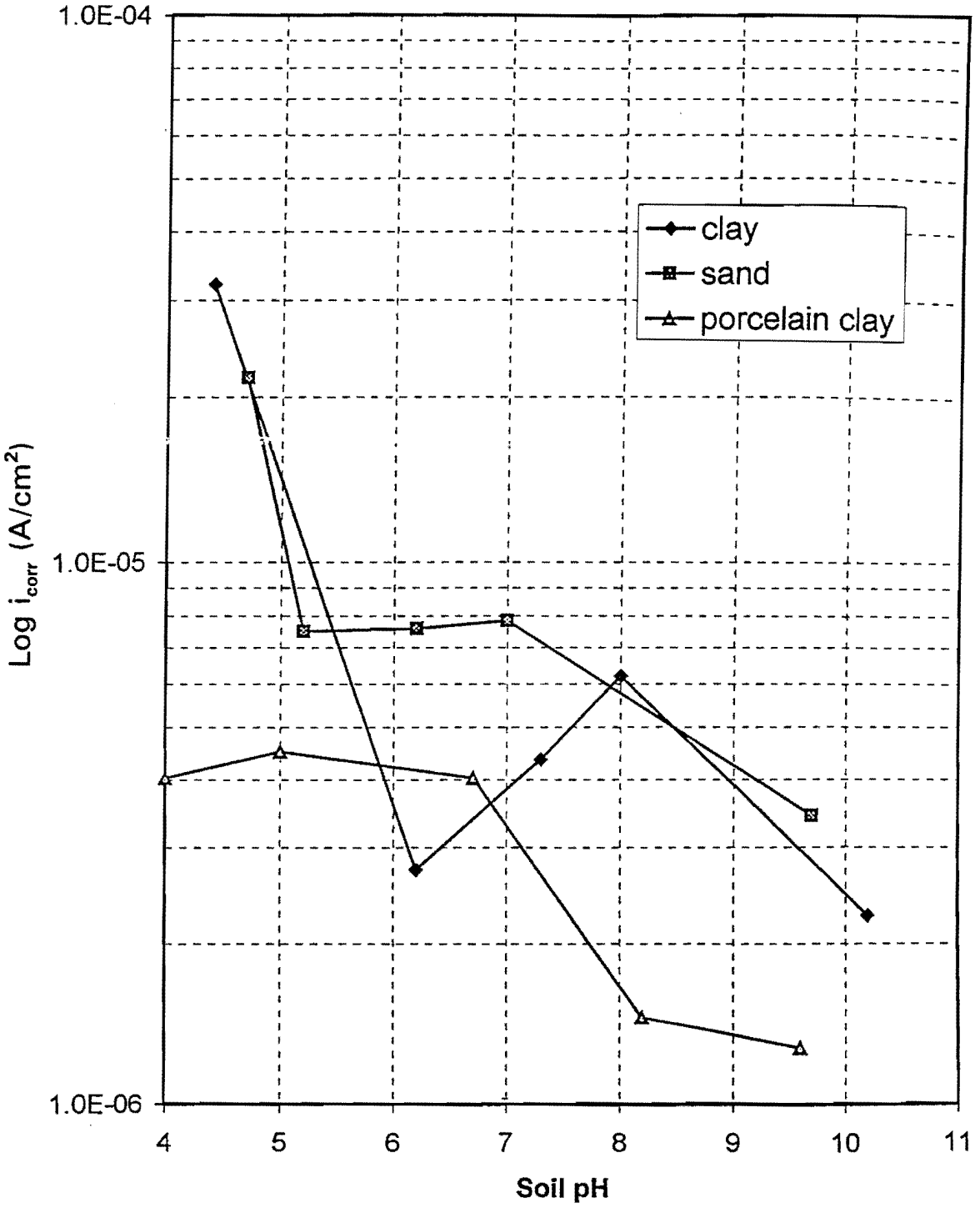

Figure 131. Comparison of Corrosion Current Density with Variations of Soil pH

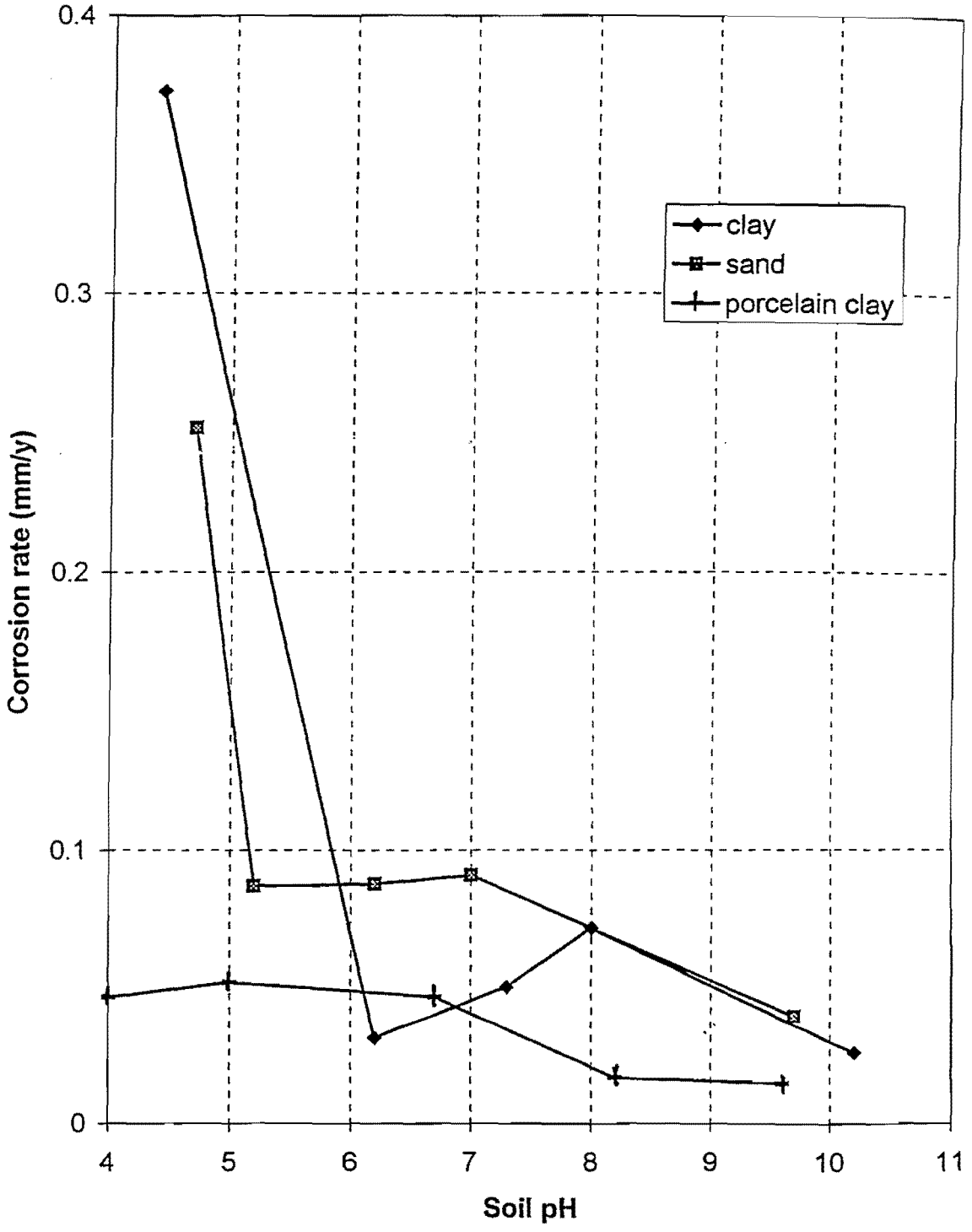

Figure 132. Comparison of Corrosion Rate with Variations of Soil pH (Polarization Resistance Measurement)

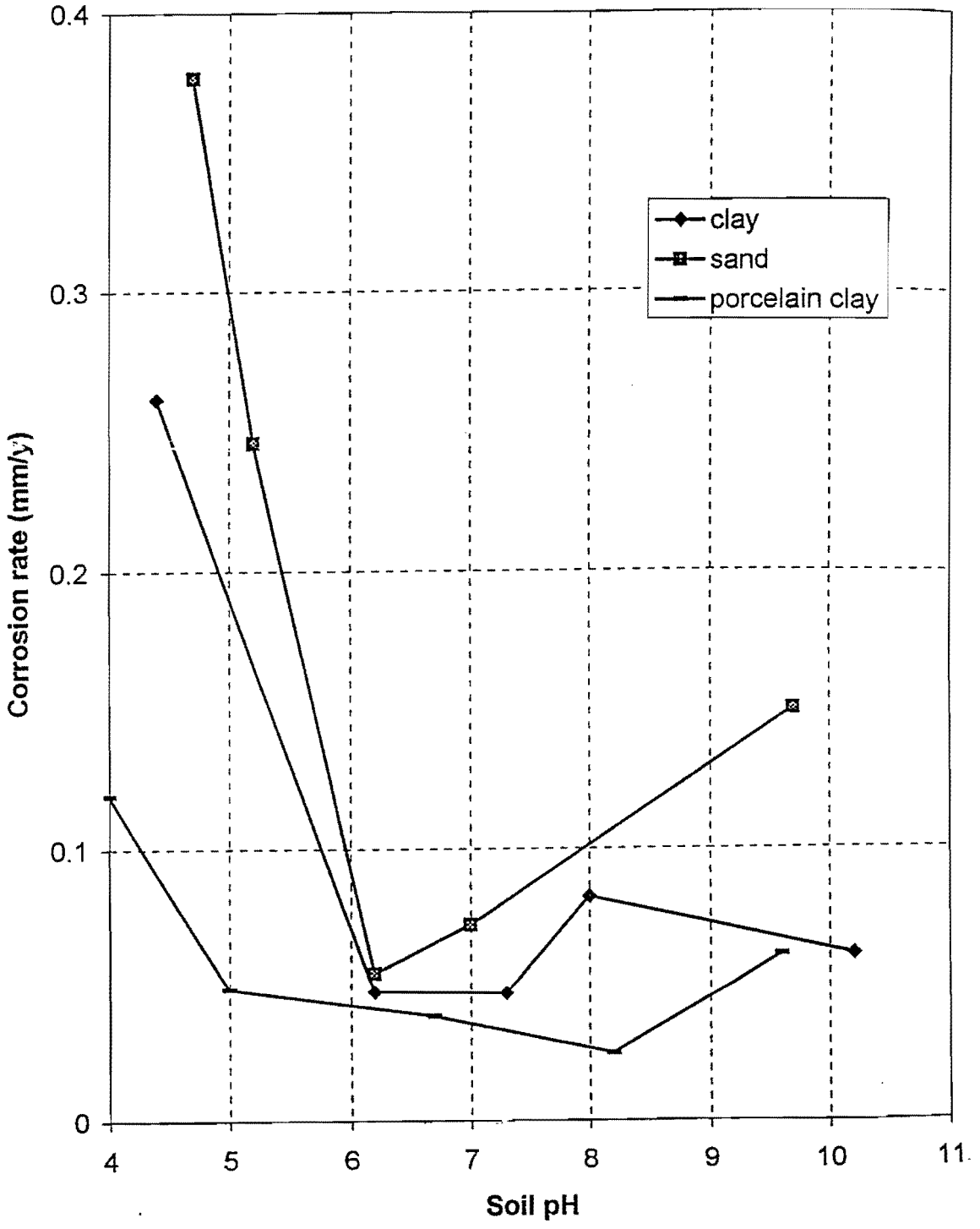

Figure 133. Comparison of Corrosion Rate with Variations of pH in Different Soils (Tafel Extrapolation Method)

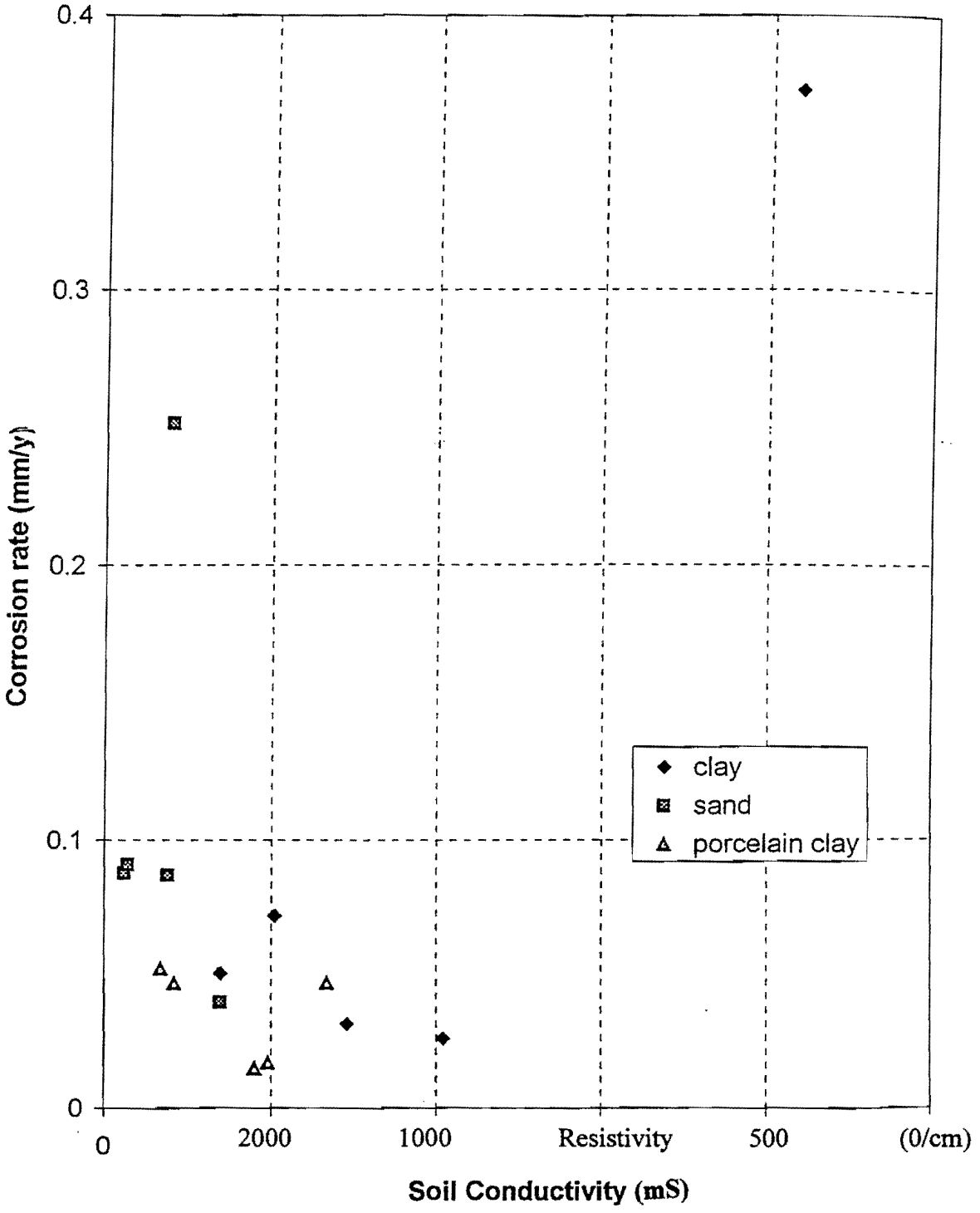

Figure 134. Comparison of Corrosion Rate with Variations in Soil Conductivity (Polarization Resistance Measurement)

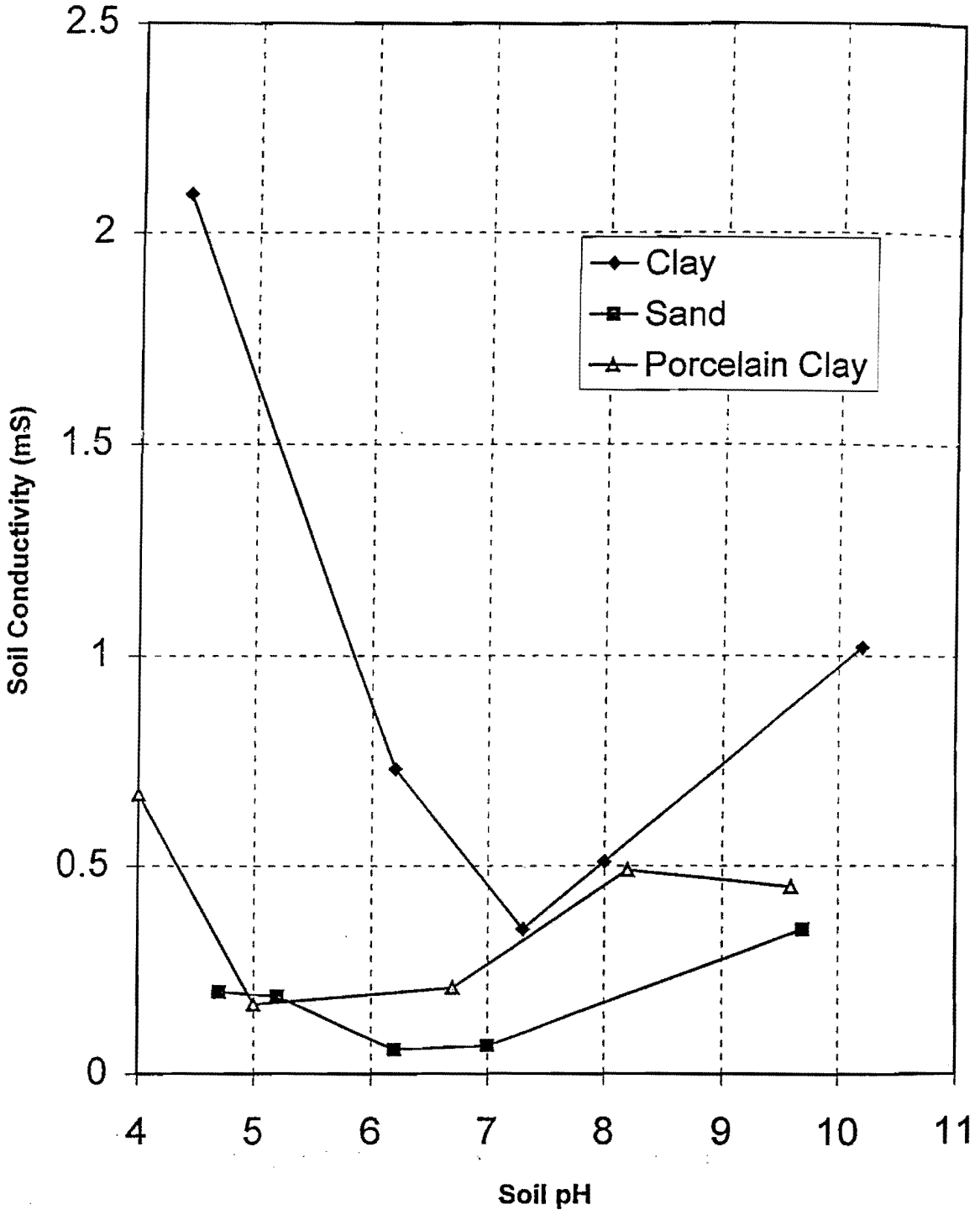

Figure 135. The Relationship Between Soil Conductivity and Soil pH

Table 21. The Results of Polarization Resistance Measurement

a. Clay

pH	Test No.	E_{corr} (mV)	I_{corr} (A/cm²)	Rp (Ohms cm²)	Corrosion Rate (mm/y)
4.4	1	-625.5	1.8E-05	1412	0.214
	2	-623.5	4.6E-05	569.9	0.530
6.2	1	-600.4	1.2E-06	21610	0.013
	2	-693.5	4.3E-06	6122	0.049
7.3	1	-696.7	5.3E-06	4964	0.060
	2	-722.5	3.5E-06	7540	0.040
8	1	-714.4	6.1E-06	4285	0.070
	2	-680.3	6.3E-06	4135	0.073
10.2	1	-600.7	2E-06	12720	0.023
	2	-586	2.4E-06	10660	0.028

b. Sand

pH	Test No.	E_{corr} (mV)	I_{corr} (A/cm²)	Rp (Ohms cm²)	Corrosion Rate (mm/y)
4.7	1	-540.4	1.6E-05	1594	0.189
	2	-544.1	2.7E-05	965.3	0.313
5.2	1	-544.8	6.6E-06	3965	0.076
	2	-532.6	8.4E-06	3099	0.097
6.2	1	-632.8	4.4E-06	5972	0.050
	2	-520.8	1.1E-05	2415	0.124
7	1	-609.9	9.1E-07	28560	0.010
	2	-598.1	1.5E-05	1766	0.171
9.7	1	-487.5	2.6E-06	10030	0.030
	2	-487	4.3E-06	6119	0.049

c. Porcelain Clay

pH	Test No.	E_{corr} (mV)	I_{corr} (A/cm²)	Rp (Ohms cm²)	Corrosion Rate (mm/y)
4	1	-588.1	2.5E-06	10560	0.028
	2	-609.2	5.6E-06	4660	0.064
5	1	-669.5	4.4E-06	5895	0.051
	2	-653.6	4.6E-06	5669	0.053
6.7	1	-702	3.4E-06	7569	0.039
	2	-684.4	4.6E-06	5648	0.053
8.2	1	-733.2	1E-06	26040	0.011
	2	-698.3	1.9E-06	13570	0.022
9.6	1	-748.6	1.5E-06	17210	0.017
	2	-736.9	1E-06	25050	0.012

3.5.6.2.3 Porcelain Clay, Variations of Soil pH

Figures 125 through 128 show information on the corrosion characteristics of porcelain clays with variations in soil pH. Measurements of corrosion rate in porcelain clay were carried out as a function of soil pH as a reference data. In general, the corrosion rate of steel specimens embedded in porcelain clay is independent of variations of soil pH. As seen in Figure 128, the steel specimen in high-acidic porcelain clay (pH 4) shows a low corrosion rate (0.046 mm/y (LPR), 0.119 mm/y (TE)). As a result of polarization resistance measurements, the range of corrosion rate with variation of soil pH are between 0.014 mm/y and 0.052 mm/y which are relatively uniform and significantly low.

The variations of the corrosion potential, E_{corr} of bare steel specimen in different soil pH is presented in Figure 125. The E_{corr} values are inversely proportional to the soil pH and in the range of -588 mV and -748 mV.

3.5.6.2.4 The Effect of Soil Conductivity on Corrosion Rate of Steel Specimen

Figure 134 shows the corrosion rate of steel specimens with variations of soil conductivity. As can be seen, the data are so scattered that a reasonable trend cannot be obtained from these experiments. Even though soil conductivity is considered to be an important factor in underground corrosion, these particular tests do not identify a reasonable relationship.

Corrosion data suggest that resistivity tends to be higher in acid soils than alkaline soils. This effect is associated with moisture content, as highly neutral and alkaline soils generally contain a significant clay fraction. This will tend to lead to a higher moisture content, which will reduce the resistivity of soil (Elias, 1990).

Figure 135 shows the relationship between soil conductivity and soil pH for three different types of soil samples. As can be seen, the highly acidic (<5) and alkaline (>9) soil indicate high soil conductivity in most of cases. The soil conductivity of clay is extremely high compared to the sand and the porcelain clay.

The results of potentiodynamic polarization measurements can be summarized as follows. Figures 129 through 135 summarize the comparison of electrochemical parameters of steel specimens embedded in the different types of soil samples. Uncoated steel specimens embedded in clay and sand with low pH environments show high corrosion rates of 0.53 mm/y and 0.31 mm/y, respectively. However, steel specimens in porcelain clay with pH>4 have a relatively low corrosion rate. The steel specimens in a natural pH condition showed low corrosion rates and no significant difference in corrosion rates with respect to the soil type. In the case of soil beyond pH 6, the corrosion rates are constant with variations of soil pH. This result implies that steel specimens in neutral and alkaline environments have a lower probability of corrosion occurring.

3.5.7 Electrochemical Impedance Spectroscopy (EIS)

The objectives of this experiment are the evaluation of corrosion behavior for coating/metal systems including cement grouting. Electrochemical Impedance Spectroscopy (EIS) has been used successfully to determine the characteristic of the electrochemical interface, of interest, under controlled conditions. The laboratory experiments were devised to simulate the possible causes of corrosion attack in tieback anchors. EIS results can aid in the selection of coating materials and guidelines for corrosion protection of tieback anchors.

3.5.7.1 Background

EIS monitors the response of corroding electrodes to small-amplitude alternating potential signals of widely varying frequency. Bard et al. (1980) has expressed the time-dependent signal $I(t)$ on an electrode surface to a sinusoidal alternating potential signal $V(t)$ as an angular frequency (ω), where

$$\begin{aligned} Z(\omega) &= V(t) / I(t), \\ V(t) &= V_o \sin \omega t, \\ I(t) &= I_o \sin(\omega t + \theta), \text{ and} \\ \theta &= \text{phase angle between V(t) and I(t).} \end{aligned}$$

Since the electrochemical processes absorbs electrical energy at discrete frequencies, it causes a time delay and phase angle between excitation and response signals. Circuit analog models are used to model the electrochemical processes and reactions. In this report, the Bode plot was used to analyze the data.

It consists of two types of plots such as the bode magnitude and phase plot shown in Figure 136. The bode magnitude plot can be obtained from the magnitude of the impedance versus the frequency on a log scale. The Bode phase plot displays the relationship between the phase shift and the frequency in semilogarithmic scale. A resistor has an impedance which is independent of frequency and has zero phase angle. However, a capacitor has an impedance, which decreases linearly with frequency and has a 90-degree phase angle.

Electrochemical reactions allow the use of equivalent electrical circuits for evaluation purposes. Resistors and capacitors represent the electrical properties of various components of the coated specimens and electrolytes. The use of electrical circuits in a circuit analog model is the basis of Electrochemical Impedance Spectroscopy (EIS). EIS is an AC system that measures the resultant impedance for a given frequency. Impedance measurements are taken over a broad frequency range (10^{-3}~10^{4} Hz). The results expressed in terms of impedance are used to find the representative values for the resistors and capacitors for these circuits.

Figure 137 shows the Randles circuit representing an uncoated metal specimen. The solution resistance, R_{soln} is the resistance of the electrolyte between the reference electrode and the working

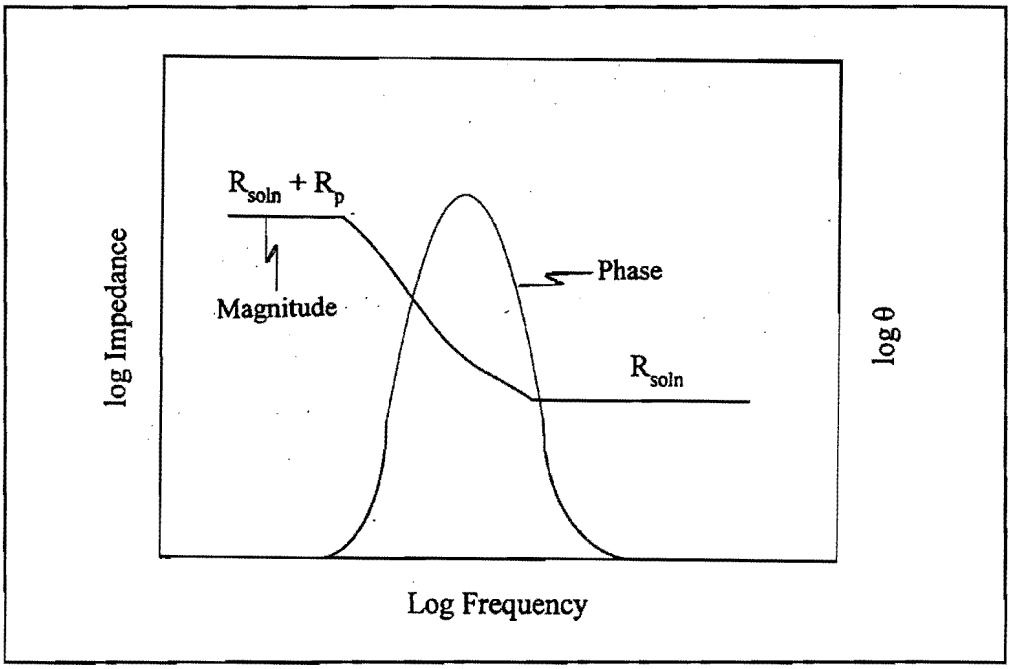

Figure 136. Bode-Magnitude and Phase Plot for an Uncoated Specimen

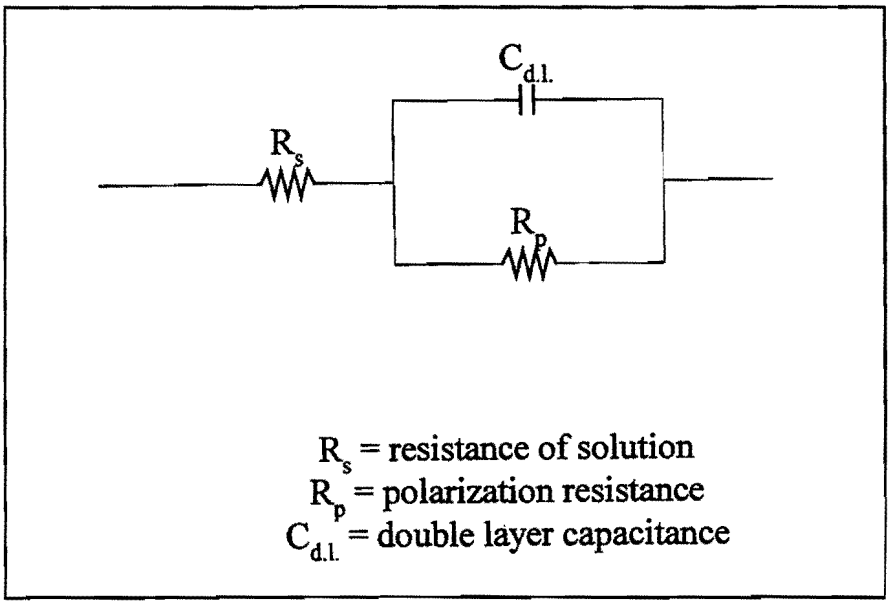

Figure 137. Equivalent Electronic Circuit for a Simple Cell with an Uncoated Specimen

electrode. The polarization resistance, R_p, is the charge transfer at the electrode/solution interface or more specifically at the anodic and cathodic reaction. The double layer capacitance, C_{dl}, is an electrochemical capacitor formed by the interactions of ions from the solution and the specimen at the surface of the substrate.

At low frequencies the capacitor acts as an open circuit and measurements of the various resistances in series can be performed. At high frequencies the capacitor acts as a short and the solution resistance can be measured. Results for the Randles circuit are typically presented in Bode-Magnitude plots (Figure 136).

The equivalent circuit shown in Figure 138 is representative of a metallic substrate with a nonconductive coating. Pore resistance, R_{pore}, is a measure of the holidays within the coating. In the case where no penetration of the coating by the electrolyte has occurred, the pore resistance is not observed in the Bode plot.

The coating capacitance, C_c, is similar in nature, with respect to its behavior, to the double layer capacitance. At high frequency, both capacitors act as a short and the solution resistance can be measured. At lower frequencies, the coating capacitor acts as an open circuit and the double layer capacitor as a short, such that the sum of the pore and solution resistance can be measured. At the lowest range of frequencies both capacitors act as an open circuit and the total resistance can be measured. A typical Bode plot for the equivalent circuit is shown in Figure 139.

3.5.7.2 Test Conditions

EIS measurements were also used to determine the effects of coating systems and cement grouting on the steel specimens. The experiments were carried out by measuring corrosion rates as a function of time in several samples and the results were compared with each other. The following list presents the sample conditions to be tested (Figure 140):

1. A natural soil
2. Cement grouting without a crack
3. Cement grouting with a crack
4. Variations of grouting thickness
5. Painted epoxy coating
6. Fusion bonded epoxy coating

(Conditions 1, 2, and 3 were performed on the acrylic coated and uncoated steel surface. The acrylic coating was sprayed on the surface of the steel.)

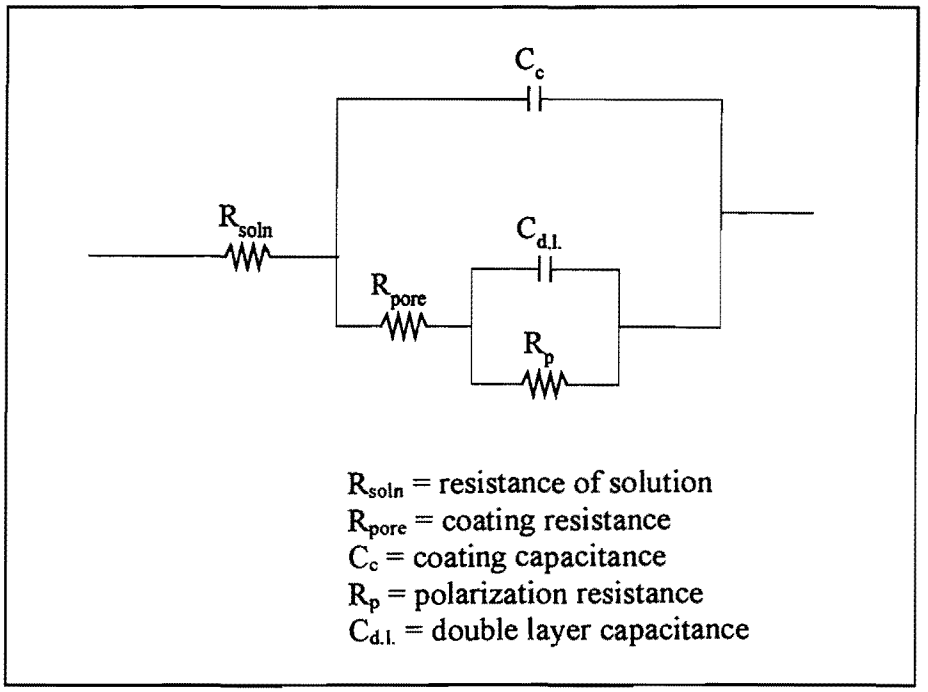

Figure 138. Equivalent Electronic Circuit for a Coating Specimen

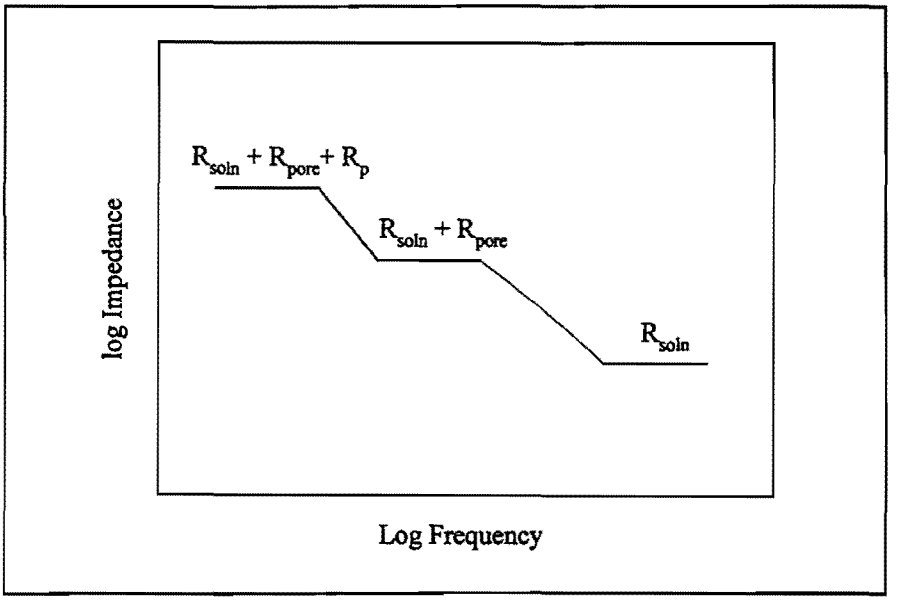

Figure 139. Bode-Magnitude Plot for a Coated Specimen

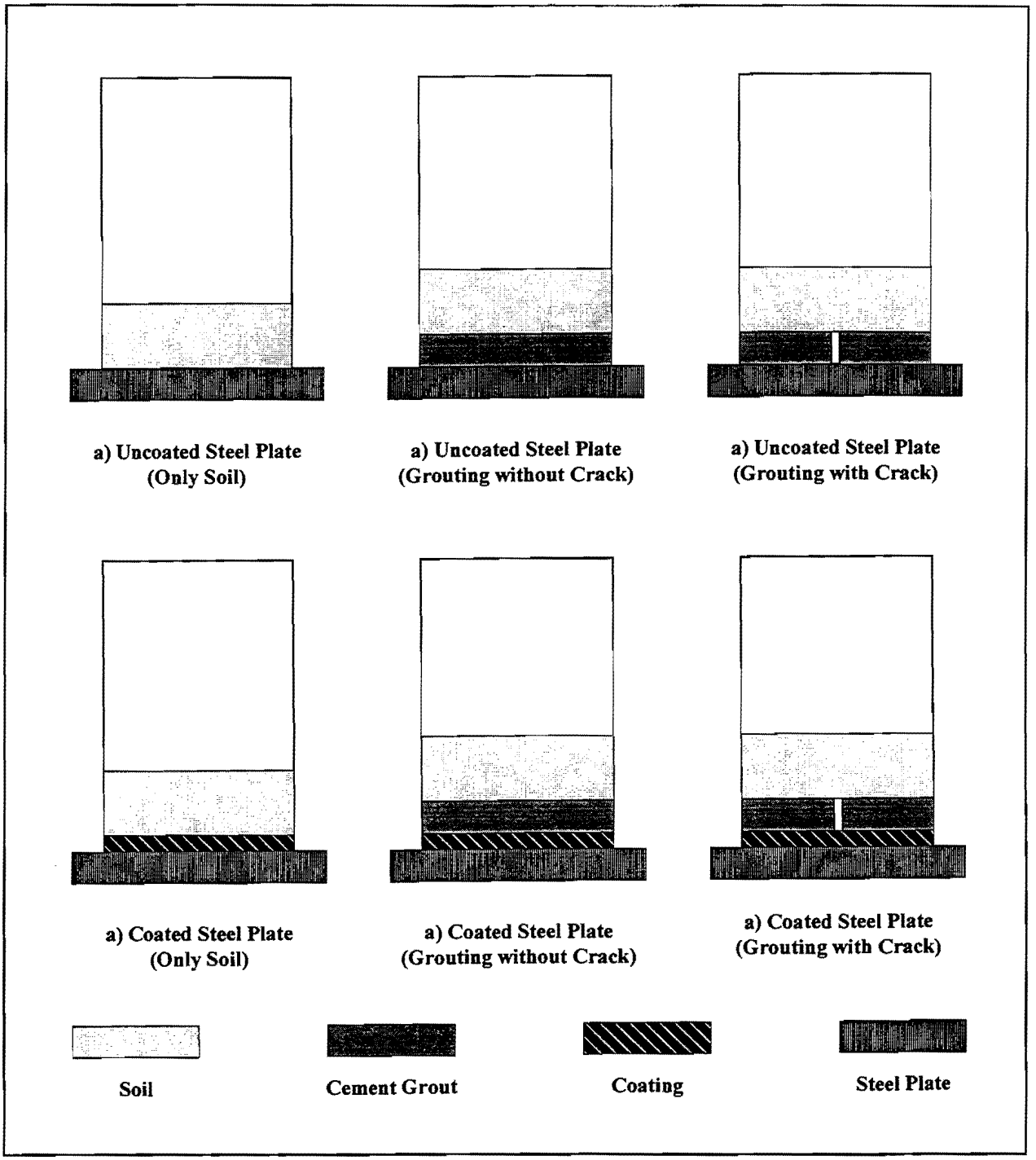

Figure 140. Preparation of Environment Cells for EIS. Various Combinations Used During the EIS Testing

3.5.7.3 Test Methods and Procedures

The following items represent the test procedures for measuring corrosion by EIS.

1. The environment cell design was prepared as shown in Figure 141. The soil was compacted in a 66 mm diameter environment cell. The thickness of the grout and of the soil sample is 5, 10, and 20 mm respectively. The diameter of soil and grout specimen is 65 mm. The surface of the steel plate was sanded to remove the light rust and degreased in methanol before use.

2 The surface of the steel plate was coated with acrylic, epoxy, or fusion-bonded epoxy.

3. These tests were performed on the grout with and without cracks. The grouting was made of Portland cement and water by mixing, with a water/cement ratio of 0.40. In the case without cracks, the grout was cured for a day in an air condition location and, then for a week in water to prevent the propagation of cracks in the surface. For the cases with cracks, the crack, in the grout passed through the center and was 1 mm or 2 mm in width.

4. The soil covering the grout surface was maintained at 35% moisture content, to simulate the field condition.

5. A Model 5301 Lock-in Amplifier and a Model 273 Potentiostat from EG&G Princeton Applied Research were used for controlling the experiment and for data acquisition for the EIS test. Manipulation of the data was performed on a 286 pc using the M388 software. This instrumentation employs a combination of two methods to collect data over a wide range of frequencies:

    1) the fast Fourier transform technique (0.01Hz to 5Hz)
    2) phase-sensitive lock-in detection (5Hz to 10kHz)

    Since the system also includes a computer with dedicated software, it is possible to automatically sequence data acquisition and merge the data from the two methods.

3.5.7.4 Data Reduction and Results

1. Initially plot a Z (Impedance) versus frequency (Hz) to obtain the polarization resistance (Bode Plot) for every specimen (Figures 142 through 149).

2. Observe the polarization resistance as a function of time (initially, three days, 10 days, and one month).

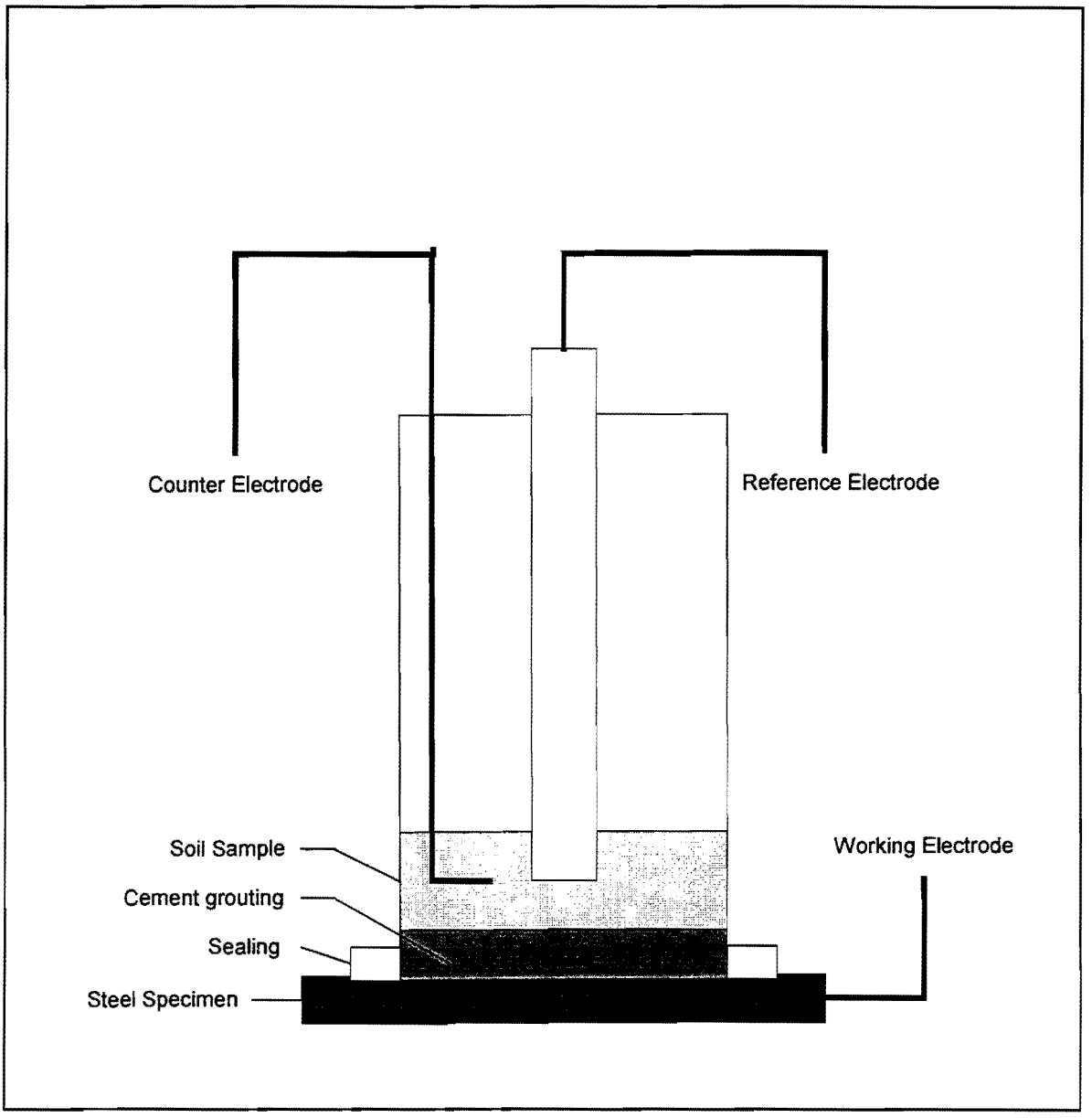

Figure 141. A Schematic of Environment Cell Design

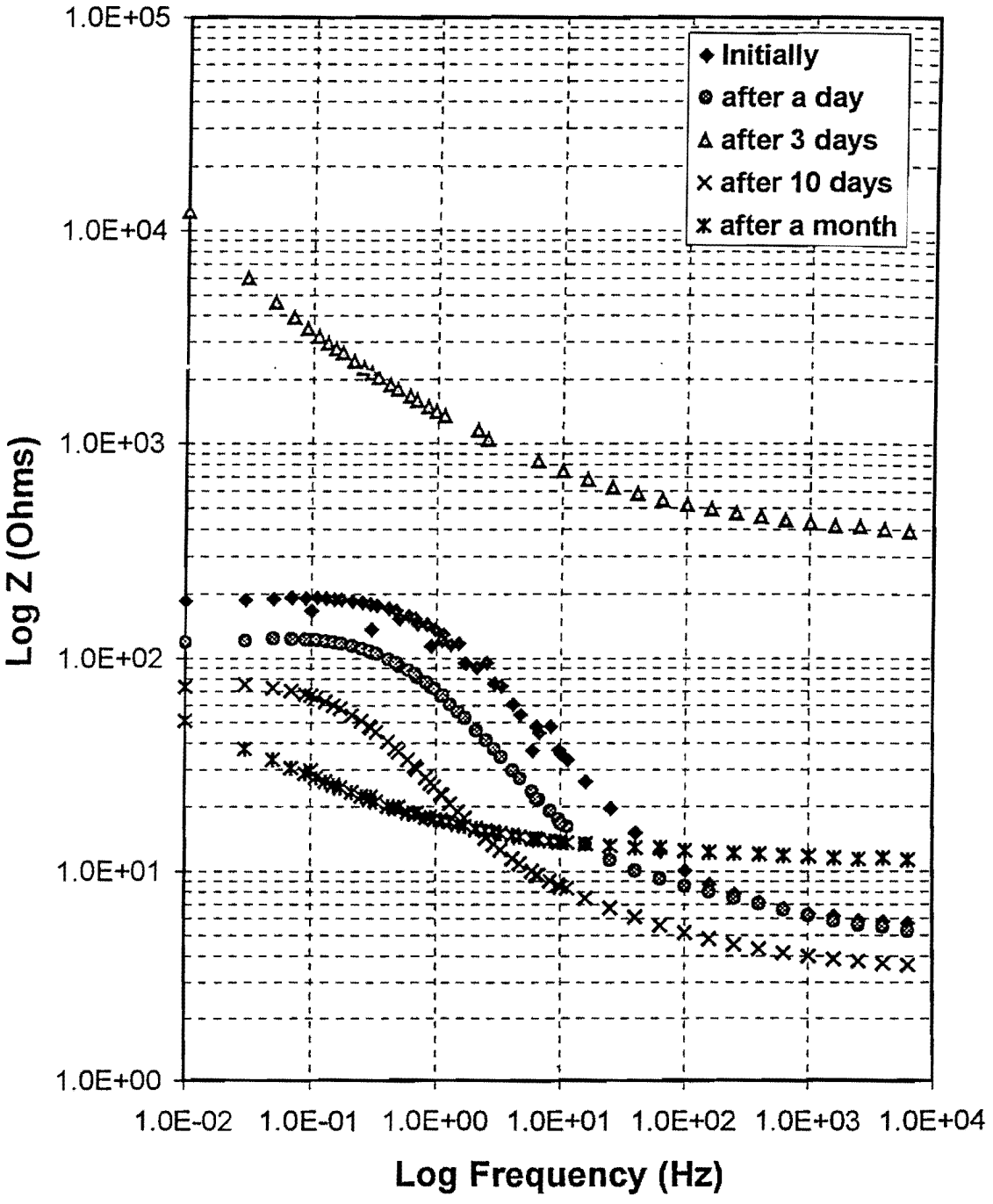

Figure 142. Bode-Magnitude Plots as a Function of Time (Uncoated Steel Specimen in Clay)

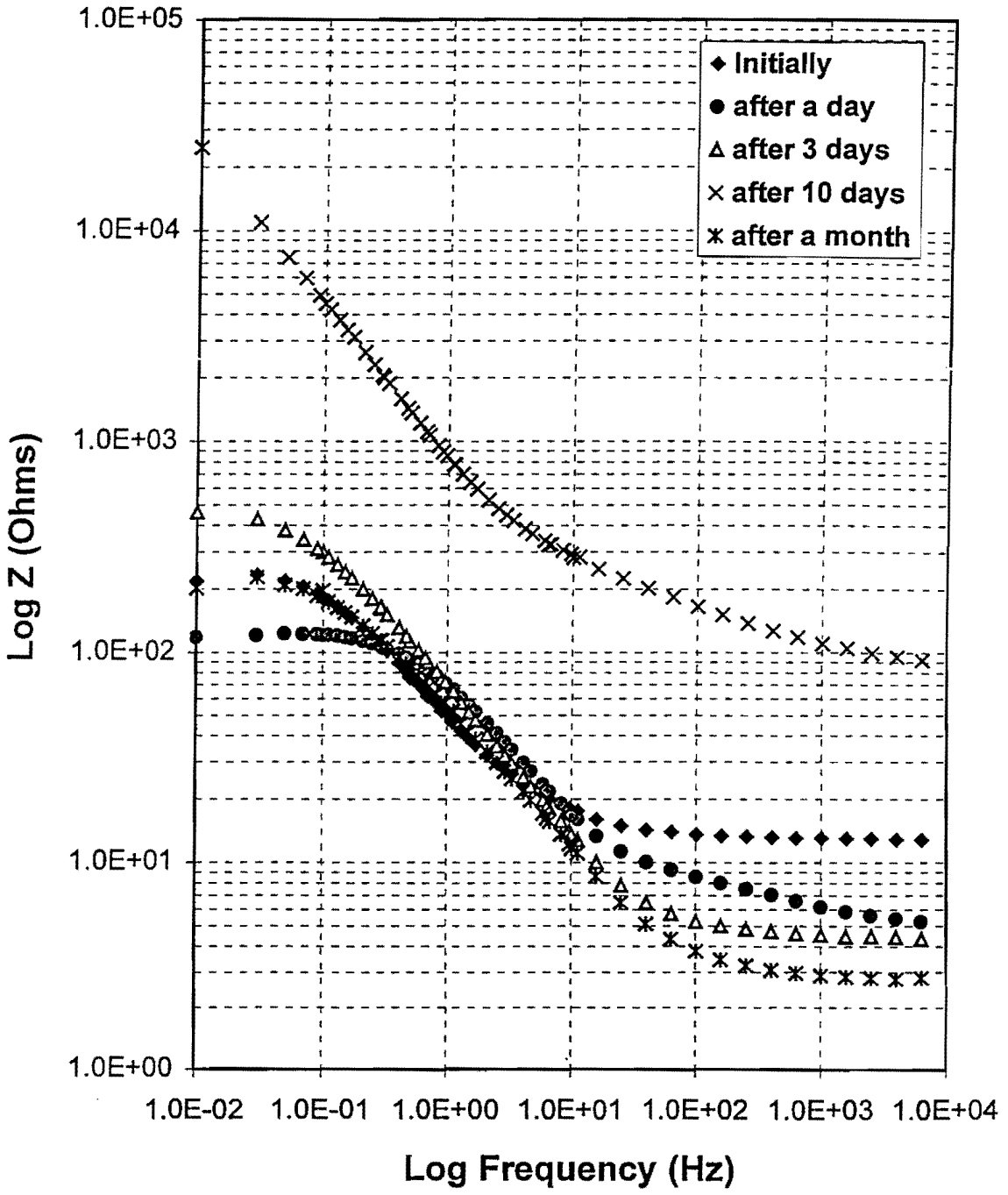

Figure 143. Bode-Magnitude Plots as a Function of Time (Coated Specimen in Clay)

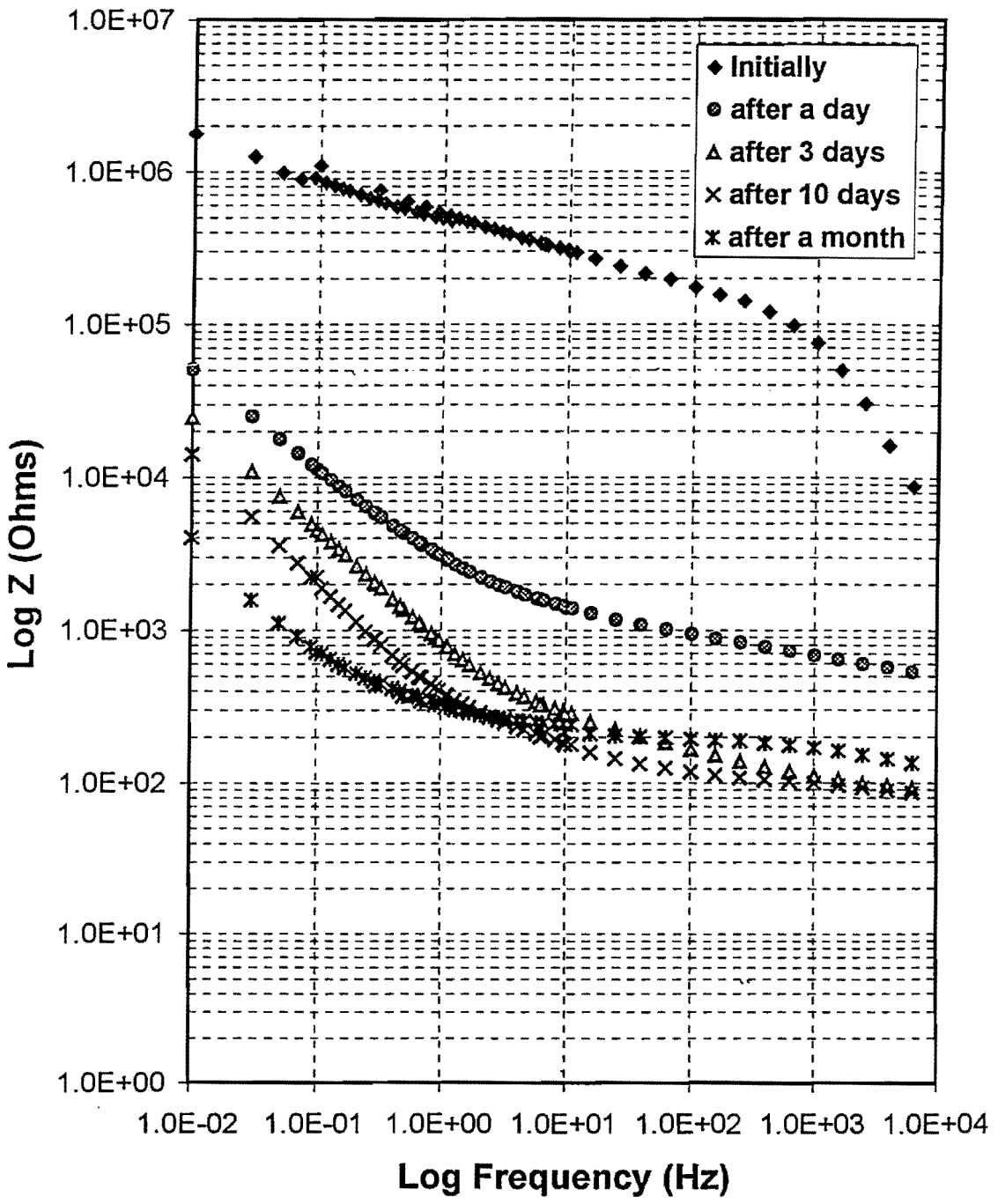

Figure 144. Bode-Magnitude Plots as a Function of Time (Uncoated Steel Specimen in the Grouting)

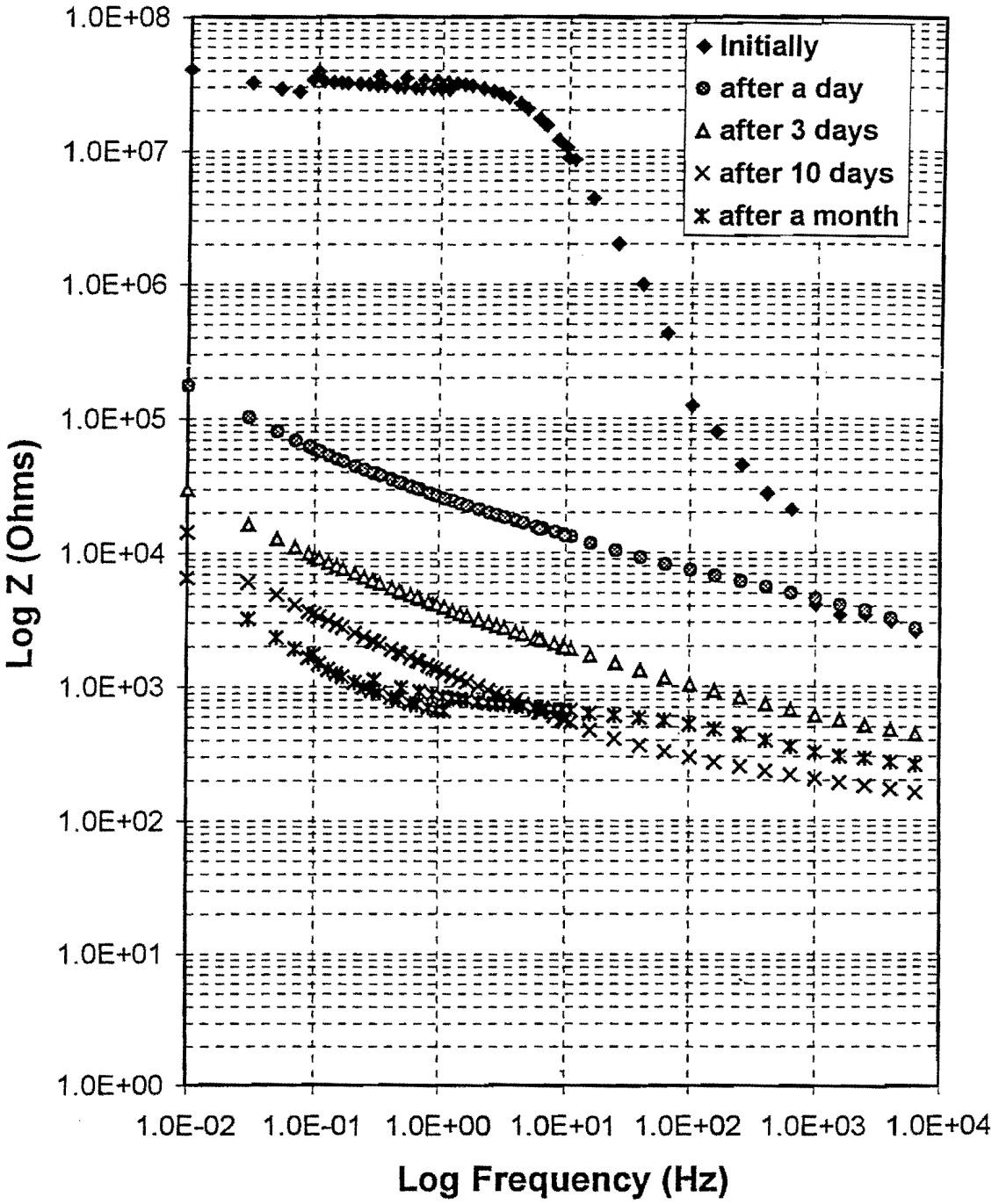

Figure 145. Bode-Magnitude Plots as a Function of Time (Coated Steel Specimen in the Grouting)

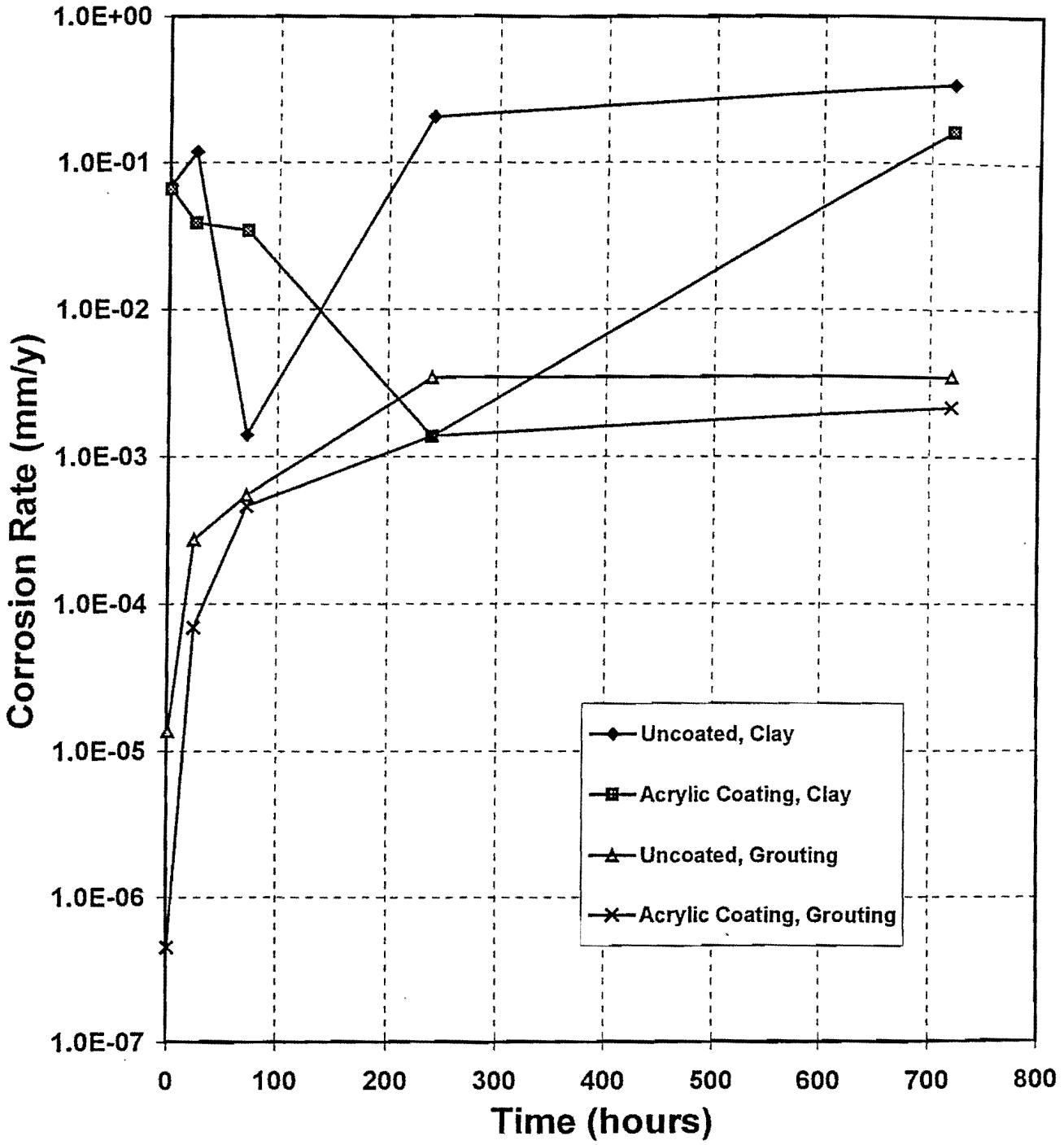

Figure 146. Corrosion Rate of Steel Specimen as a Function of Time (Embedded in Clay or Grouting)

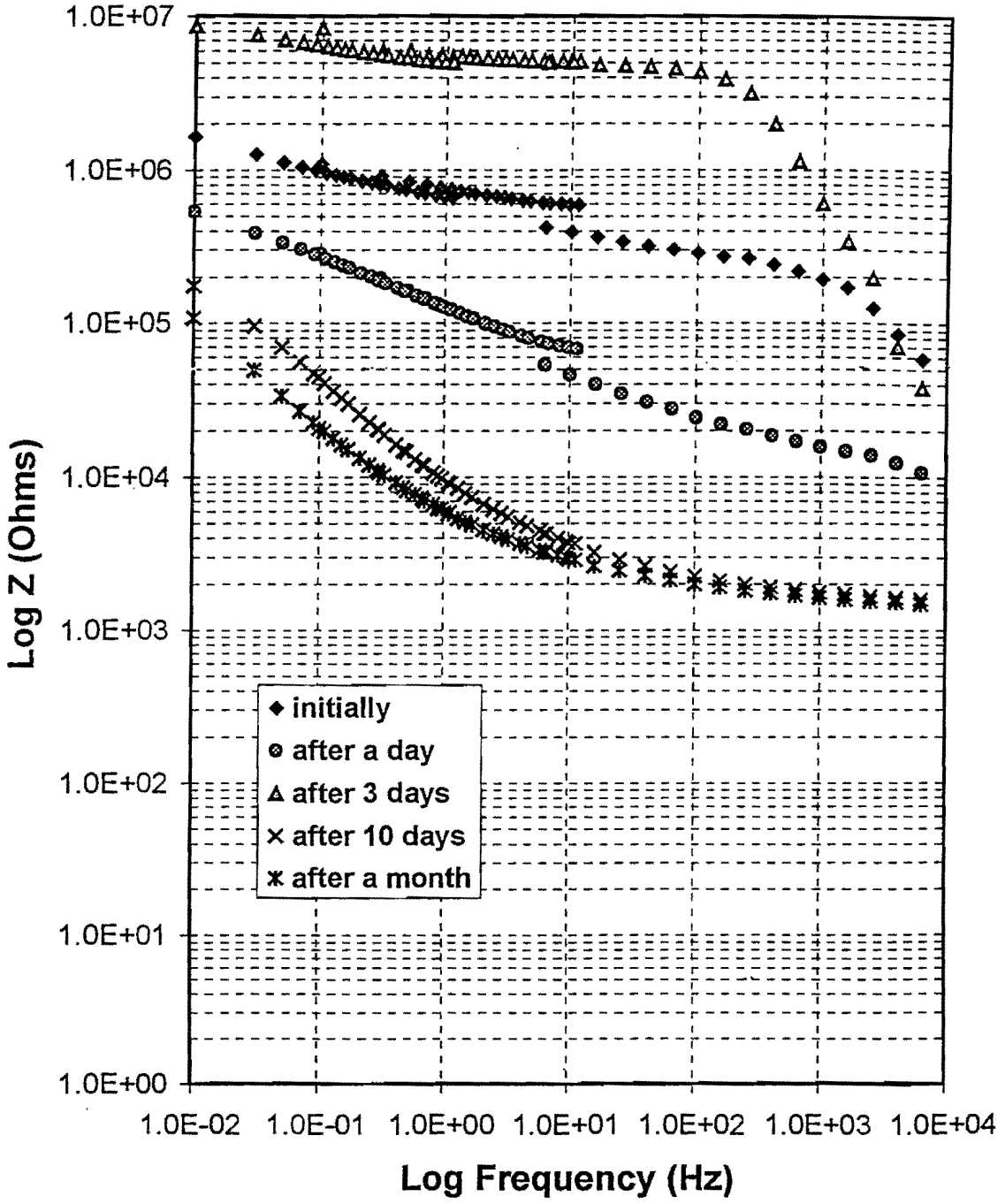

Figure 147. Bode-Magnitude Plots as a Function of Time (Uncoated Steel Specimen in Grouting with 1 mm Crack)

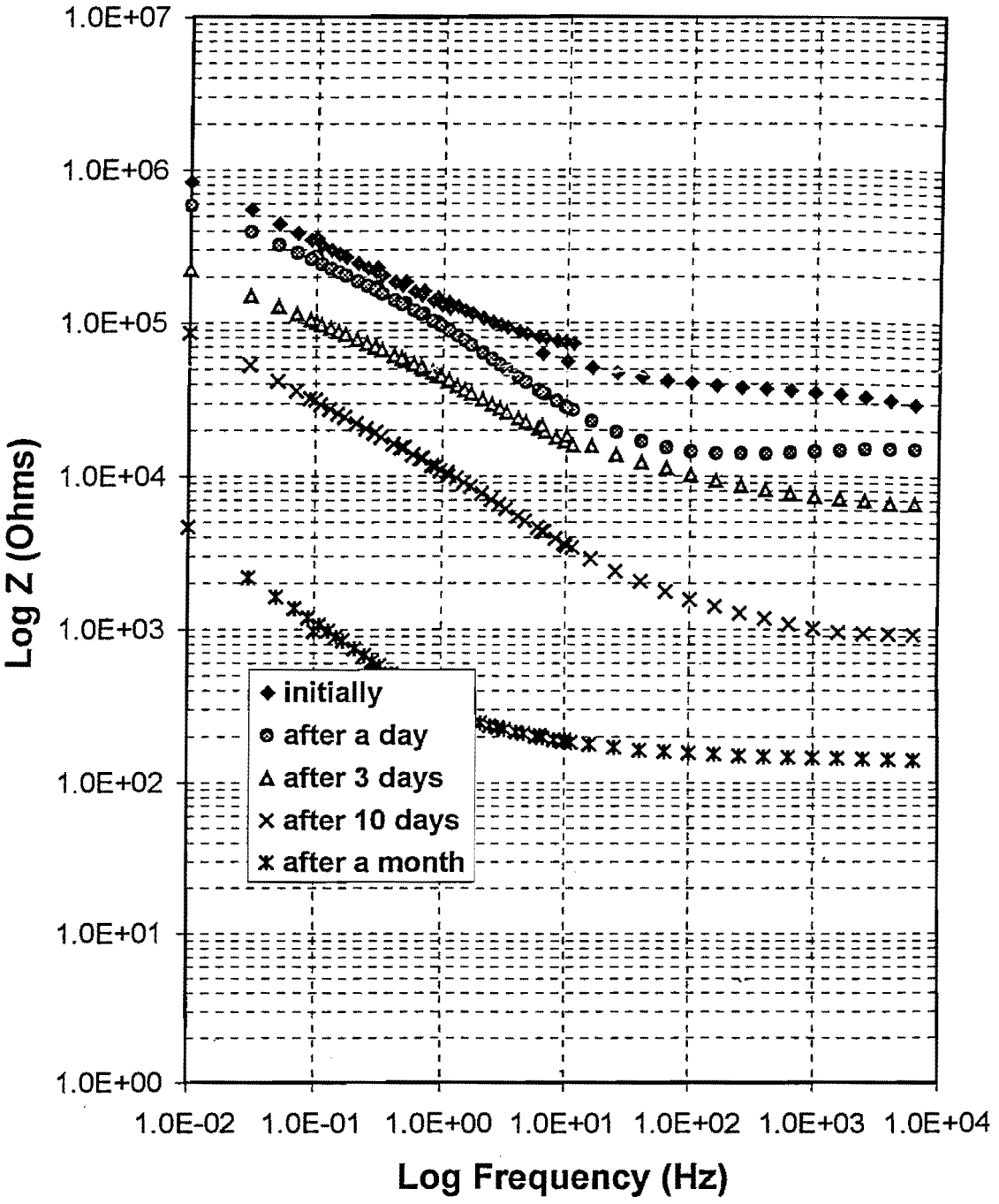

Figure 148. Bode-Magnitude Plots as a Function of Time (Uncoated Steel Specimen in Grouting with 2 mm Crack)

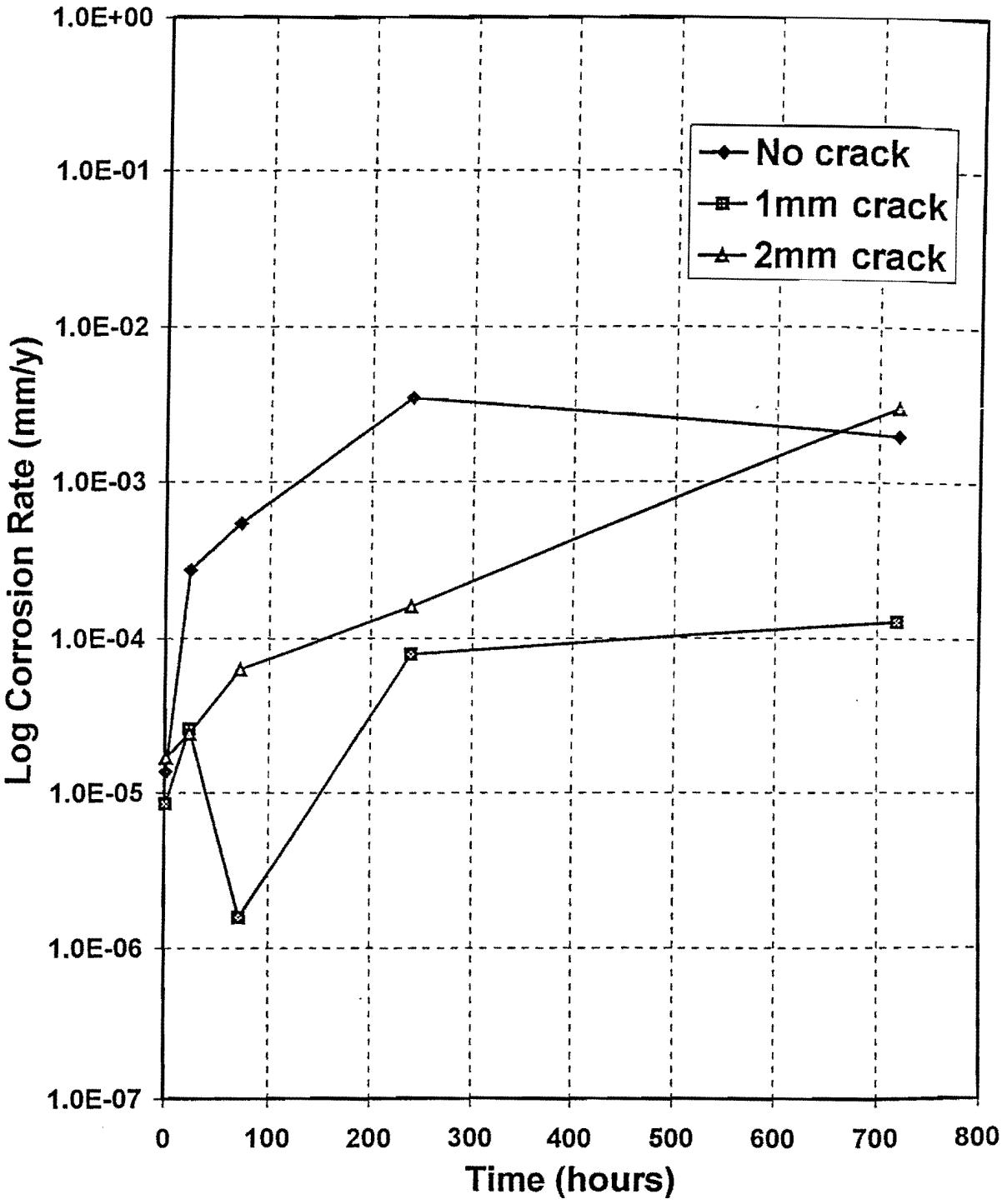

Figure 149. Corrosion Rate of Uncoated Steel Specimen as a Function of Time (Variations of Width of Crack in the Grouting)

3. Calculate the corrosion rate from the polarization resistance value for a given condition.

4. Based on above the results, evaluate the effectiveness of the coating and the grout on the steel surface.

3.5.7.4.1 Uncoated and Acrylic Coated Steel Specimens, Clay

Figure 142 shows the Bode-Magnitude plots as a function of time for uncoated steel specimen embedded in only clay sample collected at the NGES site. As shown in Figure 142, the total resistance of the steel specimen decreases with time except for the three-day data. The decrease of polarization resistance indicates that the corrosion rates for steel specimens embedded in clay tend to increase as time passes. As can be seen in Figure 146, the corrosion rates were estimated to be: 0.07 mm/y, 0.117 mm/y, 0.027 mm/y, and 0.205 mm/y for the respective time periods. The corrosion rate after one-month exposure reaches about 0.34 mm/y, which is significantly larger than any other cases. The initial corrosion rate of the steel specimen in natural clay is about 0.07 mm/y, which is almost equal to the value obtained from polarization resistance measurement. In general, since the grouting forms an alkaline environment around the steel surface, the lack of grouting in the samples has a significant effect on the corrosion rate of steel.

The Bode-Magnitude plot as a function time for acrylic-coated steel specimens covered by only soil is shown in Figure 143. The trend of the plot is similar to the previous one; however, the corrosion rate for the coated steel specimen is slightly lower than that of the uncoated steel specimen. The estimated corrosion rate after a month exposure reaches 0.16 mm/y. Even though the corrosion rate of coated steel specimen is lower than that of uncoated steel specimen, it is hard to conclude that the coating system using acrylic is effective in resisting corrosion in this environment. As a result of the experiments, the usefulness of an acrylic coating may be doubtful in wet conditions.

3.5.7.4.2 Steel in the Grout

According to the Pourbaix diagram (Pourbaix, 1973), when an alkaline environment (pH 11-13) surrounds steel, it is possible to prevent corrosion of steel. The grout should be able to provide this alkaline environment. Hydrated cement normally has a pH value of 12.6, which inhibits the dissolution of Fe or forms a protective passive film on the surface of the Fe that reduces the corrosion rate to minimal levels. However, due to the damage of the passive film or the ingress of aggressive anions in the grout, significant corrosion phenomena may occur in steel tendons. The permeability of grout can allow carbonates and sulfates to react between the gases from the atmosphere and the cement grout. This reaction enables the pH of the grout to reduce and to increase the corrosion rate of steel at the same time. It is obvious that the thicker and denser the cement grouting, the more effective it is inhibiting corrosion in the steel member.

3.5.7.4.3 Uncoated and Acrylic-Coated Steel Specimens, Grouting without Crack

Figure 144 shows the Bode-Magnitude plots as a function of time for uncoated steel specimens embedded with 5 mm thick grouting. Under this condition, the steel is normally expected to be passivated due to the high pH environment. Initially, the grout was cured for a week to allow the alkaline environment over the steel plate to form. The initial polarization resistance was estimated to be 10^6 ohms corresponding to a corrosion rate of 1.37×10^{-5} mm/y. After a day's exposure, the total impedance drastically decreased to 5×10^4 ohms. This result indicated that the highly alkaline environment formed by grouting had deteriorated due to penetration of water and corrosive agents through the suspected fine crack in the grout. The corrosion rates after 10 days and a month exposure were observed to be between 0.0034 mm/y and 0.0035 mm/y, which indicated the corrosion rate should be constant with time. This compared with a value of 0.205 mm/y and 0.342 mm/y measured for the steel specimen without grouting. This test indicates that the use of grout had a great significance on the corrosion resistance of the steel.

Figure 145 shows the Bode-Magnitude plot as a function of time for the acrylic coated steel specimens covered with 5 mm thick grouting. The initial corrosion rate was estimated to be the lowest value corresponding to 4.52×10^{-7} mm/y as shown in Figure 146. Due to the degradation of the coating system with time, the polarization resistance of coated steel specimens dropped to the range of 2×10^5 and 6×10^3 Ohms. The results indicated that the acrylic coating plays a small role in resisting soil corrosion. Initially, the coated specimen showed a lower corrosion rate than the uncoated specimen, however, as time passed, the difference in corrosion rates was reduced.

3.5.7.4.4 Uncoated Steel Specimens, Variations of Width of Crack in Grouting

Cracks in cement grouting have almost always been associated with corrosion of the bonded length in tieback anchors. It is found that water, oxygen, and corrosive agents can reach the steel member in concrete more abundantly through wider cracks (Callahan, 1970). As a result of moisture penetration, the pH of the concrete in the vicinity of crack decreases and the corrosion accelerates. If a crack occurs in grouting over steel tendons in the underground, it may permit ingress of water, air, and deleterious chemicals and accelerate the corrosion in an amount corresponding to the width of the crack. The tensile stress along the tendon, which produces cracks in the grout is of importance with regard to corrosion in view of the crack-corrosion correlation.

Figures 147 and 148 show the bode-magnitude plots as a function of time for uncoated steel specimens covered with grout of different crack widths in the middle of the section. Figure 149 presents the effect of crack width in the grouting on corrosion rates as a function of time. The measured corrosion rate represents a general corrosion rate over an entire area of grouting. An interesting phenomenon was observed for the steel specimen with 1 mm and 2 mm cracks through the grouting section. The initial corrosion rates at both cases were in the range of 0.0005 mm/y and 0.001 mm/y, which are relatively low values. As can be seen in Figure 149, as exposure time increases, the acceleration of the corrosion can be observed in the case of 2 mm crack.

3.5.7.4.5 Uncoated Steel Specimens, Variations of Grouting Thickness

It is generally recognized that the thickness of grouting over the steel tendon controls to a large extent the corrosion protection. However, it is reported that increases in thickness of concrete that cover beyond 50 mm do not significantly increase corrosion protection (Houston et al., 1982). Figures 150 and 151 represent the bode magnitude plots as a function of time for 10 mm and 20 mm of grout thickness, respectively.

Corrosion rates as a function of time for uncoated steel specimens embedded in grouting with variations in thickness are shown in Figure 152. The highest corrosion rates were observed with the 10 mm thick grout. However, the differences in corrosion rates are not significant. The corrosion rates of these samples after a month were 0.0035, 0.011, and 0.007 mm/y for 5, 10, and 20 mm thick grout, respectively. The sample with 5 mm grouting thickness shows a very low corrosion rate (1.4×10^{-5} mm/y) initially. After 30 days of exposure in cement grouting, the corrosion rate increased up to 0.0035 mm/y. The low initial values are related to the diffusion of moisture to the interface. In most cases, the corrosion rate curve had a tendency to be constant after 10 days.

3.5.7.4.6 Epoxy-Coated Steel Specimens, Variations of Grouting Thickness

Measurements of corrosion rates on epoxy-coated steel specimens (0.1 mm thickness) are carried out with variation of grouting thickness. Since the primary interest in this test was on the evaluation of the coating system, the corrosion rate of steel specimens in different coating materials will be compared.

Bode-Magnitude and corrosion rate plots of epoxy-coated steel specimens with variations of grouting thickness are shown in Figures 153 through 156. The epoxy-coated steel specimens showed low corrosion rates regardless of time. These were in the range of 10^{-7} mm/y and 10^{-6} mm/y after a month of exposure. Epoxy-coated steel specimens with 20 mm grouting thicknesses showed the lowest corrosion rates, in the range of 9.01×10^{-8} mm/y and 3.32×10^{-7} mm/y. In most cases, the exposure time did not have a significant effect on the corrosion rate of epoxy-coated steel specimens as shown in Figure 156. In addition to the exposure time, the grouting thickness is independent of corrosion rate.

3.5.7.4.7 Fusion Bonded Epoxy-Coated Steel Specimens

An effective method of preventing corrosion is the use of fusion bonded epoxy coatings on the steel surfaces. In order to select appropriate coating materials, the resistance against corrosion, and the flexibility for its intended use should be considered. This test was carried out to evaluate the potential performance of fusion bonded epoxy coating with respect to corrosion attack. The thickness of coating was 0.3 mm.

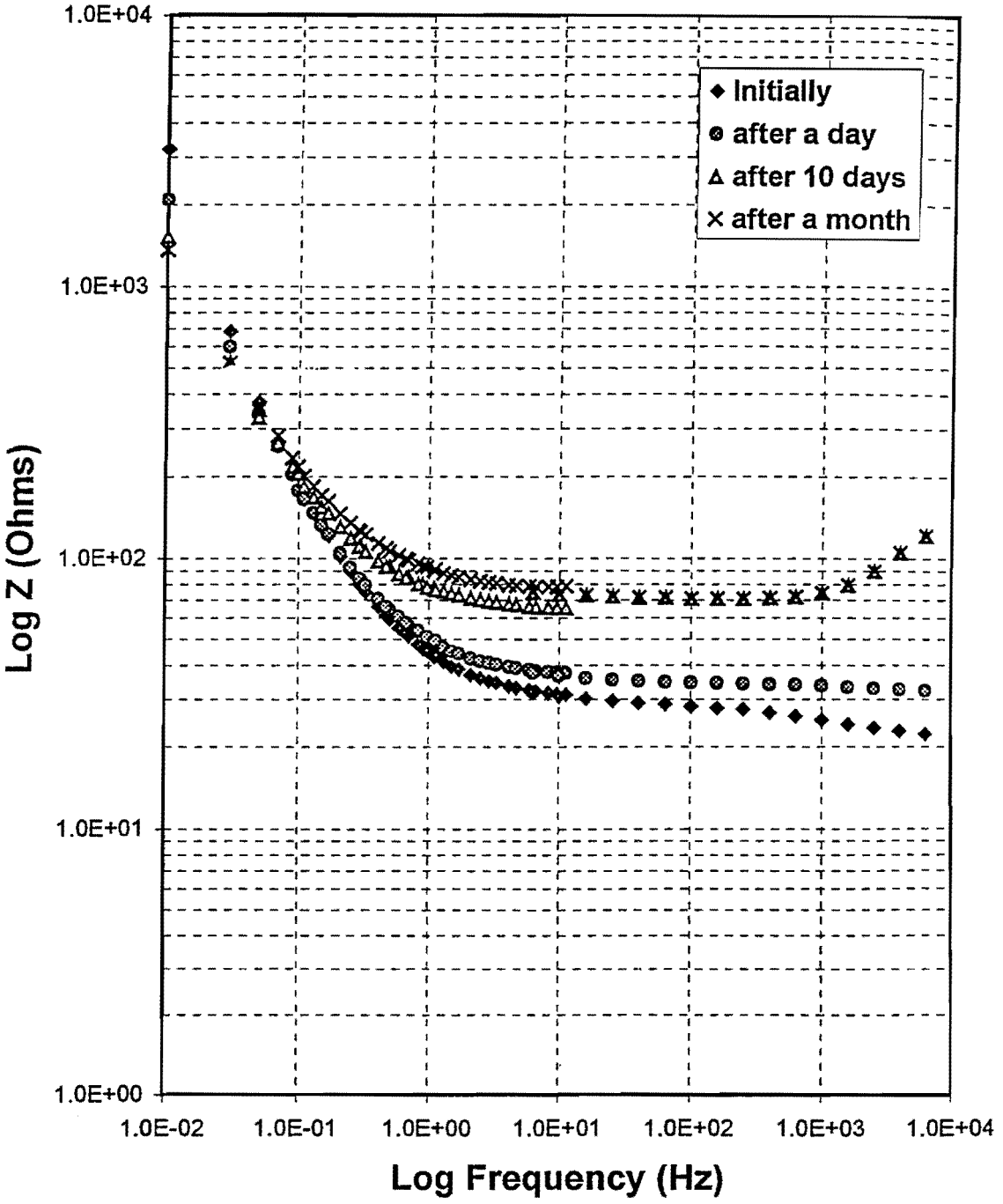

Figure 150. Bode-Magnitude Plots as a Function of Time (Uncoated Steel Specimens with 10 mm Grouting Thickness)

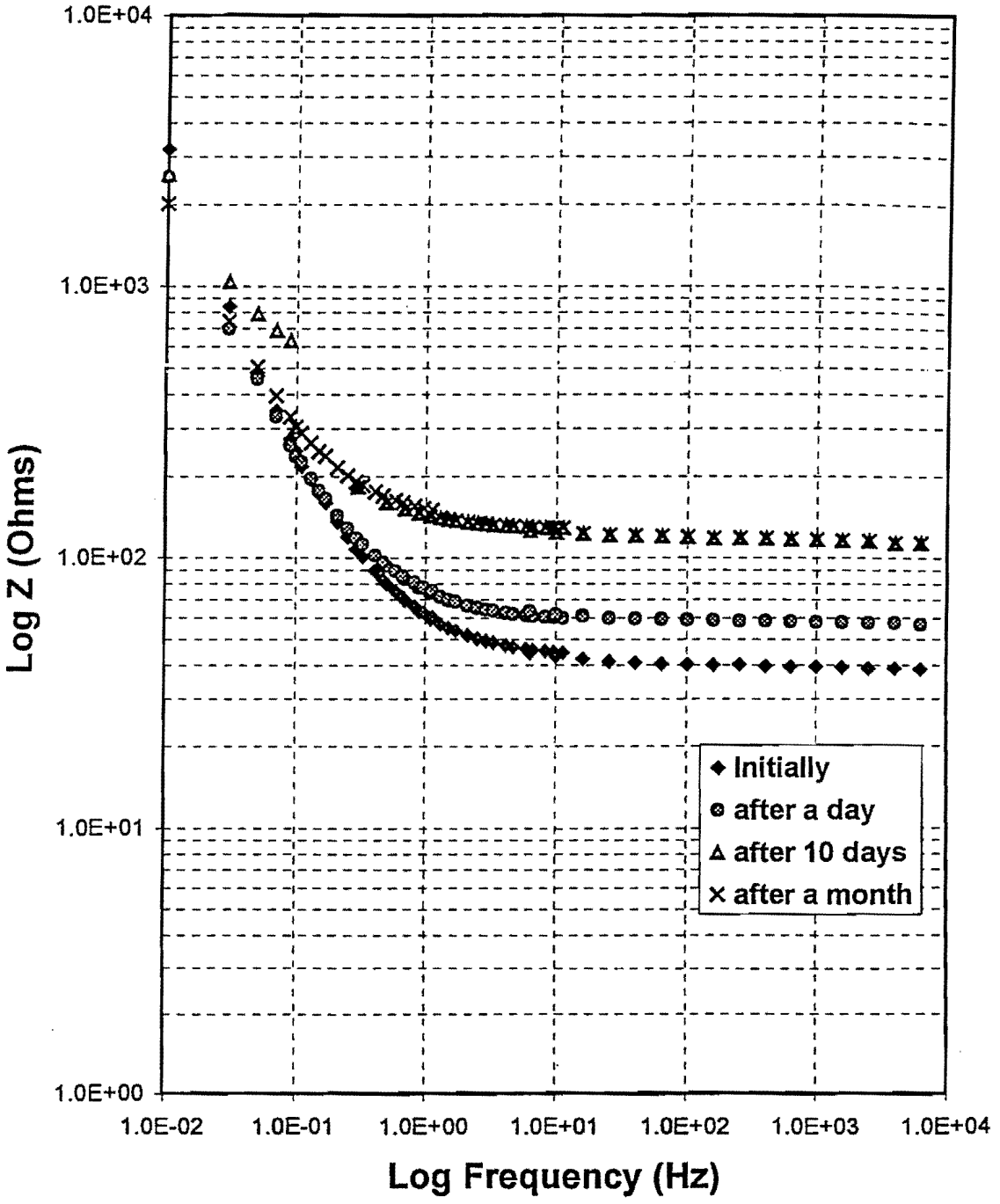

Figure 151. Bode-Magnitude Plots as a Function of Time (Uncoated Steel Specimens with 20 m Grouting Thickness)

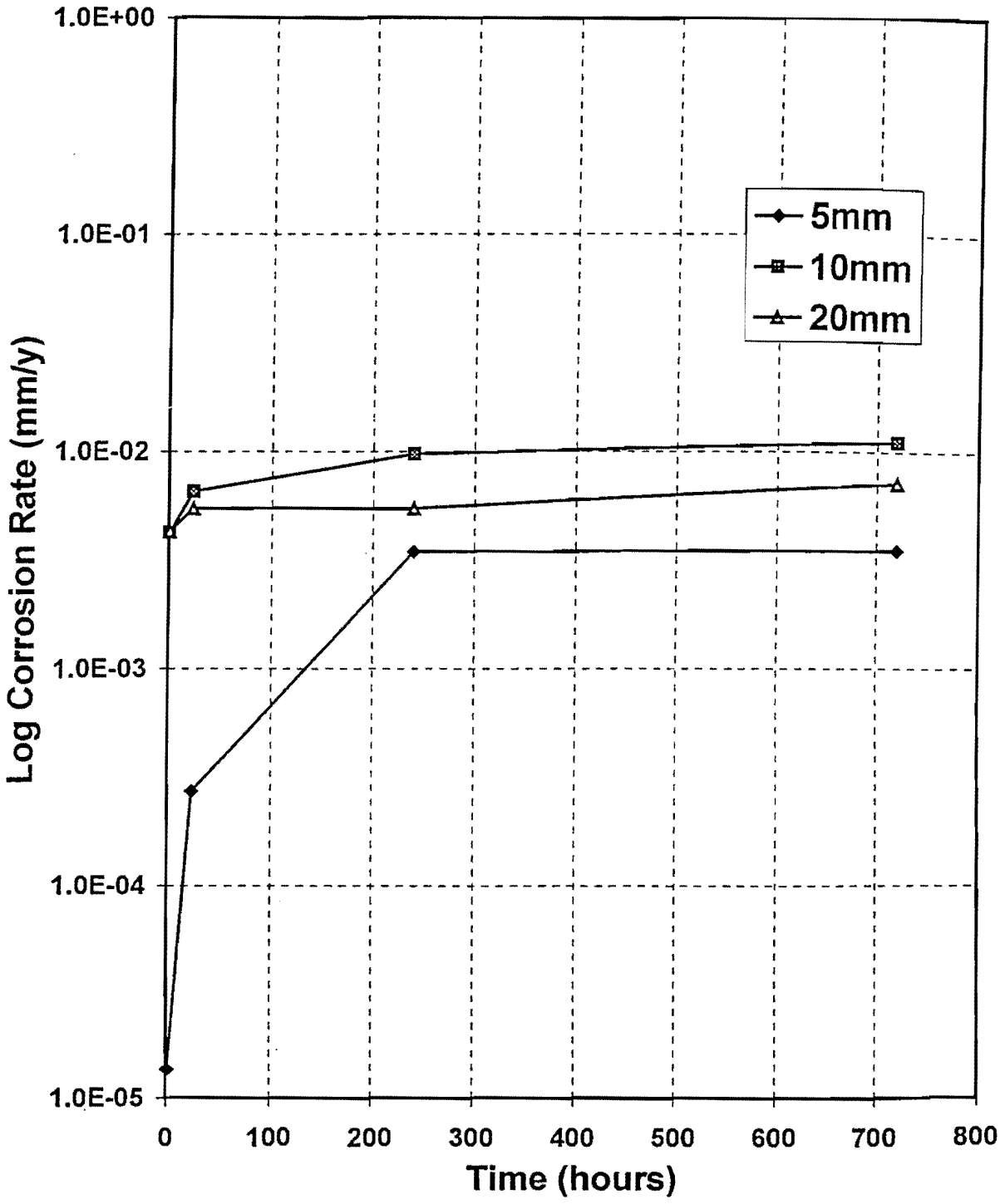

Figure 152. Corrosion Rates of Uncoated Steel Specimen as a Function of Time (Variations of Grouting Thickness)

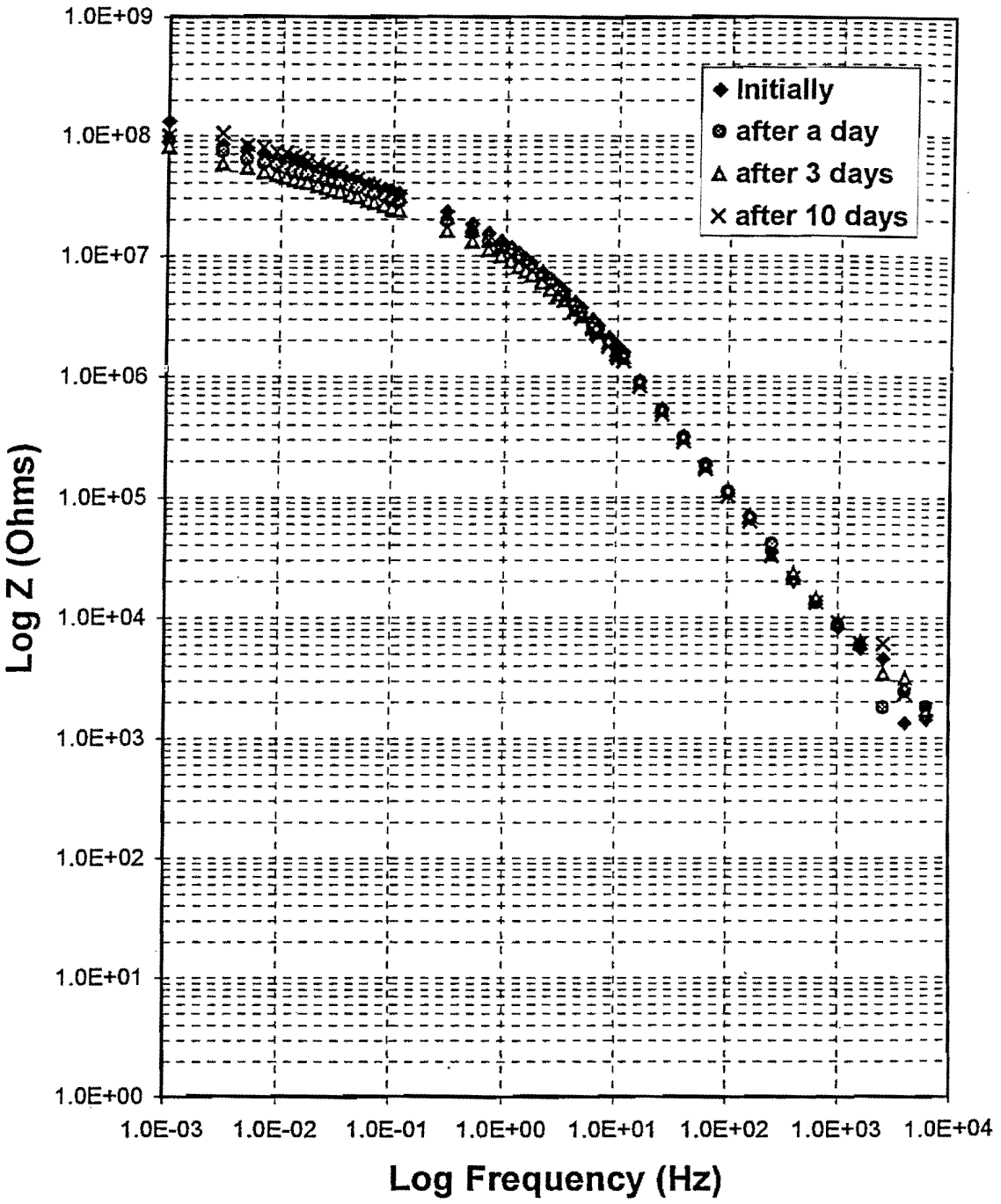

Figure 153. Bode-Magnitude Plots as a Function of Time (Epoxy-Coated Steel Specimens with 5 mm Grouting Thickness)

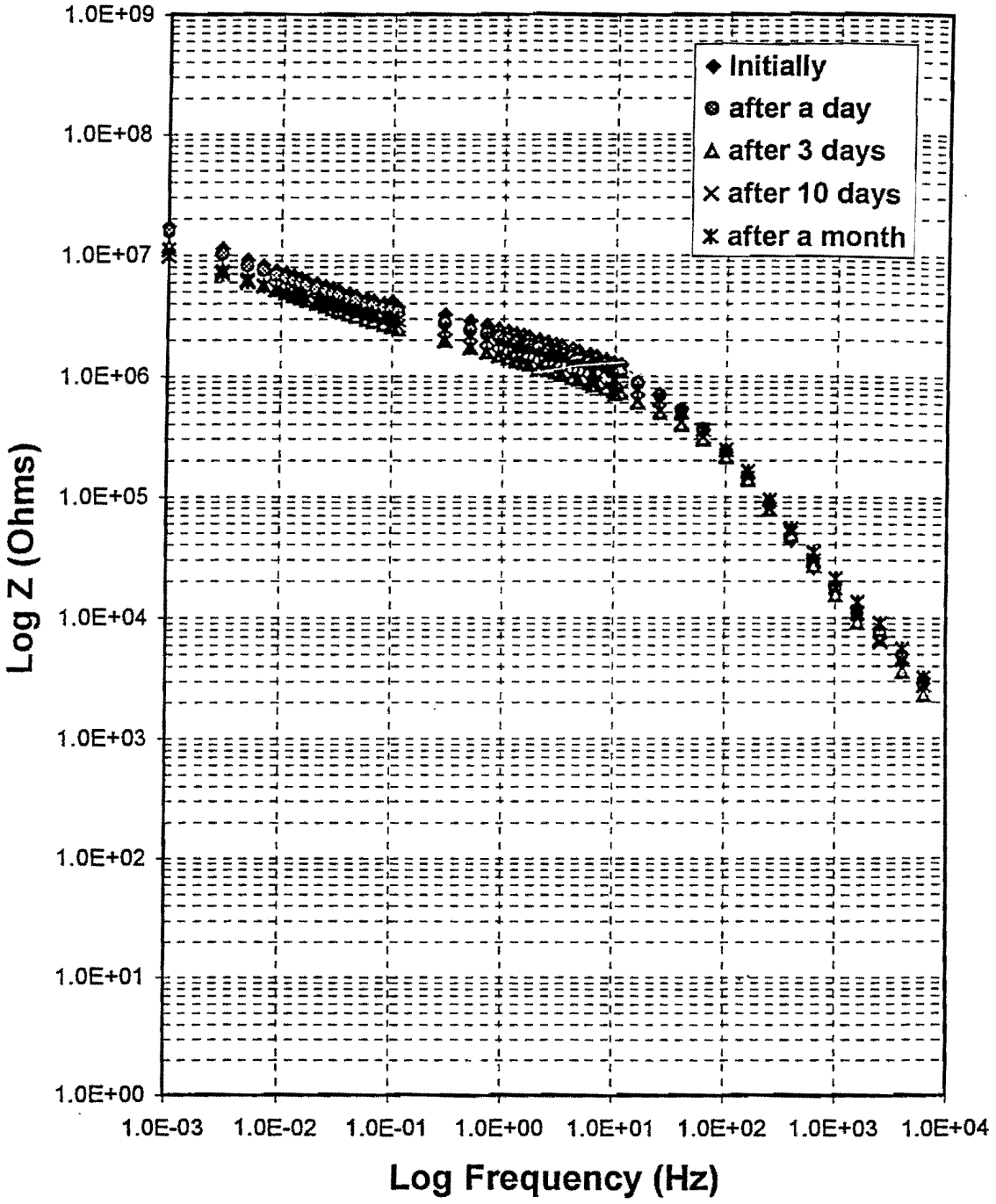

Figure 154. Bode-Magnitude Plots as a Function of Time (Epoxy-Coated Steel Specimens with 10 mm Grouting Thickness)

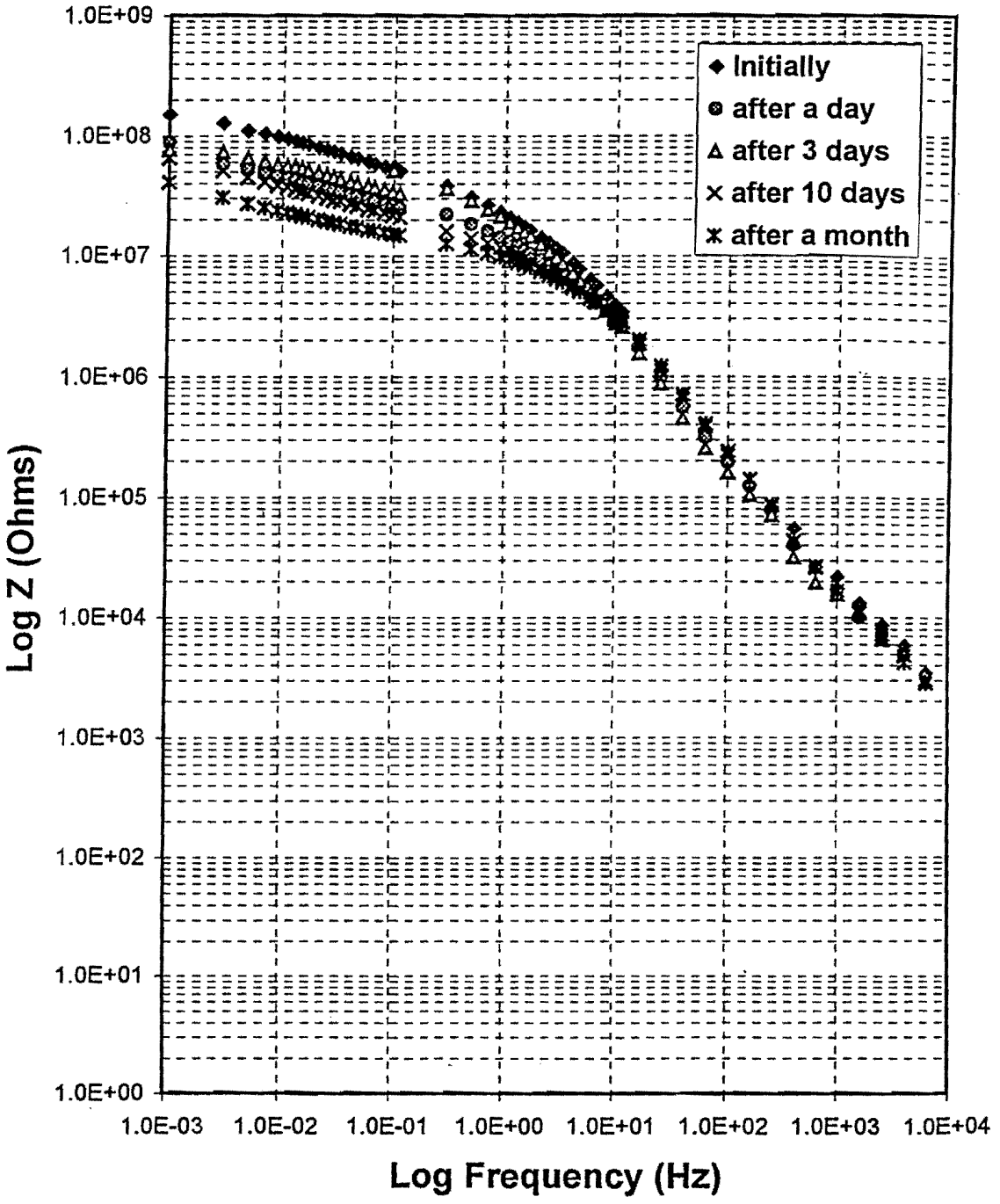

Figure 155. Bode-Magnitude Plots as a Function of Time (Epoxy-Coated Steel Specimens with 20 mm Grouting Thickness)

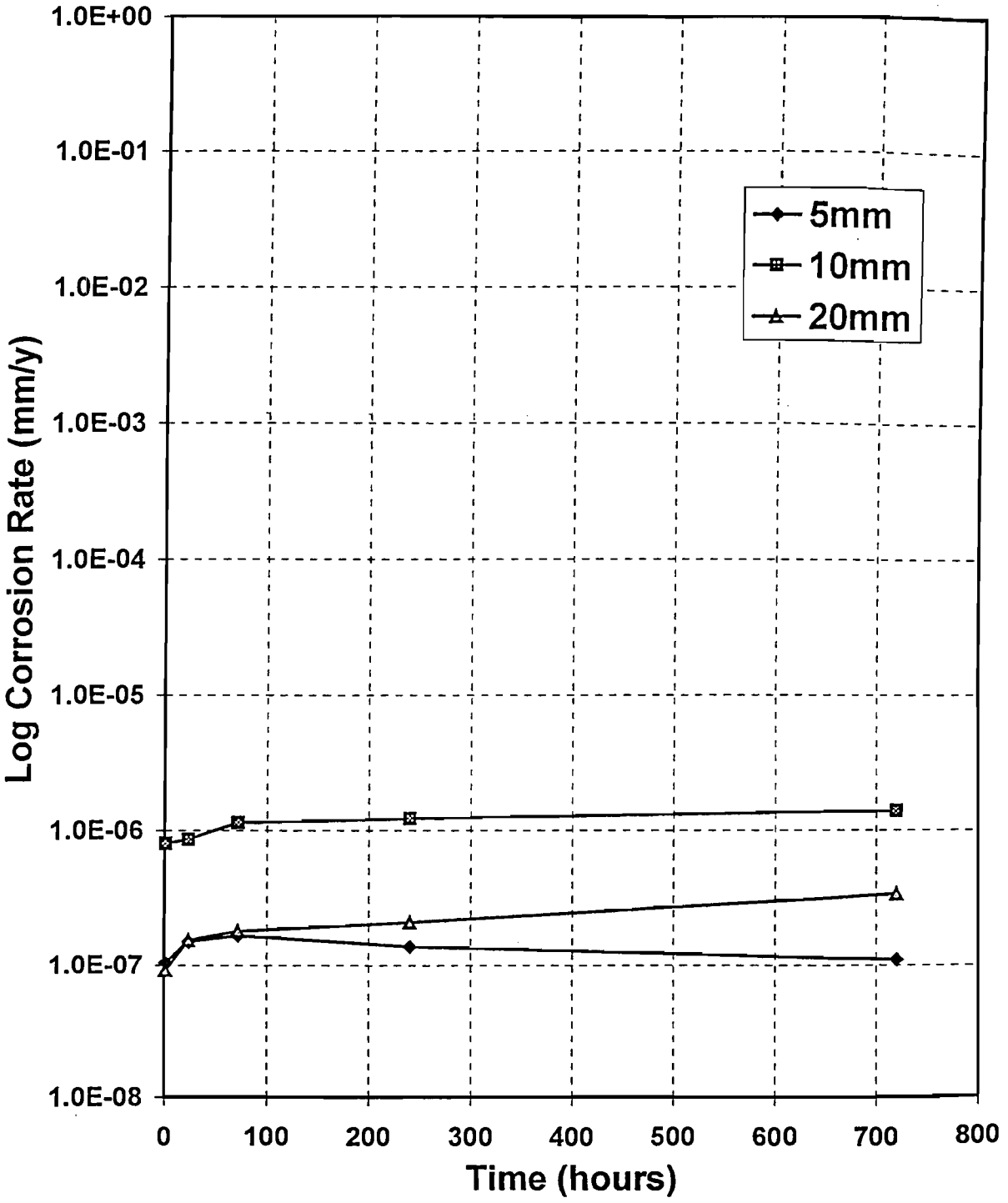

Figure 156. Corrosion Rate of Epoxy-Coated Steel Specimen as a Function of Time (Variations of Grouting Thickness)

Bode-Magnitude plots of fusion bonded epoxy-coated steel specimens in cement grouting are shown in Figures 157 and 158. The data are so scattered that it is hard to obtain the nice shape of a curve. The measured corrosion rates are at the lower limit of the instrument to detect changes in the system. Based on the polarization resistance, variations of corrosion rate of fusion bonded epoxy-coated specimens are presented in Figure 159. As can be seen, these samples embedded in cement grouting showed the lowest corrosion rates up to the maximum exposure time of 30 days. The corrosion rates were in the range of 2.5×10^{-9} mm/y measured for 10 days exposure time, up to 3.66×10^{-8} mm/y measured for three days exposure time. The following section introduces the comparison of corrosion resistance for different types of coating systems.

3.5.7.4.8 The Effect of Coating System on Corrosion Rates

Figure 160 shows the comparison of corrosion rates for steel specimens covered with different types of coatings. The experiments were carried out on steel specimens covered by cement grouting. As shown in Figure 160, the samples coated with acrylic and epoxy showed initially low corrosion rates in the range of 5×10^{-8} and 2×10^{-7} mm/y. The data indicate that the coating systems initially create favorable barriers against corrosion, which results in high polarization resistance of the substrate. However, in the case of acrylic coatings, the corrosion rates after 24 hours showed a large increase, and then remained constant up to 720 hours reaching values of 0.001 mm/y. This indicates that an acrylic coating is not as useful for underground corrosion problems. The two epoxy coatings are four to five orders of magnitude lower than the acrylic coating. Tables 22 through 26 show the results of corrosion rate measurements for each test.

3.6 PROPOSED SCREENING TEST

One concern about placing anchors in new soil is the relative corrosion characteristics of the particular soil. While apparently reasonable estimates can be made from soil descriptors, such as soil resistivity and pH, it is abundantly clear that this information is not sufficient especially if there is no prior experience with the particular soil. As part of this project, the authors used the Electrochemical Impedance Spectroscopy test to evaluate the corrosion characteristics of steel under a variety of coatings. This work is described in section 3.5.7 of this report. As a result of this work, the researchers realized that this test has the potential to be used as a screening test for new soil that is being proposed as a site for permanent ground anchors.

The procedure for the proposed test would be the following:

1. Soil samples from the proposed site would be collected and sent to a laboratory capable of running the EIS tests.

2. Steel similar or the same as the proposed ground anchor material would be prepared as flat specimens. (It would be possible to use round specimens with a modification of the test setup.)

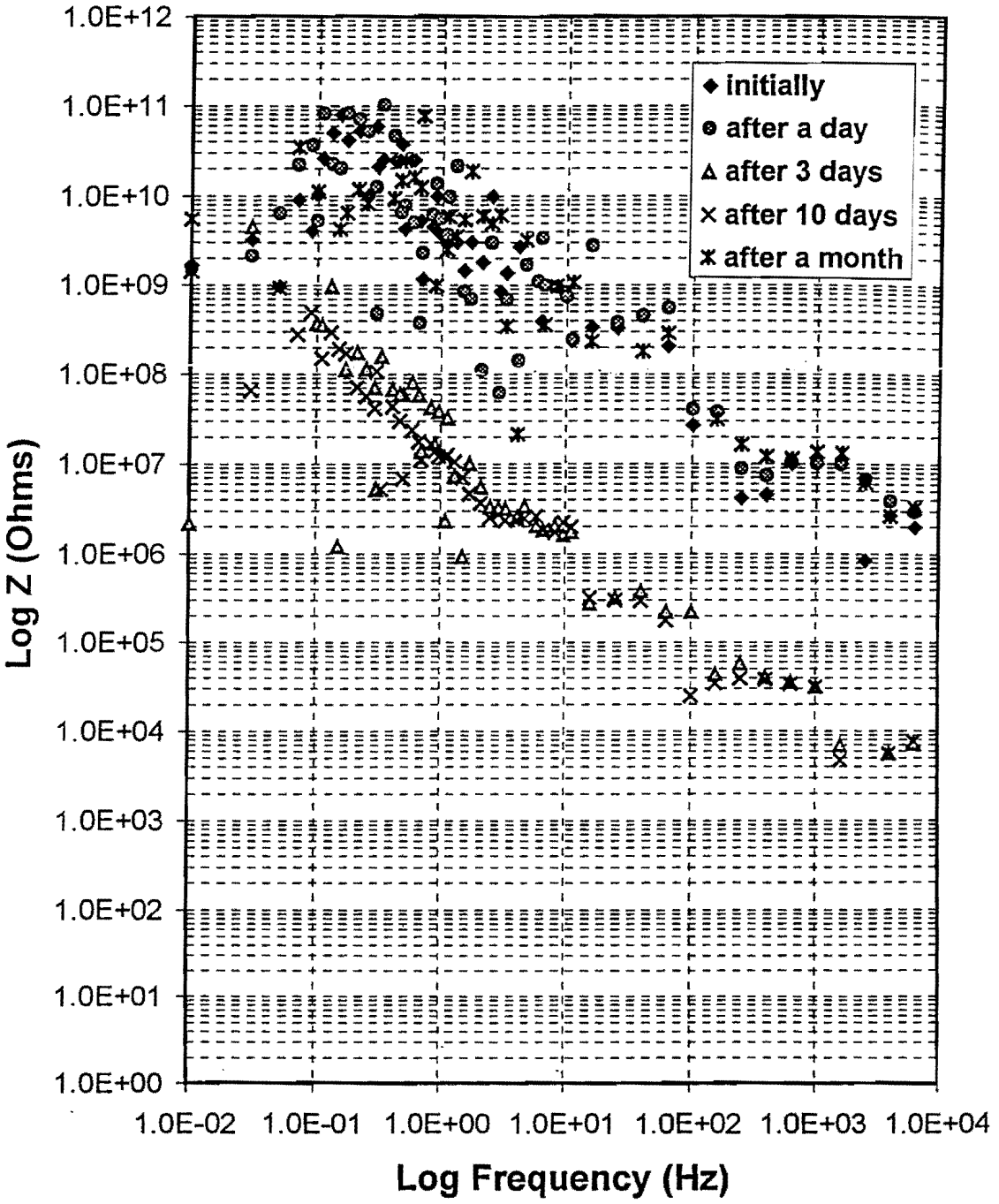

Figure 157. Bode-Magnitude Plots as a Function of Time (Fusion Bonded Epoxy Coating Specimen 1)

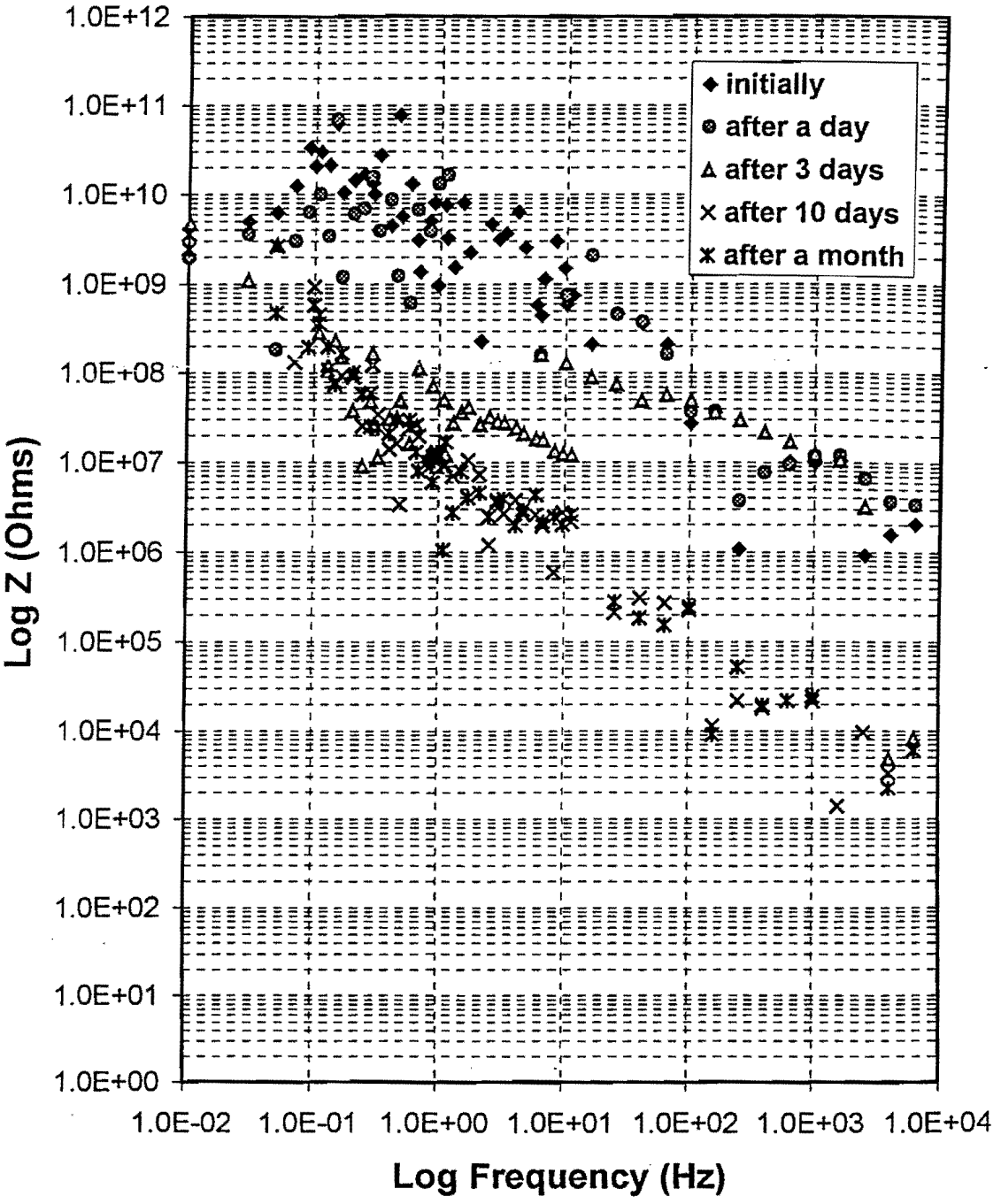

Figure 158. Bode-Magnitude Plots as a Function of Time (Fusion Bonded Epoxy Coating Specimen 2)

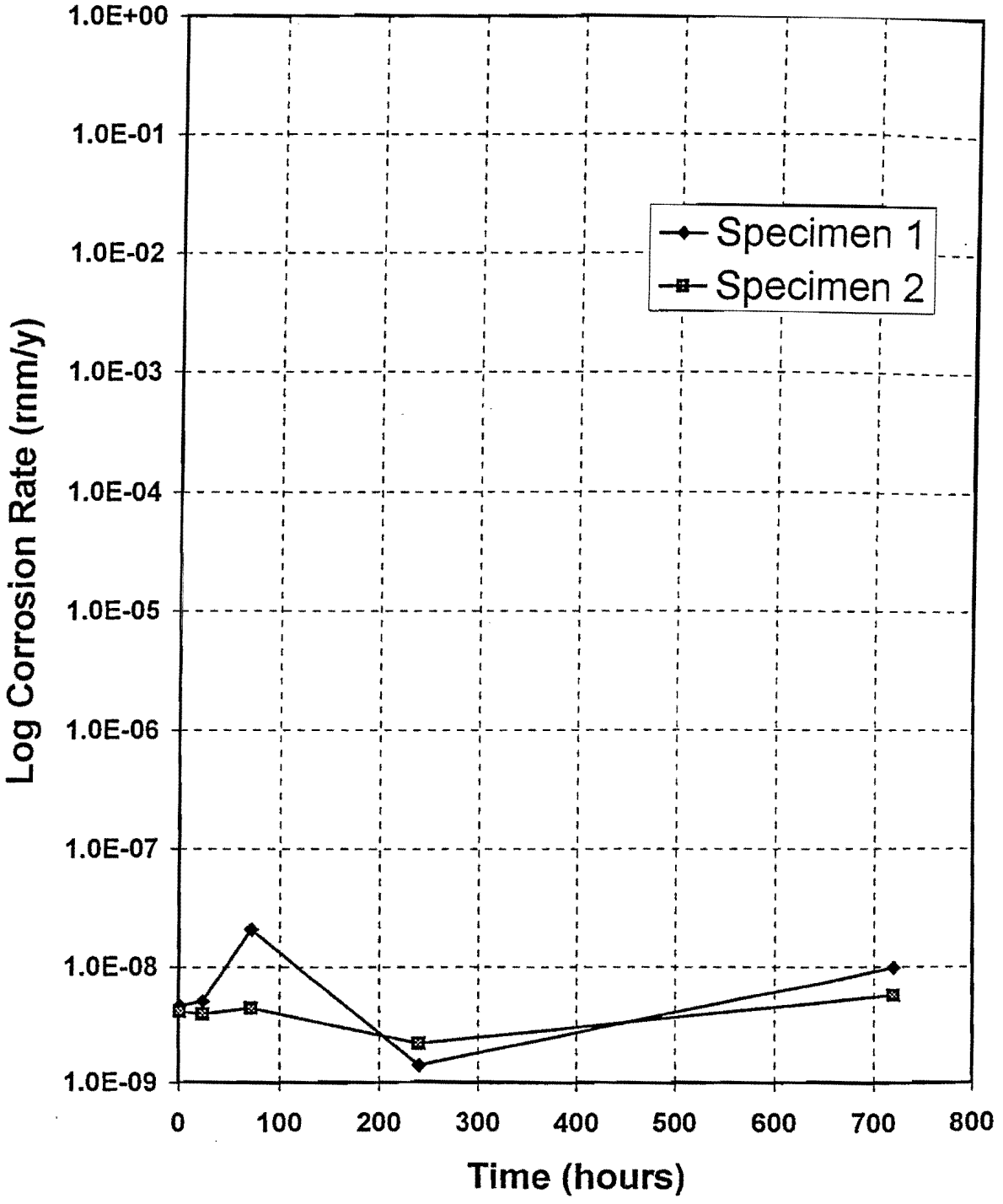

Figure 159. Corrosion Rate of Fusion Bonded Epoxy Coating Specimens as a Function of Time

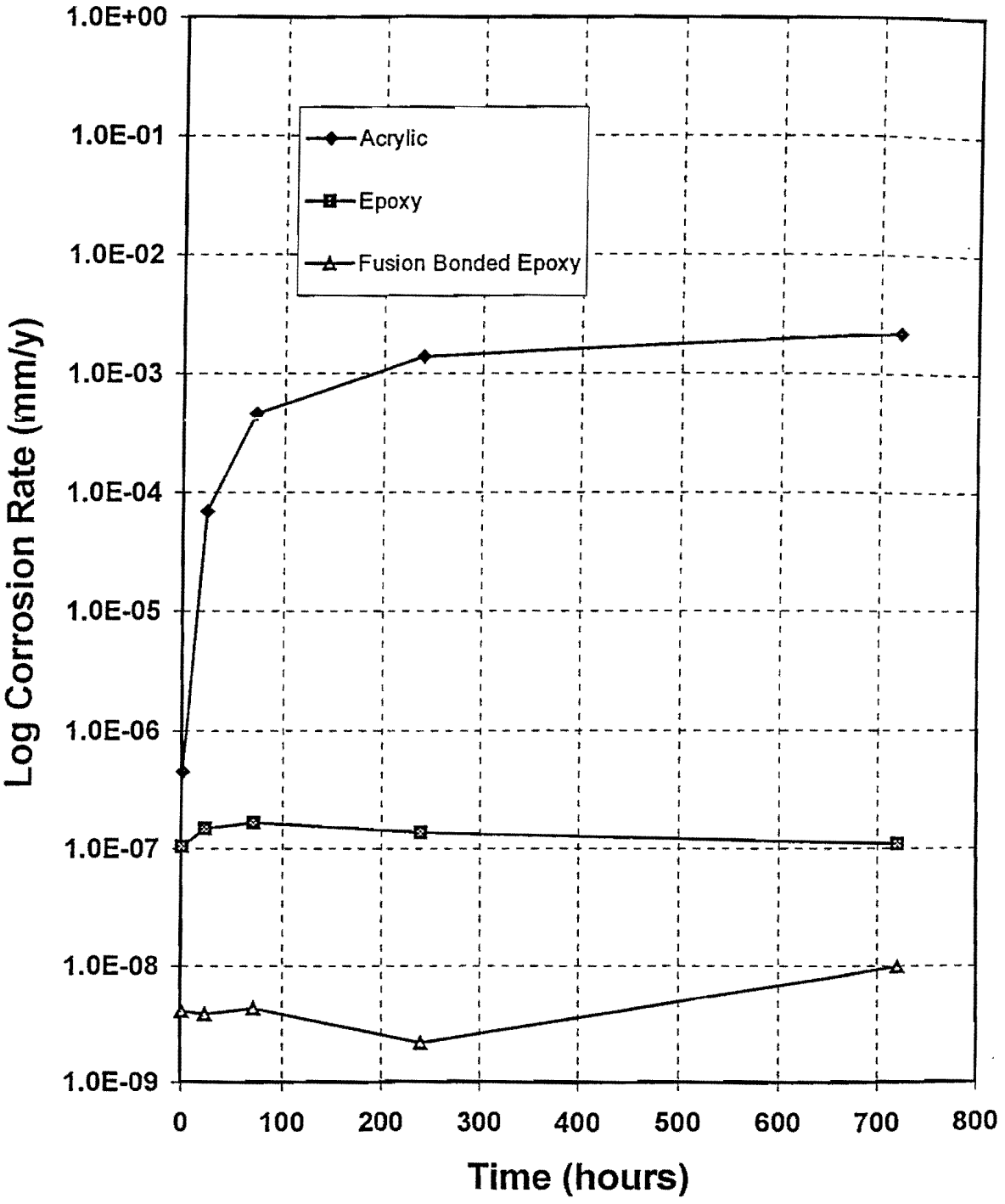

Figure 160. Comparison of Corrosion Rate at Different Type of Coating Materials as a Function of Time

Table 22. Summary of Corrosion Rate of Steel Specimens (Clay, Grouting without Crack)

Initial

Specimen Condition	Rp+Rs (Ohms)	Rs (Ohms)	Rp (Ohms)	β_a	β_c	I_{corr} (A/cm^2)	Corrosion Rate (mm/y)
NS	200	6	194	0.148	0.224	6.02E-06	0.069831
CS	220	14	206	0.148	0.224	5.67E-06	0.065763
NG	1000000	10000	990000	0.148	0.224	1.18E-09	1.37E-05
CG	30000000	3000	29997000	0.148	0.224	3.89E-11	4.52E-07

After a day

Specimen Condition	Rp+Rs (Ohms)	Rs (Ohms)	Rp (Ohms)	β_a	β_c	I_{corr} (A/cm^2)	Corrosion Rate (mm/y)
NS	120	5	115	0.148	0.224	1.02E-05	0.117802
CS	350	0.5	349.5	0.148	0.224	3.34E-06	0.038762
NG	50000	500	49500	0.148	0.224	2.36E-08	0.000274
CG	200000	3000	197000	0.148	0.224	5.93E-09	6.88E-05

After 3 days

Specimen Condition	Rp+Rs (Ohms)	Rs (Ohms)	Rp (Ohms)	β_a	β_c	I_{corr} (A/cm^2)	Corrosion Rate (mm/y)
NS	1000	400	496	0.148	0.224	2.35E-06	0.000014
CS	400	4	9600	0.148	0.224	1.22E-07	0.034297
NG	25000	100	24900	0.148	0.224	4.69E-08	0.000544
CG	30000	500	29500	0.148	0.224	3.96E-08	0.000459

After 10 days

Specimen Condition	Rp+Rs (Ohms)	Rs (Ohms)	Rp (Ohms)	β_a	β_c	I_{corr} (A/cm^2)	Corrosion Rate (mm/y)
NS	70	4	66	0.148	0.224	1.77E-05	0.205261
CS	10000	100	197	0.148	0.224	5.93E-06	0.001368
NG	4000	80	3920	0.148	0.224	2.98E-07	0.003456
CG	10000	200	9800	0.148	0.224	1.19E-07	0.001382

After 30 days

Specimen Condition	Rp+Rs (Ohms)	Rs (Ohms)	Rp (Ohms)	β_a	β_c	I_{corr} (A/cm^2)	Corrosion Rate (mm/y)
NS	50.6	11.083	39.517	0.148	0.224	2.96E-05	0.342821
CS	8.89E+01	5.4127	83.5083	0.148	0.224	1.4E-05	0.162226
NG	3992.7	125.62	3867.08	0.148	0.224	3.02E-07	0.003503
CG	6484.4	245.53	6238.87	0.148	0.224	1.87E-07	0.002171

NS: Uncoated specimen embedded in only soil
CS: Coated specimen embedded in only soil
NG: Uncoated specimen covered by grouting
CG: Coated specimen covered by grouting

Table 23. Summary of Corrosion Rate of Uncoated Steel Specimens (Variations of Grouting Crack Width)

Initial

Width of Crack	Rp+Rs (Ohms)	Rs (Ohms)	Rp (Ohms)	β_a	β_c	I_{corr} (A/cm^2)	Corrosion Rate (mm/y)
No	1000000	10000	990000	0.148	0.224	1.18E-09	1.37E-05
1mm	1.64E+06	3.84E+04	1601239	0.148	0.224	7.29E-10	8.46E-06
2mm	8.33E+05	2.61E+04	806395	0.148	0.224	1.45E-09	1.68E-05

After a day

Width of Crack	Rp+Rs (Ohms)	Rs (Ohms)	Rp (Ohms)	β_a	β_c	I_{corr} (A/cm^2)	Corrosion Rate (mm/y
No	50000	500	49500	0.148	0.224	2.36E-08	0.000274
1mm	5.34E+05	9.11E+03	524850.5	0.148	0.224	2.22E-09	2.58E-05
2mm	5.81E+05	1.54E+04	565842	0.148	0.224	20.6E-09	2.39E-05

After 3 days

Width of Crack	Rp+Rs (Ohms)	Rs (Ohms)	Rp (Ohms)	β_a	β_c	I_{corr} (A/cm^2)	Corrosion Rate (mm/y)
No	25000	100	24900	0.148	0.224	4.69E-08	0.000544
1mm	8.66E+06	1.95E+04	8638626	0.148	0.224	1.35E-10	1.57E-06
2mm	2.22E+05	6.49E+03	215962.2	0.148	0.224	5.41E-09	6.27E-05

After 10 days

Width of Crack	Rp+Rs (Ohms)	Rs (Ohms)	Rp (Ohms)	β_a	β_c	I_{corr} (A/cm^2)	Corrosion Rate (mm/y)
No	4000	80	3920	0.148	0.224	2.98E-07	0.003456
1mm	1.74E+05	1.54E+03	172713.4	0.148	0.224	6.76E-09	7.84E-05
2mm	8.61E+04	9.54E+02	85137.78	0.148	0.224	1.37E-08	0.000159

After 30 days

Width of Crack	Rp+Rs (Ohms)	Rs (Ohms)	Rp (Ohms)	β_a	β_c	I_{corr} (A/cm^2)	Corrosion Rate (mm/y)
No	3992.7	125.62	3867.08	0.148	0.224	3.02E-07	0.003503
1mm	1.07E+05	1.45E+03	105866.9	0.148	0.224	1.1E-08	0.000128
2mm	4.64E+03	1.40E+02	4502.14	0.148	0.224	2.59E-07	0.003009

Table 24. Summary of Corrosion Rate of Uncoated Steel Specimens (Variations of Grouting Thickness)

Initial

Grouting Thickness	Rp+Rs (Ohms)	Rs (Ohms)	Rp (Ohms)	β_a	β_c	I_{corr} (A/cm^2)	Corrosion Rate (mm/y)
5mm	1000000	10000	990000	.0148	0.224	1.18E-09	1.37E-05
10mm	3.22E+03	2.19E+01	3195.612	0.148	0.224	3.65E-07	0.004239
20mm	3.20E+03	3.89E+01	3157.843	0.148	0.224	3.7E-07	0.00429

After a day

Grouting Thickness	Rp+Rs (Ohms)	Rs (Ohms)	Rp (Ohms)	β_a	β_c	I_{corr} (A/cm^2)	Corrosion Rate (mm/y)
5mm	50000	500	49500	0.148	0.224	2.36E-08	0.000274
10mm	2.10E+03	3.20E+01	2063.121	0.148	0.224	5.66E-07	0.006566
20mm	2.53E+03	5.63E+01	2474.41	0.148	0.224	4.72E-07	0.005475

After 10 days

Grouting Thickness	Rp+Rs (Ohms)	Rs (Ohms)	Rp (Ohms)	β_a	β_c	I_{corr} (A/cm^2)	Corrosion Rate (mm/y)
5mm	4000	80	3920	0.148	0.224	2.98E-07	0.003456
10mm	1.53E+03	1.32E+02	1394.46	0.148	0.224	8.37E-07	0.009715
20mm	2.59E+03	1.11E+02	2480.41	0.148	0.224	4.71E-07	0.005462

After 30 Days

Grouting Thickness	Rp+Rs (Ohms)	Rs (Ohms)	Rp (Ohms)	β_a	β_c	I_{corr} (A/cm^2)	Corrosion Rate (mm/y)
5mm	3992.7	125.62	3867.08	0.148	0.224	3.02E-07	0.003503
10mm	1.36E+03	1.32E+02	1226.16	0.148	0.224	9.52E-07	0.011049
20mm	2.01E+03	1.11E+02	1900.41	0.148	0.224	6.14E-07	0.007129

Table 25. Summary of Corrosion Rate of Epoxy-Coated Steel Specimens

Initial

Grouting Thickness	Rp+Rs (Ohms)	Rs (Ohms)	Rp (Ohms)	β_a	β_c	I_{corr} (A/cm^2)	Corrosion Rate (mm/y)
5mm	1.3E+08	1235.8	1.3E+08	0.148	0.224	8.98E-12	1.04E-07
10mm	1.70E+07	1939.6	1.7E+07	0.148	0.224	6.87E-11	7.97E-07
20mm	1.5E+08	1485.6	1.5E+08	0.148	0.224	7.77E-12	9.01E-08

After a day

Grouting Thickness	Rp+Rs (Ohms)	Rs (Ohms)	Rp (Ohms)	β_a	β_c	I_{corr} (A/cm^2)	Corrosion Rate (mm/y)
5mm	91415000	1.19E+03	9.1E+07	0.148	0.224	1.28E-11	1.48E-07
10mm	1.58E+07	1.93E+03	1.6E+07	0.148	0.224	7.37E-11	8.56E-07
20mm	8.85E+07	2.29E-03	8.8E+07	0.148	0.224	1.32E-11	1.53E-07

After 3 days

Grouting Thickness	Rp+Rs (Ohms)	Rs (Ohms)	Rp (Ohms)	β_a	β_c	I_{corr} (A/cm^2)	Corrosion Rate (mm/y)
5mm	8.15E+07	1.04E+03	8.1E+07	0.148	0.224	1.43E-11	1.66E-07
10mm	1.20E+07	1.42E+03	1.2E+07	0.148	0.224	9.76E-11	1.13E-06
20mm	7.60E+07	1.51E+03	7.6E+07	0.148	0.224	1.54E-11	1.78E-07

After 10 days

Grouting Thickness	Rp+Rs (Ohms)	Rs (Ohms)	Rp (Ohms)	β_a	β_c	I_{corr} (A/cm^2)	Corrosion Rate (mm/y)
5mm	9.88E+07	1.28E+03	9.9E+07	0.148	0.224	1.18E-11	1.37E-07
10mm	1.11E+07	1.70E+03	1.1E+07	0.148	0.224	1.05E-10	1.22E-06
20mm	6.50E+07	2.30E+03	6.5E+07	0.148	0.224	1.8E-11	2.08E-07

After a month

Grouting Thickness	Rp+Rs (Ohms)	Rs (Ohms)	Rp (Ohms)	β_a	β_c	I_{corr} (A/cm^2)	Corrosion Rate (mm/y)
5mm	1.24E+08	1.60E+03	1.2E+08	0.148	0.224	9.43E-12	1.09E-07
10mm	9.78E+06	1.95E+03	9775448	0.148	0.224	1.19E-10	1.39E-06
20mm	4.08E+07	2.05E+03	4.1E+07	0.148	0.224	2.86E-11	3.32E-07

Table 26. Summary of Corrosion Rate of Fusion-Bonded Epoxy Coating Steel Specimens

Initial

Test	Rp+Rs (Ohms)	Rs (Ohms)	Rp (Ohms)	β_a	β_c	I_{corr} (A/cm^2)	Corrosion Rate (mm/y)
1	1.66E+09	1.71E+06	1.66E+09	0.148	0.224	7.03E-13	8.16E-09
2	1.87E+09	1739300	1.86E+09	0.148	0.224	6.27E-13	7.27E-09

After a day

Test	Rp+Rs (Ohms)	Rs (Ohms)	Rp (Ohms)	β_a	β_c	I_{corr} (A/cm^2)	Corrosion Rate (mm/y)
1	1.53E+09	1999700	1.53E+09	0.148	0.224	7.65E-13	8.88E-09
2	1.97E+09	2616400	1.97E+09	0.148	0.224	5.93E-13	6.88E-09

After 3 days

Test	Rp+Rs (Ohms)	Rs (Ohms)	Rp (Ohms)	β_a	β_c	I_{corr} (A/cm^2)	Corrosion Rate (mm/y)
1	3.71E+08	7.36E+03	3.71E+08	0.148	0.224	3.15E-12	3.66E-08
2	1.76E+09	3.18E+06	1.76E+09	0.148	0.224	6.65E-13	7.72E-09

After 10 days

Test	Rp+Rs (Ohms)	Rs (Ohms)	Rp (Ohms)	β_a	β_c	I_{corr} (A/cm^2)	Corrosion Rate (mm/y)
1	5.42E+09	8.16E+03	5.42E+09	0.148	0.224	2.15E-13	2.5E-09
2	3.52E+09	6.89E+03	3.52E+09	0.148	0.224	3.32E-13	3.85E-09

After 30 days

Test	Rp+Rs (Ohms)	Rs (Ohms)	Rp (Ohms)	β_a	β_c	I_{corr} (A/cm^2)	Corrosion Rate (mm/y)
1	1.40E+09	2.46E+06	1.39E+09	0.148	0.224	8.37E-13	9.71E-09
2	2.41E+09	7.86E+03	2.41E+09	0.148	0.224	4.85E-13	5.62E-09

3. Soil characteristics would be measured: conductivity or resistivity, pH, chloride, sulfate, water content, and microbes. These measurements would be made in the field, where appropriate, and in the laboratory. (This would help in developing a database for future use.)

4. The test setup would be similar to Figures 140 and 141.

5. The soil would be saturated with water, and that level would be maintained throughout the test time.

6. The EIS test would be run as a function of time over a two-week time span.

7. Replicates would be run for each test to determine the reproducibility of the test.

8. The corrosion rate as a function of time would be determined.

9. After testing, the metallic surface would be examined for the extent of corrosion and for evidence of localized corrosion.

In performing the tests, the metallic surface may be coated with grout or an organic coating or some combination of the two as was done during TxDOT Project No. 1391. The results would enable the engineer to have a useful estimate of the corrosion of the permanent ground anchor in that particular soil. Additionally, examining the corroded surface of the metal would indicate the likelihood of localized corrosion being a problem. The experience gained in this project would suggest that two weeks of testing would be sufficient to be able to comfortably establish the uniform corrosion rate. From Figures 146, 149, 152, and 160, it is apparent that approximately 200 ±40 h is needed for the experiment to reach the steady state corrosion rate. The proposed test would have great flexibility in terms of the soil-coating interface combination that could possibly be used.

3.7 LIFE PREDICTIONS/PROTECTION OPTIONS

The life prediction for permanent ground anchors is a difficult problem. Figure 161 represents a failure diagram that might be considered for permanent ground anchors. There would appear to be seven different ways that a permanent ground anchor might fail or be declared not suitable for service. The initial portion of this report discusses in detail the creep characteristics of soils and overload failures. There is some experience with respect to interfacial failures and designers take these failuresrs into consideration. The latter part of this report addresses the corrosion failures.

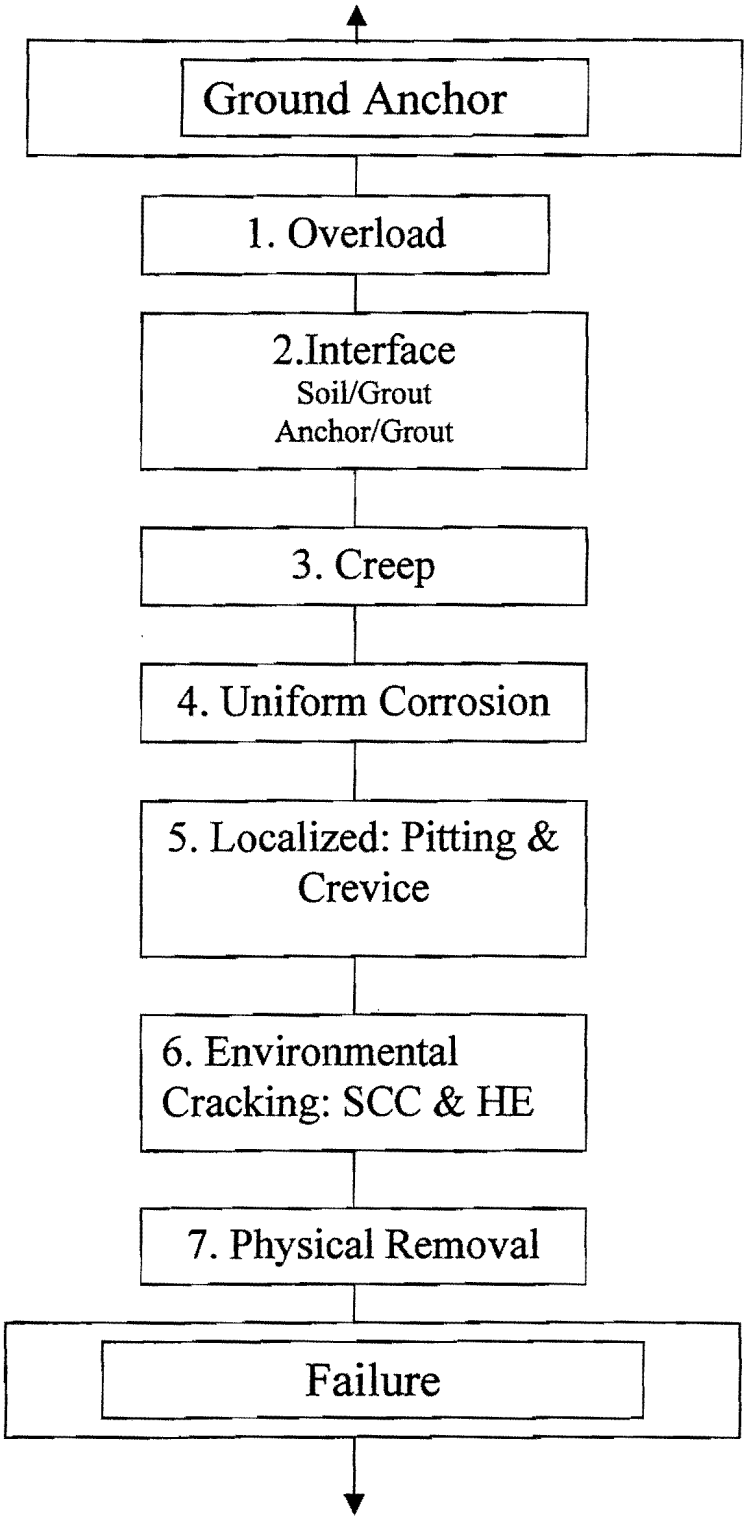

Figure 161. Lifetime Prediction for a Permanent Ground Anchor

For a corrosion life prediction, all of the various failure modes need to be considered. We have obtained data that gives us information with respect to uniform corrosion. Using the corrosion rates determining a prediction can be made similar to that for steel and galvanized steel in soil.

3.7.1 Uniform Corrosion Life Prediction Modes

3.7.1.1 Elias Model for Steel and Galvanized Steel in Soil

The model presented is by Elias (1990) and is based upon a previous model suggested by Romanoff (1957). This original model was developed from lengthy burial tests conducted by the National Bureau of Standards (currently, NIST). These tests involved extensive field testing of metal pipes and sheet steel at various sites throughout the United States, beginning as early as 1901. The data showed indications that the corrosion rate was greatest in the first few years, then reduced to a steady, substantially slower rate several years into the corrosion process. Based on these studies, Romanoff suggested that the average loss of thickness (x) due to uniform corrosion at some time (t) may be represented by a power law model:

$$x = Kt^n$$

where K and n are site and soil-dependent constants (n is less than unity). Values of n and K for low alloy and carbon steels, respectively, were determined by Romanoff to range from 0.5 to 0.6 and between 150 μm and 180 μm respectively for the first year after burial. The n values for galvanized steels were not evaluated, however, K values of 5 μm to 70 μm can be inferred. Extensive laboratory testing in France has shown that the corrosion rate for galvanic steels changes according to the presence or absence of a coating. These experiments involved carefully controlled tests on buried boxes and electrochemical cells for a 10-year period, and indicated that the constant n may be taken as 0.60 while the zinc coating is still present, and from 0.65 to 1 for carbon steel once significant corrosion has occurred. The value of the constant K after the first year of burial varied between 3 μm and 50 μm.

Using Romanoff's model and data from the NBS and French burial tests, Elias (1990) suggests that the following equations predict the loss due to uniform corrosion of galvanized steel (zinc coated):

$$x = 25t^{0.65} \qquad \text{(Average)}$$

$$x = 50t^{0.65} \qquad \text{(Maximum)}$$

For carbon steels, the equations become:

$$x = 40t^{0.80} \qquad \text{(Average)}$$

$$x = 80t^{0.80} \qquad \text{(Maximum)}$$

The expression for the maximum suggests rates during the first few years of corrosion activity, whereas the "average" rates are for the long-term life of the member, i.e., 2-3 years after corrosion begins. The total loss of a member would be the sum of the galvanic coating loss and, assuming the coating has been destroyed, the corrosion of carbon steel. British recommendations for average loss rates in mildly aggressive environments advise K values of 22 and an n value of 0.67 for galvanized steels. For more aggressive environments, the values of K and n become 40 and 0.80, respectively.

It is to be noted that these rates are models of uniform corrosion and do not account for localized corrosion or environmental cracking of the member. Should either of these occur, the anchors would be subject to stress risers and would be more prone to failure.

3.7.1.2 Predictions of Steel Anchors in Soil

Using the Elias models, the lifetime for a single permanent ground anchor, 25.4 mm (1 in) diameter with various thickness galvanic coatings can be estimated. The anchor will be assumed to be subjected to 60% of its yield strength under a constant load (Steel, ASTM 722-95). The ultimate tensile strength of the anchor is a minimum of 1035 MPa (150,000 psi) and the yield strength is a minimum of 880 MPa (127,600 psi). The estimate will consist of determining the time to deterioration of the zinc coating plus the time required for the steel to be reduced in cross sectional thickness to a level where failure will occur by overload. Elias (1990) models will be used for determining the time to failure. Using the definition of stress with respect to an applied load, calculate the magnitude of the constant load (assumed to be tensile in nature) using $\sigma = (60\%)*\sigma_{yield}$ and the cross sectional area taken as $\pi d^2/4$ can be calculated. These relationships give a stress of 528 MPa (76,560 psi). The maximum depth due to corrosion loss will be determined by computing the critical radius at which failure will occur. Because the plastic nature of the steel is not known, the critical stresses will be assumed as both the yield and UTS and the results compared. Failure occurs at:

Yield $$880 = \frac{A_0 528}{\pi r^2} \rightarrow r_{critical} = 9.84 \text{ mm}$$

UTS $$1035 = \frac{A_0 528}{\pi r^2} \rightarrow r_{critical} = 9.07 \mu\text{m}$$

Solving the Elias model of maximum corrosion in plain carbon steels for the time (t) (in years) gives the following equation.

$$Ln(t) = \frac{Ln(x) - Ln(80)}{0.8}$$

Table 27 contains time to failure of zinc coated bars of steel for different thicknesses of Zn. The number of years was determined using Elias's model.

Table 27. Time to Loss and Failure of 25.4 mm (1 in) Anchor Subjected to 60% Yield with Various Zinc Coating Thicknesses

	5 mil coating	10 mil coating	15 mil coating	20 mil coating	25 mil coating	Yield Stress (MPa)	UTS (MPa)
Coating Thickness mm	0.127	0.254	0.381	0.508	0.635		
Time to Loss (years)	4.2	12.1	22.7	35.4	49.9		
Lifetime (Yield)	87.4	87.4	87.4	87.4	87.4	880	
Total Life Est.	91.6	99.5	110.1	122.8	137.3		
Lifetime (UTS)	117.7	117.7	117.7	117.7	117.7		1035
Total Life Est.	121.9	129.8	140.4	153.1	167.6		

The predicted values apply to mildly aggressive environments only with no grout cover, and do not account for any type of corrosion (i.e., localized or environmental cracking) other than uniform attack. These values are only intended as approximations and should not be taken as an assumed lifetime for all anchors in every environment. A more accurate prediction should be made according to site conditions. Even more important, there is no consideration of the grout cover on these materials.

3.7.1.3 Prediction of Anchor Lifetime Using Data Developed in the Current Study

For uniform corrosion, we measured the corrosion rates under a variety of conditions, and several examples are shown in Table 28. Using the corrosion rates determined from this study, the following lifetimes were predicted. As the results indicate, for an epoxy coated ground anchor, the lifetime would be many years. The same assumptions with respect to these anchors were used in this example as in the one above, Section 3.7.1.2. All five examples shown in Table 28 used soil as the electrolyte.

Table 28. Estimated Lifetime for a 25.4 mm (1 in) Diameter Permanent Ground Anchor Under Various Conditions with Soil as the Electrolyte

Coating/E;ectrp;ute	Corrosion Rate, mm/y	Estimated Lifetime, yrs.
No Coating/Soil	0.34	8.4
Sprayed Acrylic/Soil	0.16	17.9
Grouting/Soil	0.003	954
Acrylic, Grout/Soil	0.001	318
Painted Epoxy, Grout/Soil	1×10^{-7}	2.9×10^{7}
Fusion Bonded Epoxy, Grout/Soil	1×10^{-8}	2.9×10^{8}

The above analysis will work well for uniform corrosion, but can not be applied to pitting or environmental cracking situations. The weak link in the lifetime prediction is the lack of information on the effects of localized corrosion and environmental cracking.

3.7.2 Protection Options

The purpose of protection against corrosion is to make sure that the possibility of corrosion occurring is small during the design life of the permanent or temporary anchorage. In extremely aggressive environments, or where there is risk of local corrosion by pitting, unprotected anchors may fail in only a few weeks. It is necessary to provide graded protection according to the aggressiveness of environment for its safe working life. The choice of corrosion protection depends on the consequence of failure, aggressiveness of the environment, and cost of protection.

3.7.2.1 Requirements of Protective System

A protective system should satisfy the following requirements as standards (Hanna, 1982).

The effective life of the anchor protection system must have an effective life equal to the anticipated service life of the anchorage.

It should not react with the corrosive environment.

It should not restrict movement of the free length in order to transfer load down to the fixed anchor zone.

The protective materials should be mutually compatible with the deformability and permanence of the anchor.

The system must be sufficiently strong and flexible so that it does not fail.

3.7.2.2 Materials of Protection

3.7.2.2.1 Coatings and Coverings

There are a variety of protective coatings and coverings acting as a physical barrier between the surface and the environment. This protective system can enclose the metal within a covering or sheath so that it will not to react with the atmosphere or the soil. It is very important to maintain the continuity of the covering through the entire tendon length. Partial protection will only induce more severe corrosion on the unprotected parts. Coating the anchor length of the tendon provides protection in addition to the grout. In order to protect against corrosion effectively, the following are necessary (Weatherby, 1982):

- Be resistant to chemical attacks from the grout and the environment,
- Uniform coating along the tendon,
- Be resistant to abrasion and impact,
- Be resistant to handling and installation damage, and
- Be capable of elongation with the tendon without debonding.

3.7.2.2.2 Grouting

Cement grouting is the medium used to transfer the fixed anchor loads to the soil around the anchor tendon. Although the grout injected tends to have an alkaline environment, it is doubtful that the grout can be considered as a part of the protection system because of its quality and integrity.

When tendons in cement grout are stressed, cracks within the tendon bond length tend to occur at about 50 mm to 100 mm intervals and of widths up to 1 mm or more (Meyer, 1977). In order to prevent crack problems, it is necessary to specify a minimum grout cover of 20 mm and design centralizers (Hanna, 1982). Decreasing the crack width in the alkaline environment of a cement grout can reduce the rate of tendon corrosion. In order to reduce and control the width of crack, the spiral steel cages or meshes within the grout are quite effective.

3.7.2.2.3 Nonhardening Materials

Nonhardening materials such as grease can be used to inhibit corrosion by providing an impermeable layer of protection against oxygen, water, and other agents. However because they have some limitations: (i) susceptibility to dry out, (ii) liability to leakage, (iii) possibility of displacement, and (iv) uncertainty of their long-term chemical stability, they should not be regarded as a permanent physical barrier to corrosion.

3.7.2.3 Cathodic Protection

3.7.2.3.1 Impressed Current System

These systems use an external power source to apply a direct current to protect the anchor, and the corrosion occurs at an anode away from the anchor. Unless impressed current systems are maintained properly, hydrogen may be involved at cathodic areas on the metal, which may cause hydrogen embrittlement. Impressed current protection systems may use automatic monitoring and control units which could adjust the applied voltage to each anchor and make impressed systems safe for use with anchors (Weatherby, 1982). Other difficulties are in maintaining the electrical connections necessary to insure the anchors are protected, and inspecting the system regularly to observe whether or not it is performing adequately.

3.7.2.3.2 Sacrificial Anode Cathode Protection System

By applying a bonded metallic coating such as zinc or magnesium (sacrificial anode), corrosion of the tendon will be halted until the metallic coating is consumed. This method is acceptable for temporary anchorages, given that the thickness and type of coating are appropriate for the expected life of the tendon and suited to the corrosiveness of the soil. An estimated life for a Zn-coated anchor was included earlier in this report in Section 3.5.7.4.7.

3.7.2.4 Degree of Protection against Corrosion

The following criteria are used to determine the protection level required for the various types of anchors and their intended economic life. Table 29 shows the classes of protection for ground anchorages.

Table 29. Classes of Protection for Ground Anchorages (after Littlejohn, 1990)

Anchorage Category	Class of Protection
Temporary	Temporary without protection
	Temporary with single protection
	Temporary with double protection
Permanent	Permanent with single protection
	Permanent with double protection

3.7.2.4.1 Temporary Anchors

Temporary anchors will remain in service up to six months. It is acceptable that the cement grout will protect the fixed anchor length, and the specified minimum cover is normally provided for most fixed anchor types. Some protection is sometimes recommended over the free length in the case of extremely aggressive conditions.

3.7.2.4.2 Permanent Anchors

In general, permanent anchors should be protected, usually with double protection. This protection is based on the assumption that an aggressive environment will exist, and that environmental change is hard to predict during the service life. After considering the many variable parameters involved, the engineers have to decide the effective protective system.

3.7.2.4.3 Single and Double Protection

The single protection is applied as a physical barrier between the steel tendon and the corrosive medium, while the double protection consists of outer and inner barriers. The purpose of the outer barrier is to protect the inner barrier against damage during tendon handling.

3.7.2.5 Protective Systems on the Ground Anchor

Since it is very hard to predict the localized corrosion rates, where aggressivity is recognized, the designer should provide some degree of protection. Especially junctions between the fixed length, free length, and anchor head are particularly vulnerable. Choice of class of protection is the responsibility of the designer. The choice depends on such factors as consequence of failure, aggressiveness of the environment, and cost of protection. Typical examples of protection for the tieback anchor are illustrated in Figures 162 through 166.

3.7.2.6 Protective Systems of the Bonded Length

The fixed anchor length must receive the same degree of protection as the free length. The following materials should enhance the resistance for corrosion and be capable of transferring high tensile stress to the ground. Certain materials, notably epoxy, fusion-bonded epoxy, and resins have appropriate strength, ductility, and resistance to corrosion.

3.7.2.6.1 Cement Grout

Cement grout is the agent used to transfer the fixed anchor load to the ground. Although it maintains the alkaline environment around the tendon, it is hard to consider as a reliable barrier against corrosion. However, the minimum cover for a given area should be provided.

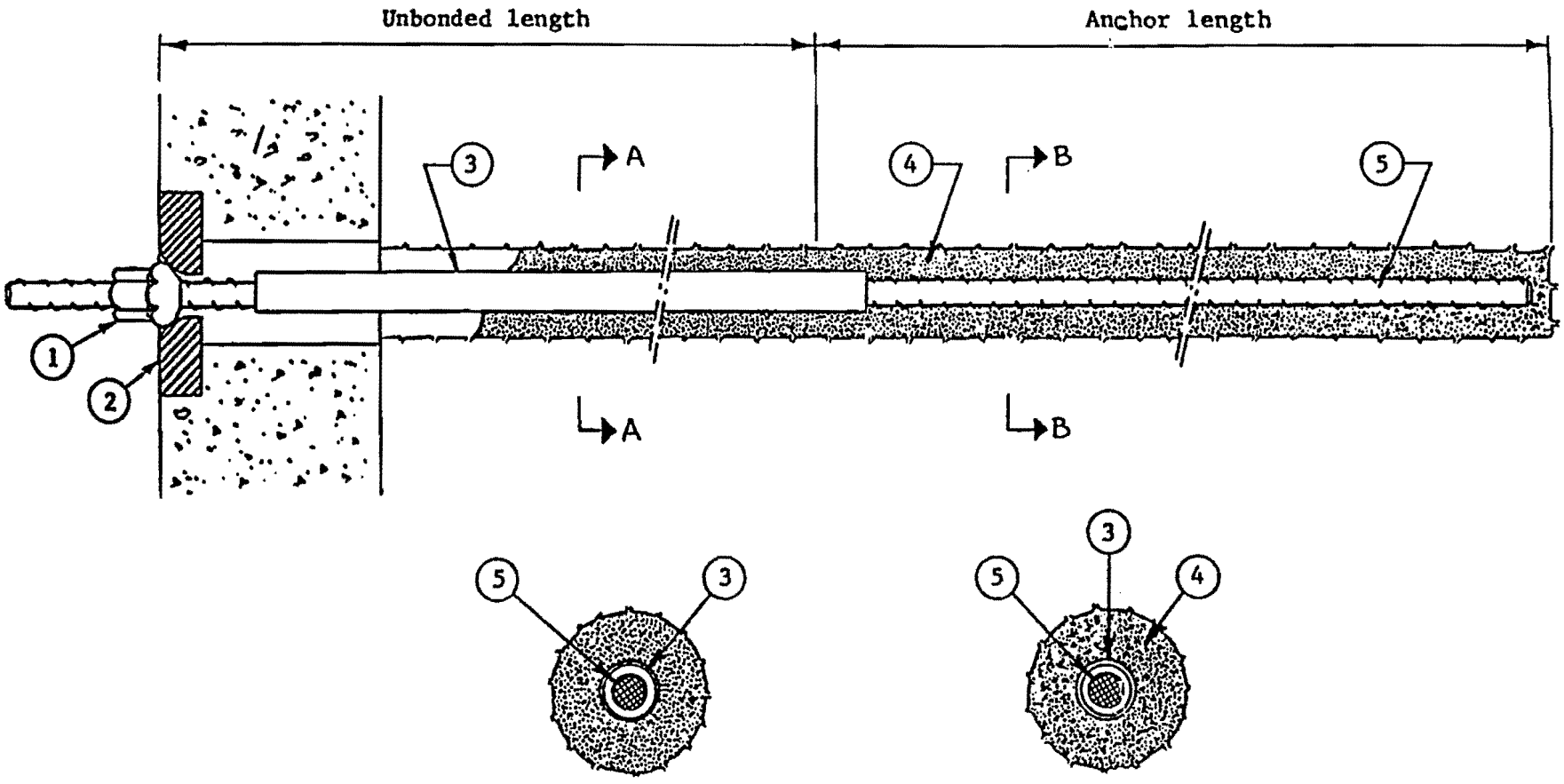

Figure 162. Unprotected Bar Tieback (Weatherby, 1982)

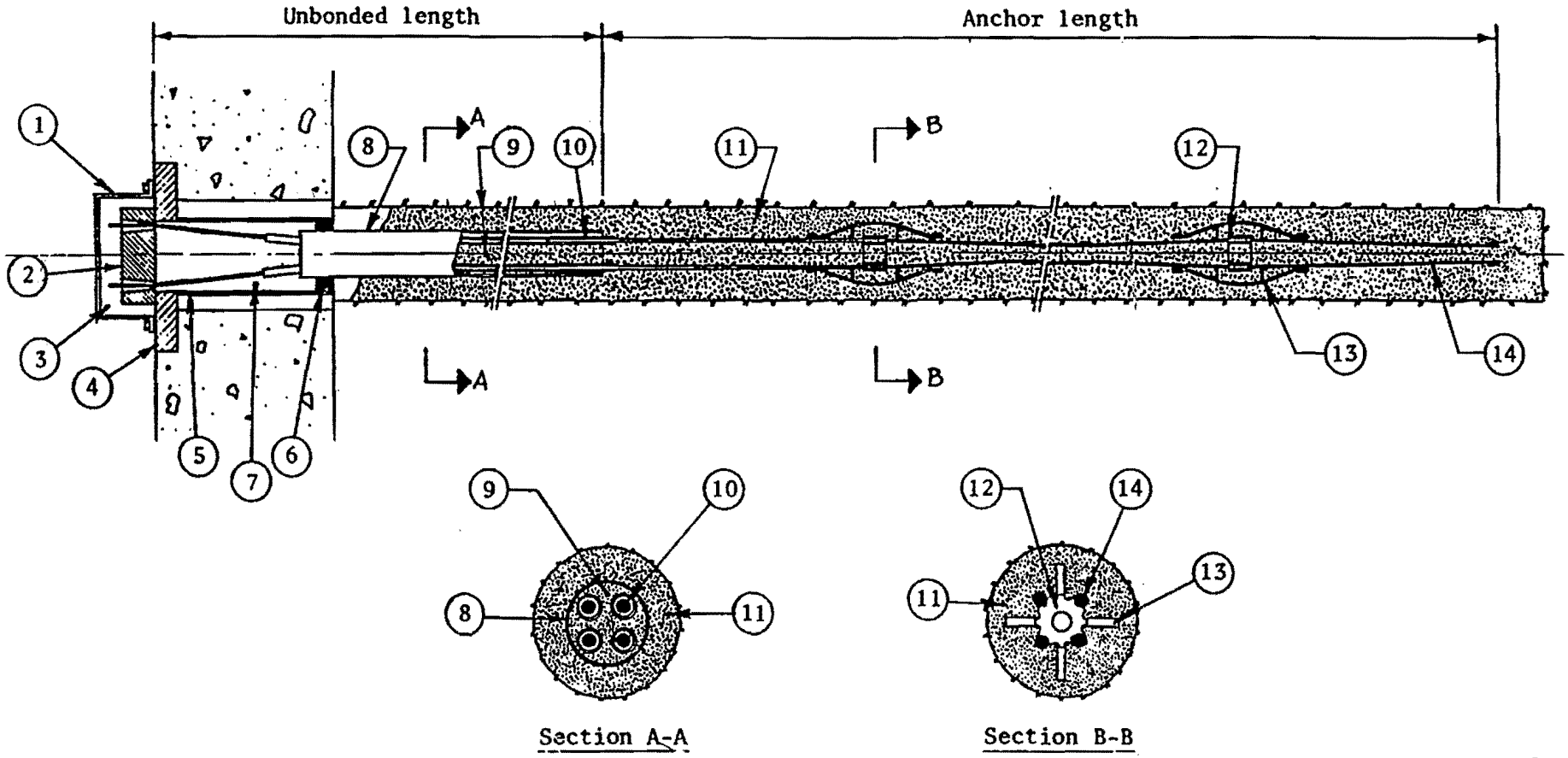

Legend:

1. Anchorage cover
2. Anchor head and wedges
3. Anticorrosion grease or grout
4. Bearing plate
5. Trumpet
6. Seal
7. Anticorrosion grease or grout
8. Steel, PVC or polyethylene tube
9. Grout
10. Individually greased & sheathed strands
11. Anchor grout
12. Spacer
13. Centralizer
14. Tendon

Figure 163. Simple Corrosion Protected Strand Tieback (Weatherby, 1982)

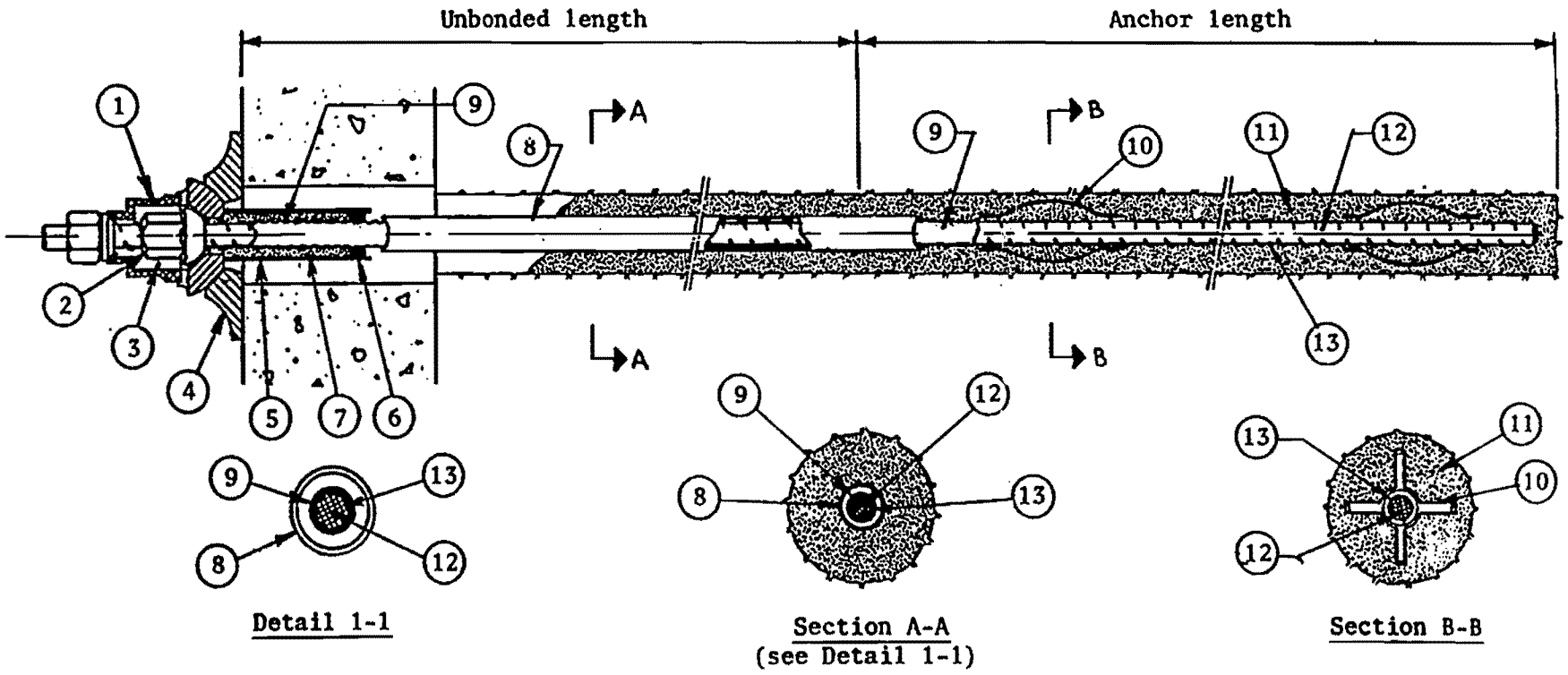

Legend:

1. Anchorage cover
2. Nut
3. Anticorrosion grease
4. Bearing plate
5. Trumpet
6. Seal
7. Anticorrosion grease or grout
8. PVC or polyethylene tube
9. Heat shrinkable tube
10. Centralizer
11. Anchor grout
12. Tendon
13. Electrostatically applied epoxy

Figure 164. Simple Corrosion Protected Bar Tieback (Weatherby, 1982)

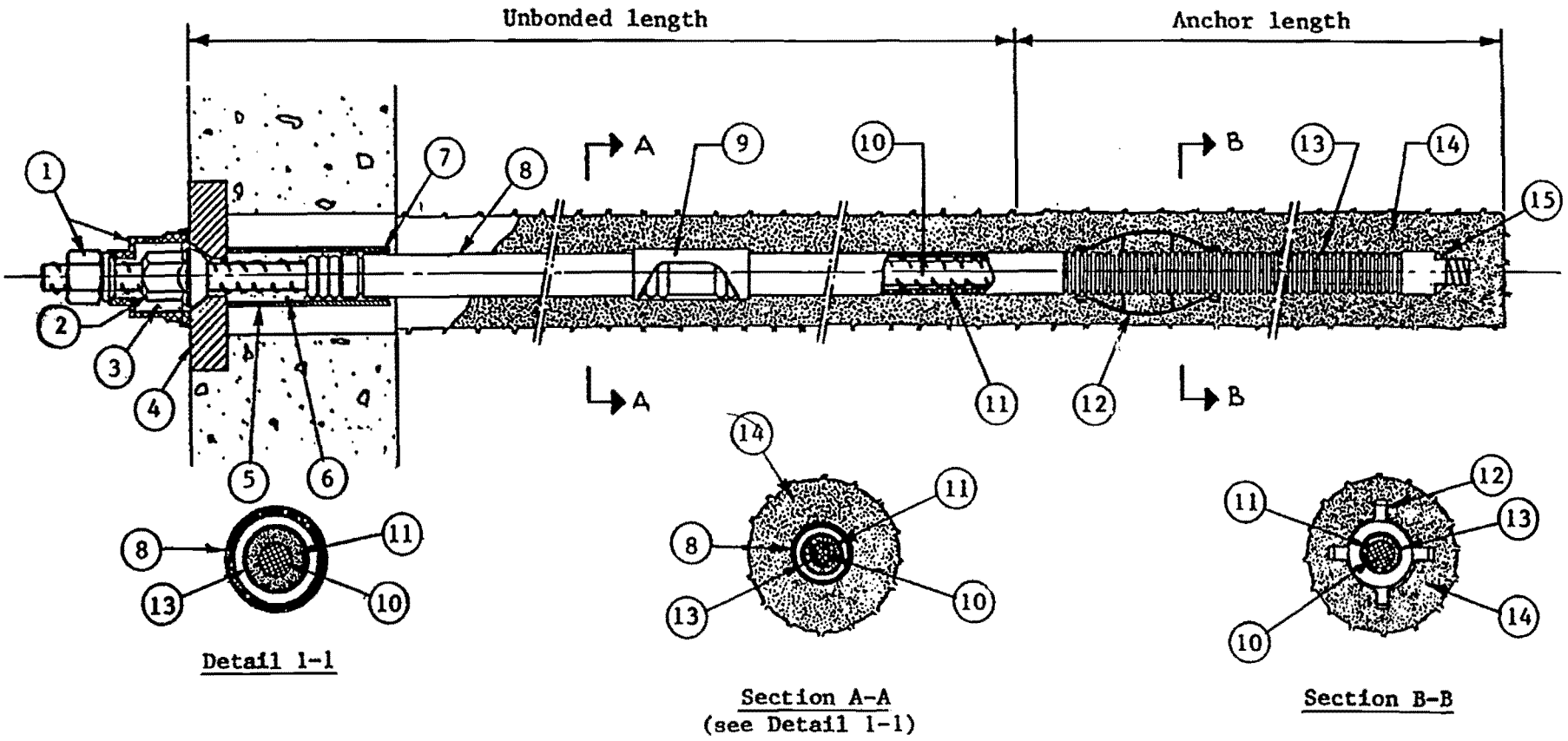

Legend:

1. Anchorage cover
2. Nut
3. Anticorrosion grease
4. Bearing plate
5. Trumpet
6. Anticorrosion grease or grout
7. Seal
8. PVC bond breaker
9. Protected bar coupler
10. Bar tendon
11. Encapsulation grout
12. Centralizers
13. Corrugated PVC
14. Anchor grout
15. End cap

Figure 165. Encapsulated Bar Tieback (Weatherby, 1982)

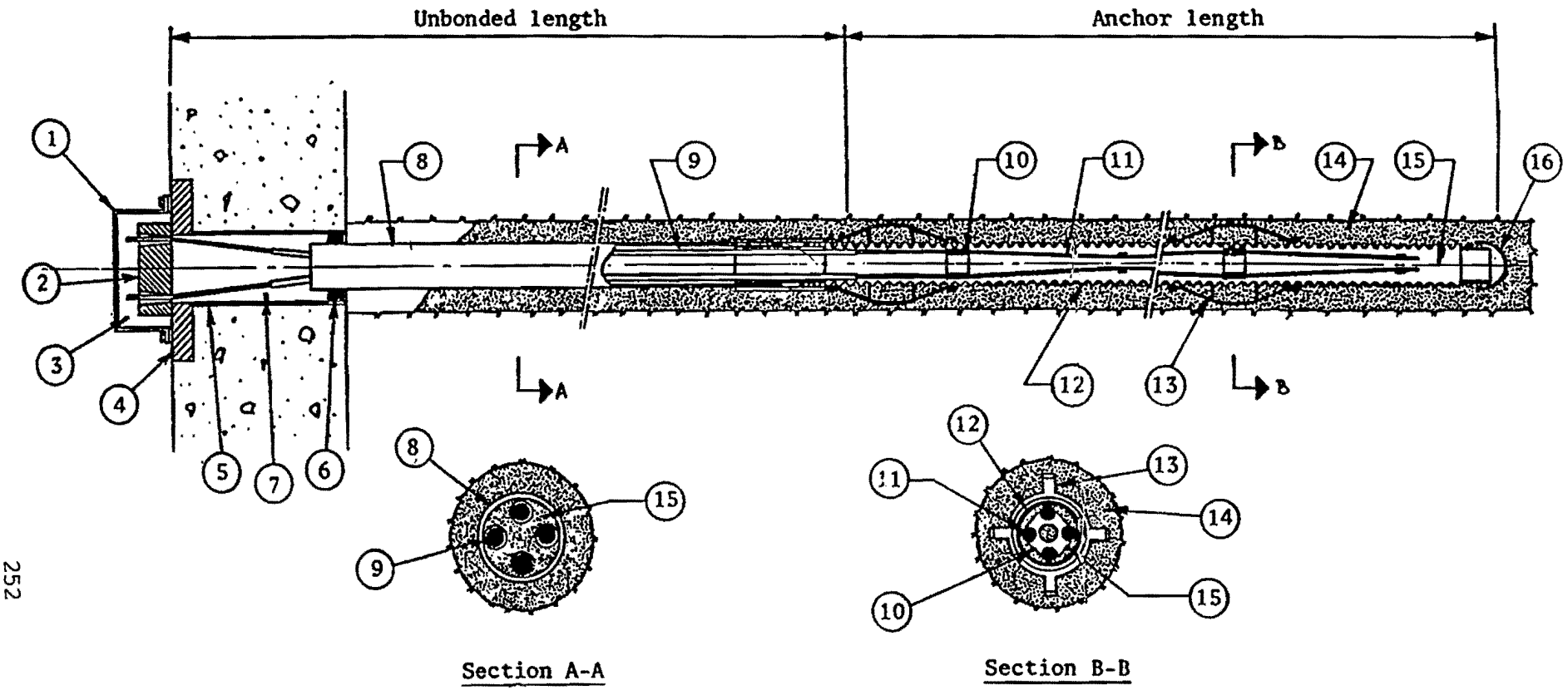

Legend:

1. Anchorage cover
2. Anchor head and wedges
3. Anticorrosion grease or grout
4. Bearing plate
5. Trumpet
6. Seal
7. Anticorrosion grease or grout
8. PVC or polyethylene tube
9. Individually greased & sheathed strands
10. Spacer
11. Strand tendon
12. Corrugated polyethylene or PVC
13. Centralizer
14. Anchor grout
15. Grout or polyester resin
16. End cap

Figure 166. Encapsulated Strand Tieback (Weatherby, 1982)

3.7.2.6.2 Epoxy

Epoxy exhibits eletrochemical durabilities as well as strength and protective qualities that make them suitable for corrosion protection. The effectiveness of the coated bars has been proven by pull-out tests and creep tests. Epoxy coated bars with average film thickness of 0.127 mm to 0.28 mm have shown acceptable bond strengths to cement grout. When used alone as a bonding agent between the tendon and the ground, resins can be formulated to deform without cracking, and are thus suitable for corrosion protection without the necessity of sheathing. Clifton et al. (1975) concluded that the optimum film thickness of epoxy coating on steel bars is 0.178 mm, with an acceptable deviation of 0.05 mm.

3.7.2.6.3 Fusion-Bonded Epoxy Coating

As an alternative to development of plastic material possessing the required strength and aging properties for use in ground anchor systems, fusion-bonded epoxy coatings on steel reinforcements have been used on a number of projects and provide an alternative solution (Elias,1990). These coatings need to be hard and durable to withstand abrasion under normal construction conditions and have strong bonding properties to the anchor tendon to long-term integrity. As our results in Section 3.5.7.4.8 showed, there is exceptional corrosion protection from the epoxy when the coating is intact.

3.7.2.7 Protective Systems of the Unbonded Length

Protection is achieved generally either by the injection of fluids to enclose the tendon or by pre-applied coatings, or by a combination of both. Injection of fluids, cement-based grouts, viscoelastic fluids, and grease have been used in unbonded length.

As protective systems in the unbonded length, impermeable polypropylene or polyethylene sheaths are also acceptable and commonly used where a higher degree of protection is required (Littlejohn, 1990). Sheaths are effective as coatings provided the internal annular space is filled with the appropriate resin, cementitious material, or grease to exclude the atmosphere (*Corrosion and Corrosion Protection of Prestressed Ground Anchorages*, 1986). Jointing systems should allow for injection of cementitious material or grease with simultaneous displacement of air.

3.7.2.8 Protective Systems of the Anchor Head

At the anchor head, the system is required to grip the strand or bar. This area is the most critical and must be protected from corrosion attack. Since, the environment at the anchor head is corrosive due to oxygen, moisture, and aggressive agents, most corrosion failures occur at the anchor head area. The basic principle is to enclose the exposed head and also to allow load change to occur in the anchor. In the inner head section, cement grouts are unsuitable due to the flow of water

through the anchor head area. The annular space around the tendon is normally filled with anticorrosion grease. The protection at this location is to ensure effective overlap with the free length protective system. In the outer head section, the protective system depends on the details of the stressing and locking method. Usually greases are used within plastic or steel caps where restressing is not required.

3.8 RECOMMENDATIONS

The literature available on anchor failures due to corrosion was searched and reviewed. It was found that the failures were due mainly to a lack of protection of the tendon and to bending of the tendon near the anchor head. About half of the failures occurred near the anchor head, about half within the unbonded length, and very few within the bonded length. The time to failure varied drastically from a few weeks to 31 years. It appears that there are a lot less failures today (1998) than there were 40 years ago because of the increase in knowledge; however, it is essential to ensure that proper protection against corrosion exists particularly around the anchor head and along the unbonded length.

Laboratory tests were performed on three different soils to check the influence of soil resistivity and soil pH on the corrosion of bare steel. Linear polarization resistance measurements and Tafel extrapolation methods were used to obtain the corrosion rate in each experiment. One natural clay, one natural sand, and one prepared porcelain clay were tested. For unprotected steel, the corrosion rate ($\dot{c}$) was found to be higher when the pH was less than 5 ($\dot{c} > 0.3$ mm/yr) than when the pH was more than 5. The corrosion rate was relatively constant for pH values between 5 and 10.

Laboratory tests were performed to check the influence of various coatings on the corrosion rate. The Electrochemical Impedance Spectroscopy test (EIS) was used to measure the corrosion rate in each experiment. It was found that the corrosion rate varied drastically from 0.34 mm/yr for bare steel to 10^{-8} mm/yr for steel covered with fusion-bonded epoxy with 3×10^{-3} mm/yr for steel covered with grout (Table 30). A variation in grout thickness from 5 mm to 20 mm did not change the corrosion rate. However, cracks in the grout increased the corrosion rate. It is clear from Table 30 that coatings improve the resistance of steel to uniform corrosion.

Table 30. Corrosion Rates and Ratios of Corrosion Rates for Five Conditions

Condition	No Coating	Sprayed Acrylic Coating	With Grouting	Painted Epoxy Coating	Fusion-Bonded Epoxy
Corrosion Rates (mm/y)	0.34	0.16	0.003	10^{-7}	10^{-8}
Ratio of Corrosion Rate	1	0.47	0.009	3×10^{-7}	3×10^{-8}

The decision of using particular types of protection depends on the soil at the site. It appears that when the soil has a low moisture content, a high resistivity and a high pH, then the anchor may be used without special protection and has a substantial useful life. When there is any question about the corrosiveness of the soil, some type of protection system should be used. Fusion-bonded epoxy appears to be an excellent candidate. If the grout bonding to the epoxy is a problem, it may be preferrable to use the double protection system: coating on the steel, grout layer covering the first coating, with that layer enclosed in a corrugated polymer.

For all new installations, it would be beneficial to install several test anchors that could be pulled at given times and examined. These anchors could be examined by an acoustic monitoring system that would identify when an anchor broke. Such a program would lead to useful long-term corrosion data in the field.

Resistivity and pH are indicators of corrosion potential but do not give the corrosion rate. The Electrochemical Impedance Spectroscopy test is proposed as a standard test to estimate the corrosion of a soil-anchor-protection system. This test gives a corrosion rate which can be used by the engineer to predict the useful life of the anchors.

4. REFERENCES

1. *ABAQUS User's and Theory Manuals*, 1992, Version 5.2, Hibbit, Karlson, and Sorensen Inc., Pawtucket, Rhode Island, NJ, U.S.A.
2. Atkinson and Van Droffelaar, 1982, "Corrosion and Its Control," NACE.
3. Bard, J., and Faulkner, L. R., 1980, *Electrochemical Methods*, Wiley, New York, pp. 183.
4. Bredenkemp, S., and Lytton, R., 1994, "Reduction of Sulfate Swell in Expansive Clay Subgrades in the Dallas District," Research Report 1994-5, Texas Transportation Institute, College Station, TX, U.S.A.
5. Briaud, J.-L., 1992, "The Pressuremeter," A. A. Balkema, Brookfield, VT, U.S.A.
6. Briaud, J.-L., 1993, "The National Geotechnical Experimentation Sites at Texas A&M University: Clay and Sand, Data Collected Until 1992," Research Report NGES-TAMU-001 to the Federal Highway Administration and the National Science Foundation, Civil Engineering, Texas A&M University, College Station, TX, U.S.A.
7. Broms, B. B., 1968, "Swedish Tieback System for Sheet Pile Walls," *Proceedings* of the 3rd Budapest Conference on Soil Mechanics and Foundation Engineering, pp 391-403.
8. Bustamante, M., and Doix, B., 1985, "Une Methode pour le Calcul des Tirants et des Micropieux Injectes," Bulletin de Liaison du Laboratoire des Ponts et Chaussees, No. 140, Nov.-Dec., LCPC, Paris, France.
9. Callahan, J. P., et al., 1970, "Bridge Deck Deterioration and Crack Control, *Journal of the Structural Division*, ASCE, Vol. 96, ST10, pp. 2021-2036.
10. *Canadian Foundation Engineering Manual*, 1985, 2nd Edition, Canadian Geotechnical Society, c/o BiTech Publishers, Ltd., Vancouver, B.C., Canada.
11. Casagrande, A., and Wilson, S. D., 1951, "Effect of Rate of Loading on the Strength of Clays and Shales at Constant Water Content," *Geotechnique*, London, England, 2(3), pp. 251-263.
12. Chaouch, A., and Briaud, J.-L., 1991, "Pull Out Test on a Drilled and Grouted Pile Loaded from the Top," Research Report to UNOCAL Corporation, Civil Engineering, Texas A&M University, College Station, TX, U.S.A.
13. Chaouch, A., and Briaud, J.-L., 1992, "Pull Out Test on a Drilled and Grouted Pile Loaded from the Bottom," Research Report to UNOCAL Corporation, Civil Engineering, Texas A&M University, College Station, TX, U.S.A.
14. Cheney, R. S., 1988, "Permanent Ground Anchors," Report FHWA-DP-68-1R, Federal Highway Administration, Washington, DC, U.S.A.
15. Chung, M., and Briaud, J.-L., 1993, "Behavior of a Full Scale Tieback Wall in Sand," Research Report to Schnabel Foundation and the Federal Highway Administration, Civil Engineering, Texas A&M University, College Station, TX, U.S.A.
16. Clifton, J. R., Beeghly, H. F., and Mathley, R. G., 1975, "Nonmetallic Coatings for Concrete Reinforcing Bars," U.S. Department of Commerce, National Bureau of Standards, Washington, DC.
17. Clough, W. G., 1984, "User's Manual for Program SOIL STRUCT," Department of Civil Engineering, Virginia Polytechnic Institute, Blacksburg, VA, U.S.A.
18. *Corrosion*, 1987, ASM International, Metals Handbook, Vol. 13, 9th Ed., Metals Park, OH.
19. *Corrosion and Corrosion Protection of Prestressed Ground Anchorages*, 1986, (FIP) Federation Internationale de la Precontrainte, Thomas Telford Ltd., London, England.

20. Duncan, J. M., Byrne, P. M., Wong, K. S., and Marby, P., 1980, "Strength, Stress-strain and Bulk Modulus Parameters for Finite Element Analyses of Stresses and Movements in Soil Mass," Report No. UCB/GT/80-01, University of California, Berkeley, CA, U.S.A.
21. Dunlop, P., and Duncan, J. M., 1970, "Development of Failure Around Excavated Slopes," *Journal of Soil Mechanics and Foundation*, ASCE, Vol. 96, No. 2, pp. 471-493.
22. EG&G Princeton Applied Research, 1982, "Basics of Corrosion Measurements," Princeton, NJ.
23. Elias, V., 1990, "Durability/Corrosion of Soil Reinforced Structures," Federal Highway Administration Report No. FWHA-RD-89-186.
24. Escalante, S. I., and Cohen, M., 1980, "Measuring the Rate of Corrosion of Reinforcing Steel in Concrete," National Bureau of Standards, NBSIR 80-2012, March.
25. Feld, J., and White, R. E., 1974, "Prestressed Tendons in Foundation Construction," *Prestressed Concrete Foundations and Ground Anchors*, Seventh FIT Congress, New York, NY, pp. 25-32.
26. Fontana, M. G., 1986, *Corrosion Engineering*, McGraw-Hill Book Co., New York, NY, U.S.A.
27. Halliburton, T. A., 1968, "Numerical Analysis of Flexible Retaining Structures," *Proceedings*, ASCE, Vol. 94, SM3, ASCE, New York, NY, U.S.A.
28. Hanna, T. H., 1982, *Foundation in Tension-Ground Anchors*, First Edition, McGraw-Hill Book Co., New York, NY.
29. Houghton, R. C., and Dietz, D. L., 1990, "Design and Performance of a Deep Excavation Support in Boston, Massachusetts," *Proceedings*, ASCE Specialty Conference on Design and Performance of Earth Retaining Structures, ASCE, New York, NY, U.S.A.
30. Houston, J. T., Atimtay, E., and Ferguson, P. M., 1982, "Corrosion of Reinforcing Steel Embedded in Structural Concrete."
31. Jennings, S., Mathewson, C. C., Yancey, T., and Briaud, J.-L., 1996, "The National Geotechnical Experimentation Sites at Texas A&M University, Clay and Sand: Geology," Research Report NGES-TAMU-005 to the Federal Highway Administration and the National Science Foundation, Civil Engineering, Texas A&M University, College Station, TX, U.S.A.
32. Jones, D. A., 1996, *The Principles and Prevention of Corrosion*, Prentice-Hall, 2nd Ed.
33. Kim, N.-K., and Briaud, J.-L., 1994, "A Beam Column Method for Tieback Walls," Research Report to Schnabel Foundation and the Federal Highway Administration, Civil Engineering, Texas A&M University, College Station, TX, U.S.A.
34. King, R. A., 1977, "A Review of Soil Corrosiveness with Particular Reference to Reinforcing Earth," Transport and Road Research Laboratory, Crowthorne, Supplementary Research Report No. 316.
35. Kramer, S. L., 1993, "Evaluation of Tieback Performance," Final Report Number WA-RD 269.1, Washington State Department of Transportation, Washington University, Seattle, WA, U.S.A.
36. Kulhawy, F. H., and Jackson, C. S., 1989, "Some Observations of Undrained Side Resistance of Drilled Shafts," *Foundation Engineering: Current Principles and Practices*, Vol. 2, ASCE, New York, NY, pp. 1011-1025.
37. Lim, Y. J., and Briaud, J.-L., 1996, "Three Dimensional Nonlinear Finite Element Analysis of Tieback Walls and of Soil Nailed Walls Under Piled Bridge Abutment," Report to the Federal Highway Administration and the Texas Department of Transportation, Department of Civil Engineering, Texas A&M University, College Station, TX, U.S.A.
38. Littlejohn, G. S., 1968, "Recent Developments in Ground Anchor Construction," *Ground Engineering*, Vol.1, Number 3, pp. 32-36 and 46.

39. Littlejohn, G. S., 1970, "Soil Anchors," Ground Engineering, *Proceedings* of an Institution of Civil Engineers Conference, ICE, London, England, pp. 36-40.
40. Littlejohn, G. S., 1990, "Ground Anchorage Practice," Design and Performance of Earth Retaining Structures, Geotechnical Special Publication No. 25, American Society of Civil Engineers, New York, NY, U.S.A., pp. 692-733.
41. Lockwood, M. E., 1988, "Retention System Monitoring Demonstration Project No. 68," Report for the Ohio Department of Transportation, Cincinnati, OH, U.S.A.
42. Marcontell, M., and Briaud, J.-L., 1994, "The National Geotechnical Experimentation Sites at Texas A&M University: Clay and Sand, Data Collected from January 1993 to July 1994," Volumes 1 and 2, Research Report NGES-TAMU-003 to the Federal Highway Administration and the National Science Foundation, Civil Engineering, Texas A&M University, College Station, TX, U.S.A.
43. Matlock, H., Bogard, D., and Lam, I., 1981, "BMCOL 76: A Computer Program for the Analysis of Beam-Columns Under Static Axial and Lateral Loading," Program developed at the University of Texas at Austin under grant from Fugro Inc., and documented at Ertec Inc., Long Beach, CA, U.S.A.
44. Meyer, A., 1977, Report on discussion to Session VI by J. M. Mitchell, *A Review of Diaphragm Walls*, Thomas Telford Ltd., London.
45. Miller, F. P., Foss, J. E., and Wolf, D. C., 1981, "Soil Survey: Their Synthesis, Confidence Limits, and Utilization for Corrosion Assessment of Soil," *Underground Corrosion*, ASTM STP 741, Edward Escalante, Ed., American Society for Testing and Materials, pp. 3-22.
46. Munger, D. F., Jones, P. T., and Johnson, J., 1990, "Temporary Tieback Wall," Bonneville Navigation.
47. Murff, J. D., 1980, "Pile Capacity in a Softening Soil," *International Journal for Numerical and Analytical Methods in Geomechanics*, Vol. 4, pp 185-189, John Wiley and Sons, New York, NY, U.S.A.
48. Neely, W. J., and Montague-Jones, M., 1974, "Pull-out Capacity of Straight-Shafted and Under-reamed Ground Anchors," Die Siviele Ingenieur in Suid-Africa, Jaargang 16, NR 14, pp. 131-134.
49. Nernberger, U., 1980, "Analyse und Auswertung von Schadensfallen an Spannstahlen," ("Analysis and Evaluation of Failure in Prestressed Steel"), Report No. 308, German Department of Transportation, pp. 248-295.
50. Nicholson, P. J., Uranowski, D. D., and Wycliffe-Jones, P. T., 1982, "Permanent Ground Anchors: Nicholson Design Criteria," Report FHWA/RD-81/151, Federal Highway Administration, Washington, DC, U.S.A.
51. Otta, L., Pantucek, M., and Goughnour, R. R., 1982, "Permanent Ground Anchors: Stump Design Criteria," Report FHWA/RD-81/152, Federal Highway Administration, Washington, DC, U.S.A.
52. Pfister, P., Evers, G., Guillaud, M., and Davidson, R., 1982, "Permanent Ground Anchors: Stump Design Criteria," Report FHWA/RD-81/150, Federal Highway Administration, Washington, DC, U.S.A.
53. Pope, D. H., 1986, "A Study of Microbiologically Influenced Corranda Practical Guide for Its Treatment and Prevention," Final Report, EPRI, CS-5495, Electric Power Research Institute, Palo Alto, CA.

54. Pope, D. H., and Morries, E. A., 1995, "Some Experiences with Microbiologically Influenced Corrosion of Pipelines," Materials Performance, 00134, No. 5, pp. 23-28.
55. Portier, J., 1974, "Protection of Tie-Backs Against Corrosion," *Prestressed Concrete Foundations and Ground Anchors*, Seventh FIT Congress, New York, NY, pp. 39-53.
56. Pourbaix, M., 1973, "Lectures on Electrochemical Corrosion."
57. Powers, W. F., and Briaud, J.-L., 1993, "Behavior of 10 Full Scale Ground Anchors Installed in Stiff Clay," Research Report to Schnabel Foundation and the Federal Highway Administration, Civil Engineering, Texas A&M University, College Station, TX, U.S.A.
58. Reese, L. C., and O'Neill, M. W., 1988, "Drilled Shafts: Construction Procedures and Design Methods," Report No. FHWA-41-88-042, Federal Highway Administration, Washington, DC, p. 564.
59. Romanoff, M., 1957, *Underground Corrosion*, NBS Circular 579, NTIS PB 168 350, U.S. Department of Commerce, National Bureau of Standards, April.
60. Sapio, G., 1975, "Comporamento di Tiranti de Ancoraggio in Formazioni de Argille pre Consolidate," XII Convegno Nationale de Geotecnica, Consenza, Italy.
61. Simon, P. A., and Briaud, J.-L., 1996, "The National Geotechnical Experimentation Sites at Texas A&M University: Clay and Sand, Soil Data in Electronic Form 1995-1996," Report to NGES-TAMU-006, Department of Civil Engineering, Texas A&M University, College Station, TX, U.S.A.
62. Soto, A. A., Briaud, J.-L., and Yeung, A.T., 1997, "Observed Long-Term Behavior of Permanent Ground Anchors in Clay and Sand," Report submitted to the Department of Civil Engineering of Texas A&M University for requirements of the degree of Master of Engineering, April.
63. Suroor, A. H. M., Yeung, A. T., and Briaud, J.-L., 1998, "Delayed Failure of Overconsolidated Clays Under Sustained Loads," Research Report, Department of Civil Engineering, Texas A&M University, College Station, TX, pp. 153.
64. Tao, C., and Briaud, J.-L., 1995, "The National Geotechnical Experimentation Sites at Texas A&M University: Clay and Sand, Soil Data in Electronic Form 1977 - 1995," Research Report NGES-TAMU-004 to the Federal Highway Administration and the National Science Foundation, Civil Engineering, Texas A&M University, College Station, TX, U.S.A.
65. Terzaghi, K., and Peck, R. B., 1967, *Soil Mechanics in Engineering Practice*, John Wiley and Sons, 2nd ed., New York, NY, U.S.A.
66. Tomashov, N. D., and Mikhailovsky, Y. N., 1959, *Corrosion*, 15, 77t.
67. Uhlig, H. H., and Revie, R. W., 1985, *Corrosion and Corrosion Control*, Wiley, New York, pp. 178-185.
68. Weatherby, D. E., 1982, "Tiebacks," Report FHWA/RD-82/047, Federal Highway Administration, Washington, DC, U.S.A.